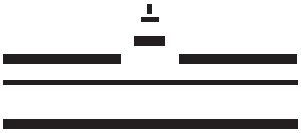

Westfälische
Wilhelms-Universität
Münster

Mass spectroscopy of hydrogen cluster-jets and beam density optimisation studies

Inaugural-Dissertation zur Erlangung des Doktorgrades
der Naturwissenschaften im Fachbereich Physik
der Mathematisch-Naturwissenschaftlichen Fakultät
der Westfälischen Wilhelms-Universität Münster

vorgelegt von
ESPERANZA DIANE KÖHLER
aus Wuppertal

– 2015 –

Dekan: Prof. Dr. C. Weinheimer
Erster Gutachter: Prof. Dr. A. Khoukaz
Zweiter Gutachter: Prof. Dr. D. Frekers

Tag der mündlichen Prüfung: 21.09.2015
Tag der Promotion: 21.09.2015

Zusammenfassung

Entscheidend für die Verwirklichung von Speicherringexperimenten ist die Beschaffenheit und Leistungsfähigkeit des internen Targets sowie das Verständnis für die Targetstrahleigenschaften, wie beispielsweise Geschwindigkeit, Dichte oder Masse. Umfassende Analysen dieser Größen ermöglichen Optimierungen des Targetdesigns für ein maximales Leistungsvermögen und liefern die Grundlage für präzise Datenanalysen und Simulationen. Die Entwicklung eines mit Wasserstoff betriebenen Cluster-Jet Targets für das $\overline{\text{P}}$ANDA (antiProton ANnihilation at DArmstadt) Experiment der zukünftigen internationalen Beschleunigeranlage FAIR (Facility for Antiproton and Ion Research) steht im Fokus dieser Arbeit. Detaillierte Untersuchungen der Clustergeschwindigkeiten, Flächendichten und Clustermassen führten zum Aufbau und Betrieb des weltweit leistungsfähigsten, mit Wasserstoff betriebenen Cluster-Jet Targets ($\overline{\text{P}}$ANDA Prototyp), das zudem tiefere Einblicke in den komplexen Clusterproduktionsprozess gewährt. Die Auswirkungen zwei verschiedener Produktionsprozesse zeigen sich deutlich innerhalb der Analyse der Clustereigenschaften. Diese sind verantwortlich für Geschwindigkeiten zwischen 200 m/s und 1000 m/s sowie für Flächendichten von 10^{10} Atomen/cm^2 bis zu mehr als 2×10^{15} Atomen/cm^2 infolge der Extraktion intensiver Kernstrahlen. Zudem ermöglichte die Entwicklung und der Einsatz eines Massenspektrometers die Untersuchung der Clustermassenverteilung und der mittleren Clustergröße. Der Clusterstrahl weist demnach eine logarithmisch normalverteilte Masse mit durchschnittlich 10^5 Atomen bis erwartungsgemäß mehr als 10^9 Atomen auf. Basierend auf den Resultaten dieser Arbeit und den damit verbundenen, sorgfältigen Optimierungsarbeiten wurde das Design und der Aufbau des finalen Cluster-Jet Targets für $\overline{\text{P}}$ANDA geprägt und ausgelegt. Die Voraussetzungen für $\overline{\text{P}}$ANDA, einschließlich des Zugangs zu höchsten Luminositäten, werden vollständig von diesem Target abgedeckt, das somit den aktuellen Qualitätsmaßstab der Cluster-Jet Target Technologie definiert.

Abstract

The realisation of a storage ring experiment hinges largely on the performance of the internal target and the precise knowledge of the target beam characteristics, e.g. the velocity, density, or mass. A comprehensive analysis of these parameters enables improvements of the target design for an optimal performance and provides the basis for an accurate data analysis and simulation.
This thesis focusses on the development of a hydrogen cluster-jet target for the $\overline{\mathrm{P}}$ANDA (antiProton ANnihilation at DArmstadt) experiment at the future international accelerator facility FAIR (Facility for Antiproton and Ion Research). The detailed investigation on the cluster velocity, areal density, and cluster mass lead to the most efficient hydrogen cluster-jet target worldwide ($\overline{\mathrm{P}}$ANDA prototype) and moreover to deeper insights into the complex cluster production process. The impact of two different production processes is in evidence within the study of the cluster beam characteristics and is responsible for cluster velocities ranging from 200 m/s to 1000 m/s as well as for areal densities within 10^{10} atoms/cm^2 up to more than 2×10^{15} atoms/cm^2 with the extraction of highly intense core beams. Moreover, it reveals log-normal distributed cluster masses with around 10^5 atoms to most likely more than 10^9 atoms on average. The final cluster-jet target for $\overline{\mathrm{P}}$ANDA was designed and constructed on the basis of the results gained throughout this work and the associated particular optimisation studies. It covers all requirements for $\overline{\mathrm{P}}$ANDA, including the access to the high luminosity mode, and defines the state of the art of cluster-jet target technology.

Contents

1. Introduction

Science is always searching for the truth and *the immediate point* [...] *is merely that the most obvious, ubiquitous, important realities are often the ones that are hardest to see and talk about* [Wal12]. The understanding of the strong force or strong interaction represents one of the biggest challenges in modern particle physics. The strong force is one of the four fundamental interactions in nature and interacts between all colour charge carrying particles, i.e. quarks and gluons, and is thus responsible for nucleons bound in the atomic nuclei. Being the most established theory regarding particle interactions, the standard model of particle physics comprises six quarks, namely: up, down, charm, strange, top, and bottom. Every quark can have one of the colour charges red, blue, or green. The strong interaction among them is mediated by eight gluons carrying a colour as well as an anticolour, and consequently interact strongly with each other. Quarks do not appear isolated and therefore cannot be observed individually, a phenomenon known as confinement. They occur in colour neutral combinations named hadrons and can be classified into two categories, baryons and mesons. Baryons, such as protons or neutrons, are composed of three quarks, whereas mesons contain a quark and an antiquark. The fundamental theory describing the strong force is called Quantum ChromoDynamics (QCD). It allows exotic hadrons, colour neutral states, that do not fit the simple and usual hadron model. This includes, for instance, quark molecules, hybrids containing a quark-antiquark pair with an excited gluon, or pure gluonic states called glueballs (cf. Chapter 2). The observation and investigation of hadrons and especially exotic hadrons will allow insights into the nature of strong interaction. In order to progress into a mass region where exotic hadrons are accessible, antiproton annihilation experiments at an accelerator facility with a high momentum range of more than $2\,\mathrm{GeV}/c$ [PAN12a] are required.

The $\overline{\mathrm{P}}$ANDA (antiProton ANnihilation at DArmstadt) experiment, which will be installed at the High Energy Storage Ring (HESR) of the future Facility for Antiproton and Ion Research (FAIR) at Darmstadt (Germany), will face this challenge. Cooled antiprotons in a momentum range of $1.5\,\mathrm{GeV}/c$ to $15\,\mathrm{GeV}/c$ [PAN12a] will interact with the protons of an internal target. The resulting mass range and scientific programme will allow completely new insights into the physics of strong interaction (cf. Chapter 3).

$\overline{\text{P}}$ANDA is a fixed target experiment and will operate with two different internal target types, a cluster-jet and a pellet target, both windowless cryogenic targets. In either case, the cooled target material passes a target specific nozzle, which defines the characteristics of the resulting target beam. The cluster-jet target provides a homogeneous supersonic beam, which is constant in time. The containing clusters are particles in the nanometre scale. However, the pellet target supplies a high frequency beam of tiny frozen droplets with a diameter of a few ten micrometre [W$^+$07]. Depending on the experimental programme and the required target density, both targets provide significant advantages.

Internal targets are installed directly at the storage ring, where the accelerator beam will interact with the target beam after each revolution. Therefore, internal targets must fulfil challenging and partially contrary requirements. The target particles must be closed and localised to prevent an excessive residual gas background. Furthermore, the areal target density or thickness has to be, in case of the $\overline{\text{P}}$ANDA experiment, distinctly below $10^{16}\,\text{atoms/cm}^2$ [PAN12a], to avoid large beam heating effects, that cannot be compensated with the available beam cooling techniques (e.g. electron and stochastic cooling). On the other hand, the target thickness must be high enough to achieve high luminosities (up to $2 \times 10^{32}\,\text{cm}^{-2}\text{s}^{-1}$ [PAN12a]) or event rates for studies of rare processes. To ensure an optimal exploitation of the injected antiproton beam at $\overline{\text{P}}$ANDA, a maximal target thickness of $4.5 \times 10^{15}\,\text{atoms/cm}^2$ [PAN12a] is necessary. In addition, the internal $\overline{\text{P}}$ANDA target source must be installed at a distance of 2.1 m from the interaction point to achieve almost 4π acceptance of the $\overline{\text{P}}$ANDA detector. Gas-jet targets, thin solid foils, or wires are thus completely inappropriate for the $\overline{\text{P}}$ANDA experiment (cf. Chapter 4).

As already stated in a previous diploma thesis [Köh10], the hydrogen cluster-jet target prototype for $\overline{\text{P}}$ANDA was built up at the University of Münster in complete $\overline{\text{P}}$ANDA geometry and was set successfully into operation. The entire prototype contains the cluster source, an interaction chamber with a beam diagnostic system as well as a beam dump. In context of this thesis, systematic measurements on cluster-jet beams were carried out, referring in particular to cluster velocity measurements (published in [T$^+$13]) and the current maximal target thickness in the order of $8 \times 10^{14}\,\text{atoms/cm}^2$ (published in [T$^+$11]) at the required distance of 2.1 m from the cluster source.

The prototype still holds a lot of potential for improvements, such as the increase of the maximal thickness or the reduction of the beam size and thus background at the future interaction point. Moreover, a possibility to run target adjustment checks during the operation at $\overline{\text{P}}$ANDA is desirable as well as the visualisation of the target/accelerator beam overlap region (cf. Chapter 5). Besides the target thickness, investigations on the cluster mass are also essential, particularly because the cluster characteristics depend

strongly on the cluster size (cf. Chapter 6). All mentioned points were further developed, improved, and mastered in the context of this thesis as follows:

The improvement of the target thickness occurs via the observation and extraction of highly intense core beams with a novel nozzle tilting system. Systematic studies of these intensive core beams concentrate in particular on their thickness, reproducibility, and stability with the aim to get access to the high luminosity mode at $\overline{\mathrm{P}}$ANDA (cf. Section 5.2).

Moreover, investigations on the cluster beam size and its shape are carried out within the master thesis of A.-K. Hergemöller [Her13] and this thesis, with the intention to minimise the target extension without restrictions on the thickness and the vertex zone. The advantage of this approach is the reduction of background reactions for a precise vertex reconstruction and a prolonged lifetime of the antiproton beam at $\overline{\mathrm{P}}$ANDA (cf. Section 5.3).

This work as well as the bachelor thesis of A. Zannotti [Zan13] adress efforts to realise a two-dimensional real time observation and monitoring of an ionised cluster-jet beam with MicroChannel Plates (MCPs). The objective is to run target beam adjustment checks during target operation and to develop a new diagnostic tool for vertex zone studies at storage ring experiments (cf. Section 5.3.3, published in [K$^+$14b]).

Additionally, the investigation of the cluster mass presents another main focus of this thesis. For this purpose a mass diagnostic technique via retardation field was applied to delimit the cluster mass at various temperature and pressure settings and to gain conclusions on the cluster mass distribution (cf. Section 6.2).

The detailed analysis of the presented cluster beam characteristics, which are emphasised within this thesis, enables the development, construction, and optimal performance of the final $\overline{\mathrm{P}}$ANDA cluster-jet target. Furthermore, the results yield insights into the complex cluster production process and are fundamental for data analysis and simulations, especially with regard to the $\overline{\mathrm{P}}$ANDA experiment.

2. Fundamentals of exotic hadrons

The understanding of the strong force constitutes a major challenge in modern particle physics. This is mainly due to the fact that the strong interacting particles, the quarks, cannot be isolated and observed individually. Through this effect, called confinement, they only occur in colour neutral states (hadrons), which are either composed of three quarks (baryons) or contain a quark-antiquark pair (mesons). In order to discover the nature of strong interaction, the investigation of 'unusual' particles that do not fit the simple hadron model represents a promising opportunity. The $\overline{\text{P}}$ANDA (antiProton ANnihilation at DArmstadt) experiment at the future Facility for Antiproton and Ion Research FAIR at Darmstadt (Germany) has been designed in order to study hadrons as well as exotic particles. The annihilation of antiprotons of the accelerator beam with the protons of the internal cluster-jet target, which is emphasised in this thesis, will open a way for further investigations on hybrids, quark molecules, glueballs, and more.

2.1. Strong interaction

The strong force belongs to the four fundamental interactions and has an effect on all strong charge carrying (anti)particles. Strong charge, also known as colour charge, is a quantum number, which can assume the discrete values: (anti)red, (anti)blue, and (anti)green. Colour charged particles cover quarks, colour neutral quark systems, named hadrons, and the strong interaction mediating particles, the gluons.
A quark is a charged, point-like elementary particle with spin 1/2, which carries a colour. The standard model comprises six quark flavours (see Figure 2.1): up, down, charm, strange, top, and bottom.

Quarks cannot be separated and studied individually due to a phenomenon known as (colour) confinement. The required energy to separate a single quark from a hadron is so high that the creation of a quark-antiquark pair becomes energetically favourable. This effect is illustrated in Figure 2.2 by the bag model [MK02], where the colour field, e.g. between a quark-antiquark pair, forms a narrow tube, splits, and a second quark-antiquark pair forms. The colour field is induced by gluon-gluon interactions.

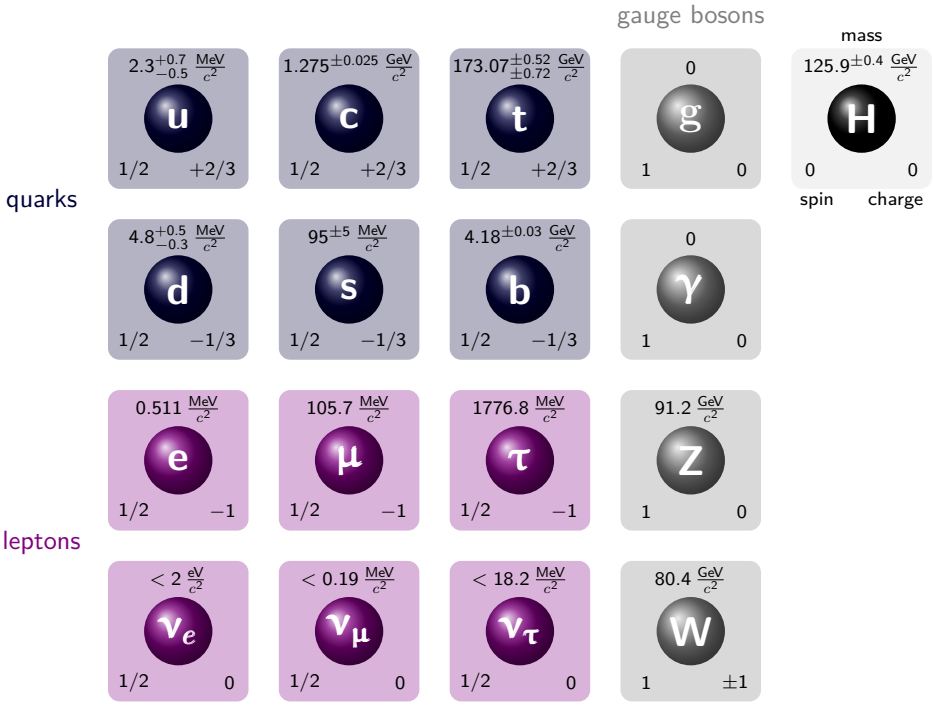

Figure 2.1.: The standard model (extracted from [B$^+$on]), which covers the elementary particles such as **quarks** - up (u), down (d), charm (c), strange (s), top (t), bottom (b), **leptons** - electron (e), electron neutrino (ν_e), muon (μ), muon neutrino (ν_μ), tauon (τ), tauon neutrino (ν_τ) as well as the **gauge bosons** - gluon (g), photon (γ), Z boson (Z) and W boson (W) and finally the **Higgs boson** (H), which explains the origin of mass (François Englert and Peter W. Higgs were awarded for the Nobel prize in physics 2013 [Nobc] for the theoretical description of the Higgs mechanism).

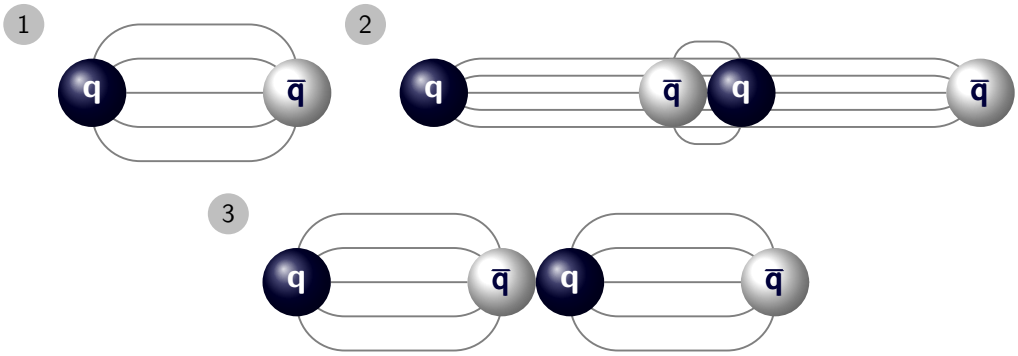

Figure 2.2.: Bag model: Hadrons are considered as bag-shaped, colour neutral volumes inside the non-perturbative Quantum ChromoDynamics (QCD) vacuum. Among a quark-antiquark pair exists a colour field (1) comparable to the electromagnetic field in Quantum ElectroDynamics (QED). The attempt to separate the quark-antiquark pair yields to the detortion of the colour field into a narrow tube (2). The necessary energy for a complete separation vastly exceeds the energy required to produce another quark-antiquark pair (3).

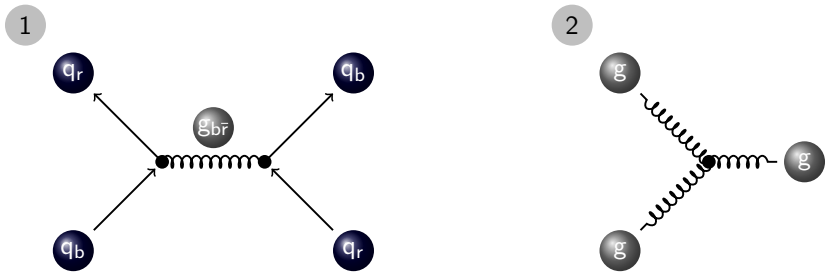

Figure 2.3.: (1) Quark-gluon interaction: Colour exchange between two quarks with red $\mathsf{q_r}$ and blue colour $\mathsf{q_b}$ mediated by a massless gauge boson, the gluon $\mathsf{g_{b\bar{r}}}$. (2) Gluon-gluon self interaction: Gluons carry colour charge (colour and anticolour) and also mediate the strong interaction among themselves.

Gluons are massless gauge bosons with spin 1 and mediate the strong interaction between quarks and themselves (see Figure 2.3), because they also carry a colour charge – both, colour and anticolour. Quantum ChromoDynamics (QCD), a non-abelian gauge theory, provides a theoretical quantum field description of the strong force. According to the SU(3) colour group, there are eight gluons mediating a colour change between quarks and gluons within the composite particles, the hadrons. One possible description of the colour states is: $\mathrm{r\bar{g}}$, $\mathrm{r\bar{b}}$, $\mathrm{g\bar{r}}$, $\mathrm{g\bar{b}}$, $\mathrm{b\bar{r}}$, $\mathrm{b\bar{g}}$, $\sqrt{1/2}(\mathrm{r\bar{r}}-\mathrm{g\bar{g}})$, $\sqrt{1/6}(\mathrm{r\bar{r}}+\mathrm{g\bar{g}}-2\mathrm{b\bar{b}})$ [P$^+$08] with the colours red r, green g, blue b, and the anticolours antired $\bar{\mathrm{r}}$, antigreen $\bar{\mathrm{g}}$, and antiblue $\bar{\mathrm{b}}$. The colour singlet state $\sqrt{1/3}((\mathrm{r\bar{r}}+\mathrm{g\bar{g}}+\mathrm{b\bar{b}})$ is invariant against a colour change, because it symmetrically comprises three colours and three anticolours.

The Lagrangian of QCD $\mathcal{L}_{QCD}$ [B$^+$on] can be described by

$$\mathcal{L}_{QCD} = \sum_q \overline{\Psi}_{q,a} \left(i\gamma^\mu \partial_\mu \delta_{ab} - g_s \gamma^\mu t^C_{ab} \mathcal{A}^C_\mu - m_q \delta_{ab} \right) \Psi_{q,b} - \frac{1}{4} F^A_{\mu\nu} F^{A\mu\nu} \tag{2.1}$$

with the components:

$\Psi_{q,a}$	quark field spinors for a quark with flavour q and mass m_q
a, b	colour index running from $a, b = 1$ to $N_c = 3$ (three colours)
γ^μ	Dirac γ-matrices
δ_{ab}	Dirac delta function
g_s	coupling constant
t^C_{ab}	eight 3×3 matrices (generators of SU(3)$_{\text{colour}}$)
$\mathcal{A}^C_\mu$	gluon fields with C running from 1 to $N_c^2 - 1 = 8$ (eight gluons)
$F^A_{\mu\nu}$	field tensor (the greek indices run over 0, 1, 2, and 3).

The field tensor $F^A_{\mu\nu}$ is given by

$$F^A_{\mu\nu} = \partial_\mu \mathcal{A}^A_\nu - \partial_\nu \mathcal{A}^A_\mu - g_s f^{ABC} \mathcal{A}^B_\mu \mathcal{A}^C_\nu, \tag{2.2}$$

where f^{ABC} are structure constants of the SU(3) group. The main difference between the Lagrangian of Quantum ElectroDynamics (QED) and QCD is the field tensor $F^A_{\mu\nu}$ and the consideration of the self-interaction of gluons. The essential parameters in QCD are the quark masses m_q and the coupling constant g_s or according to QED $\alpha_s = g_s^2/4\pi$.
In Quantum Field Theory (QFT) the coupling 'constant' α_s, which describes the strength of the interaction between quarks and gluons, is not a constant. In first order, it can approximately be described by [Loh05]

$$\alpha_s = \frac{12\pi}{(33 - 2N_f) \ln |q^2/\Lambda^2|} \tag{2.3}$$

with N_f being the number of quark flavour, q^2 the momentum transfer, and $\Lambda \approx 250\,\mathrm{MeV}/c$ [P$^+$08] the renormalisation scale, a momentum scale at which the coupling becomes strong (cf. Figure 2.4 (1)). The quark-antiquark potential results in

$$V_s = -\frac{4}{3}\frac{\alpha_s}{r} + kr, \tag{2.4}$$

where r is the distance and k the QCD string tension (cf. Figure 2.4 (2)). For small $|q^2|$-values, which correspond to a large distance r, the coupling constant α_s becomes very large (confinement). At a sufficiently large distance, the resulting energy density allows the formation of a new quark-antiquark pair. For increasing $|q^2|$-values, thus shorter distances, α_s becomes very small and the quark-antiquark bonding gets asymptotically weaker (asymptotic freedom).

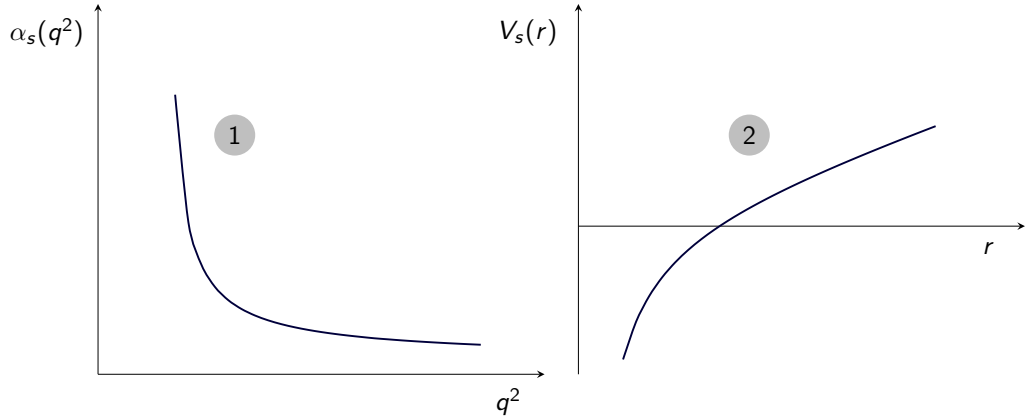

Figure 2.4.: Schematic course of the coupling constant $\alpha_s(q^2)$ (1) and the quark-antiquark potential $V_s(r)$ (2). The coupling constant becomes very large for decreasing $|q^2|$-values (large distance r, confinement) and small for increasing $|q^2|$-values (short distances, asymptotic freedom). The world average value amounts $\alpha_s(\mathrm{M}_\mathrm{Z}^2) = 0.1185 \pm 0.0006$ [B$^+$on]).

2.2. Hadron zoo

Due to colour confinement, quarks cannot be observed in isolation and only occur in composite, colour neutral states named hadrons which can be categorised into baryons and mesons. The most prominent baryons are the two nucleons, proton and neutron. All baryons consist of three quarks and due to the fermionic character of their constituents, they have half integer spin and underlie the Pauli exclusion principle for fermions. In the baryon case, a colour neutral state is composed of red, green, and blue coloured quarks. Mesons contain a quark-antiquark pair and belong to the category of bosons (integer spin particles). In this case, it is possible to form a colour neutral state through the combination of a colour and an anticolour.
The hadron structure can be described by the SU(3) flavour symmetry, considering the three lightest quarks – up, down, and strange – which have the baryon number +1/3 and differ in their isospin and strangeness quantum number. Baryons and mesons can further be classified according to the total angular momentum J and parity P, a multiplicative quantum number. The total angular momentum $\vec{J}$ is given by the total spin $\vec{S}$ and total orbital angular momentum $\vec{L}$ via

$$\vec{J} = \vec{S} + \vec{L}. \tag{2.5}$$

The parity $P(\mathsf{q}) = 1$ is assigned to quarks and $P(\overline{\mathsf{q}}) = -1$ to antiquarks, thus the parity of a baryon is given by

$$P(\mathsf{qqq}) \quad = \quad P(\mathsf{q})P(\mathsf{q})P(\mathsf{q})(-1)^{\ell} = (-1)^{\ell} \tag{2.6}$$

with an orbital angular momentum $\ell = 0$ for ground states and $\ell > 0$ for radially excited states. Similarly, the parity of the meson can be expressed as

$$P(\mathsf{q}\overline{\mathsf{q}}) = P(\mathsf{q})P(\overline{\mathsf{q}})(-1)^{\ell} = (-1)^{\ell+1}. \tag{2.7}$$

The charge conjugation, or rather C-parity, is defined by

$$C = (-1)^{\ell+s}, \tag{2.8}$$

only for $\mathsf{q}\overline{\mathsf{q}}$ states with quarks and their own antiquarks (isospin $I = 0$) with spin $s = 1$ for parallel and $s = 0$ for antiparallel quark spin combination.

With the quantum numbers $J^{P(C)}$, the hadrons can be classified in multiplets, as depicted in Figure 2.5. This includes for example particles of the baryon octet ($1/2^+$) and decuplet ($3/2^+$) as well as pseudoscalars $\left(0^{-(+)}\right)$ and vector mesons $\left(1^{-(-)}\right)$. Of course, there are also particles including a charm or a bottom quark. Mesons with only one charm quark (as heaviest constituent) are called D mesons, whereas mesons with only one bottom quark (as heaviest constituent) are named B mesons.

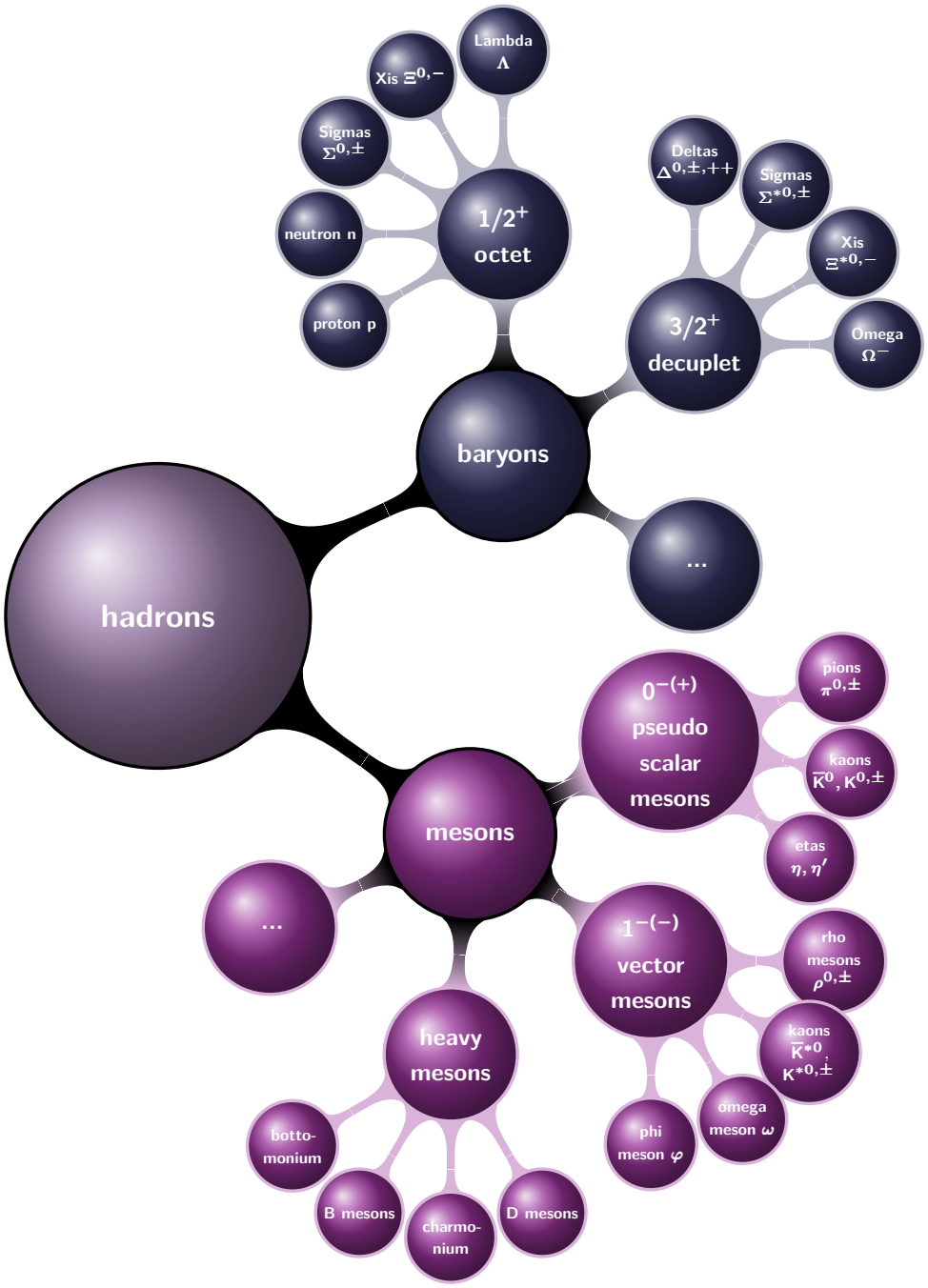

Figure 2.5.: The hadron zoo separated into a selection of baryons and mesons. The baryons are further categorised into their octet ($J^P = 1/2^+$) and decuplet ($J^P = 3/2^+$) members, consisting of the three lightest quarks, up, down, and strange. The mesons are classified in $J^{P(C)}$ multiplets, whereas the pseudoscalar $0^{-(+)}$ and vector $1^{-(-)}$ mesons are both states with $\ell = 0$, considering the lightest quarks. Furthermore, there are mesons with only one charm-quark (as heaviest constituent) called D-mesons or mesons with only one bottom-quark (as heaviest constituent), the B-mesons. Mesons consisting of their own quark and antiquark are called quarkonia, in particular charmonium and bottomonium.

Moreover, there are states with a quark and its own antiquark (quarkonia), the charmonium containing a charm and anticharm quark or bottomonium whose constituents are a bottom and antibottom quark. A toponium state does not exist, because the top quark decays weakly before a bound state can be formed. Light quarkonia, such as the mesons η and η', only occur as mixed states.
In addition to the valence or constituent quarks of a hadron, that primarily determine the hadron's properties, there are virtual quark-antiquark pairs, the sea quarks. The gluons, which are the strong force mediating particles, provide the quark cohesion inside hadrons and can temporarily split into sea quarks (cf. Figure 2.6). Valence quarks exhibit through the binding inside a hadron a higher mass than bare quarks, also known as current quarks (listed in the standard model in Fig. 2.1).

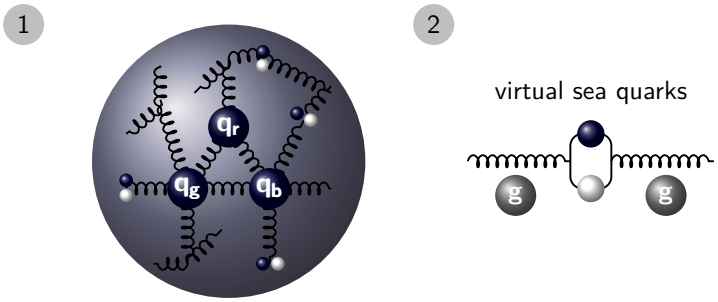

Figure 2.6.: (1) Baryon with valence quarks q_r, q_g, q_b, which contributes to its quantum number, in a sea of gluons and virtual quark-antiquark pairs. (2) Within the baryon the gluon g can split into a virtual quark-antiquark pair, the sea quarks, whereas their annihilation results again in a gluon.

2.3. The exotics

According to various QCD models, e.g. lattice QCD, bag model, flux tube model, QCD sum rules etc., more colour neutral states in addition to baryons and mesons are possible. The prediction of non-standard hadrons – like hybrids, quark molecules, tetraquarks, or glueballs – demands for experimental evidence. Figure 2.7 presents a selection of exotic hadrons and their constituents, in comparison to the baryon and meson structure.

2.3.1. Experimental evidence

Hybrids

Mesons with excited gluonic degrees of freedom are called hybrids, often denoted as $q\bar{q}g$, where g is representative for the excitation of the gluon field between the quark-antiquark pair $q\bar{q}$. Of particular interest is the possibility that hybrids could occur in exotic quantum numbers which are not accessible for a $q\bar{q}$ state, such as $J^{PC} = 0^{--}$, 0^{+-}, 1^{-+}, 2^{+-}, 3^{-+} etc. [Y+06a, AT04] compared to the pseudoscalar 0^{-+}, scalar 0^{++}, vector 1^{--}, axial $1^{+\pm}$,

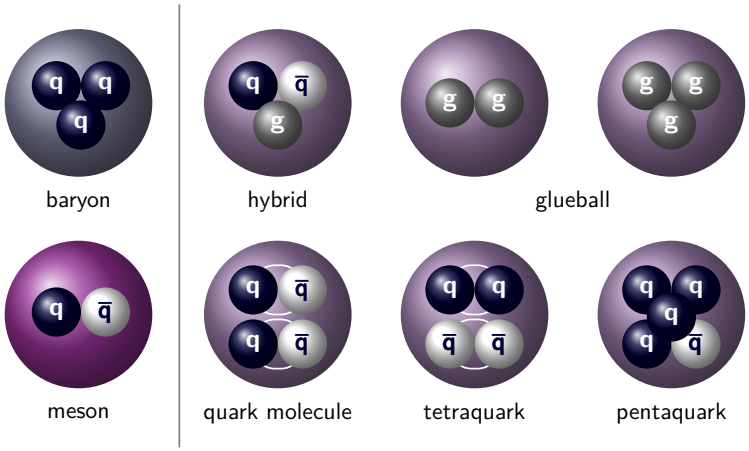

Figure 2.7.: Selection of exotic hadrons and their naive constituents compared to the baryon and meson states.

or tensor mesons 2^{++}. Depending on the model, light-quark hybrids are predicted to be in a mass range around $1.4\,\mathrm{GeV}/c^2$ (bag model) or between $1.8\,\mathrm{GeV}/c^2$ and $1.9\,\mathrm{GeV}/c^2$ (lattice QCD) [B$^+$on] and references therein. The states $\pi_1(1400)$ and $\pi_1(1600)$ are often proposed to be possible light-quark hybrids with exotic quantum number 1^{-+}. The Brookhaven National Laboratory (BNL) studied these states at $18.3\,\mathrm{GeV}/c$ via the decay mode $\eta\pi$ and $\rho\pi/\eta'\pi$ and other experiments confirmed the existence of these resonances [Kle00, AT04] (see Table 2.1). However, both states decay into two s-waves ($\ell = 0$) mesons and the flux tube model predicts the decay into an s-wave and a p-wave ($\ell = 1$), so that $\pi_1(1400)$ and $\pi_1(1600)$ might be quark molecules as well.

J^{PC}	candidate	decay channel	reaction	experiment/collaboration
1^{-+}	$\pi_1(1400)$	$\eta\pi$	$\pi^- p \to \eta\pi^- p$	BNL E852 [T$^+$97, C$^+$99]
			$\bar{p}n \to \pi^-\pi^0\eta$	Crystal Barrel [A$^+$98a]
			$\bar{p}p \to \pi^0\pi^0\eta$	Crystal Barrel [A$^+$99]
1^{-+}	$\pi_1(1600)$	$\rho\pi$	$\pi^- p \to \pi^+\pi^-\pi^- p$	BNL E852 [A$^+$98b, C$^+$02]
		$\eta'\pi$	$\pi^- N \to \pi^-\eta' N$	VES [Kho00]
			$\pi^- p \to \pi^-\eta' p$	BNL E852 [I$^+$01]
1^{--}	Y(4260)	$J/\Psi\pi^+\pi^-$	$e^+e^- \to \gamma_{ISR} J/\Psi\pi^+\pi^-$	BABAR [A$^+$05a], Belle [Y$^+$07]

Table 2.1.: Experimental evidence for the hybrid candidates $\pi_1(1400)$, $\pi_1(1600)$ [Kle00, AT04], and Y(4260) [Y$^+$06a].

Charmonium hybrids are expected to be at $4.34\,\mathrm{GeV}/c^2$ and bottomonium hybrids in a mass range of $10.7\,\mathrm{GeV}/c^2$ to $11.0\,\mathrm{GeV}/c^2$ [KZ07] and references therein. A possible candidate for a charmonium hybrid is the Y(4260) state, observed by the BABAR and also by the Belle collaboration. They studied the Y(4260) state in Initial State Radiation (ISR) $e^+e^- \to \gamma_{\mathrm{ISR}}e^+e^-$, where $e^+e^- \to \mathrm{Y}(4260) \to J/\Psi\pi^+\pi^-$ [A$^+$05a, Y$^+$07]. Y(4260) is also suggested to be a $\mathrm{D}\overline{\mathrm{D}}$ molecule.

Quark molecules, tetra-, and pentaquarks

Multiquark hadrons can occur as a meson-meson bound state (quark molecule $\mathsf{q\bar{q}q\bar{q}}$), they can cluster to diquark-antidiquark states (tetraquarks $\mathsf{qq\bar{q}\bar{q}}$), or they consist of four quarks and one antiquark (pentaquark $\mathsf{qqqq\bar{q}}$).
Light quark molecules are expected to be below $1\,\mathrm{GeV}/c^2$ [B$^+$on] and references therein. The nature of the frequently observed $\mathrm{a}_0(980)$ and $\mathrm{f}_0(980)$ states with $J^{PC} = 0^{++}$ is often interpreted to be four quark states or $\mathrm{K}\overline{\mathrm{K}}$-molecules [Y$^+$06a]. The dominant decay channel is $\mathrm{a}_0(980) \to \eta\pi$ and $\mathrm{f}_0(980) \to \pi\pi$, but $\mathrm{K}\overline{\mathrm{K}}$ and $\gamma\gamma$ are also be seen for both. The charmonium-like states X(3872) [C$^+$03], Y(4260) [Y$^+$07], and the charged $\mathrm{Z}^{\pm}(3900)$ as well as $\mathrm{Z}^{\pm}(4430)$ [C$^+$08], all observed by Belle, are possible quark molecules containing a charm-anticharm pair in combination with two light quarks. X(3872) (also confirmed by BABAR [A$^+$05b]) and $\mathrm{Z}^{\pm}(4430)$ are discovered via the exclusive decay of a B-Meson, namely $\mathrm{B}^{\pm} \to \mathrm{K}^{\pm}\pi^+\pi^- J/\Psi$ or rather $\mathrm{B} \to \mathrm{K}\pi^{\pm}\Psi'$ within the decay channels $\mathrm{X}(3872) \to \pi^+\pi^- J/\Psi$ and $\mathrm{Z}^{\pm}(4430) \to \pi^{\pm}\Psi'$. The investigation of the intermediate states of $\mathrm{Y}(4260) \to \pi^-\pi^+ J/\Psi$ indicates that the decay goes through the charged $\mathrm{Z}^{\pm}(3900)$ (also confirmed by BESIII [A$^+$13]) which in turn decays to $\pi^{\pm} J/\Psi$ [L$^+$13]. In addition, Belle observed two charged bottomonium-like states $\mathrm{Z}_b^{\pm}(10610)$ and $\mathrm{Z}_b^{\pm}(10650)$ [B$^+$12a]. The charge indicates a molecule with bottom-antibottom quark pair and two light quarks, e.g. up-antidown. Belle's measurements point to $\mathrm{B}\overline{\mathrm{B}}^*$ and $\mathrm{B}^*\overline{\mathrm{B}}^*$ molecules.
Diakonov et al. [D$^+$97a] proposed an anti-decuplet of pentaquarks with spin 1/2 and even parity. In 2003, the intensive search for pentaquarks started, especially for the Θ^+ with positive strageness ($\mathsf{uudd\bar{s}}$), a predicted mass of 1540 MeV, and a width less than 15 MeV. In the past, possible evidence (examples listed in [N$^+$10b]) was overshadowed by an underestimated background and low statistics [Y$^+$06b]. Promising observations of the LHCb (Large Hadron Collider beauty) experiment at the European Organization for Nuclear Research CERN are currently under discussion.

Glueballs

Pure gluonic bound states (gg, ggg) without quark constituents are called glueballs. Lattice QCD provides calculations on a glueball mass spectrum below 5 GeV [MP99, C$^+$06], which is presented in Figure 2.8. The ground state glueball is predicted to be a scalar 0^{++} at

1710 MeV [C$^+$06] with an uncertainty of about 100 MeV. Because of the intersecting mass range of scalar mesons and glueballs, the distinction between them is not unambiguous. Furthermore, the identification of scalar mesons or gluons is very challenging because of their large decay width (around 250 MeV [Ams98]) as well as overlapping resonances and background. Within a short mass interval, various decay channels could occur [B$^+$on]. The decay rates offer the possibility to distinguish between $\mathsf{u\bar{u}} + \mathsf{d\bar{d}}$ mesons (mainly pion decay), $\mathsf{s\bar{s}}$ mesons (mainly kaon decay) or glueballs (gamma decay suppressed). However, a mixing between nearby meson states with the flavour blind gluon is conceivable, which would lead to modified decay branching ratios [Ams98]. Nevertheless, a number of possible glueball ground state candidates have emerged, such as the resonances $f_0(1370)$, $f_0(1500)$, and $f_0(1710)$. A possible and common interpretation of the obtained data is that $f_0(1370)$ is dominantly $\mathsf{n\bar{n}}$ (two lightest quarks), $f_0(1500)$ appears mainly as glue, and $f_0(1710)$ is largely $\mathsf{s\bar{s}}$ [AT04, B$^+$on, Y$^+$06a].

The most promising candidate $f_0(1500)$ was investigated in detail by the Crystal Barrel Collaboration at CERN via $\mathrm{p\overline{p}}$ annihilation [Ams98] and by the WA102 Collaboration at CERN in central collisions [B$^+$99] (see also Fig. 2.9). $f_0(1500)$ shows a comparatively narrow decay width of about 100 MeV and decays into $\pi\pi$, $\eta\eta$, $\eta\eta'$, $\mathrm{K\overline{K}}$, and 4π were observed [Ams98]. In addition, the decay rates (mainly pion decay) indicate that $f_0(1500)$ is the predicted ground state glueball mixing with the nearby scalar mesons $\mathsf{n\bar{n}}$ and $\mathsf{s\bar{s}}$ [AT04].

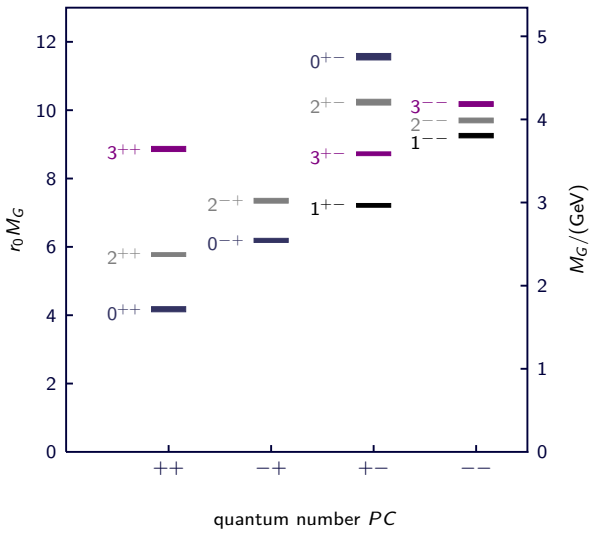

Figure 2.8.: Glueball mass spectrum with quantum number J^{PC}. The masses M_G are given in terms of the hadronic scale r_0 with $r_0^{-1} = 410$ MeV (left ordinate) and in GeV (right ordinate). The boxes indicate the statistical mass uncertainty (data extracted from [C$^+$06]) and the colour blue, black, grey, and violet, correspond to the total angular momentum 0, 1, 2, and 3.

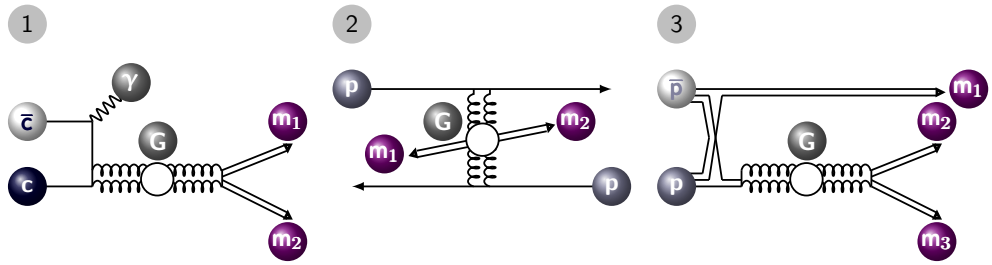

Figure 2.9.: Gluon rich processes [KZ07]: (1) radiative J/Ψ decay, (2) hadron-hadron central production (double pomeron exchange), and (3) $p\bar{p}$ annihilation with the glueball state (G) and the mesons ($m_{1,2,3}$). The pomeron is a hypothetical particle, which explains the elastic hadron or rather diffractive scattering in (2). A possible interpretation of this state is a glueball composed of two gluons.

2.3.2. Key experiments

Quite a number of new particles were discovered, which further completed the hadron spectrum and indicate the evidence for hybrids, multiquark states, and glueballs. However, the unambiguous classification is very challenging and requires for more experiments working with various methods to collect independent data with high precision and high statistics. The B-meson factories, both BABAR and Belle, are already recording a lot of results on meson spectroscopy, but there will be various upgraded or new experimental programmes, like Belle II, GlueX, or $\overline{\text{P}}$ANDA based on the previous experiments, BABAR, Belle, BESIII, or Crystal Barrel.

BABAR (B And B-bAR) [A$^+$02] is located at the Stanford Linear Accelerator Center (SLAC), which was operated by the Stanford University in California (USA) between 1999 and 2008. At the asymmetric (energy) electron-positron collider PEP-II (Positron Electron Project-II), BABAR operated at a center of mass energy of the $\Upsilon(4S)$ resonance at 10.58 GeV and at a luminosity of $3 \times 10^{33}\,\text{cm}^{-2}\text{s}^{-1}$ (and above). The electron beam with 9 GeV collides with the 3.1 GeV positron beam resulting in a Lorentz boost of $\beta\gamma = 0.56$ to the $\Upsilon(4S)$ resonance. $\Upsilon(4S)$ decays into $\text{B}^0\overline{\text{B}}^0$ and B^+B^- and the Lorentz boost enables the reconstruction of the decay vertices. The detector was primarily designed and optimised for studies of *CP*-violation in B-meson decays.

The competing **Belle** experiment [B$^+$12b] started almost simultaneously at the asymmetric electron-positron collider KEKB at the KEK laboratory in Tsukuba (Japan). With an 8 GeV electron and a 3.5 GeV positron beam the $\Upsilon(4S)$ resonance results in a Lorentz boost of $\beta\gamma = 0.425$. The world record in luminosity of $2.1 \times 10^{34}\,\text{cm}^{-2}\text{s}^{-1}$ [Yua12] was achieved at KEKB. The Belle detector was also optimised for B physics analysis, especially for the investigation of *CP*-violation in B-meson decays. Among their successes are the observation

of the new charmonium and bottomonium-like states XYZ and Z_b. Furthermore, the observation of *CP*-violation in B-meson decays led 2008 to the Nobel prize in physics for M. Kobayashi, T. Maskawa, and Y. Nambu. M. Kobayashi and T. Maskawa were awarded for their theory, which explained the source of matter/antimatter asymmetries and Y. Nambu for his theory of spontaneous symmetry breaking [Nobb].
To gain more insights into *CP*-violation, the Belle experiment will be upgraded. **Belle II** [Bel10] will continue as a B-factory by the end of 2015 [Yua12] at SuperKEKB, an upgrade version of KEKB, with a design luminosity of $8 \times 10^{34}\,\mathrm{cm}^{-2}\mathrm{s}^{-1}$. To increase the luminosity, the beams will be squeezed to nanometre scale to minimise the longitudinal size of the overlap region. SuperKEKB will be operating at 7 GeV and 4 GeV electron and positron energy, respectively. On the basis of the accelerator design, the Belle II detector is a modified and improved version of the earlier Belle detector.

The **BESIII** (Beijing Electron Spectrometer III) [A$^+$08, B$^+$11] experiment is an upgrade of the former experiments BES and BESII at the BEPII (Beijing Electron Positron collider II) of the Institute of High Energy Physics (IHEP) in China. At a beam energy of 1.89 GeV, the peak design luminosity is $10^{33}\,\mathrm{cm}^{-2}\mathrm{s}^{-1}$. Since 2008, it operates at center of mass energies in the range of 2 GeV to 4.6 GeV and collected the world largest data samples of J/Ψ, Ψ', and $\Psi(3770)$. BESIII concentrates on charmonium, D-meson, and τ physics as well as hadron spectroscopy and the search of new hadronic states.

The **Crystal Barrel** detector operated from 1989 until 1996 at the Low-Energy Antiproton Ring (LEAR) at the European Organization for Nuclear Research CERN in Geneva, Switzerland. LEAR provided antiproton beams in a momentum range between 100 MeV/c (5.3 MeV) and 2000 MeV/c (1270 MeV) [GE13] for the annihilation with the protons of a liquid hydrogen target. Besides the observation of the exotic meson $\pi_1(1600)$ with $J^{PC} = 1^{-+}$ [A$^+$98a, A$^+$99] and $f_0(1500)$ [Ams98] glueball candidate, Crystal Barrel concentrates on light meson spectroscopy. Since 2000 the Crystal Barrel detector is installed at ELSA (ELektronen-Stretcher Anlage) in Bonn (Germany) and focuses on baryon spectroscopy.

The 12 GeV upgrade of the Continuous Electron Beam Accelerator Facility (CEBAF) at the Jefferson Lab in Newport News (USA) includes the **GlueX** experiment [Glu05]. An 12 GeV electron beam from the CEBAF will interact with a wafer-thin diamond crystal. Due to the coherent bremsstrahlung technique, a linearly polarised photon beam will be produced and will further interact with a liquid hydrogen or deuterium target. Via the reaction $\gamma p \to Xp$, a mass range up to 2.5 GeV/c^2 will allow for the search for gluonic excitations.

The **$\overline{\text{P}}$ANDA** (antiProton ANnihilation at DArmstadt) [PAN12a] experiment will be conducted at the High Energy Storage Ring (HESR) at the future Facility for Antiproton and Ion Research (FAIR) at Darmstadt (Germany). Antiprotons within a momentum range of $1.5\,\text{GeV}/c$ to $15\,\text{GeV}/c$ will annihilate with the protons of different internal targets. The first operational target will be a hydrogen cluster-jet target, which this thesis is focussed on. It will be presented in more detail in Chapter 4. A peak luminosity of up to $2 \times 10^{32}\,\text{cm}^{-2}\text{s}^{-1}$ [PAN12a] is expected. The $\overline{\text{P}}$ANDA detector is designed and optimised for hadron spectroscopy, especially for the search for exotic hadrons, charmonium, and open charm spectroscopy as well as the study of in-medium influences on the hadron mass and more. The next chapter will introduce the FAIR facility and HESR and will give an overview of the physics objectives at $\overline{\text{P}}$ANDA as well as further details on the detector performance.

3. $\overline{\text{P}}$ANDA experiment at FAIR

The nature of strong interaction still holds a lot of unsolved puzzles – *Why are quarks confined and cannot be observed individually? What is the origin of the hadron masses? Are there exotic hadron states like hybrids, quark molecules, and glueballs? ...*
Focussing on these open questions, the physics programme of the $\overline{\text{P}}$ANDA (antiProton ANnihilation at DArmstadt) experiment at the future international accelerator facility FAIR (Facility for Antiproton and Ion Research), which is currently under construction, will enable new insights into the essence of hadronic matter and strong interaction.

3.1. International accelerator facility FAIR

The future Facility for Antiproton and Ion Research, FAIR, will be an upgrade of the existing GSI (Helmholtzzentrum für Schwerionenforschung GmbH) research center in Darmstadt, Germany. FAIR will cover four major research fields [GF06a], namely:

- Atomic, Plasma Physics and Applications (APPA), including the projects
  - BIOlogy and MATerial science (BIOMAT)
  - Facility for Low-energy Antiproton and heavy Ion Research (FLAIR)
  - High Energy Density matter generated by Heavy iOn Beams (HEDgeHOB)
  - Stored Particles Atomic Research Collaboration (SPARC)
  - Warm Dense Matter (WDM)
- Compressed Baryonic Matter (CBM)
- NUclear STructure, Astrophysics and Reactions (NUSTAR), including the projects
  - DEcay SPECtroscopy/HIgh-resolution SPECtroscopy (DESPEC/HISPEC)
  - ELectron-Ion Scattering in a storage ring (ELISe)
  - EXotic nuclei studied in Light-ion induced reactions at the NESR storage ring (EXL)
  - Isomeric beams, LIfetimes and MAsses (ILIMA)
  - Laser Spectroscopy (LaSpec)
  - precision Measurements of very short-lived nuclei with Advanced Trapping System (MATS)
  - Reactions with Relativistic Radioactive Beams (R3B)
  - Super FRagment Separator (SuperFRS)
- antiProton ANnihilation at DArmstadt ($\overline{\text{P}}$ANDA)

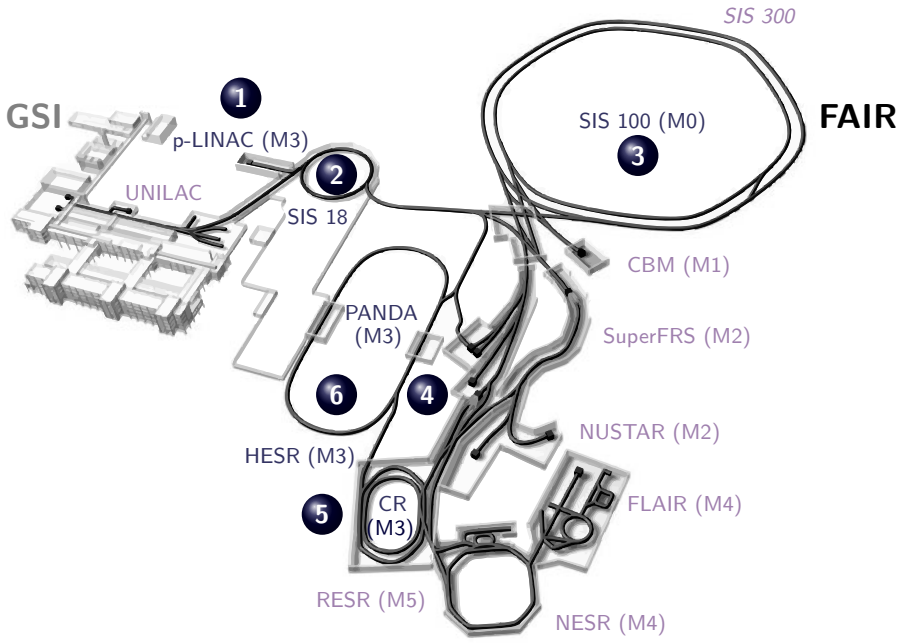

Figure 3.1.: FAIR overview (by courtesy of FAIR [Ber14], edited) and its modularised structure, whereas module (M0) to (M3) constitute the start version. **Module 0** (M0) comprises the construction of the heavy ion synchrotron SIS 100 including the connection to the existing UNIversal Linear ACcelerator (UNILAC) and the heavy ion synchrotron SIS 18 from GSI. **Module 1** (M1) covers experimental areas for CBM and APPA. **Module 2** (M2) includes a Super FRagment Separator (Super-FRS) for NUSTAR. **Module 3** (M3) implements the new proton LINear ACcelerator (p-LINAC), the target for antiproton production, the Collector Ring (CR) and the High Energy Storage Ring (HESR). **Module 4** (M4) contains experimental areas for NUSTAR and APPA (FLAIR) as well as the New Experimental Storage Ring (NESR). **Module 5** (M5) holds the Re-used Experimental Storage Ring (RESR) for NUSTAR and also $\overline{P}$ANDA for higher beam intensities. FAIR can be further extended with the heavy ion synchrotron *SIS 300*. The numbering indicates the production and separation (1 to 4), collection (5), and acceleration area at FAIR (6) of antiprotons for the $\overline{P}$ANDA experiment.

Ion beams from protons to uranium as well as antiprotons can be provided and will be accessible for an efficient parallel operation. An overview of FAIR, whose construction is modularised, is represented in Figure 3.1. FAIR comprises six modules (module (M0) to (M5)), whereas module (M0) to (M3) constitute the start version of FAIR [GF09], including all main components for the $\overline{P}$ANDA experiment for antiproton production, separation, collection, and acceleration [GF06b].

The antiproton production occurs via the reaction $pp \rightarrow ppp\overline{p}$. The threshold energy results from the total energy $E^{\mathrm{cm}}_{\mathrm{total}}$ in the center-of-mass frame (with $c = 1$) of a two-body reaction with stationary target [Hin08]:

$$E^{\mathrm{cm}}_{\mathrm{total}} = \sqrt{(2E_1 m_2 + m_1^2 + m_2^2)}, \tag{3.1}$$

where E_1 and m_1 correspond to the energy and mass of the projectile and m_2 is the mass of the stationary target particle. Projectile and target both are protons with a mass of $m_1 = m_2 = m_\mathrm{p} = 938.27\,\mathrm{MeV}/c^2$. Due to baryon number conservation, an antiproton occurs with three protons, so that $E^\mathrm{cm}_\mathrm{total}$ must be at least $4m_\mathrm{p}$. Equation 3.1 is then simplified to

$$4m_\mathrm{p} = \sqrt{\left(2E_1 m_\mathrm{p} + 2m_\mathrm{p}^2\right)} \tag{3.2}$$

and yields to the total energy with $E_1 = 7m_\mathrm{p}$. With the projectile's rest energy the minimal kinetic energy or threshold energy arises from $E_\mathrm{thr} = 6m_\mathrm{p}$ with 5.63 GeV [Hin08]. A new proton LINear ACcelerator (p-LINAC cf. Fig. 3.1 (1)) will provide 50 MeV proton beam pulses for the existing heavy ion synchrotron SIS 18 (2), which will be operating as an energy and intensity booster. Protons with an energy of 2 GeV can be injected to the new heavy ion synchrotron SIS100 (3), with a circumference of 1080 m. After injection, a bunch of up to 2.5×10^{13} protons can be accelerated in SIS100 to an energy of 29 GeV. Antiprotons will be produced due to the interaction with an iridium target [K$^+$12] (4). Approximately 10^8 antiprotons will be collected and pre-cooled at the Collector Ring (CR (5)) and then transferred to the High Energy Storage Ring (HESR (6)).

3.2. High Energy Storage Ring HESR

The High Energy Storage Ring (HESR) [PAN09, PAN12a] will provide antiprotons in a momentum range between 1.5 GeV/c and 15 GeV/c (energy range: 0.83 GeV and 14.1 GeV) at an injection momentum of 3.8 GeV/c. Two operation modes are proposed: the High Resolution (HR) mode at 1.5 GeV/c and 8.9 GeV/c with a peak luminosity of $2 \times 10^{31}\,\mathrm{cm}^{-2}\mathrm{s}^{-1}$ with 10^{10} antiprotons and a momentum spread of $\Delta p/p \leq 4 \times 10^{-5}$ and the High Luminosity (HL) mode at 1.5 GeV/c and 15 GeV/c with a peak luminosity of $2 \times 10^{32}\,\mathrm{cm}^{-2}\mathrm{s}^{-1}$ with 10^{11} antiprotons and a momentum spread of $\Delta p/p \sim 4 \times 10^{-4}$. The latter mode will be accessible with the construction of the Re-used Experimental Storage Ring (RESR, FAIR module 5).

Besides Radio Frequency (RF) cavities, the HESR features two beam cooling systems, namely stochastic and electron cooling, to compensate the antiproton beam heating induced by the internal targets [PAN12a, T$^+$07, S$^+$08]. RF cavities are special resonators, usually conducting chambers containing an electromagnetic field. This electromagnetic field can be used for acceleration, deceleration, and for bunch manipulation. In addition, a barrier bucket cavity in combination with a stochastic cooling system (pick-up and kicker) will compensate the mean energy loss induced by the interaction with the internal target (above 3.8 GeV/c [PAN09]). Therefore, the barrier bucket cavity generates a bunch which fills 80 % to 90 % [S$^+$08] of the storage ring. A pick-up electrode will measure the particle's position and transmits the information to a kicker-electrode for

angle adjustments. Moreover, the HESR will be equipped with an electron cooler (up to 8.9 GeV/c [PAN09]), thereby a cold intense electron beam will be merged with the hot ion beam. Due to Coulomb collisions, a momentum transfer occurs leading to an improvement of the antiproton's momentum spread [Hin08, Wil96]. In the start up phase of HESR, the 2 MeV electron cooling system for the COoler SYnchrotron (COSY) in Jülich (Germany) will be transferred and first operated for beam cooling at antiproton injection energy [D$^+$11, K$^+$14a].

3.3. Experimental programme and objectives

Protons and antiprotons are baryons or antibaryons containing three quarks (uud) or antiquarks ($\overline{\mathsf{uud}}$), respectively. Their interaction is not comparable to the electron-positron annihilation, due to the fact that not all incoming quarks and antiquarks have to annihilate, but rather rearrange [K$^+$05]. Therefore, the annihilation of nucleons, such as antineutrons and protons, is also possible and was carried out, e.g. at the Crystal Barrel or OBELIX experiment at the Low Energy Antiproton Ring (LEAR) at the European Organization for Nuclear Research CERN in Geneva, Switzerland. Crystal Barrel concentrated on light meson spectroscopy and observed the exotic candidates $\pi_1(1600)$ [A$^+$98a, A$^+$99] and $f_0(1500)$ [Ams98]. LEAR [GE13] was operated until 1996 and provided antiproton beams in a momentum range between 100 MeV/c (5.3 MeV) and 2000 MeV/c (1270 MeV). Proton-antiproton annihilation was also investigated at the synchrotron Tevatron of the Fermi National Accelerator Laboratory (USA). Tevatron provided protons and antiprotons with an energy up to 1 TeV and was running until 2011. One of the greatest achievements of Tevatron was the discovery of the top quark in 1995 [A$^+$95].
The antiproton annihilation at the $\overline{\mathrm{P}}$ANDA experiment will be realised with antiproton beams in a momentum range of 1.5 GeV/c (0.83 GeV) to 15 GeV/c (14.1 GeV). Within the resulting mass range of up to 5.5 GeV/c^2, which is presented in Figure 3.2, the $\overline{\mathrm{P}}$ANDA experiment enables the search for exotic hadrons like hybrids, quark molecules, and glueballs (see Section 2.3). In addition, the experimental programme covers charmonium and open charm spectroscopy as well as the study of open and hidden charm in nuclei. Investigations on hypernuclear physics and electromagnetic processes are also included.

3.3.1. Charmonium and open charm spectroscopy

Mesons composed of a quark and its own antiquark are called quarkonia. The first discovered quarkonia state was J/Ψ, an excited charmonium state containing charm and anticharm quark. J/Ψ was observed simultaneously in electron positron annihilations at SLAC and BNL in 1974. Two years later, Burton Richter and Samuel C. C. Ting were awarded with the nobel prize in physics for their discovery [Noba]. The investigation of charmonium allows for studies of the quark-antiquark potential and the properties of the

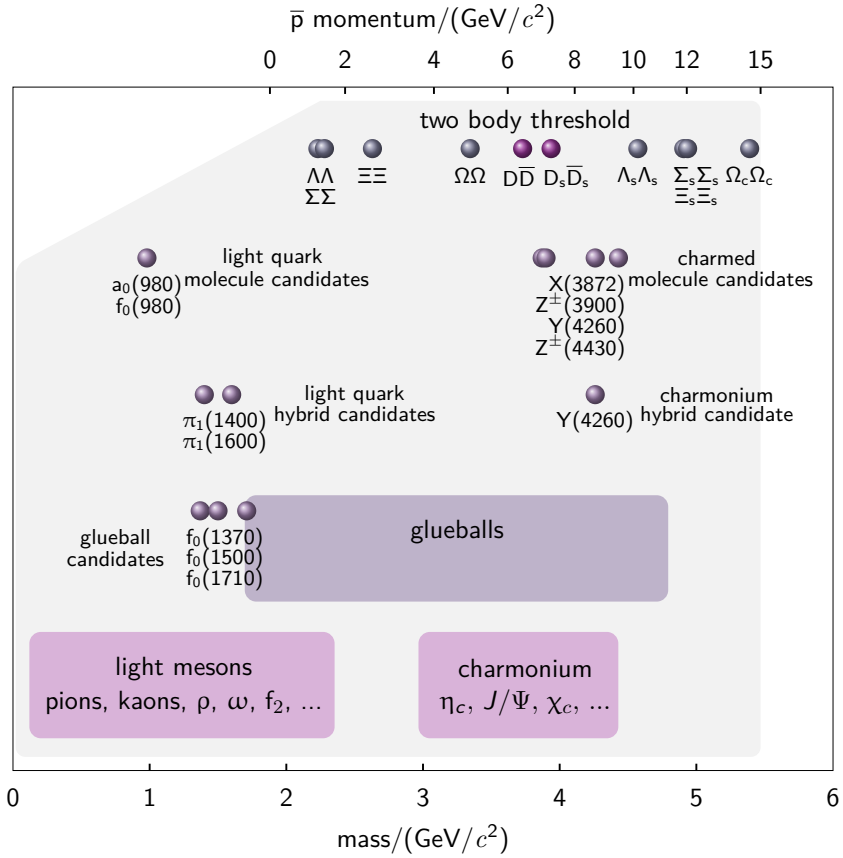

Figure 3.2.: Resulting mass range (bottom abscissa) at the $\overline{\text{P}}$ANDA experiment with an antiproton momentum of 1.5 GeV/c up to 15 GeV/c (top abscissa) [PAN12a]. Moreover, the mass range of light mesons, charmonium states, and glueball states are depicted as filled boxes. A selection of possible candidates for glueballs, hybrids, and quark molecules are marked with dots as well as the two body threshold of several hadrons (baryons and mesons).

strong force in vacuum. Charmonium states below the D$\overline{\text{D}}$ threshold have already been determined very precisely. The B-Factories Belle and BABAR discovered a lot of new charmonium-like states above the D$\overline{\text{D}}$ threshold. New states like X(3872), Y(4260), and Z(4430) occurred as possible candidates for hybrid or quark molecules [A$^+$09]. Other resonances like X(3930), X(3940), X(3945), X(4360) etc. might be new charmonium states. For an unambiguous classification, precise mass measurements and the study of the decay properties are required. The $\overline{\text{P}}$ANDA experiment will concentrate on charmonium spectroscopy below and especially above the D$\overline{\text{D}}$ threshold. In contrast to electron positron annihilation, with restriction in the quantum numbers due to the production of the virtual photon ($\text{e}^+\text{e}^- \to \gamma^* \to \text{c}\overline{\text{c}}$ with $J^{PC} = 1^{--}$), charmonium states can be directly produced in antiproton proton annihilations ($\overline{\text{p}}\text{p} \to \text{c}\overline{\text{c}}$) without any quantum number restrictions. Mass measurements can be performed with an accuracy in the order of 100 keV and decay

widths with a precision of 10% [PAN09]. In addition, $\overline{\text{P}}$ANDA will investigate on open charm spectroscopy, i.e. the study of D-mesons containing a charm and a light quark or D_s-mesons composed of a charm and a strange quark.

3.3.2. Open and hidden charm in nuclei

What is the origin of the hadron mass? Quarks cannot be observed individually, they are confined into hadrons. Quark models allow for quark mass determinations and show a high mass difference between bare quarks (current quarks) and bound constituent quarks. The Lagrangian of QCD in Equation 2.1 shows a chiral symmetry for vanishing quark masses [B^+on]. That implies the distinction between left- and right-handed quarks in good approximation for up and down quarks. Within hadrons, the chiral symmetry is broken and can be partially restored inside a nuclear medium. Various experiments, like CLAS (CEBAF Large Acceptance Spectrometer) at Jefferson Lab (USA), Crystal Barrel at ELSA (ELektronen-Stretcher Anlage) in Bonn (Germany), HELIOS (High-Energy Lepton and IOn Spectrometer), and CERES (ChErenkov Ring Electron Spectromter) at CERN (Switzerland) observed mass shifts and an abbreviated lifetime. Therefore, investigations on spontaneous chiral symmetry breaking and the partial restoration will lead to further indications of the origin of the hadron mass. The $\overline{\text{P}}$ANDA experiment [PAN09, PAN12a] will focus on in-medium modifications of charmed hadrons via antiproton nucleus collisions. Furthermore, the cross section of J/Ψ and D-meson production in antiproton annihilation on a nuclear target can be analysed.

3.3.3. Hypernuclear physics and electromagnetic processes

Hypernuclei were discovered by M. Danysz and J. Pniewski in 1952 and are nuclei composed of nucleons and at least one hyperon. Hyperons are baryons containing one strange quark or more, such as Λ, Σ, Ξ, or Ω. They are not restricted to Pauli's exclusion principle and can populate all nuclear states. Studies on hypernuclei allow for insights into the nuclear structure and the investigation of the nuclei-hyperon interaction. Furthermore, $\overline{\text{P}}$ANDA will focus on double hypernuclei and hyperon-hyperon interactions via a two-step production [PAN09]. Ξ^- will be produced in the reaction $\overline{\text{p}}\text{p(n)} \rightarrow \Xi^-\overline{\Xi}^+(\overline{\Xi}^0)$ and re-scatter in a secondary target converting double Λ hypernuclei in the reaction $\Xi^- + \text{p} \rightarrow \Lambda\Lambda$. Additionally, the analysis of electromagnetic processes $\overline{\text{p}}\text{p} \rightarrow \text{e}^+\text{e}^-$ enables further studies on the nuclear structure.

3.4. $\overline{\text{P}}$ANDA detector

The $\overline{\text{P}}$ANDA experiment is a fixed target experiment. Contrary to colliding beam experiments, where two particle jets are accelerated in opposite directions to induce a

collision, at fixed target experiments an accelerated beam interacts with a fixed positioned external or internal target. An internal cluster-jet target will be the first operating target at $\overline{P}$ANDA and will be presented and discussed in detail in the following chapters. The $\overline{P}$ANDA detector consists of a shell-like Target Spectrometer (TS), which surrounds the interaction region. Moreover, $\overline{P}$ANDA is equipped with a Forward Spectrometer (FS), because the particles are mainly emitted in forward direction due to the Lorentz boost. Figure 3.3 shows an overview of the complete detector. The 4π target spectrometer and the forward spectrometer include the following components [PAN05, PAN12a]:

- **MVD** – Micro Vertex Detector (TS) – The MVD [PAN12b] encloses the vertex zone and its tasks include the tracking of charged particles, especially for the determination of secondary vertices of hyperons and charmed mesons. The half-shell/half-disc structure contains four barrel layers and six disks with pixel detectors and double sided silicon strip detectors.
- **STT** – Straw Tube Tracker (TS) – Furthermore, the $\overline{P}$ANDA detector is equipped with an STT [PAN12c] for particle tracking in the solenoid field. It contains Al-Mylar drift tubes with an axial length of 150 cm and an internal diameter of 1 cm. They are filled with an Ar/CO_2 (90/10) mixture and use Au plated W/Re wires.
- **GEM** – Gas Electron Multiplier (TS) – The GEM-tracker will cover tracks with polar angles between 5 degree and 22 degree in forward direction. Up to four GEM-discs are planned.
- **DIRC** – Detector for Internally Reflected Cherenkov light (TS) – For the particle identification, such as hadrons and leptons, DIRC detectors (barrel and disc shape at the forward endcap) are included.
- **EMC** – ElectroMagnetic Calorimeter (TS and FS) – An EMC [PAN08a], which surrounds the barrel DIRC, and another EMC at the forward spectrometer require more than 15500 $PbWO_4$ crystals for the detection of photons, electrons, and hadrons.
- **MUO** – MUOn detector (TS and FS) – Additionally, muon detectors [PAN08b] will be installed in both target and forward spectrometer.
- **TOF** – Time Of Flight system (TS and FS) – To measure the particle's velocity, a TOF system will be installed.
- **RICH** – Ring Imaging CHerenkov (FS) – RICH composed of aerogel cherenkov counters will also enable particle identification.

- **Solenoid (TS)** – The $\overline{P}$ANDA solenoid magnet will provide a maximum magnetic field of 2 T.
- **Dipole magnet and drift chambers (FS)** – They allow for momentum separation of charged particles with angles from up to ±10 degree horizontally and ±5 degree vertically with respect to the beam direction.
- **Luminosity Monitor (FS)** – The luminosity monitor is based on the angle reconstruction of scattered antiprotons with polar angles between 3 mrad and 8 mrad for the determination of the time integrated luminosity (see Section 4.1.1).

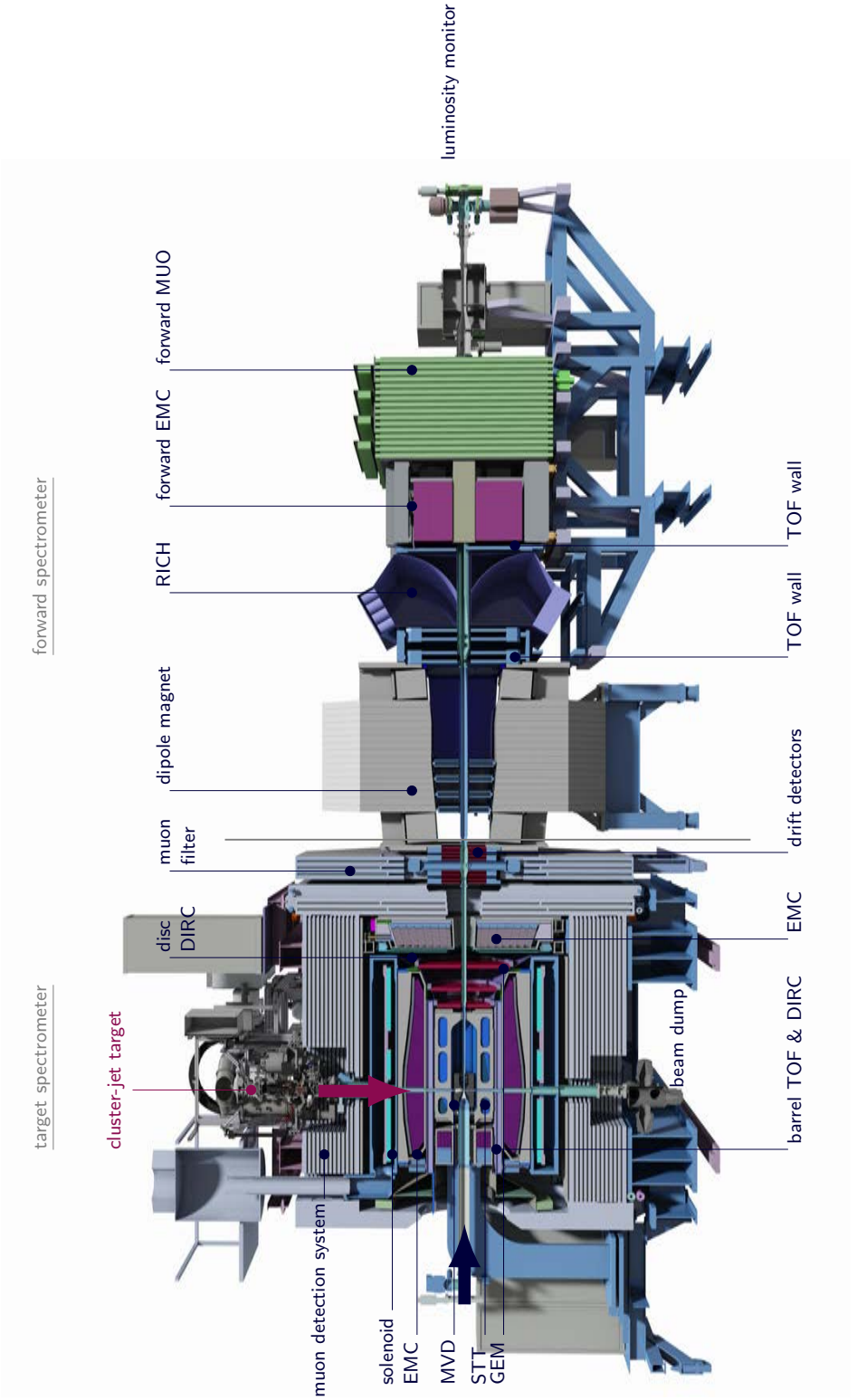

Figure 3.3.: The $\overline{P}$ANDA detector with a total length of about 15 m (generated by D. Bonaventura with Autodesk Showcase, edited). The horizontal blue arrow represents the antiproton beam and the vertical violet one the cluster-jet beam.

4. Internal $\overline{\text{P}}$ANDA cluster-jet target

The $\overline{\text{P}}$ANDA experiment is a fixed target experiment, in which the accelerator beam will interact with a stationary, internal target. Internal targets [Eks95] are directly installed at the storage ring, such as gas-jet, cluster-jet, or pellet targets as well as thin fibres, foils, wires etc. Therefore, the accelerator beam will interfere with the target after each circulation (multi-pass experiment). Interactions with an external target occur only once with an extracted beam and usually with a solid target (single-pass experiment). $\overline{\text{P}}$ANDA will be operated with an internal cluster-jet and a pellet target, depending on the experimental programme and the required target density. This thesis focuses on the cluster-jet target for the $\overline{\text{P}}$ANDA experiment and the cluster beam characteristics. In regard to the requirements of $\overline{\text{P}}$ANDA, an overview of internal targets and the advantages of cluster-jets are outlined in this chapter. Furthermore, the cluster-jet target prototype as well as the design of the final target will be presented.

4.1. Requirements for internal targets

Internal targets must fulfil challenging and partially contrary requirements. To avoid large beam heating effects that cannot be compensated effectively with the available beam cooling techniques, such as stochastic and electron cooling, the areal target density or thickness is usually between $10^{12}\,\text{atoms/cm}^2$ to $10^{19}\,\text{atoms/cm}^2$. In order to guarantee a stable stored beam with moderate beam heating, the target thickness at $\overline{\text{P}}$ANDA has to be distinctly below $10^{16}\,\text{atoms/cm}^2$ [PAN12a]. On the other hand, the target thickness must be high enough to achieve high luminosities or event rates to study rare processes.

4.1.1. Luminosity

The performance of accelerators and storage rings constructed for scattering experiments is characterised by the beam energy and the luminosity $\mathcal{L}$, which describes the context between the event rate $\dot{N}_d$ (within a detector) and the cross section σ of the particular interaction by [Wil96, Hin08]

$$\dot{N}_d = \mathcal{L}\sigma. \tag{4.1}$$

At fixed target experiments with an external target, the luminosity is given by the number of projectiles per unit of time $\dot{N}_p$ and the number of target particles per unit area N_t/A (areal density or thickness ρ_{areal}, cf. Chapter 5):

$$\mathcal{L} = \dot{N}_p \frac{N_t}{A} = \dot{N}_p \ \rho_{\text{areal}} \tag{4.2}$$

with $[\mathcal{L}] = \text{cm}^{-2}\text{s}^{-1} = 10^{33}\,\text{nb}^{-1}\text{s}^{-1}$. For experiments with internal targets, such as $\overline{\text{P}}$ANDA, $\dot{N}_p$ is defined by $\dot{N}_p = N_b N f$, where N_b is the number of bunches, N the number of particles within a bunch and the revolution frequency f. Therefore, the luminosity for fixed target experiments with internal target yields

$$\mathcal{L} = N_b N f \rho_{\text{areal}}. \tag{4.3}$$

With Equation (4.1) and (4.3) the thickness for internal targets can be described via

$$\rho_{\text{areal}} = \frac{\dot{N}_d}{\sigma N_b N f}. \tag{4.4}$$

At $\overline{\text{P}}$ANDA, the event rate or rather the antiproton production rate will be $2 \times 10^7\,\text{s}^{-1}$ with a cross section for the $\overline{\text{p}}$p annihilation of around 100 mb [B$^+$on]. The High Energy Storage Ring HESR will provide an accelerator beam with 10^{11} antiprotons and a revolution frequency of 443 kHz. With complete detector efficiency and full geometrical acceptance, the thickness results in $4.5 \times 10^{15}\,\text{atoms/cm}^2$ and yields a luminosity of $2 \times 10^{32}\,\text{cm}^{-2}\text{s}^{-1}$ [PAN12a].
For studies of rare processes, the total amount of collected events, depending on the measurement duration, is important and can be described by the integrated luminosity

$$\mathcal{L}_{\text{int}} = \int \mathcal{L}\ dt \tag{4.5}$$

with $[\mathcal{L}_{\text{int}}] = \text{nb}^{-1}$.

4.1.2. Internal targets

A target thickness of $4.5 \times 10^{15}\,\text{atoms/cm}^2$ will ensure a maximum luminosity and an optimal exploitation of the injected antiproton beam, which is in particular essential for rare particle beams. A selection of internal targets and their typical densities is shown in Table 4.1 and it should be noted, that thin fibres, foils, or wires are too dense ($(10^{17}$ to $10^{19})\,\text{atoms/cm}^2$ [Eks95]) and would lead to a limited beam lifetime and beam heating. Therefore, gas-jet, cluster-jet, and pellet targets are the potential target candidates for $\overline{\text{P}}$ANDA.

internal target	density	remarks
gas-jet	$10^{17}\ \frac{\text{atoms}}{\text{cm}^2}$	very close to the nozzle
	$10^{14}\ \frac{\text{atoms}}{\text{cm}^3}$*	interaction length around 3 mm to 5 mm, distance to the nozzle below one metre
cluster-jet	$\gg 10^{14}\ \frac{\text{atoms}}{\text{cm}^2}$	distance to the nozzle below one metre (cf. Tab. 4.2)
pellet	$\gg 10^{15}\ \frac{\text{atoms}}{\text{cm}^2}$	beam diameter typically 2 mm to 4 mm, pellet diameter around 20 µm to 30 µm with an average pellet distance of 5 mm
thin fibres, foils, wires	$(10^{17}$ to $10^{19})\ \frac{\text{atoms}}{\text{cm}^2}$	e.g. 7 µm carbon fibre in 9 mm wide beam results in $5 \times 10^{16}\ \frac{\text{atoms}}{\text{cm}^2}$

Table 4.1.: Review of selected internal targets and their typical volume density* (atoms/cm^3) or thickness (atoms/cm^2) [Eks95], respectively. The volume density of gas-jet and cluster-jet targets decreases with the distance s to the nozzle (with s^{-2} for cluster-jets).

Supersonic **gas-jet targets** (cf. Figure 4.2 left), e.g. the internal gas-jet target for the ESR (Experimental Storage Ring) at GSI, can be operated with various gas types, from helium, hydrogen or deuterium to xenon [R$^+$97]. Thereby, the (cooled) gas passes a Laval nozzle (cf. Section 4.2.1) with an inlet pressure of up to 20 bar and expands into the vacuum. Due to the specific convergent-divergent shape of the Laval nozzle, a supersonic flow of the target material is generated. Furthermore, the gas beam passes a differential pumping system equipped with orifices, the skimmers. This ensures a small jet divergence and a reduced background pressure. The gas-jet target for the ESR at GSI [G$^+$89] operated with hydrogen and a nozzle diameter of 70 µm at the narrowest point. With an inlet gas pressure of 10 bar at 200 K, a molecular density of 1×10^{14} molecules/cm^3 within an interaction length of 3 mm to 5 mm was reached at the ESR. The Laval nozzle was installed at a distance of less than one metre from the interaction point. However, the $\overline{\text{P}}$ANDA experiment requires a distance from the interaction point of $s = 2.1$ m to achieve almost 4π acceptance. Since the target density decreases with distance, gas-jet targets are not able to provide a defined target beam at such a distance (cf. Figure 5.13). Cryogenic targets like the cluster-jet or pellet target allow for focussed target beams at the required distance.

Similar to the gas-jet target, a **cluster-jet target** (cf. Figure 4.2, center) also operates with a Laval nozzle. Cooled gas, frequently hydrogen or deuterium (other gases, such as carbon, nitrogen, argon, and methane are also possible), passes the nozzle and expands

into a vacuum chamber. A supersonic flow is generated at the narrowest point and the expansion into the vacuum (below the inversion temperature) causes a decrease of the target flow temperature, an effect known as adiabatic cooling. Supersaturation and an increased collision rate of the particles lead to the formation of clusters, which are typically composed of more than 10^6 constituents. Cluster-jet targets are also operating with a differential pumping system equipped with orifices to separate the condensated clusters from the residual gas (skimmer) and for beam shaping (collimator). Table 4.2 shows a selection of cluster-jet targets and their performance with hydrogen as target material. The cluster-jet targets at COSY (COoler SYnchrotron) [D$^+$97b] for the experiments COSY-11 (completed) and ANKE (Apparatus for Studies of Nucleon and Kaon Ejectiles) [B$^+$01, Mie07, Pap08, Gos09, Sch12, Gos13, Fri14] both were designed at the University of Münster. In regard to the distance between cluster source and interaction point, they provided the highest thickness of more than 10^{14} atoms/cm^2 at 0.65 m. The cluster-jet target prototype for $\overline{P}$ANDA, which is designed in complete $\overline{P}$ANDA geometry, will be presented in the next section. Although the target density decreases with the squared distance (s^{-2}), this prototype provides a target thickness of more than 10^{15} atoms/cm^2 at the required distance of 2.1 m. The possibility to provide such high thicknesses represents an important result of this work and will be discussed in detail in Chapter 5. Furthermore, cluster-jet targets show a wide flexibility in the density or thickness, respectively, which can be continuously adjusted between 10^{12} atoms/cm^2 and 10^{15} atoms/cm^2 depending on the experimental programme. In addition, this offers the possibility to optimise the target thickness during operation according to the conditions of the accelerator beam. This ensures a continuous luminosity and an efficient data acquisition. Thereby, the target thickness is constant over time, luminosity fluctuations in the data acquisition can be minimised. By using highly purified target material, background reactions are effectively reduced. Moreover, the cluster beam size and its shape are defined by the use of an orifice and can be adapted for each experiment.

A **pellet target** (cf. Figure 4.2 right) provides a target beam of frozen hydrogen or deuterium droplets. The WASA-at-COSY pellet target of the Wide Angle Shower Apparatus experiment is the only one operating at a storage ring experiment worldwide [A$^+$04, Ber09, Win11, Hus12, Dem13, Hü14]. Hydrogen is liquefied, close to the triplet point (13.957 K, 0.0736 bar [L$^+$09]) and pressed through a glass nozzle into the droplet chamber. The glass nozzle, with an inner diameter around 12 µm to 14 µm [Hus12], is connected to a piezoelectric element and due to the excitation, the hydrogen breaks up into evenly sized and spaced droplets. The droplet chamber is filled with helium gas with a pressure slightly below the triple point (20 mbar [W$^+$07]). A capillary extracts the droplet beam into a vacuum chamber (around 10^{-3} mbar [W$^+$07]), where the droplets freeze out to pellets and obtain a divergence as well as a defined velocity. Subsequently,

pellets with small divergence (< 1 mrad) pass through a skimmer. The WASA pellet generator allows for a pellet beam with a thickness of more than 10^{15} atoms/cm^2 at 14 K and 400 mbar to 800 mbar [W$^+$07]. Due to the small velocity of the pellets (60 m/s to 80 m/s [Hus12, W$^+$07]) in comparison to the supersonic gas-jet and cluster-jets, a pellet target can only be operated vertically. The pellet beam diameter is typically between 2 mm and 4 mm with pellets around 20 µm to 30 µm with an average distance of 5 mm [Hus12,W$^+$07]. The density can only be varied through the average number of pellets at the interaction point. A cryogenic droplet target operates very similar to a pellet target, where liquid hydrogen or helium passes through a nozzle, an aperture with a diameter of ≤ 5 µm, and expands into a vacuum chamber. The continuous liquid jet spontaneously breaks up into a stream of droplets. However, investigations with a cryogenic droplet target at the ESR at GSI show that areal densities of up to 10^{14} atoms/cm^2 with hydrogen and helium as target material can be covered.

The development and implementation of cryogenic targets is still progressing. A further application presents the investigation on laser induced particle acceleration, a novel technique to generate multi-MeV ion beams, where a highly intense laser pulse impinges on a mass-limited target. Mainly thin solid foils or gas jets are used, but their applicability is partially restricted. Alternatively, a cryogenic target can be implemented. First measurements with a cluster-jet target set-up, also constructed and tested at the University of Münster [Gri14], will be started at the ILPP (Institut für Laser und PlasmaPhysik) in Düsseldorf [Gri15].

	PROMISE/WASA at CELSIUS (Uppsala, Sweden) [Eks95]	**E835 at FERMILAB** (Illinois, USA) [A$^+$98c]	**ANKE, COSY11 at COSY** (Jülich, Germany) [D$^+$97b]
nozzle diameter	< 100 µm	37 µm	11 µm to 16 µm
gas temperature	20 K to 35 K	15 K to 40 K	20 K to 35 K
gas pressure	1.4 bar	< 8 bar	18 bar
distance *s*	0.325 m	0.26 m	0.65 m
max. density/ thickness	1.3×10^{14} $\frac{\text{atoms}}{\text{cm}^2}$	$> 3.2 \times 10^{14}$ $\frac{\text{atoms}}{\text{cm}^3}$	$\approx 10^{15}$ $\frac{\text{atoms}}{\text{cm}^2}$

Table 4.2.: Selection of cluster-jet targets and their performance with hydrogen as target material. The volume density decreases with the reciprocal value of the squared distance s^{-2} (cf. Chapter 5).

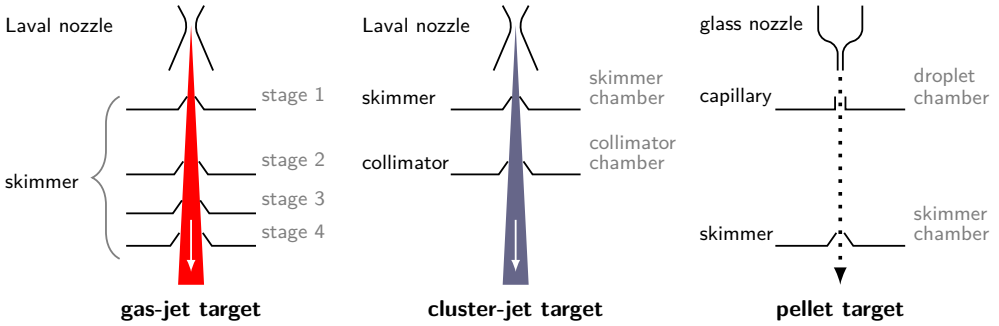

Figure 4.1.: Internal targets (gas-jet, cluster-jet, and pellet target) and their basic components. Beam direction is from top to bottom.

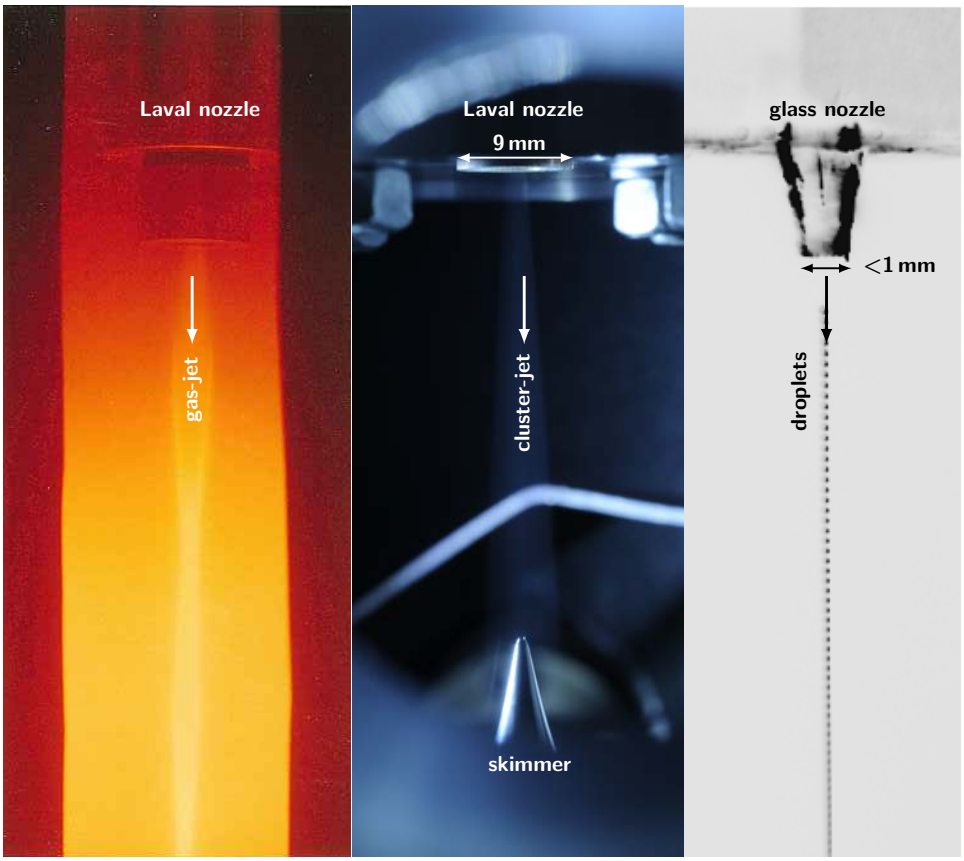

Figure 4.2.: Internal target beams (beam direction top down). Left: Gas-jet at the first stage (taken by G. Gaul [Gau86]). Center: Cluster-jet in the skimmer chamber (taken by D. Bonaventura). Right: Pentan droplets (taken by P. Hüsemann [Hü13]).

4.2. Cluster-jet target prototype

The cluster-jet target prototype for the $\overline{\text{P}}$ANDA experiment was constructed in complete $\overline{\text{P}}$ANDA geometry to investigate and optimise cluster beam characteristics (see Chapter 5 and 6). In context of a recent diploma thesis [Köh10], systematic measurements on the cluster velocity as well as the determination of the maximum target thickness were carried out. This thesis further concentrates on optimisation studies with regard to the maximal thickness at minimal target extension and also focuses on the investigation of the cluster mass. To achieve luminosities of up to $2 \times 10^{32}\,\text{cm}^{-2}\text{s}^{-1}$, $\overline{\text{P}}$ANDA requires an internal target with a thickness of the order of $10^{15}\,\text{atoms/cm}^2$ in a distance of more than two metres from the target source. Through the observation of highly intense core beams and the realisation of a novel cluster beam tilting system to extract them, systematic measurements could be carried out. Within this thesis, the target thickness was improved by more than a factor of two, from initially $8 \times 10^{14}\,\text{atoms/cm}^2$ [T$^+$11]. Details on this optimisation studies will be presented in Chapter 5 and constitute an important result of this work.
The complete cluster-jet target prototype presented in Fig. 4.3 and 4.4 comprises a cluster source including the novel tilting system, an interaction chamber with beam diagnostics as well as a beam dump, which can be extended with a microchannel plate detection system (see Section 5.3.3 and Chapter 6).

4.2.1. Cluster source

The heart of every cluster-jet target built up at the University of Münster constitutes a Laval nozzle, which is crucial for the production of clusters. Mainly purified and cooled hydrogen or deuterium is used as target material. The application of a differential pumping system ensures a well defined cluster beam with minimal residual gas background. Two adjustable orifices are installed for beam extraction and definition. Furthermore, this prototype features a novel nozzle tilting system, which affects the nozzle alignment and enables the investigation of observed highly intense core beams.
Laval nozzles have a specific convergent-divergent shape. Typically, Laval nozzles with a conical short inlet zone are used, which converge to the narrowest point and merge into a divergent long outlet zone (see Fig. 4.5). At the narrowest point of the nozzle, the target material reaches supersonic speed (cf. Section 5.1.3) and expands into a vacuum chamber. The expansion through the nozzle into vacuum causes a decrease of the target flow temperature, which is known as adiabatic cooling. Supersaturation and an increased collision rate of the particles lead to the formation of clusters, an accumulation of a few to several million atoms or molecules. According to the number of constituents, clusters can be classified as [Pau00b, Ber06]: micro clusters ($N \leq 10$), small clusters ($10 < N < 100$), large clusters ($100 < N < 1000$), micro crystals ($N > 1000$), or nano particles ($N > 10^6$).

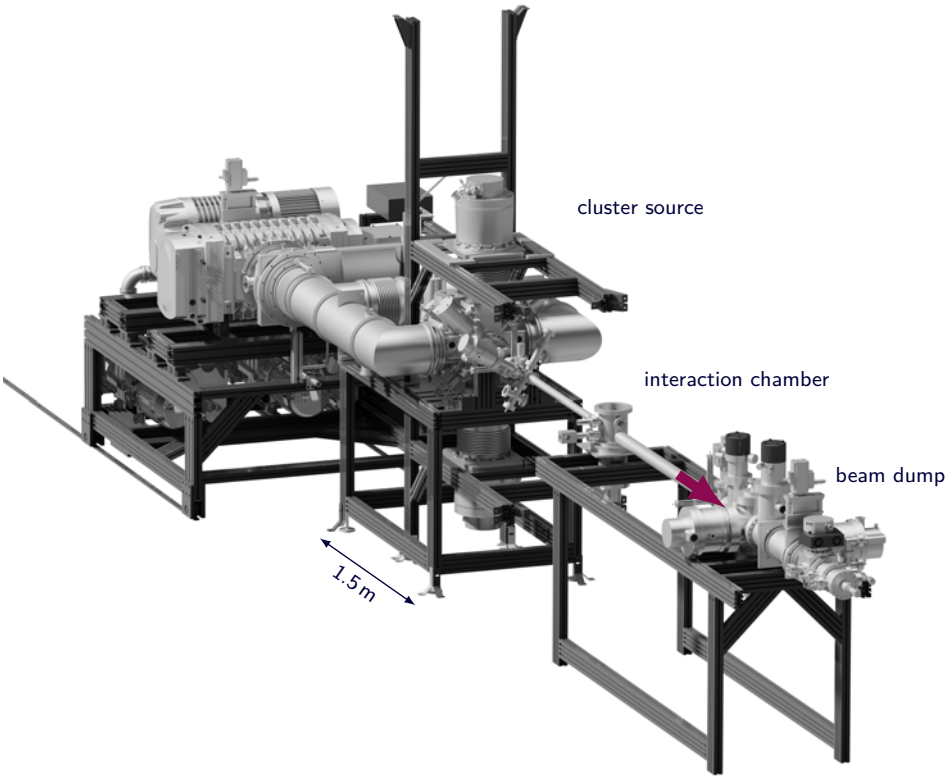

Figure 4.3.: Overview of the cluster-jet target prototype for the $\overline{P}$ANDA experiment (generated by D. Bonaventura with Autodesk Showcase, edited). The complete target has a total length of around nine metres and comprises a cluster source (currently with the pumping station for the final $\overline{P}$ANDA cluster-jet target), an interaction chamber which corresponds to the later interaction point, and a beam dump with a microchannel plate detection system. The thick violet arrow shows the cluster beam direction.

Responsible for cluster cohesion are various types of forces with binding energies between a few tenths of an eV, such as van der Waals cluster (hydrogen cluster), and some eV, e.g. metal cluster [Pau00b]. The cluster formation process and the beam characteristics, such as cluster velocity, thickness, or size etc., depend mainly on pressure and temperature of the target material at the nozzle inlet and also on the nozzle shape and its effective diameter.

The manufacture of Laval nozzles with an effective diameter below 30 µm constitutes a major technical challenge and was performed at CERN in the past. Unfortunately, the production was discontinued but an improved production process based on the initial CERN performance was developed at the University of Münster. Firstly, the new procedure foresees the manufacture of the positive model of the nozzle trumpet. It is turned and grinded out of a solid PolyMethyl MethAcrylate (PMMA)-rod (see Fig. 4.6 (1)). The next step involves the coating of the PMMA-positive with copper in

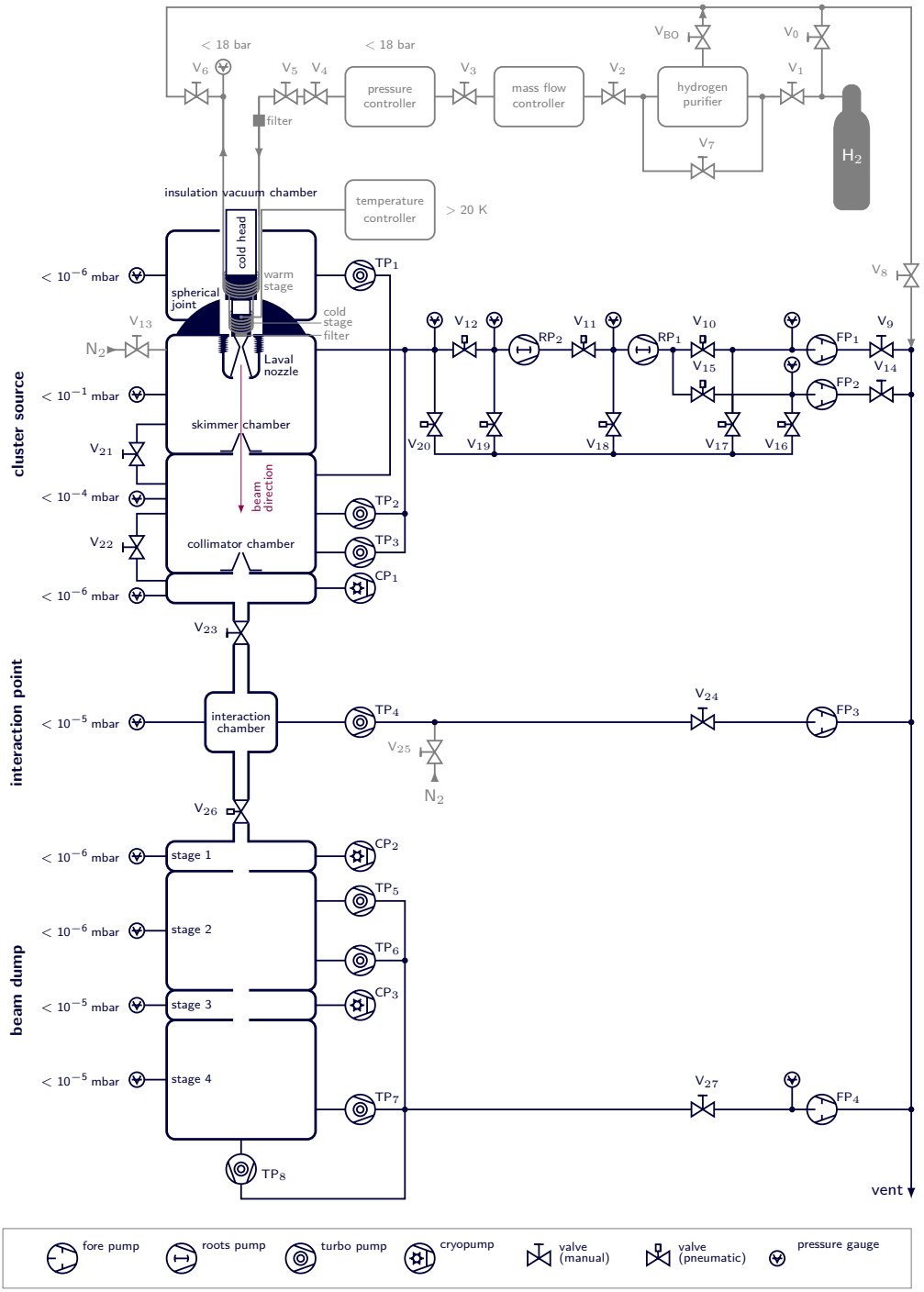

Figure 4.4.: Schematic vacuum design of the cluster-jet target prototype for $\overline{\mathrm{P}}$ANDA. Fore pumps are denoted with $\mathsf{FP}_{\mathsf{no.}}$, roots pumps with $\mathsf{RP}_{\mathsf{no.}}$, turbomolecular pumps with $\mathsf{TP}_{\mathsf{no.}}$, cryopumps with $\mathsf{CP}_{\mathsf{no.}}$, and valves with $\mathsf{V}_{\mathsf{no.}}$ (except for the Bleed Out valve V_{BO}). Hydrogen gas H_2 is used as target material and nitrogen gas N_2 is applied to ventilate the target.

a galvanic process to form the nozzle body (see Fig. 4.6 (2)). The outer shape of the nozzle is then precisely turned and after the extraction of the PMMA-positive the conical inlet zone can be machined (see Fig. 4.6 (3)). The last step connects both the inlet zone and the trumpet by drilling the space left between both cones via laser or a special drill bit [Gri15], which defines the effective diameter of the Laval nozzle. Finally a copper ring is shrunk onto the nozzle to maintain the CERN geometry.

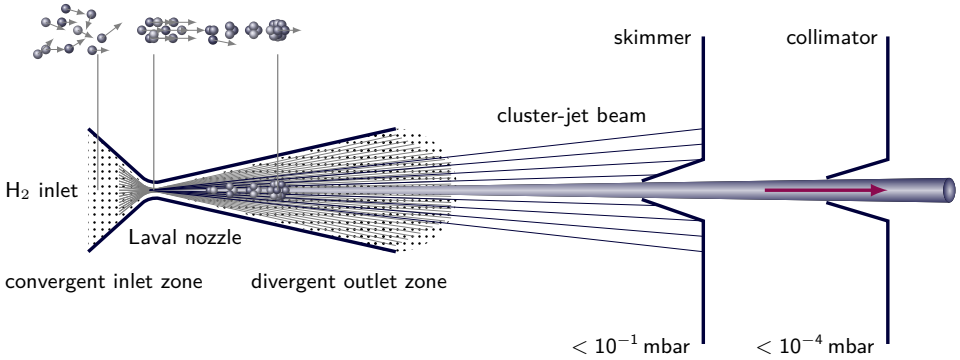

Figure 4.5.: Schematic representation of the cluster production process, beam extraction, and definition. Hydrogen passes the narrowest point of the Laval nozzle (with a pressure of up to 20 bar and temperatures down to 20 K) and expands into a vacuum chamber (vacuum pressure at highest thickness typically $< 10^{-1}$ mbar). Supersaturation and an increased collision rate of the particles lead to the formation of clusters, which is shown above the nozzle. The grey arrows present the velocity distribution of the particles inside the different nozzle sections. To separate the cluster-jet beam from the residual gas background (indicated with dots and grey lines) an orifice, the skimmer, extracts a small part of the beam into a further vacuum chamber (vacuum pressure at highest thickness typically $< 10^{-4}$ mbar). A second orifice, the collimator, defines the final size and shape of the cluster-jet beam.

Figure 4.6.: Laval nozzle production: (1) positive model of the nozzle trumpet (polymethyl methacrylate), (2) galvanised nozzle body (copper), (3) finished Laval nozzle inlet and (4) outlet part, and (5) cross-section of the Laval nozzle (Image (1) and (2) taken by W. Hassenmeier, (3) to (5) taken by D. Bonaventura).

Initial measurements with one of these new Laval nozzles have been carried out in this thesis at the $\overline{\text{P}}$ANDA target prototype. The production of new Laval nozzles opens the possibility for geometrical modifications, e.g. of the length or aperture angle of the nozzle trumpet [Gri15]. Furthermore, it allows for investigations on the cluster production process and the influence on the cluster characteristics and provides therefore another possibility for further improvements on the target thickness.

The cluster-jet target prototype is operating with especially **purified hydrogen as target material**. To avoid a clogging of the used Laval nozzle (effective diameter of 28 µm), the hydrogen gas passes a Johnson Matthey HE 20 hydrogen purifier with a silver-palladium membrane. Only hydrogen passes the membrane and impurities such as oxygen, water, carbon monoxide, carbon dioxide, nitrogen, and all hydrocarbons remain. The purifier utilises the effect that hydrogen undergoes dissociative adsorption on certain metal surfaces. Within the membrane, the hydrogen atoms ionise and diffuse through the heated silver-palladium alloy (temperature between 300 °C and 400 °C), whereas the admixture of silver stabilises the metal structure. After that, the recombination and desorption of the hydrogen molecules follows and hydrogen with a purity level of $9.0 \mathrel{\widehat{=}} 99.99999990\%$ can be provided directly behind the purifier's outlet [Joh98]. In addition, the installation of two sinter filters (with pore sizes around 0.5 µm and 20 µm) within the gas system ensures that unintended coarse impurities, e.g. imported during installation or maintenance, are retained from the nozzle. The gas flow (maximal $10\,\ell_{\text{n}}$/min, where n denotes under normal conditions) and pressure (maximal 24 bar) are both gauged and can be regulated by two controllers made by Brooks Instruments (Model 5850E and 5866). Furthermore, the static pressure at the nozzle inlet is gauged by a capacitance manometer (MKS Baratron 750B54MCB2GA) at the end of an additional outlet gas pipe (see Fig. 4.4).

The **gas cooling** occurs via the cooling of the gas pipes. Therefore, a dual stage cold head is used in combination with a compressor (Leybold COOLPOWER 10 MD and COOLPAK 6000 MD) according to the Gifford-McMahon process. One stage includes two volumes where helium can be compressed and expanded in a closed circuit. The compressor is filled with around 20 bar helium and provides a low pressure (< 20 bar) and high pressure (≈ 20 bar) connection for the cold head. The pressure variation is then induced by a displacer (moveable piston) with included regenerator (heat exchanger). Through this cooling cycle the first (warm) stage achieves a refrigeration capacity of approximately 110 W at 80 K and the second (cold) stage 18 W at 20 K, respectively. The gas pipes are directly wound around the stages, whereas copper is used instead of stainless steel at this point, because of its thermal conductivity. Copper ($384\,\text{W}/(\text{m}\cdot\text{K})$ at 20 °C [F$^+$05]) ensures the heat transmission at the warm and cold stage of the cold head and stainless steel ($14\,\text{W}/(\text{m}\cdot\text{K})$ at 20 °C [F$^+$05]) minimises the heat transmission at the transfer parts (see also Fig. 4.4 and 4.7). The Laval nozzle is also mounted on the cold stage and is sealed with an indium ring (outer diameter: 18 mm, inner diameter: 10 mm).

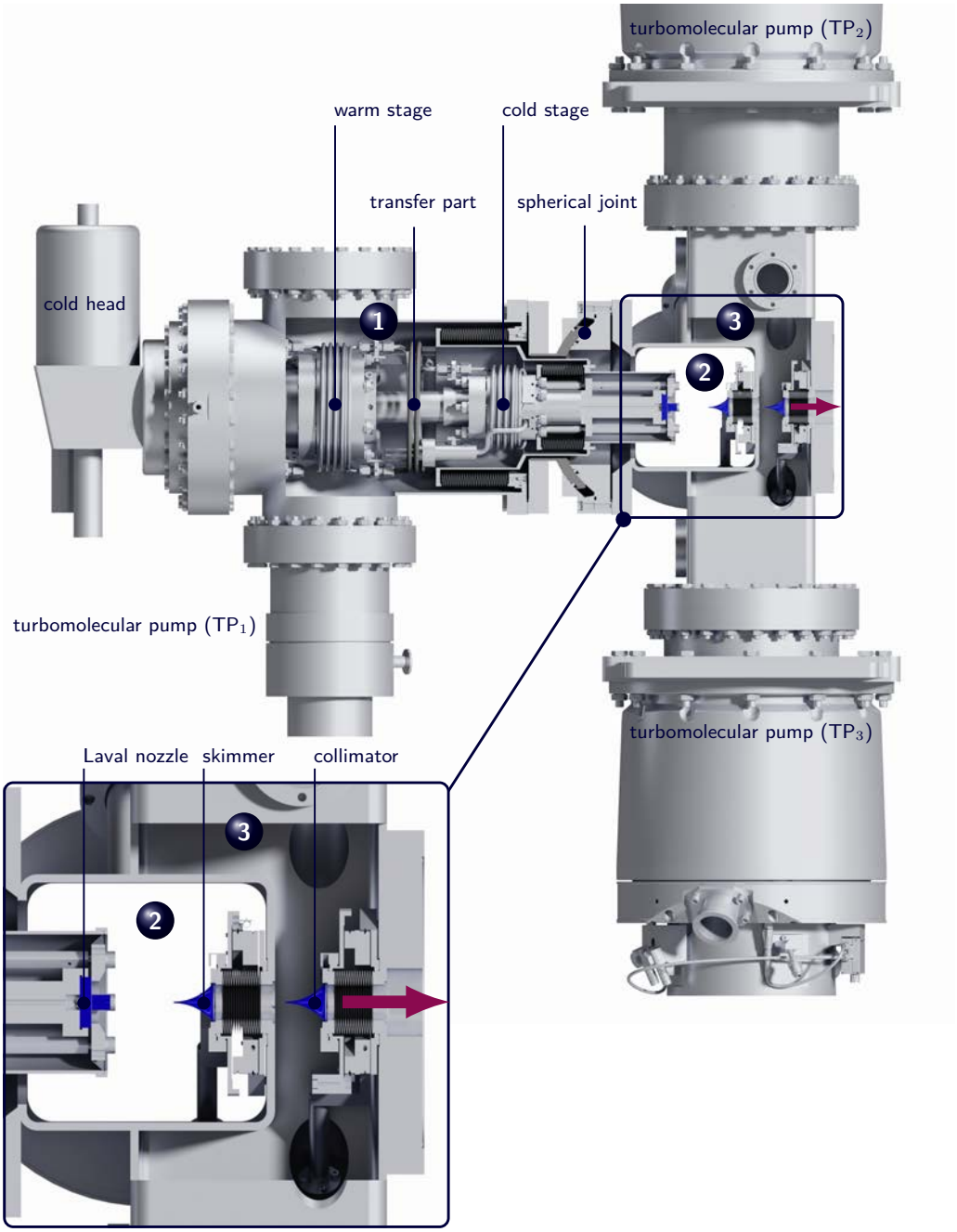

Figure 4.7.: Cluster source (generated by D. Bonaventura with Autodesk Showcase, edited) and their components: (1) insulation vacuum chamber with cold head and gas pipes, which is connected to the skimmer chamber via a spherical joint, (2) skimmer chamber including the Laval nozzle and skimmer, (3) collimator chamber with collimator for beam definition. The violet arrow corresponds to the cluster beam direction.

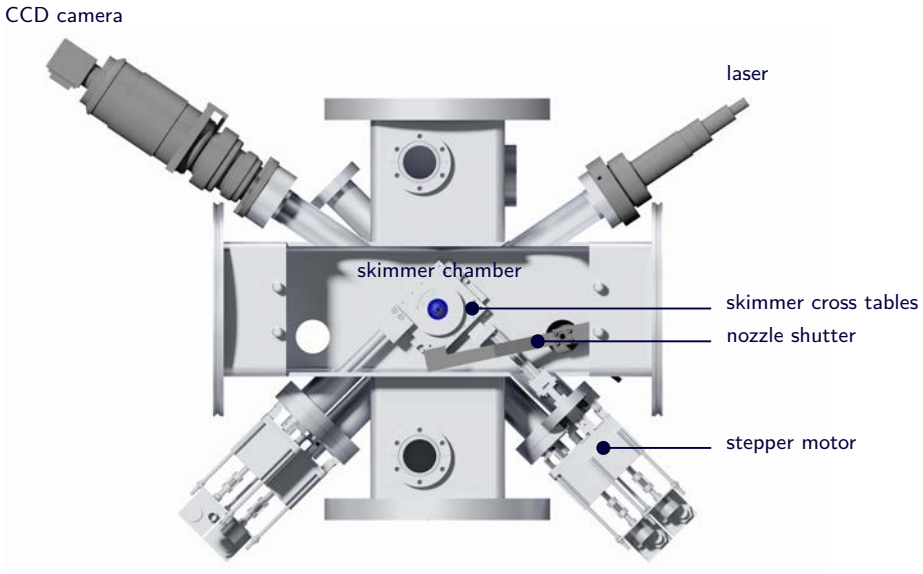

Figure 4.8.: Insight into the skimmer chamber (generated by D. Bonaventura with Autodesk Showcase, edited), which features a moveable skimmer installed on cross tables, a nozzle shutter as well as a CCD camera combined with a diode laser for illumination. The beam axis points into the plane.

Moreover, the cold stage or nozzle holder, respectively, is equipped with a thermal diode to monitor the temperature. Measurements directly in the gas flow and at the copper nozzle holder provided equal temperature results. Temperature stabilisation and regulation is covered by a Lakeshore temperature controller (Model 331) linked to a heating cartridge with maximal 50 W. The complete cold head and the surrounding gas pipes are enclosed by the insulation vacuum chamber to minimise thermal transfer (vacuum pressure around 10^{-6} mbar). The target prototype reaches temperatures below 20 K at 18 bar.

To prepare a well defined cluster-jet beam with minimal residual gas background, the cluster source contains a **differential pumping system**. The cluster beam passes the skimmer and collimator chamber (vacuum pressure at highest thickness around 10^{-1} mbar and 10^{-4} mbar, see Fig. 4.4, 4.5, and 4.7) through special orifices of the same denomination. The skimmer separates the cluster-jet beam from the residual gas background and extracts a small part of the beam into the collimator chamber, where the beam obtains its final size and shape. A Beam Dynamics skimmer with a sharp edged orifice with a diameter of 0.5 mm and a nickel wall thickness of 10 µm is installed. A small exterior and large interior angle minimises the scattering of the clusters induced by reflected clusters at the outer surface or fractured clusters at the inner surface of the skimmer, respectively. The size and shape of the beam is then defined by a stainless steel collimator with an orifice

diameter of 0.7 mm installed by default. In addition, this thesis focuses especially on the application of slit collimators and their influences on the target thickness, which was also investigated in the scope of the master thesis of A. Hergemöller [Her13] and will be presented in detail in Section 5.3. Skimmer and collimator are both installed on cross tables combined with a stepper motor control for horizontal and vertical fine adjustments perpendicular to the beam axis (see Fig. 4.8). The cross tables can be shifted ±2 mm at an angle of 45 degree to avoid interactions of the cluster beam with the following beam tubes.

Moreover, a nozzle shutter is installed at the skimmer chamber, which offers the possibility for an on/off mode of the beam by reflecting the cluster beam on a copper sheet metal (cf. Fig. 4.8). This prevents the penetration of the beam through the skimmer into the collimator chamber and the following vacuum chambers. Furthermore, the skimmer chamber is equipped with a CCD camera (PCO pixelfly qe) and a macro lense (Zeiss Makro-Planar T* 2.0/100 mm ZF) as well as a diode laser (Flexpoint, point type, up to 1 mW, 650 nm) with beam expander (BEX-633-5X, beam diameter around 20 mm) to monitor the condition of the illuminated cluster-jet beam. Camera and laser are both mounted extraneous at two opposite viewports in an angle of 35 degree perpendicular to the beam axis via a spherical joint for further adjustments (see Fig. 4.8). This enables the observation of highly intense core beams and points to an increase of the attained maximal target thickness.

Investigations on these core beams were performed in this thesis due to the possibility to adjust the propagation of the cluster beam. Therefore, the skimmer chamber features a novel **nozzle tilting system** to adjust the angle of the cluster-jet beam with the narrowest point of the nozzle as point of rotation. The nozzle tilting system includes a spherical joint and a nozzle extension with a thermal shielding. The spherical joint is installed between the insulation vacuum and skimmer chamber. It consists of a rotation and sliding surface connected through a retaining ring, all surrounded by two CF-200 flanges (see Figure 4.9). The components are sealed with viton O-rings and the gap between the sliding surface and the retaining ring is pumped differentially (not included in Figure 4.4). The nozzle extension ensures the initial distance of the nozzle to the skimmer of 56 mm. It is turned out of copper and connected via an indium sealing. A thermal shielding made of stainless steel encloses the nozzle extension in the skimmer chamber which is connected to the insulation vacuum chamber (cf. Fig. 4.7) and sealed with a Mylar foil (polyester film). Angles of up to ±3.5 degree can be adjusted in horizontal and vertical direction (see Figure 4.10). This system allows for adjustments of the cluster beam and extraction of intense core beams. Systematic measurements on these highly intense core beams were carried out in this thesis and are presented in Chapter 5.

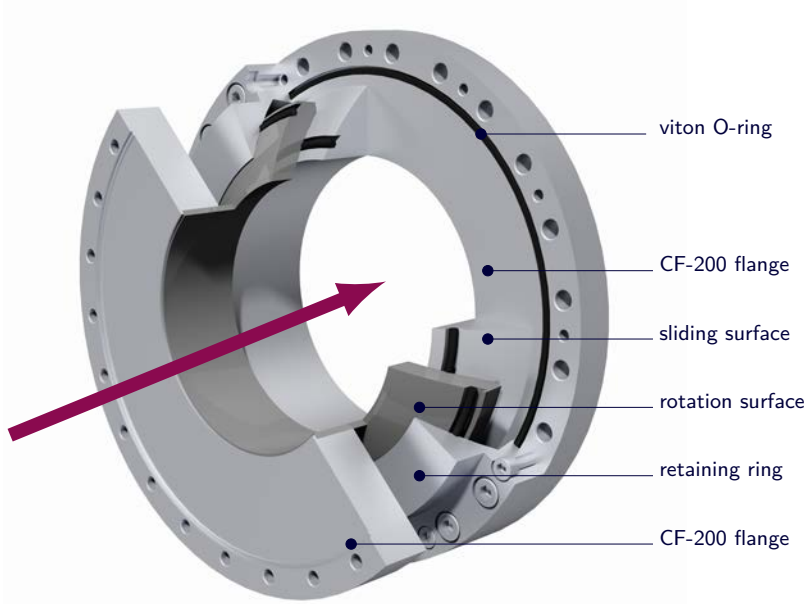

Figure 4.9.: Spherical joint (generated by D. Bonaventura with Autodesk Showcase, edited), connected via CF-200 flanges between insulation vacuum and skimmer chamber, and its components (retaining ring, rotation, and sliding surface). All segments are sealed with viton O-rings and the gap between the sliding surface and the retaining ring is pumped differentially. The arrow shows the cluster beam direction.

The cluster-jet target prototype not only enables the investigation on the beam characteristics and the development of new technical constituents, but also offers the possibility to test new components of the final $\overline{\text{P}}$ANDA cluster source for the first time, which is currently under construction [Her15]. Therefore, the design and especially the **pumping system** of the prototype varies.
Depending on the occurring gas flow and the required vacuum pressure in each vacuum chamber, the prototype is equipped with various types of vacuum pumps (cf. Fig. 4.4), namely: rotary vane pumps as fore pumps ($\mathsf{FP}_{\mathsf{no.}}$) combined with roots ($\mathsf{RP}_{\mathsf{no.}}$) and/or turbomolecular pumps ($\mathsf{TP}_{\mathsf{no.}}$), and even cryopumps ($\mathsf{CP}_{\mathsf{no.}}$). Since cryopumps repeatedly need to regenerate, they are substituted by turbomolecular pumps in the vacuum design of the final $\overline{\text{P}}$ANDA cluster source and the beam dump. The waiver of cryopumps was also effectively tested at the beam dump of the cluster-jet target prototype (cf. Chapter 6 and Appendix A.6). All mentioned vacuum pressures apply to the operation at highest thickness and can be improved through the installation of vacuum pumps with higher pumping speed. An overview of the particular pumping speed of each pump installed at the prototype is given in Table 4.3.

Previously, the cluster source was equipped with three pumping stations, each containing a series of a fore pump and two roots pumps. Two pumping stations were provided for the

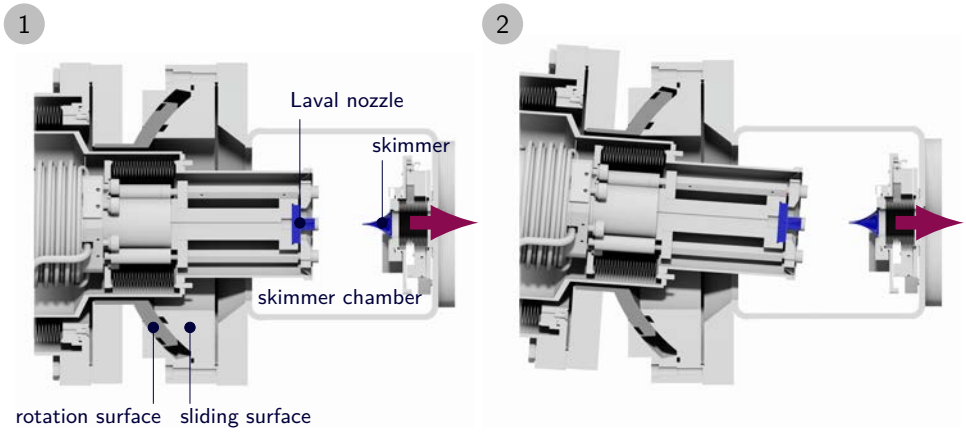

Figure 4.10.: Spherical joint (generated by D. Bonaventura with Autodesk Showcase, edited) in initial position (1) and at maximal vertical deviation (2). The violet arrow shows the cluster beam direction.

skimmer chamber and the third station acted as a pre vacuum system for the installed turbomolecular pumps at the insulation vacuum and collimator chamber [Köh10]. The pumping stages are currently replaced by the final pumping station for $\overline{\text{P}}$ANDA, which assumes the function as primary pumping system for the skimmer chamber (vacuum pressure typically below 10^{-1} mbar at 80 mbar ℓ/s) and in parallel as a pre vacuum system for the installed turbomolecular pumps (TP_2, TP_3) at the collimator chamber (vacuum pressure typically below 10^{-4} mbar). The exhaust of the turbomolecular pump (TP_1) of the insulation vacuum chamber (vacuum pressure typically around 10^{-6} mbar) is directly connected to the collimator chamber.

In order to avoid a shifting of the cluster-jet beam by asymmetric evacuation as shown in [Köh10], the skimmer chamber is enclosed with an ISO-250 pipe system for symmetrical evacuation. The vacuum in the skimmer chamber must be strictly below 10^{-1} mbar to provide the basis for a stable cluster-jet beam [K$^+$99]. The $\overline{\text{P}}$ANDA pumping station contains two parallel fore pumps (Leybold SOGEVAC SV300B, explosion proof, FP_1, FP_2) and two roots pumps (Leybold RUVAC WS2001 RP_1 and WH7000 RP_2) connected in series, installed on a KANYA aluminium frame as presented in Figure 4.11. In combination with a frequency converter the pumping speed of both roots pumps (RP_1, RP_2) can be varied. Furthermore, gate valves are located between each pump (V_{11}, V_{12}) as well as an additional parallel vacuum pipe, also equipped with valves (V_{15} to V_{19}), to evacuate each section independently (see also Fig. 4.4).

no.	fore pump $FP_{no.}$ in m^3/h	roots pump $RP_{no.}$ in m^3/h	turbo pump $TP_{no.}$ in ℓ/s
1	300	2000	360
2	300	7000	2000
3	25	–	2000
4	200	–	360
5	–	–	1000
6	–	–	360
7	–	–	1000
8	–	–	1000
9	–	–	300

Table 4.3.: List of the installed vacuum pumps of the cluster-jet target prototype and their nominal pumping speed for air. Roots pump (RP_1) and (RP_2) can be operated with maximal 100 Hz and 70 Hz, which results in a pumping speed of 4000 m^3/h and 9800 m^3/h.

4.2.2. Interaction chamber and beam dump

After the production, extraction, and definition of the cluster-jet beam at the cluster source, the beam passes a cryopump (CP_1). The prototype is equipped with special cryopumps designed at the University of Münster, which are provided with activated carbon coated cold sheets. The cluster beam passes each cold sheet of the cryopump through a 40 mm opening (cf. cluster beam diameter at cryopump $CP_1 > 0.7$ mm). Surrounding residual gas background stays on the cold sheets (temperatures below 16 K) and a pumping speed around 22000 ℓ/s can be achieved [Kho92]. Despite of their enormous pumping speed, cryopumps repeatedly need to regenerate. Therefore, the vacuum design of the final $\overline{\mathrm{P}}$ANDA cluster source and the beam dump includes only turbomolecular pumps at the high vacuum sections [PAN12a] (10^{-7} mbar to 10^{-3} mbar).

In a distance of 2.1 m from the Laval nozzle, the cluster beam enters the **interaction chamber**, the future $\overline{\mathrm{P}}$ANDA interaction point. The interaction chamber features a turbomolecular pump (TP_4) combined with a fore pump (FP_3) and a beam diagnostic system (see Fig. 4.12). It contains two moveable rods, which are scanning successively the target beam in vertical and horizontal direction. Through the interaction of the clusters at the rod, the clusters break up and cause a pressure increase. The recorded vacuum pressure in dependence on the rod position results in a beam profile presented in Fig. 4.13, which allows the determination of the beam position, size, and density or thickness, respectively.

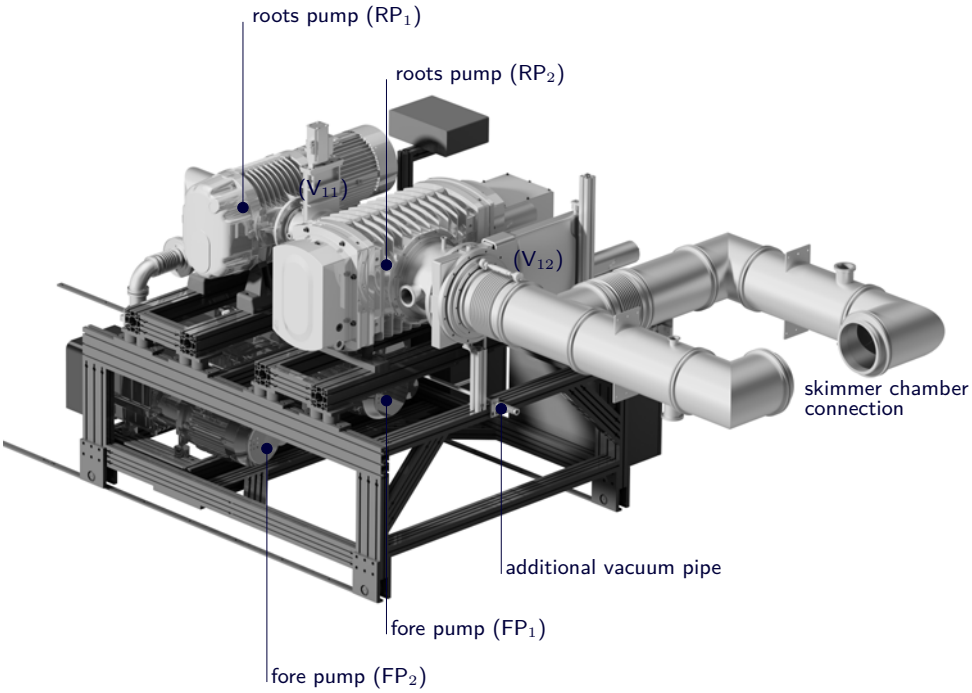

Figure 4.11.: Pumping station of the final cluster-jet source for $\overline{P}$ANDA (generated by D. Bonaventura with Autodesk Showcase, edited). The station includes two parallel fore pumps (FP_1, FP_2) and two roots pumps (RP_1, RP_2) in series (also see 4.4). Valves are denoted with (V_{11}, V_{12}).

The prototype's **beam dump** comprises four stages alternately equipped with cryopumps (CP_2, CP_3) and turbomolecular pumps (TP_5 to TP_8, see Fig. 4.14 setup (1)). All turbomolecular pumps are connected in parallel with a fore pump (FP_4). At the last stage, the cluster-jet beam impinges on the first rotor disc of the turbomolecular pump (TP_8), fractures, and will be exhausted. The individual stages prevent the backstreaming of the cluster fragments made of hydrogen molecules. At highest thickness, the vacuum pressures are typically between 10^{-5} mbar and 10^{-6} mbar. Turbomolecular pump (TP_8) can be replaced by a special MicroChannel Plate (MCP) detection system, which will be presented in detail in Section 5.3.3 and Chapter 6. The basic component contains an arrangement of a grounded grid followed by two MCPs in chevron assembly and a phosphor screen. If an ionised cluster beam, e.g. ionised through an electron beam, impacts on the first MCP, it causes an electron avalanche within the according channels, which will be enhanced by the second MCP. The visualisation adopts a phosphor screen combined with a CCD camera. The recorded images allow a direct observation of an ionised cluster-jet beam and even the vertex zone of a cluster and accelerator beam, which was also investigated at the ANKE cluster-jet target at COSY [K^+14b] within this thesis (cf. Section 5.3.3). Furthermore, the basic MCP system can be extended through a turbomolecular pump

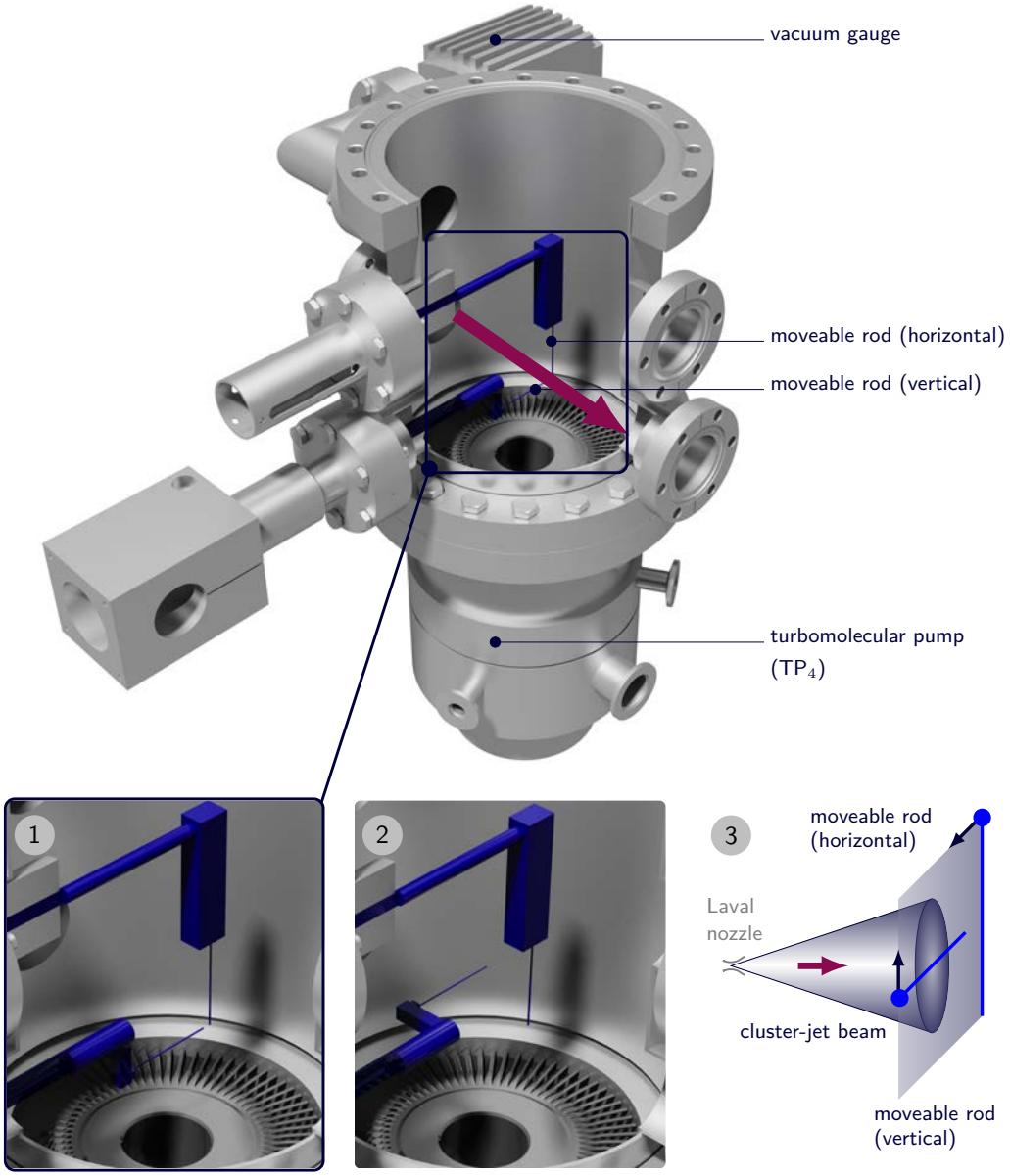

Figure 4.12.: Interaction chamber with beam diagnostic system (generated by D. Bonaventura with Autodesk Showcase, edited). The moveable rods are in their initial position, i.e. beyond the cluster beam path (violet arrow). Subfigure (1) shows an enlargement of the framed part, in (2) the vertical rod is postponed and will interact with the cluster beam as schematically indicated in (3) .

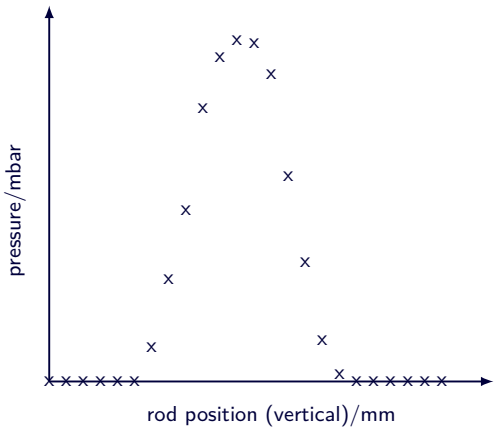

Figure 4.13.: Schematic representation of a recorded beam profile in vertical direction. The width of the distribution corresponds to the beam diameter and the position of the maximal pressure increase shows the beam position at the interaction chamber. The maximal pressure increase is proportional to the target thickness.

(TP_9) with an associated fore pump (FP_5) and a additional grid arrangement, which provides a retardation field to investigate the cluster mass (cf. Fig. 4.14 (2)). The results are outlined in Chapter 6 and present one main emphasis of this thesis.

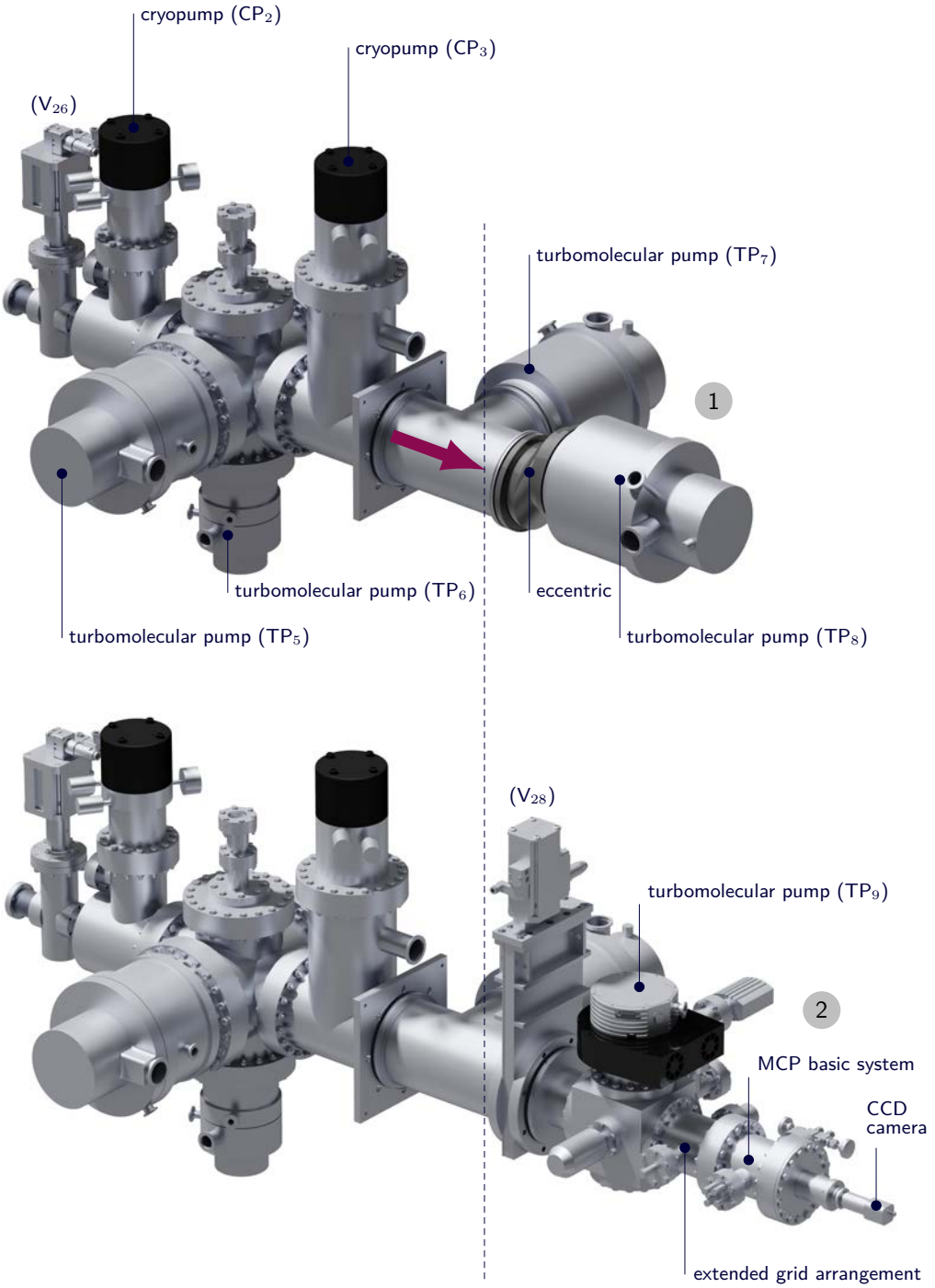

Figure 4.14.: Beam dump setup (1) and (2) of the cluster-jet target prototype (generated by D. Bonaventura with Autodesk Showcase, edited), which is alternately equipped with a cryopump (CP_2, CP_3) and turbomolecular pumps (TP_5 to TP_8). (1) Due to the installed eccentric, the cluster-jet beam (violet arrow) impinges and fractures on the first rotor disc of the turbomolecular pump (TP_8) and will be exhausted. Turbomolecular pump (TP_8) can be replaced by a microchannel plate detection system (2) with turbomolecular pump (TP_9). Installed valves are denoted with (V_{26}, V_{28}).

4.3. Final cluster-jet target

The construction of the final cluster-jet source for $\overline{\mathrm{P}}$ANDA [Her15, Het15] is in progress and is at an advanced stage. As shown in Figure 4.15, the compact target design features: an insulation vacuum, skimmer, and collimator chamber with a stepper motor controlled nozzle tilting system, skimmer, and collimator. In addition, two cameras will be installed to observe the cluster beam in the skimmer chamber as well as a nozzle shutter. The connection through the HESR pipe occurs via a special locking system and guarantees an optimal fitting.

The complete cold head system was constructed and tested in regard to overpressure strength, leakages, and minimal temperature within this thesis (see also [Zan13, Her13]). For these tests, the Laval nozzle was replaced by a closed nozzle dummy and the insulation vacuum chamber was evacuated by a turbomolecular pump (145 ℓ/s) combined with a fore pump (16 m^3/h). The gas system withstands a helium pressure of up to 32 bar. With 10 bar helium in the gas system and 6×10^{-3} mbar insulation vacuum, the leakage rate amounts 5×10^{-7} mbar ℓ/s. Furthermore, the cold stage reaches temperatures below 10 K with 10 bar helium (in the gas system) at 6×10^{-7} mbar insulation vacuum. In addition, the cold head system was tested with a 40 µm Laval nozzle in combination with the described final $\overline{\mathrm{P}}$ANDA pumping station. At 1.2 bar hydrogen pressure before the Laval nozzle inlet (mass flow around 5.6 ℓ_{n}/min), the minimal temperature is 16.5 K. The selected pressure corresponds to the maximal mass flow at the target prototype which is operating with a 28 µm Laval nozzle at highest thicknesses. The initial operation of the complete $\overline{\mathrm{P}}$ANDA cluster source is planned for this summer.

Figure 4.16 presents the integration of the cluster source at the $\overline{\mathrm{P}}$ANDA target spectrometer and shows the selected position for the pumping station and the associated target accessories.

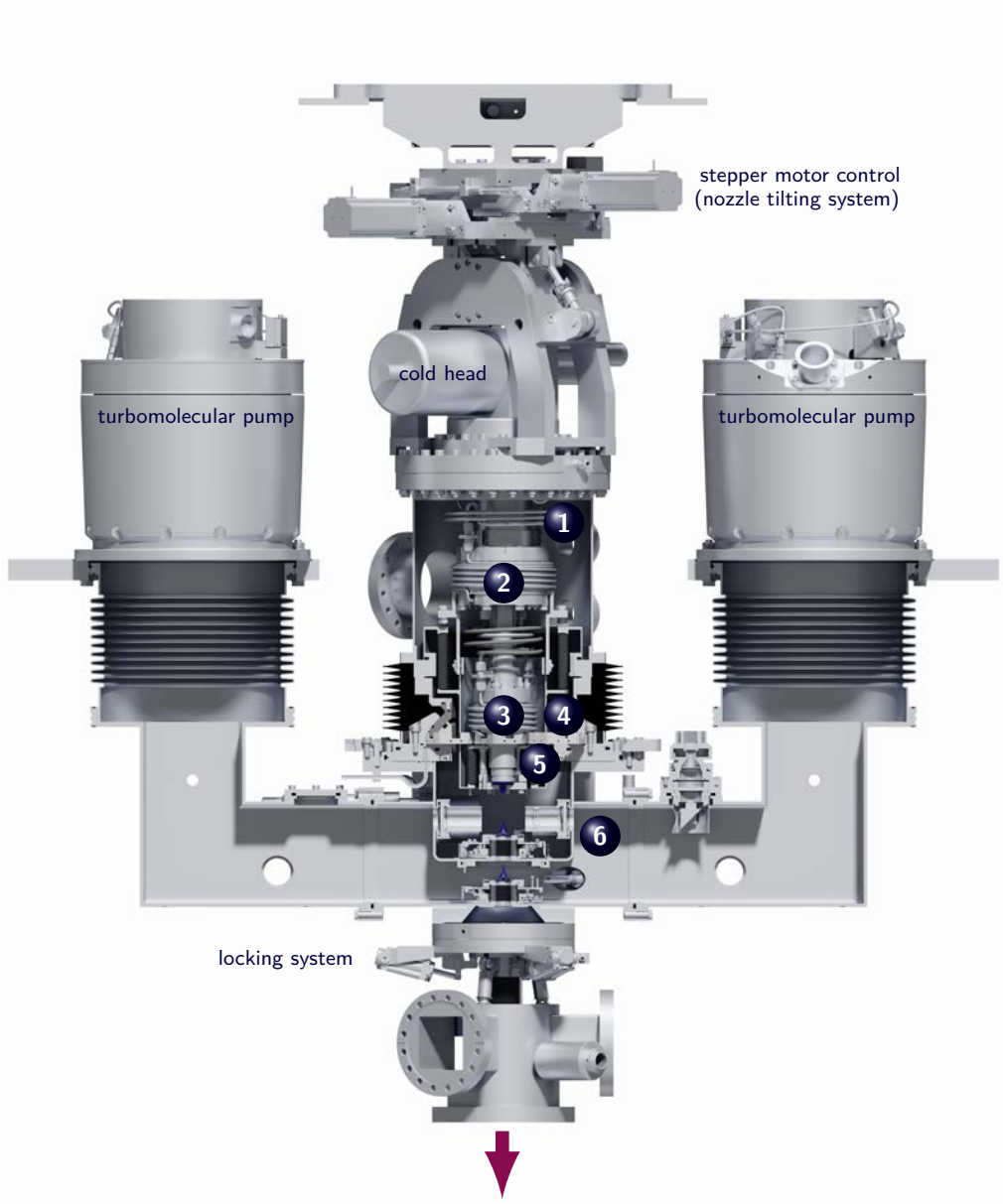

Figure 4.15.: Main components of the final cluster source for the $\overline{\text{P}}$ANDA experiment (generated by D. Bonaventura with Autodesk Showcase, edited). The insulation vacuum chamber (1) contains the cold head including warm stage (2) and cold stage (3). The spherical joint (4) of the nozzle tilting system is located between insulation vacuum and skimmer chamber (5) and is controlled via stepper motors. After the production (Laval nozzle) and extraction (skimmer) of the cluster jet beam (violet arrow) follows the definition (collimator) within the collimator chamber (6). A special locking system guarantees an optimal fitting to the HESR beam pipe.

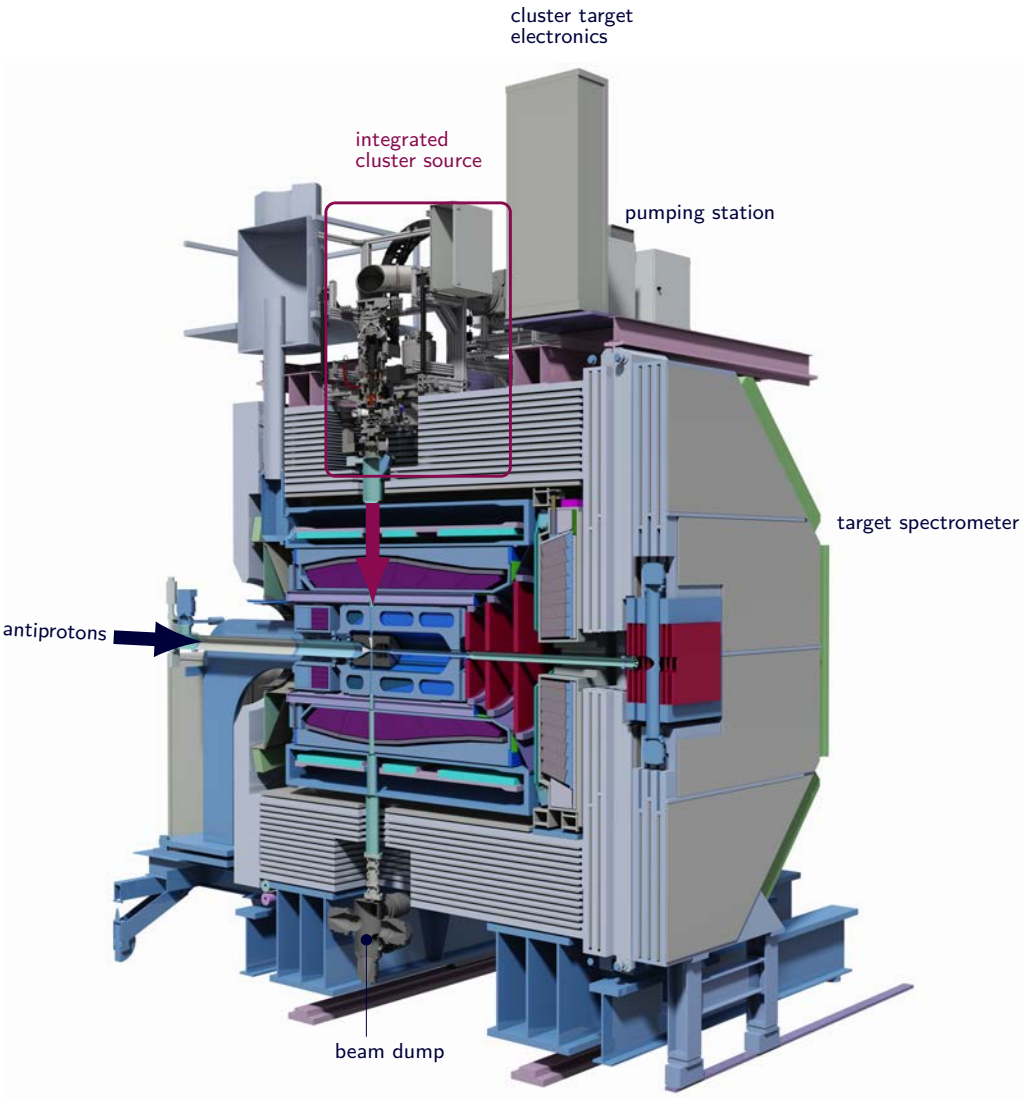

Figure 4.16.: $\overline{P}$ANDA target spectrometer with integrated cluster-jet target (generated by D. Bonaventura with Autodesk Showcase, edited). The pumping station and target equipment is located on the upper platform. The violet arrow presents the cluster beam and the blue arrow the antiproton beam.

5. Density optimisation studies of hydrogen cluster-jet beams

The particle density is an essential parameter for the application of internal targets in particular with regard to storage ring experiments and the desired event rate or luminosity (cf. Section 4.1.1). The (number) density is commonly specified by volume density ρ (atoms/cm^3) and areal density ρ_{areal} or thickness (atoms/cm^2). The conversion occurs via the integrated volume density along a path x:

$$\rho_{areal} = \int \rho \, \mathrm{d}x. \tag{5.1}$$

At the $\overline{\mathrm{P}}$ANDA experiment, a luminosity of up to $2 \times 10^{32}\,\mathrm{cm}^{-2}\mathrm{s}^{-1}$ [PAN12a] is required, which corresponds to an areal density at the interaction point of $4.5 \times 10^{15}\,\mathrm{atoms/cm}^2$ (cf. Section 4.1.1). With a target beam overlap of 1 cm, the volume density results to a value of $4.5 \times 10^{15}\,\mathrm{atoms/cm}^3$ (cf. Equation (5.16) and (5.44)). Furthermore, the distance from the internal target source to the interaction point amounts more than two metres for an almost 4π acceptance of the $\overline{\mathrm{P}}$ANDA detector. Due to the propagation of the cluster-jet beam according to the intercept theorem, the radius of a cylindrical volume element increases with the distance (see Figure 5.1 with comparison approximated volume V_{I} and V_{II}). Therefore, the volume density decreases with the reciprocal value of the squared distance (s^{-2}). Doubling the distance results in the decrease of the volume density by a factor four.

The comparability between the densities of different targets or various target types is complex and can only occur at equal distance from the nozzle of a specific volume or area. A selection of cluster-jet targets and their performance is shown in Table 4.2 in Chapter 4 and presents a maximal thickness of around $10^{15}\,\mathrm{atoms/cm}^2$ at 0.65 m from the nozzle [D$^+$97b]. With regard to the distance at $\overline{\mathrm{P}}$ANDA, the density of the cluster-jet target must be increased by more than one order of magnitude. This provides a major challenge which was finally mastered in the scope of this thesis, due to the extraction of highly intense core beams.
Before the results are presented, this chapter will shortly introduce the experimental possibilities for density investigations and will then elaborate the selected technique and its required parameters, especially the cluster velocity. This method provides accurate

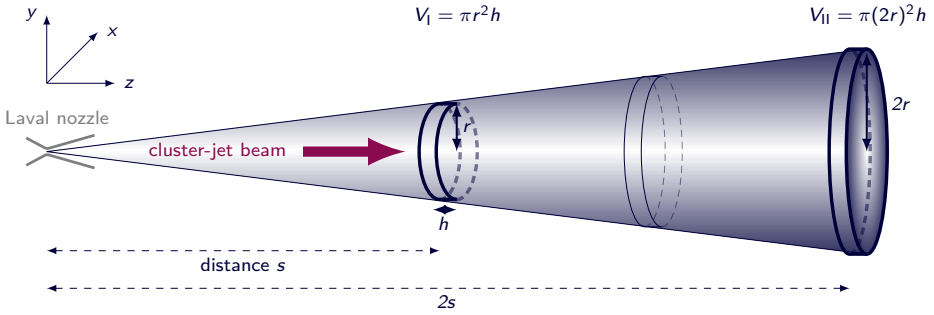

Figure 5.1.: Illustration of the decreasing volume density of a propagating cluster-jet beam (from left to right) with comparison volume V_I and V_{II}. The doubling of the distance s results in the decrease of the volume density by a factor four ($\rho \propto s^{-2}$).

target densities for various beam shapes (e.g. circular or rectangular). Besides, the optimisation of the maximal target thickness, reproducibility, and stability measurements will be shown. Furthermore, the minimisation of the target expansion through specially shaped collimators (cf. [Her13]) will be discussed, which will lead to reduced background reactions, a precise vertex reconstruction, and a prolonged lifetime of the accelerator beam. Finally, the visualisation of the cluster beam shape (cf. [Zan13]) as well as the imaging of the beam/target interaction zone with a microchannel plate detection system will be presented.

5.1. Density determination of molecular target beams

The determination of the target density can be performed through various techniques, which are based on particle scattering or the retaining of the target beam. Since the particle scattering methods exert only a slight influence on the target beam propagation, they are classified as 'non destructive'. Consequently, the retaining of the complete or partial target beam is categorised as 'destructive' method.

5.1.1. Non destructive methods

The scattering of charged particles, e.g. protons or electrons, enables the investigation of the density distribution of a target beam and belongs to the non destructive methods. Compared to protons, electrons offer the advantage of good availability, convenient handling, and detection [T+79]. Density investigations with electrons can be executed, e.g. via electron beam attenuation, fluorescence, or elastic scattering followed by a density calibration.

The **attenuation** of an electron beam arises through multiple small angle scattering, where the interaction depends on the target density. Only the unaffected electrons will be caught in a Faraday cup and the resulting current is then related to the density. The measurable density range depends on the electron's energy. Density investigations with gas-jets and 20 keV electrons (current below 5 µA) lead to a density range of 0.5 µg/cm^2 to 100 µg/cm^2 [T$^+$79] ($\approx$ (3 to 600) $\times 10^{17}$ atoms/cm^2, directly behind the nozzle).

Inelastic scattering of electrons with atoms of the target beam causes the excitation to higher electronic states and subsequently the emission of radiation (**fluorescence** within 10^{-8} s [McK88]). The occurring photo current is thus a measure for the density. It has been shown that the excited state life-time should be below 10^{-7} s to reduce quenching (intensity decrease) and to avoid intensity losses at the detection field caused by the comparatively high velocity of the target stream [T$^+$79]. The maximal accessible density depends on the mean free path and therefore on temperature and pressure of the corresponding target material [Wä88]. Depending on the detector sensitivity, a density range of 0.5 µg/cm^3 to 50 µg/cm^3 [T$^+$79] ($\approx$ (3 to 300) $\times 10^{17}$ atoms/cm^3, directly behind the nozzle) of argon gas-jets and 0.02 µg/cm^3 to 20 µg/cm^3 [T$^+$79] ($\approx$ (0.12 to 120) $\times 10^{17}$ atoms/cm^3, directly behind the nozzle) of nitrogen gas-jets can be covered.

Moreover, the **elastic scattering** of electrons can be utilised for density investigations. The scattering probability depends mainly on the scattering angle, the atomic mass number of the target material, and the density, whereas Rutherford scattering is prevailing above 5 degrees [T$^+$79]. Rutherford's differential scattering cross section $d\sigma/d\Omega$ is given by [P$^+$08]

$$\frac{d\sigma}{d\Omega}(\vartheta) = \left(\frac{1}{4\pi\epsilon_0}\frac{Ze^2}{4E}\right)\sin^{-4}\left(\frac{\vartheta}{2}\right) \tag{5.2}$$

with scattering angle ϑ, atomic mass number Z, elementary charge e, the electron energy E, and the electric constant ϵ_0. In addition, corrections in regard to the electron spin (Mott scattering), relativistic mass increase, and shielding of the Coulomb potential through orbital electrons should be considered. The density limit for this method is restricted by the increase of multiple angle scattering with rising density. For argon gas-jets and 20 keV electrons, the density is limited to 15 µg/cm^3 [T$^+$79] ($\approx 10^{19}$ atoms/cm^3, directly behind the nozzle).

This method was successfully applied at the University of Münster and further improved at a gas-jet [Pfa86, Wä88] as well as at a cluster-jet target [Hö88, Dom89, Kho92, Kho96]. The resulting density profiles of carbon, nitrogen, argon, methane, and hydrogen cluster-jets were analysed. Density calibration can follow via the mass flow through the nozzle, the residual gas background, or the scattering on a carbon foil [Dom89]. However, the electron

energy must be adjusted to the density range and the use of detectors with high sensitivity is mandatory for precise insights and results. High background (emission electrons) is also expected and therefore, the destructive methods remain of great interest. Optical methods, e.g. Schlieren photographs [BKS79] or the installation of a Mach-Zehnder interferometer, are only applicable directly behind the nozzle.

5.1.2. Destructive methods

In order to investigate the density distribution of the hydrogen cluster-jet beam of the target prototype for $\overline{\mathrm{P}}$ANDA, a mechanical monitoring system was selected, which belongs to the destructive methods. These techniques are based on the retaining of the complete or partial cluster-jet beam and are especially suited for investigations in the laboratory environment. Thereby, the clusters fracture and cause a pressure increase, which is a measure for the target density. Retaining can occur via the implementation of, e.g. plates, rods, or thin wires, which was tested at several cluster-jet targets constructed at the University of Münster [Que97, Rau04, Ott07, Gen08]. The gradual scan in vertical and horizontal direction with a rod has proven particularly suitable, due to the durable construction and the resulting pressure or beam profiles, respectively. In this case, the determination of the volume density ρ depends fundamentally on two parameters: the maximal pressure increase p_0 and the cluster velocity v via

$$\rho \propto \frac{p_0}{v}. \tag{5.3}$$

The maximal pressure increase can be extracted through an accurate adaptation of the resulting beam profiles with an appropriate distribution, depending on the beam shape (e.g. circular or rectangular). Moreover, p_0 corresponds directly to the volume density and therefore varies with the selected stagnation conditions (temperature and pressure) at the Laval nozzle.
The cluster velocity v also changes with the pressure and temperature settings and can be determined through time-of-flight measurements [Köh10] or predicted by model calculations of a quasi-one-dimensional flow [Tä12]. In addition, the mean velocity and the velocity distribution allow insights into the cluster production process and the determination of the cluster mass (see Chapter 6). Details on the correlation with the volume density as well as the determination of both fundamental parameters p_0 and v will be discussed in this and the following section.

As presented in Section 4.2.2 the interaction chamber of the cluster-jet target prototype for $\overline{\mathrm{P}}$ANDA is equipped with movable rods [Köh10, Tä12, Her13], where the recorded beam profiles (cf. Fig. 4.13) deliver the beam width and position in addition to the maximal pressure increase.

The proportionality to the volume density results from the retained cluster beam, which induces a pressure variation p in the interaction chamber. Furthermore, p is correlated to the volume flow q_{pV} of a volume V and the pumping speed S of the vacuum system via

$$p = \frac{q_{pV}}{S}. \tag{5.4}$$

The pumping speed S of the interaction chamber can be estimated ($(215.4 \pm 6.0)\,\ell/\mathrm{s}$ cf. Appendix A.1) and the volume flow q_{pV} conceals the demanded volume density and the cluster velocity v, which will become evident as follows (cf. [Tä12, Her13]):

Volume flow q_{pV} and mass flow q_m

The current strength of a flow q arises from the time derivation of a quantity, e.g. volume or mass. Under the assumption of an ideal gas (corresponding to the fractured cluster)

$$pV = \frac{m\,R\,T}{M} \tag{5.5}$$

with mass m, the universal gas constant R, temperature T, and the molar mass of the gas M, the time derivation leads to

$$\underbrace{p\frac{\mathrm{d}V}{\mathrm{d}t}}_{q_{pV}} = \underbrace{\frac{\mathrm{d}m}{\mathrm{d}t}}_{q_m}\frac{R\,T}{M} \tag{5.6}$$

$$q_{pV} = q_m\frac{R\,T}{M} \tag{5.7}$$

with q_m being the mass flow. The mass $m(x)$ can be estimated through the retained volume density ρ of a cluster beam propagating in z direction, caused by a rod at position x with diameter $d = 1\,\mathrm{mm}$ with an infinite length in y direction compared to the dimensions of the target beam (cf. Figure 5.1):

$$m(x) = \int_{x-d/2}^{x+d/2}\mathrm{d}x' \int_{-\infty}^{+\infty}\mathrm{d}y' \int \mathrm{d}z'\rho\,(x', y', z'). \tag{5.8}$$

Then the mass flow $q_m(x)$ is given by

$$q_m(x) = \frac{\mathrm{d}}{\mathrm{d}t}\int_{x-d/2}^{x+d/2}\mathrm{d}x' \int_{-\infty}^{+\infty}\mathrm{d}y' \int \mathrm{d}z'\rho\,(x', y', z'). \tag{5.9}$$

Within the z direction, a change of the volume density ρ is not expected, therefore only the dependence in x and y direction will be considered in the following. Furthermore,

the variation over the time in z direction $\mathrm{d}z/\mathrm{d}t$ is defined by the cluster velocity v (more details in Section 5.1.3). Therefore, $\mathrm{d}z'$ can be substituted by $(\mathrm{d}t\ v)$ and Eq. (5.9) yields

$$\begin{aligned} q_m(x) &= \frac{\mathrm{d}}{\mathrm{d}t} \int_{x-d/2}^{x+d/2} \mathrm{d}x' \int_{-\infty}^{+\infty} \mathrm{d}y' \int \overbrace{(\mathrm{d}t\ v)}^{\mathrm{d}z'}\ \rho\,(x', y') \\ &= v \int_{x-d/2}^{x+d/2} \mathrm{d}x' \int_{-\infty}^{+\infty} \mathrm{d}y' \rho\,(x', y')\,. \end{aligned} \tag{5.10}$$

Equation (5.7) delivers in combination with the mass flow q_m in Eq. (5.10)

$$q_{pV} = \frac{v\,R\,T}{M} \int_{x-d/2}^{x+d/2} \mathrm{d}x' \int_{-\infty}^{+\infty} \mathrm{d}y' \rho\,(x', y')\,. \tag{5.11}$$

Maximal pressure increase p_0 and volume density ρ

With Equation (5.11), the proportionality between the pressure in Eq. (5.4) and the volume density becomes apparent. In addition, the residual gas background p_{back} must be considered and yields

$$p(x) = \frac{v\,R\,T}{S\,M} \int_{x-d/2}^{x+d/2} \mathrm{d}x' \int_{-\infty}^{+\infty} \mathrm{d}y' \rho\,(x', y') + p_{\mathrm{back}}. \tag{5.12}$$

The volume density distribution $\rho\,(x', y')$ can be separated into absolute height ρ_0 and shape $\widetilde{\rho}\,(x', y')$ via

$$\rho\,(x', y') = \rho_0\,\widetilde{\rho}\,(x', y')\,. \tag{5.13}$$

The Function $\widetilde{\rho}\,(x', y')$, which is normalised to one (cf. Equation (5.26)), provides the advantage that the value ρ_0 can directly be identified with the maximal volume density. Furthermore, $\widetilde{\rho}\,(x', y')$ can be varied depending on the applicated collimator and resulting beam shape, in particular circular or rectangular.

The adaptation of the recorded beam profile within the interaction chamber with

$$p(x) = \underbrace{\rho_0 \frac{v\,R\,T}{S\,M}}_{p_{0/a}} \int_{x-d/2}^{x+d/2} \mathrm{d}x' \int_{-\infty}^{+\infty} \mathrm{d}y' \widetilde{\rho}\,(x', y') + p_{\mathrm{back}} \tag{5.14}$$

provides the maximal volume density $[\rho_0] = {}^{kg}/_{\mathrm{cm}^3}$ with

$$\rho_0 = \frac{p_{0/a}}{v}\frac{S\,M}{R\,T}, \tag{5.15}$$

whereas $p_{0/a}$ corresponds to the maximal height of the measured pressure or density profile, of the accumulated area, respectively. The particle volume density $[\rho_N] = {}^{\mathrm{atoms}}/_{\mathrm{cm}^3}$ is given by the quotient of ρ_0 and the mass $m = {}^{M_a}/_{N_A}$ with the molar mass M_a of an individually atom and the Avogadro constant N_A:

$$\rho_N = \frac{p_{0/a}}{v}\frac{S\,M}{R\,T}\frac{N_A}{M_a}. \tag{5.16}$$

Especially for hydrogen cluster, the volume density ρ_{H} is given by

$$\rho_{\mathrm{H}} = \frac{p_{0/a}}{v}\frac{2\,S\,N_A}{R\,T}. \tag{5.17}$$

Equation (5.17) clearly emphasises that the determination of the density with the installed mechanical monitoring system (destructive method) depends mainly on two crucial measurands: the maximal pressure increase of the accumulated area $p_{0/a}$ and the cluster velocity v. Both values vary with the stagnation parameters (hydrogen pressure and temperature) within the Laval nozzle at cluster production point and can be gained from the recorded beam profiles and the time-of-flight measurements (cf. Section 5.1.3), respectively.

Beam profile adaptation with $\widetilde{\rho}$

The precision of the reconstructed density depends on the quality of the selected adaptation function $\widetilde{\rho}$. For the $\overline{\mathrm{P}}$ANDA experiment, circular (standard) and rectangular beam shapes are of prime importance (see Section 5.3). Both beam profiles can roughly be described with a step function, but only the weighting with a Gaussian distribution enables a complete adaptation, which considers the beam shaping and collimator edge effects like smearing (see also applications in [Her13, Gri14]). In the following, the convolution for the description of the resulting beam profiles of circular and rectangular-shaped beams are presented in detail.

The adaptation to the recorded **circular** beam profiles, e.g. in horizontal direction $\widetilde{\rho}_{\mathrm{circ}}(x)$ (see Figure 5.2), can be realised via the convolution of a step function $f(x)$

$$f(x) \;=\; \begin{cases} 1 & \text{if } |x| \leq R_{\mathrm{c}} \\ 0 & \text{if } |x| > R_{\mathrm{c}} \end{cases} \tag{5.18}$$

with cluster beam radius R_c and a normalised Gaussian distribution $g(x)$ with $a = \sqrt{b/2\pi}$:

$$g(x) \quad = \quad a \ \exp\left(\frac{-b\ x^2}{2}\right). \tag{5.19}$$

The function $\widetilde{\rho}_\mathrm{circ}\,(x)$ is then given by

$$\widetilde{\rho}_\mathrm{circ}\,(x) = f(x) * g(x) \quad = \quad \int\limits_{-\infty}^{\infty} f(\tau)\ g(x-\tau)\ \mathrm{d}\tau. \tag{5.20}$$

Within its limits, the rectangular function is $f(x) = 1$ and leads to

$$\begin{aligned} \widetilde{\rho}_\mathrm{circ}\,(x) \quad &= \quad \int\limits_{-R_\mathrm{c}}^{R_\mathrm{c}} g(x-\tau)\ \mathrm{d}\tau \\ &= \quad a \int\limits_{-R_\mathrm{c}}^{R_\mathrm{c}} \exp\left(\frac{-b\ (x-\tau)^2}{2}\right)\mathrm{d}\tau. \end{aligned} \tag{5.21}$$

The substitution of $\dfrac{b\ (x-\tau)^2}{2} = \Theta^2$ yields

$$\begin{aligned} \widetilde{\rho}_\mathrm{circ}\,(x) \quad &= \quad -a\ \sqrt{\frac{2}{b}} \int\limits_{\sqrt{b/2}\ (x+R_\mathrm{c})}^{\sqrt{b/2}\ (x-R_\mathrm{c})} \exp\left(-\Theta^2\right)\ \mathrm{d}\Theta \\ &= \quad -a\ \sqrt{\frac{2}{b}} \left(\int\limits_{0}^{\sqrt{b/2}\ (x-R_\mathrm{c})} \exp\left(-\Theta^2\right)\ \mathrm{d}\Theta - \int\limits_{0}^{\sqrt{b/2}\ (x+R_\mathrm{c})} \exp\left(-\Theta^2\right)\ \mathrm{d}\Theta \right). \end{aligned} \tag{5.22}$$

The primitive can be expressed in terms of the error function which is defined as

$$\mathrm{erf}(\hat{z}) = \frac{2}{\sqrt{\pi}} \int\limits_{0}^{\hat{z}} \exp\left(-\vartheta^2\right)\mathrm{d}\vartheta. \tag{5.23}$$

Therefore, $\widetilde{\rho}_\mathrm{circ}\,(x)$ results in

$$\widetilde{\rho}_\mathrm{circ}\,(x) \quad = \quad -a\ \sqrt{\frac{2}{b}}\ \frac{\sqrt{\pi}}{2}\ \left(\mathrm{erf}\left(\sqrt{\frac{b}{2}}\ (x-R_\mathrm{c})\right) - \mathrm{erf}\left(\sqrt{\frac{b}{2}}\ (x+R_\mathrm{c})\right)\right), \tag{5.24}$$

where $\sqrt{2/b} = \tilde{s}$ represents the smearing parameter, which leads in combination with parameter a to

$$\widetilde{\rho}_\mathrm{circ}\,(x) = \frac{1}{2}\ \left(\mathrm{erf}\left(\frac{x+R_\mathrm{c}}{\tilde{s}}\right) - \mathrm{erf}\left(\frac{x-R_\mathrm{c}}{\tilde{s}}\right)\right). \tag{5.25}$$

For $x > 0$ and ${}^{R_c}/_{\tilde{s}} \gg 1$ arises

$$\widetilde{\rho}_{\mathrm{circ}}(x) = \frac{1}{2}\left(1 - \mathrm{erf}\left(\frac{x - R_c}{\tilde{s}}\right)\right). \tag{5.26}$$

In the case of vertical beam profiles, the same approach follows.

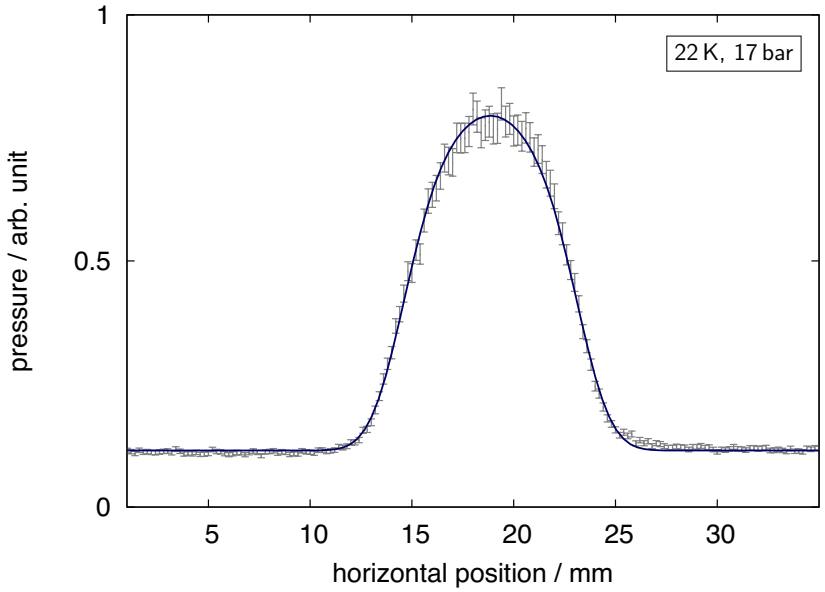

Figure 5.2.: Recorded beam profile, where the maximal pressure increase corresponds to the target density. In addition, the beam width and position in the interaction chamber can be determined. The applied fit function results from a convolution of a rectangular function with a Gaussian distribution (see Equation (5.26)).

The adaptation to the recorded beam profiles of a cluster-jet beam with **rectangular** shape $\widetilde{\rho}_{\mathrm{rect}}$ (see Figure 5.3) follows analogously from the convolution of a two-dimensional step function $f(x, y) = f(x)f(y)$

$$f(x, y) \quad = \quad \begin{cases} 1 & \text{if} - R_x < x < R_x \wedge -R_y < y < R_y \\ 0 & \text{else} \end{cases} \tag{5.27}$$

and a normalised Gaussian distribution $g(x, y) = g(x)g(y)$

$$g(x, y) \quad = \quad a^2 \ \exp\left(\frac{-b\ (x^2 + y^2)}{2}\right), \tag{5.28}$$

whereas $\pm R_{x,y}$ defines the horizontal and vertical geometrical limits of the unsmeared cluster beam and parameter a^2 equals ${}^{b}/_{2\pi}$. The reversed process $(g(x, y) * f(x, y))$

was investigated within the master thesis of A.-K. Hergemöller [Her13]. The function $\widetilde{\rho}_{\text{rect}}(x,y)$ is given by

$$\begin{aligned}
\widetilde{\rho}_{\text{rect}}(x,y) &= f(x,y) * g(x,y) \\
&= \int_{-\infty}^{\infty}\int_{-\infty}^{\infty} f(\tau_x,\tau_y)\; g(x-\tau_x, y-\tau_y)\; \mathrm{d}\tau_x\; \mathrm{d}\tau_y \\
&= \int_{-\infty}^{\infty} f(\tau_x)\; g(x-\tau_x)\; \mathrm{d}\tau_x \int_{-\infty}^{\infty} f(\tau_y)\; g(y-\tau_y)\; \mathrm{d}\tau_y. \qquad (5.29)
\end{aligned}$$

Within the limits of the cluster beam $f(x,y) = 1$ is valid and $\widetilde{\rho}(x,y)_{\text{rect}}$ results in

$$\begin{aligned}
\widetilde{\rho}_{\text{rect}}(x,y) &= \int_{-R_x}^{R_x} g(x-\tau_x)\; \mathrm{d}\tau_x \int_{-R_y}^{R_y} g(y-\tau_y)\; \mathrm{d}\tau_y \\
&\overset{\text{Eq.(5.28)}}{=} a^2 \int_{-R_x}^{R_x} \exp\left(\frac{-b\;(x-\tau_x)^2}{2}\right) \mathrm{d}\tau_x \\
&\quad \cdot \int_{-R_y}^{R_y} \exp\left(\frac{-b\;(y-\tau_y)^2}{2}\right) \mathrm{d}\tau_y. \qquad (5.30)
\end{aligned}$$

The substitutions with $\frac{b\;((x)-\tau_x)^2}{2} = \Theta_x^2$ and $\frac{b\;((y)-\tau_y)^2}{2} = \Theta_y^2$ yield

$$\begin{aligned}
\widetilde{\rho}_{\text{rect}}(x,y) = a^2 \; \frac{2}{b} & \int_{\sqrt{b/2}\;(x+R_x)}^{\sqrt{b/2}\;(x-R_x)} \exp\left(-\Theta_x^2\right) \mathrm{d}\Theta_x \\
\cdot & \int_{\sqrt{b/2}\;(y+R_y)}^{\sqrt{b/2}\;(y-R_y)} \exp\left(-\Theta_y^2\right) \mathrm{d}\Theta_y.
\end{aligned} \qquad (5.31)$$

The decomposition into partial integrals with the definition of the error function (cf. Eq. (5.23)) gives

$$\begin{aligned}
\widetilde{\rho}_{\text{rect}}(x,y) = a^2 \; \frac{2}{b} \; \frac{\pi}{4} & \left(\operatorname{erf}\left(\frac{x+R_x}{\tilde{s}}\right) - \operatorname{erf}\left(\frac{x-R_x}{\tilde{s}}\right)\right) \\
& \cdot \left(\operatorname{erf}\left(\frac{y+R_y}{\tilde{s}}\right) - \operatorname{erf}\left(\frac{y-R_y}{\tilde{s}}\right)\right). \qquad (5.32)
\end{aligned}$$

The smearing parameter $\tilde{s} = \sqrt{2/b}$ (cf. Section 5.3.2) and $a^2 = b/2\pi$ yield

$$\widetilde{\rho}_{\mathrm{rect}}(x,y) = \frac{1}{4}\left(\mathrm{erf}\left(\frac{x+R_x}{\tilde{s}}\right) - \mathrm{erf}\left(\frac{x-R_x}{\tilde{s}}\right)\right) \cdot \left(\mathrm{erf}\left(\frac{y+R_y}{\tilde{s}}\right) - \mathrm{erf}\left(\frac{y-R_y}{\tilde{s}}\right)\right). \tag{5.33}$$

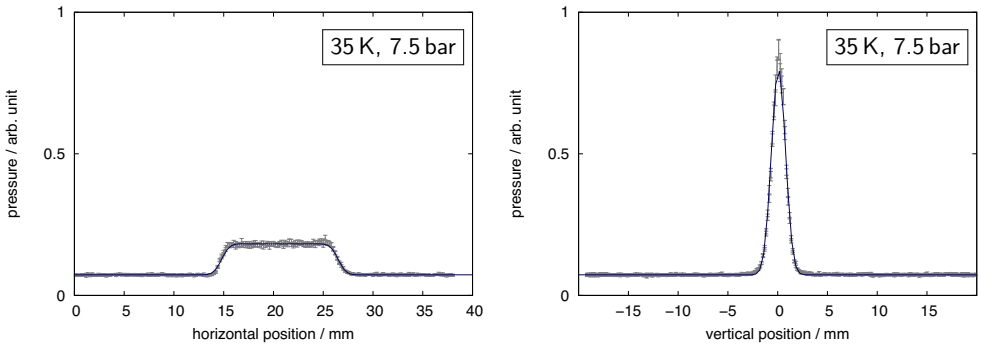

Figure 5.3.: Recorded beam profiles of a rectangular shaped cluster beam. The applied fit function results from a convolution of a two-dimensional rectangular function with a normalised Gaussian distribution (see Equation (5.33) and see also [Her13]).

5.1.3. Cluster velocity

The cluster velocity represents an essential parameter, not only for the determination of the density (Eq. (5.17)) or cluster mass (more details in Chapter 6), but also for the understanding of the cluster production process. Therefore, velocity measurements were carried out in a recent diploma thesis [Köh10] through a Time-Of-Flight (TOF) setup, which was developed and tested in [Ott07]. A large data set of time-of-flight distributions of hydrogen clusters was measured at the cluster-jet target prototype for $\overline{\mathrm{P}}$ANDA with a 28 µm Laval nozzle. Moreover, this data provided the basis for a model calculation, which was implemented in the scope of the Phd thesis of A. Täschner [Tä12]. The model calculation assumes an isentropic one-dimensional Van der Waals gas and provides cluster mean velocities with an accuracy around 5 %.

Time-of-flight setup

Figure 5.4 shows an overview of the time-of-flight setup [Köh10, Tä12], where a pulsed electron gun ionised a single cluster with a repetition rate around 20 Hz and a pulse width of about 20 µs. The detection occurs via a Channeltron after a flight path of (4.07 ± 0.02) m. Start and stop signals are registered by a micro controller MC9S08QG8, which provides the time difference or rather the time-of-flight data of the clusters. The calibration of the setup followed by the installation of a calibration source. This source offers ions, namely H^+, H_2^+, and H_3^+ with known kinetic energies as well as photons [Gen08]. Their time-of-flight allows to determine the flight path and the timing offset of the setup.

Time-of-flight distributions

The time-of-flight measurements concentrated on the determination of cluster velocities around the vapour pressure curve of hydrogen. Pressure and temperature settings at the Laval nozzle were selected, where hydrogen is in vapour, supercritical fluid, as well as fluid phase. In particular, the transition region was investigated in detail. The different hydrogen states at the cluster production have significant influences on the TOF measurements and reveal three different regimes: slow clusters (< 20 ms) with a wide distribution (standard deviation around 2.3 ms to 5.7 ms), fast clusters (> 5 ms) with narrow distribution (standard deviation around 0.05 ms to 0.2 ms), and a double peak structure. This distribution points to different cluster production processes within the Laval nozzle.
Figure 5.5 shows the hydrogen vapour pressure curve and the individual measuring points in a temperature range between 20 K to 50 K with pressures up to 17 bar. The open diamonds indicate time-of-flight measurements with a wide distribution, filled diamonds present narrow distributions with a skew, and the combination displays a double peak structure.

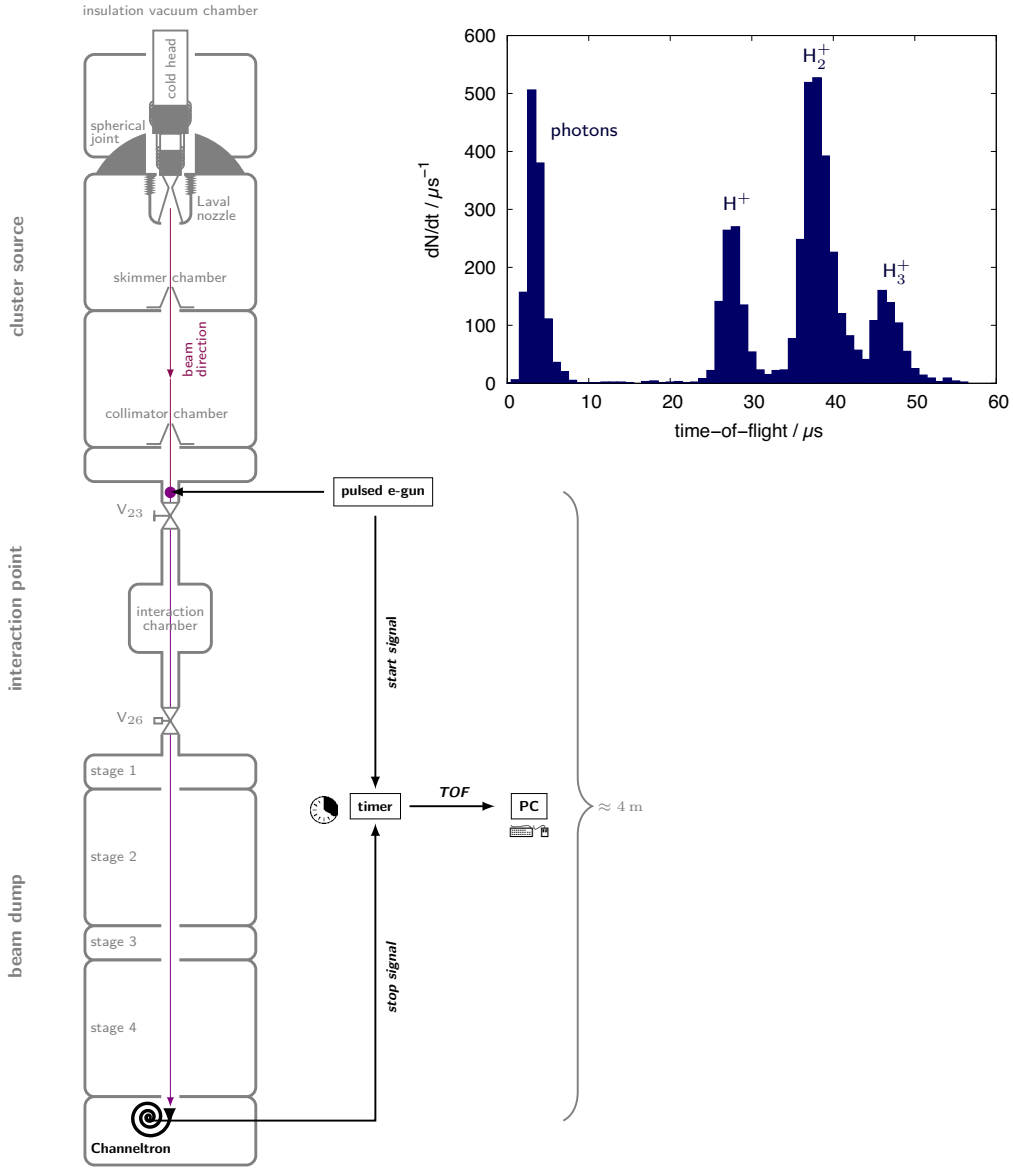

Figure 5.4.: Time-of-flight setup at the cluster-jet target prototype for $\overline{\mathrm{P}}$ANDA and its main components: pulsed e-gun, Channeltron detector, timer, and PC. The calibration source can be installed at the violet marked spot and provides H^+, H_2^+, and H_3^+ with known kinetic energies as well as photons. The inlay exemplarily shows a time-of-flight distribution with implemented calibration source at 150 eV.

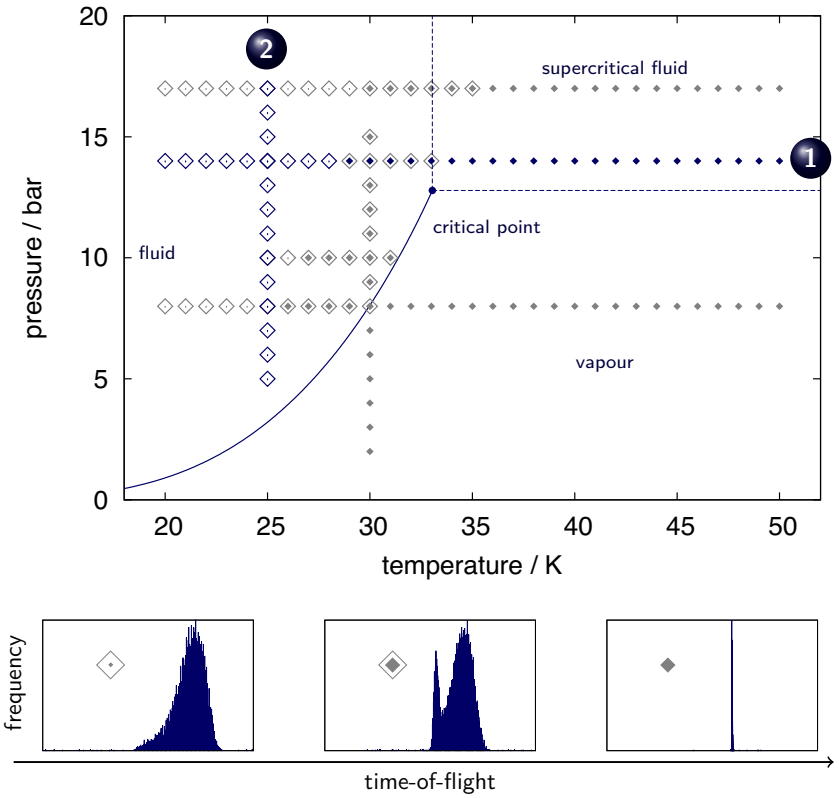

Figure 5.5.: Hydrogen vapour pressure curve with sections, where hydrogen is in a condition of a fluid, supercritical fluid, and vapour. The critical point (33.145 K, 12.964 bar [L$^+$09]) is marked by a blue point. Diamonds indicate the individual measuring points, whereas open diamonds present TOF measurements < 20 ms with a wide distribution (standard deviation around 2.3 ms to 5.7 ms), filled diamonds with TOF measurements > 5 ms show skewed narrow distributions (standard deviation around 0.05 ms to 0.2 ms) and the combination illustrates a double peak structure.

The development and gradually change of the distributions are exemplary demonstrated (see. Figure 5.5):

1. at the transition fluid ⇔ supercritical fluid
   (cf. Fig. 5.6, 14 bar between 20 K and 50 K in steps of 1 K,
   Fig. 5.7 left, 14 bar between 28 K and 29 K in steps of 0.1 K,
   Fig. 5.7 right, 14 bar between 33 K and 34 K in steps of 0.1 K)
2. within the fluid area
   (cf. Fig. 5.8, 25 K between 5 bar and 19 bar in steps of 1 bar).

More results and details can be extracted from [Köh10, Tä12, T$^+$13].
The measurement series (1) at 14 bar shows a range of the mean time-of-flight between 4 ms and 18 ms or accordingly velocities between 220 m/s and 1020 m/s (cf. Fig. 5.6).

In the supercritical fluid area (34 K to 50 K), positive skewed distributions with a standard deviation σ around 0.03 ms appear. The fluid area (20 K to 28 K) presents wide distributions with standard deviations around 1 ms to 1.5 ms. Compared to the narrow distribution, this results in a factor of 50 (σ: 0.03 ms vs. 1.5 ms). Between 29 K and 33 K, a double peak structure with a wide and narrow distribution arises. The several distributions indicate clusters originated from different production processes. In the case of a supercritical fluid (or vapour), clusters are classically formed by condensation (cf. Figure 4.5) and in the case of a fluid, clusters are produced by fragmentation. The double peak structure points to both production processes due to the fact that a supercritical fluid/liquid mixture appears within the nozzle at the transition from supercritical fluid to fluid and vice versa. These structures were also observed in other time-of-flight experiments with hydrogen and helium clusters, e.g. [K^+95, B^+90, C^+89]. Figure 5.7 shows the particular development of the (dis)appearance of the double peak within 0.1 K steps between 28 K and 29 K as well as 33 K and 34 K. This demonstrates the variation of the TOF distributions within slight temperature changes above the critical point. The cluster characteristics depend strongly on the cluster production process or rather cluster mass, which is partly very sensitive on the pressure and temperature settings at the Laval nozzle, especially around the vapour pressure curve. Comparable results also provide the measurement series at 8 bar, which covers the transition from vapour to fluid and vice versa.

Since the measurement series (2) at 25 K is located completely in the fluid area, only wide distributions emerge (cf. Fig. 5.8). The mean time-of-flight is around 15.2 ms (approximately 270 m/s), whereas the standard deviation varies from approximately 2.5 ms to 5 ms (more than factor 150 compared to the narrow distribution at 14 bar with $\sigma = 0.03$ ms). Depending on the pressure setting, the width variation is assumed to be related to the cluster mass distribution.

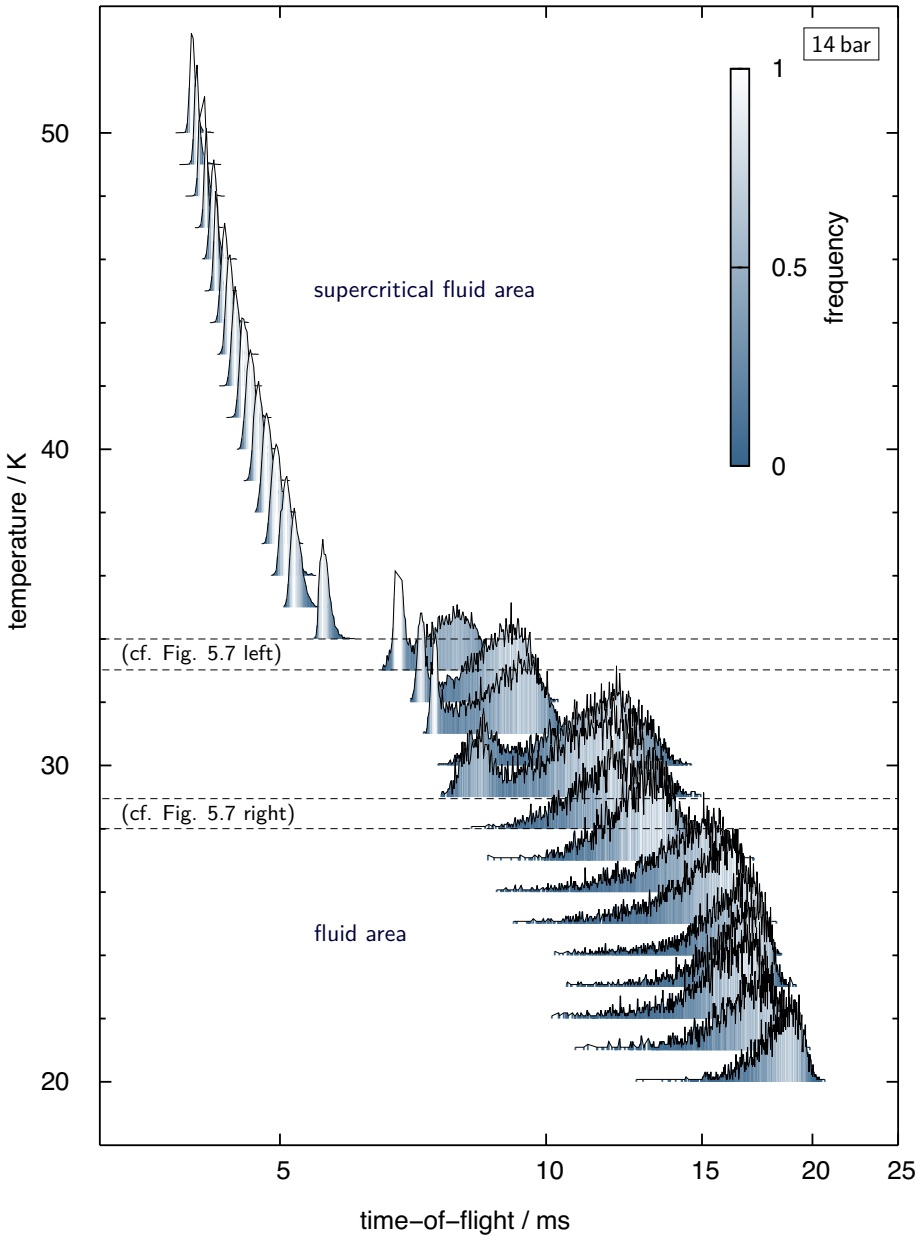

Figure 5.6.: Scaled time-of-flight distributions of hydrogen clusters at 14 bar with varying temperature (20 K to 50 K, 1 K steps). The time-of-flight is displayed on a logarithmic scale. This measurement series shows clearly three sections with various distributions, which is an indication for the transition of different cluster production processes (condensation within the supercritical fluid area vs. fragmentation within the fluid area). Within the dashed lines the development of the double peak structure can be observed in more detail in Figure 5.7.

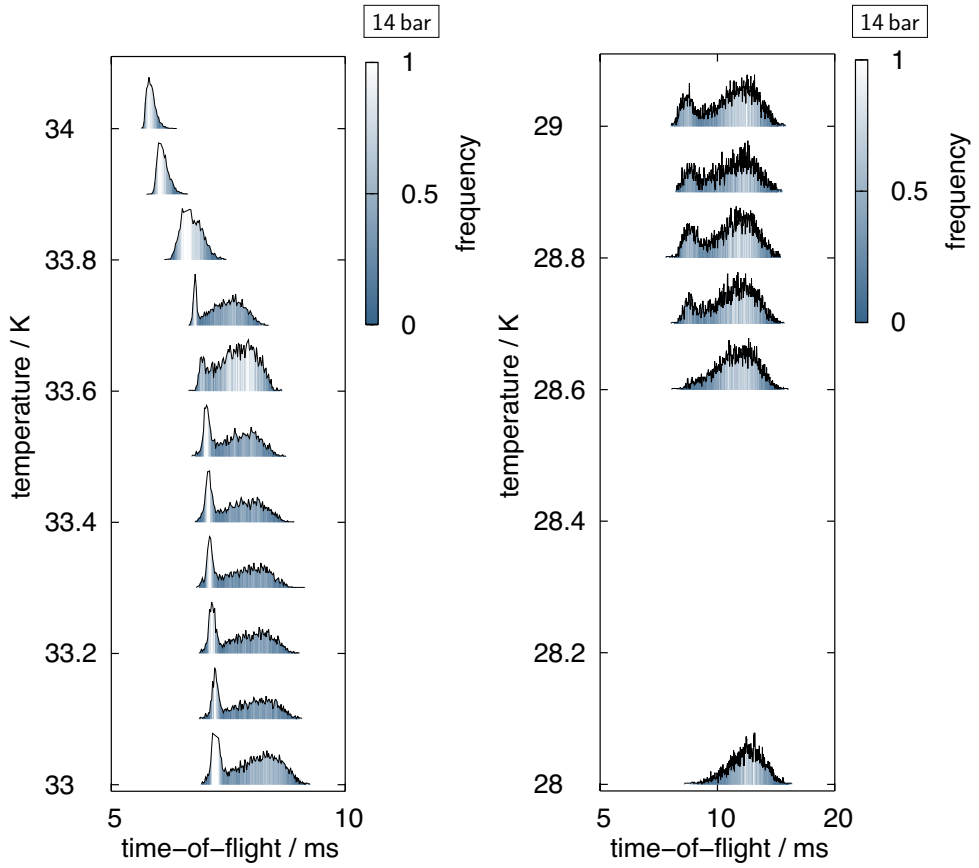

Figure 5.7.: Development of the double peak structure at 14 bar within 33 K and 34 K as well as 28 K and 29 K. The time-of-flight is displayed on a logarithmic scale with scaled maximum height. The double peak structure indicates a vapour-liquid mixture within the production process in the Laval nozzle, which is extremely sensitive to slight temperature changes. It appears around 33.7 K and disappears below 28.5 K.

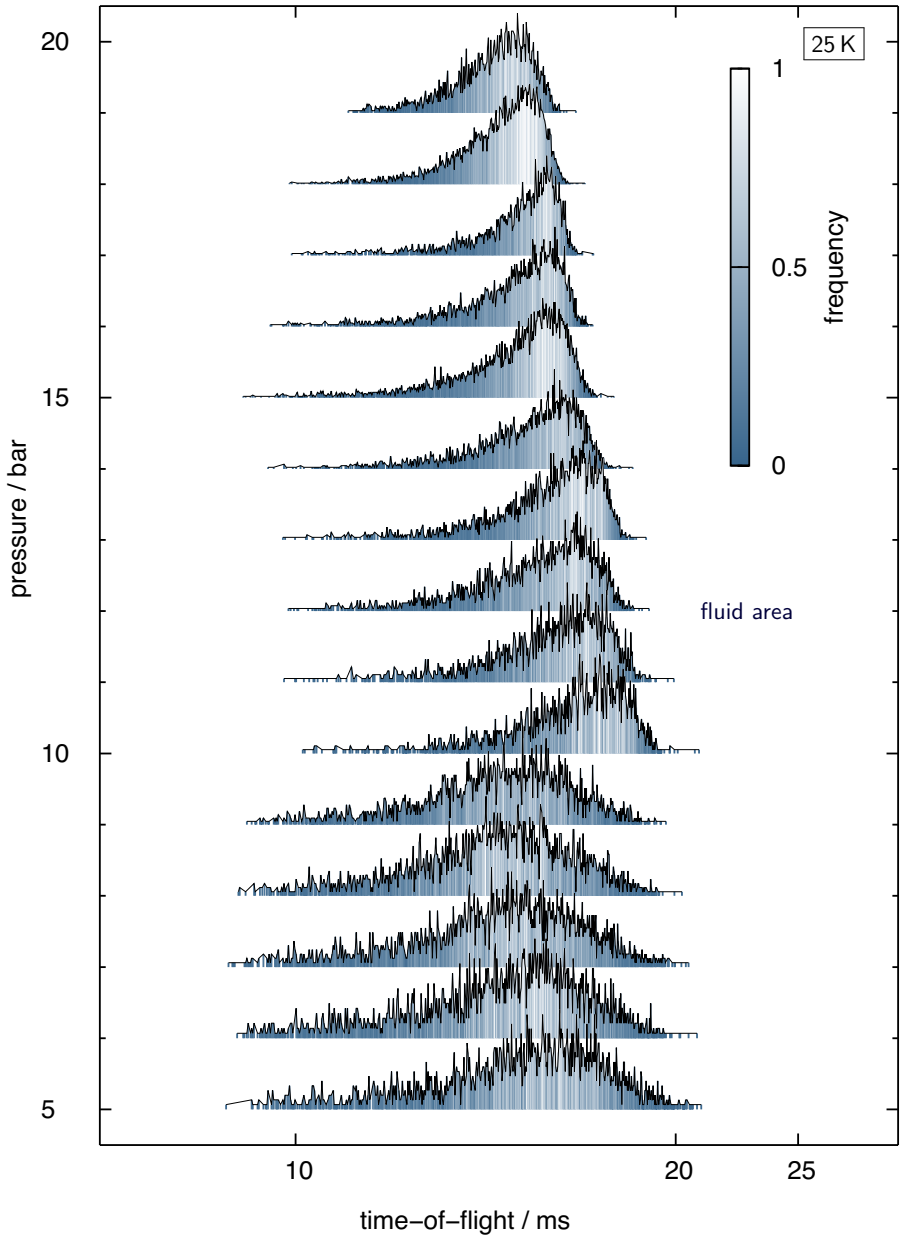

Figure 5.8.: Scaled time-of-flight distributions of hydrogen clusters at 25 K with varying pressure (5 bar to 19 bar, 1 bar steps). The time-of-flight is displayed on a logarithmic scale. Within this pressure region, hydrogen remains in the phase of liquid at the production process (fluid area) and as expected only wide distributions appear with standard deviations around 2.5 ms to 5 ms.

Model calculation

Depending on the selected stagnation conditions at the production point, the time-of-flight distribution changes, especially mean value, width, and shape. Running time-of-flight measurements for each possible parameter setting would be time-consuming and not feasible at storage ring experiments. Therefore, a precise calculation based on the implemented time-of-flight distributions was carried out in the scope of the Phd thesis of A. Täschner [Tä12]. With regard to the different cluster production processes within a Laval nozzle, this model calculation delivers precise time-of-flight and thus cluster mean velocities with an accuracy of 5 %. Amongst other uses, these velocities can be provided for the density or mass determination, which is emphasised in this thesis.

The calculation focuses on a stationary quasi-one-dimensional flow (cf. Figure 5.9), which corresponds to the flow within a Laval nozzle. In contrast to a one-dimensional flow, the stream tube area A is not constant but varies with the flow direction $A(z)$.

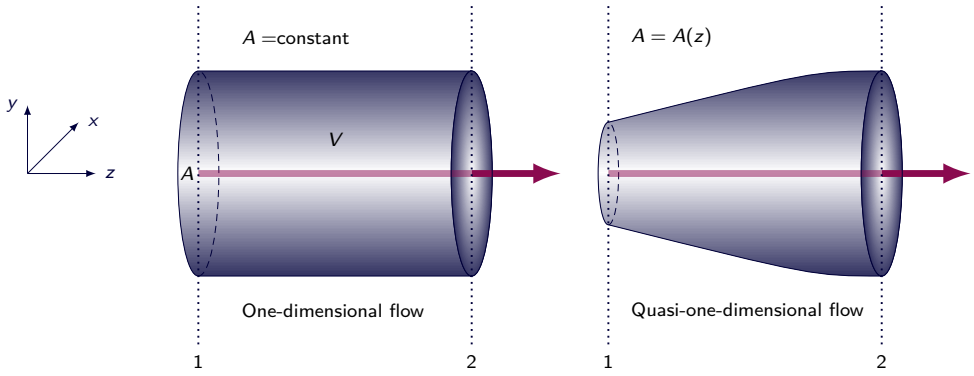

Figure 5.9.: One-dimensional vs. quasi-one-dimensional flow within volume V with constant and variable stream tube area A. The comparative positions along the z axis are marked with 1 and 2.

The crucial equations for a quasi-one-dimensional flow are the continuity, momentum, and energy equations [And90]:

$$\rho_1 \, v_1 \, A_1 \overset{\text{continuity}}{=} \rho_2 \, v_2 \, A_2 \tag{5.34}$$

$$p_1 \, A_1 + \rho_1 \, v_1^2 \, A_1 + \int_{A_1}^{A_2} p \, \mathrm{d}A \overset{\text{momentum}}{=} p_2 \, A_2 + \rho_2 \, v_2^2 \, A_2 \tag{5.35}$$

$$h_1 + \frac{v_1^2}{2} \overset{\text{energy}}{=} h_2 + \frac{v_2^2}{2} \tag{5.36}$$

with their differentials:

$$\begin{aligned} \mathrm{d}(\rho\ v\ A) &= 0 && (5.37)\\ \mathrm{d}p &= -\rho\ v\ \mathrm{d}v && (5.38)\\ \mathrm{d}h + v\mathrm{d}v &= 0, && (5.39) \end{aligned}$$

where $\rho = \rho(z)$ is the density, $v = v(z)$ the velocity, $A = A(z)$ the stream tube area (cf. Figure 5.9), $p = p(z)$ the pressure, and $h = h(z)$ the enthalpy at position z.
Considering an inviscid flow without friction, diffusion, or conduction of heat, it follows that the flow is isentropic (entropy $\hat{s}$ = constant) [And90], which results in the area-velocity relation [And90]:

$$\frac{\mathrm{d}A}{A} = (Ma^2 - 1)\frac{\mathrm{d}v}{v} \tag{5.40}$$

with the Mach number $Ma = {}^{v}/_{c_\mathrm{s}}$ and the speed of sound c_s. This relation yields the following conditions [And90, Tä12, T$^+$13]:

1. $Ma < 1$: Subsonic flow, where an increase of the velocity ($\mathrm{d}v > 0$) is related to a decrease of the area ($\mathrm{d}A < 0$) and vice versa. Consequently, the velocity increases with converging nozzle area.
2. $Ma = 1$: Sonic flow, where the velocity is equal to the speed of sound. The nozzle area is at its minimum.
3. $Ma > 1$: Supersonic flow, where an increase of the velocity ($\mathrm{d}v > 0$) is related to an increase of the area ($\mathrm{d}A > 0$) and vice versa. Consequently, the velocity increases with diverging nozzle area.

For a convergent-divergent Laval nozzle applied at cluster-jet targets (cf. Figure 4.6) the flow is thus subsonic $Ma < 1$ for $z < 0$, sonic $Ma = 1$ for $z = 0$, and supersonic $Ma > 1$ for $z > 0$ (see Figure 5.10).
Assuming that the velocity is zero before entering the nozzle $v_i = 0$, Equation (5.36) leads to

$$v(z) = \sqrt{2(h_i - h_z)} \tag{5.41}$$

with the initial enthalpy $h_i = h(T_i, \rho_i)$, the local enthalpy $h_z = h(T_z, \rho_z)$, and the depending temperature T. Proceeding from the assumption that at the narrowest position or critical point of the nozzle (designated with *) $Ma = 1$ applies, the local velocity must be equal to the speed of sound $v(z = 0) = v^* = c_s$. The critical enthalpy h^* and the entropy, which is constant $\hat{s}(T, \rho) = \hat{s}(T_i, \rho_i) = \hat{s}(T^*, \rho^*)$, deliver the critical parameters

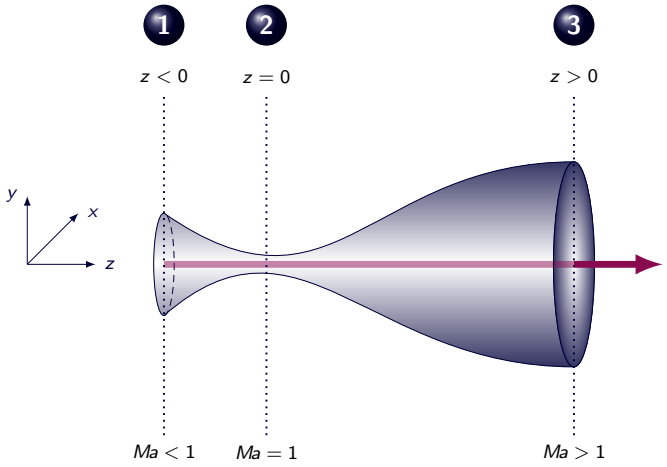

Figure 5.10.: Quasi-one-dimensional flow through a convergent-divergent Laval nozzle.

$T^*(h^*, \hat{s})$, $p^*(h^*, \hat{s})$, or $\rho^*(h^*, \hat{s})$. Furthermore, the continuity equation (5.34) provides the determination of the local parameters

$$\rho^* \; v^* \; A^* \quad = \quad \rho(h_z, \hat{s}) \; v(h_z, \hat{s}) \; A(z), \tag{5.42}$$

depending on the local enthalpy h_z and entropy $\hat{s}$.
Based on the Van der Waals equation of state for vapours and liquids, the implemented model calculation provides precise velocities with an accuracy of 5 % [Tä12, T$^+$13]. In addition, two cut-off parameters were introduced, identifying the position inside the Laval nozzle, behind which the mean velocity remains unaffected by cluster-gas interactions. These two parameters were defined, on the one hand for the cluster condensation with vapour at $z_g = (1.67 \pm 0.20)$ mm and on the other hand for fragmentation in the case of a liquid at $z_l = (0.445 \pm 0.014)$ mm [T$^+$13]. The Van der Waals equation is given by [Nol05]

$$\left(p + a \; \frac{n^2}{V^2}\right) (V - n \; b) = n \; R \; T \tag{5.43}$$

with the amount of substance $n = {}^{N}/_{N_A}$, the number of particles N, Avogadro's constant N_A, the universal gas constant R, and the material constants a, b. In contrast to a perfect gas (ideal gas with constant heat capacity), the size of the molecules and their interaction is taken into account. Depending on the temperature, this equation provides for the same pressure value up to three different densities. This ambiguity can be resolved by using the specific Gibbs free energy g in a method comparable to the Maxwell construction and the subsequent solving of the resulting non-trivial system of equations. Further details on the model calculation and the comparison between a perfect

and a Van der Waals gas are emphasised in [Tä12, T+13]. Based on these calculations, the influence of the nozzle geometry, e.g. narrowest diameter, opening angles etc., on the velocity will be investigated within the Phd thesis of S. Grieser [Gri15]. Figure 5.11 shows the experimental results of the selected measurement series at constant 14 bar and 25 K compared to the described model calculation (solid grey line). This model calculation enables a good qualitative and quantitative description of the measured mean velocities. Furthermore, it was confirmed that two production processes can occur: condensation and fragmentation.

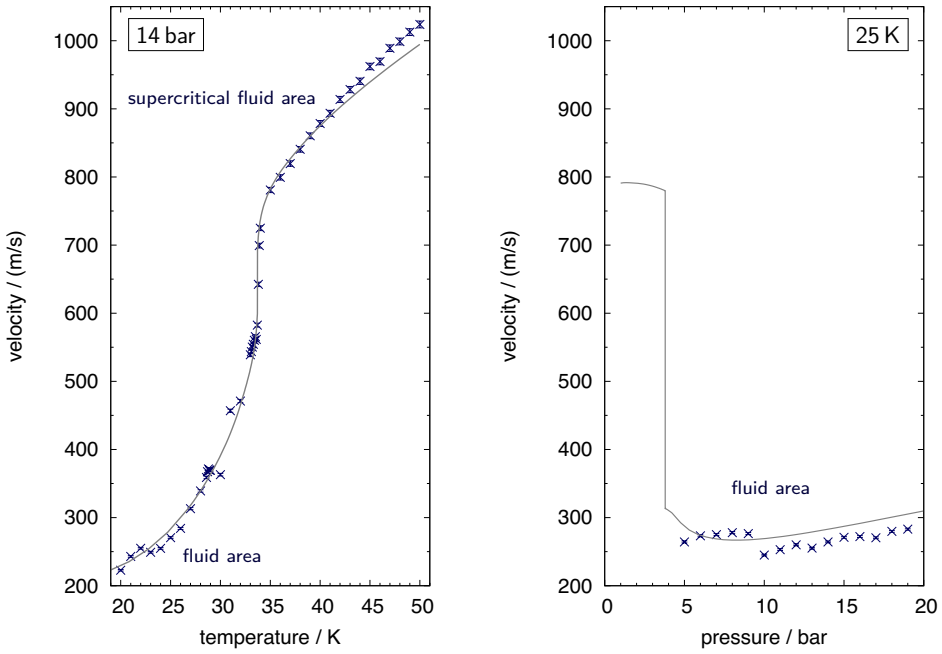

Figure 5.11.: Determined mean velocities of hydrogen clusters as a function of temperature at constant 14 bar (left) and pressure at constant 25 K (right). The solid grey line represents the results of the used Van der Waals gas model (data extracted from [Tä12]).

5.1.4. Areal density (circular beam shape)

The realisation of a storage ring experiment hinges largely on the performance of the internal target. In particular, the areal density or thickness at the interaction point is of prime importance. The $\overline{\mathrm{P}}$ANDA experiment requires an areal density of $4.5 \times 10^{15}\,\mathrm{atoms/cm^2}$ to achieve luminosities of up to $2 \times 10^{32}\,\mathrm{cm^{-2}s^{-1}}$, as discussed in Section 4.1.1. Furthermore, this thickness is demanded at a distance of 2.1 m from the Laval nozzle to ensure an almost 4π angle acceptance of the $\overline{\mathrm{P}}$ANDA detector. To determine the density of the hydrogen cluster-jet beam of the target prototype for $\overline{\mathrm{P}}$ANDA, a mechanical monitoring system was installed at the distance of the future interaction point. This monitoring system operates as a destructive method and gradually scans the cluster beam with rods in horizontal and vertical direction. On the basis of the resulting and analysed beam profiles, the volume density ρ can be determined through two essential parameters (cf. Equation (5.17)): the maximal pressure increase $p_{0/a}$ (background subtracted) of the accumulated area and the cluster velocity v. Moreover, the areal density is defined as

$$\rho_{\mathrm{areal}} \overset{\mathrm{Eq.(5.1)}}{=} \int_{-\infty}^{\infty} \rho(x, y_0)\,\mathrm{d}x, \tag{5.44}$$

with y_0 at maximal density. For a standard circular hydrogen cluster-jet beam, the areal density results with the diameter ($2\,R_\mathrm{c}$) in

$$\rho_{\mathrm{areal,circ,H}} = \frac{p_{0/a}}{v}\frac{4R_\mathrm{c}\,S\,N_A}{RT} \tag{5.45}$$

with the cluster beam radius R_c, the pumping speed S, Avogadro's constant N_A, the universal gas constant R, and standard temperature T. In the following, the focus lies on the areal density or thickness and the volume density will not be additionally specified.

The cluster velocity measurements and calculations already indicate strong changes of the beam characteristics due to the different hydrogen states at the production process. Therefore, these changes are also apparent in the research of the target thickness. In order to illustrate this point, four selected measurement series will be presented (see also vapour pressure curve in Fig. 5.12):

1. within the vapour/supercritical fluid area
   (cf. Fig. 5.13, $\boxed{13\,\mathrm{bar}}$ between 40 K and 160 K, in steps of 5 K)
2. at the transition fluid ⇔ vapour
   (cf. Fig. 5.14 top, $\boxed{8\,\mathrm{bar}}$ between 20 K and 40 K, in steps of 1 K)
3. at the transition fluid ⇔ supercritical fluid
   (cf. Fig. 5.14 bottom, $\boxed{17\,\mathrm{bar}}$ between 20 K and 50 K, in steps of 1 K)

4 and in the fluid area
(cf. Fig. 5.15, 25 K between 7 bar and 17 bar, in steps of 1 bar).

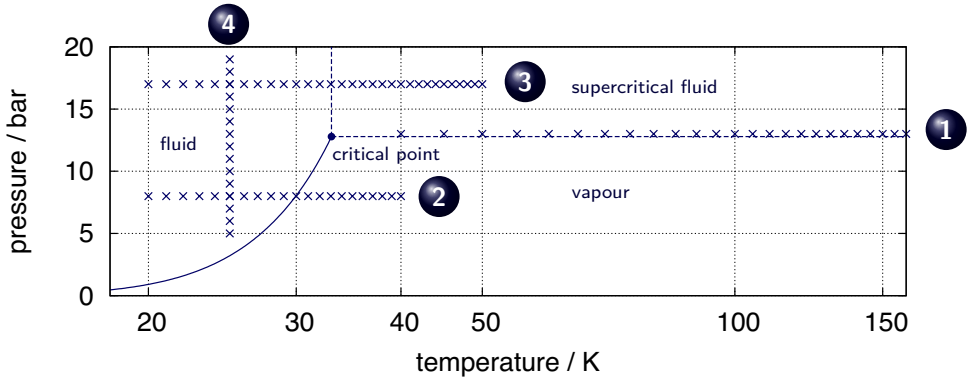

Figure 5.12.: Hydrogen vapour pressure curve with logarithmic scale for the temperature. The blue crosses show the various parameter settings of the selected measurement series, where the critical point (33.145 K, 12.964 bar [L$^+$09]) is marked by a dot.

Figure 5.13 exemplary shows recorded beam profiles from measurement series (1) at constant 13 bar within 40 K and 160 K in steps of 5 K (top) and the corresponding thicknesses (bottom). As expected from density measurements at the predecessor cluster-jet target 'MCT1' [Rau04], the target thickness increases with decreasing temperature. In addition, the transition of gas-jet to cluster-jet operation can be demonstrated. Gas-jet beams ($< 10^{10}$ atoms/cm^2 below 150 K) have a limited operating range of around one metre and cannot be localised at the interaction chamber (distance of 2.1 m from the nozzle). A high thickness at a large distance from the target source to the interaction point is one of the crucial requirements of the $\overline{\text{P}}$ANDA experiment and therefore cluster-jets are favoured to gas-jets.

The measurement series (2) at 8 bar and (3) at 17 bar (see Fig. 5.14) also present an increasing thickness with decreasing temperature. A steep rise between areal densities can be clearly observed at 30 K within measurement series (2) and around 34 K/35 K at measurement series (3) and reflects the transition from vapour to fluid and vapour to supercritical fluid (and vice versa), respectively, at the cluster production process. Moreover, variations of the target thickness within the fluid area can be noticed, reaching a maximal thickness in the order of 8×10^{14} atoms/cm^2 [Köh10, T$^+$11]. The previous results clearly show that the thickness is easy to vary over several orders of magnitude (10^{10} to approximately 10^{15}) and only depends on the selected stagnation conditions.

The observed variations within the fluid area were also confirmed by the measurement series (4) at 25 K (cf. Fig. 5.15) and can be explained by the occurrence of highly intense core beams. Within the fragmentation process of liquid hydrogen in the Laval nozzle, an inhomogeneous density distribution arises. This offers the possibility for further improvements of the target thickness and will provide access to the required areal densities in the order of 10^{15} atoms/cm^2 at the interaction point (see Section 5.2.2). The development of these core beams, the extraction and utilisation, as well as their affect on the thickness will be discussed in the following sections.

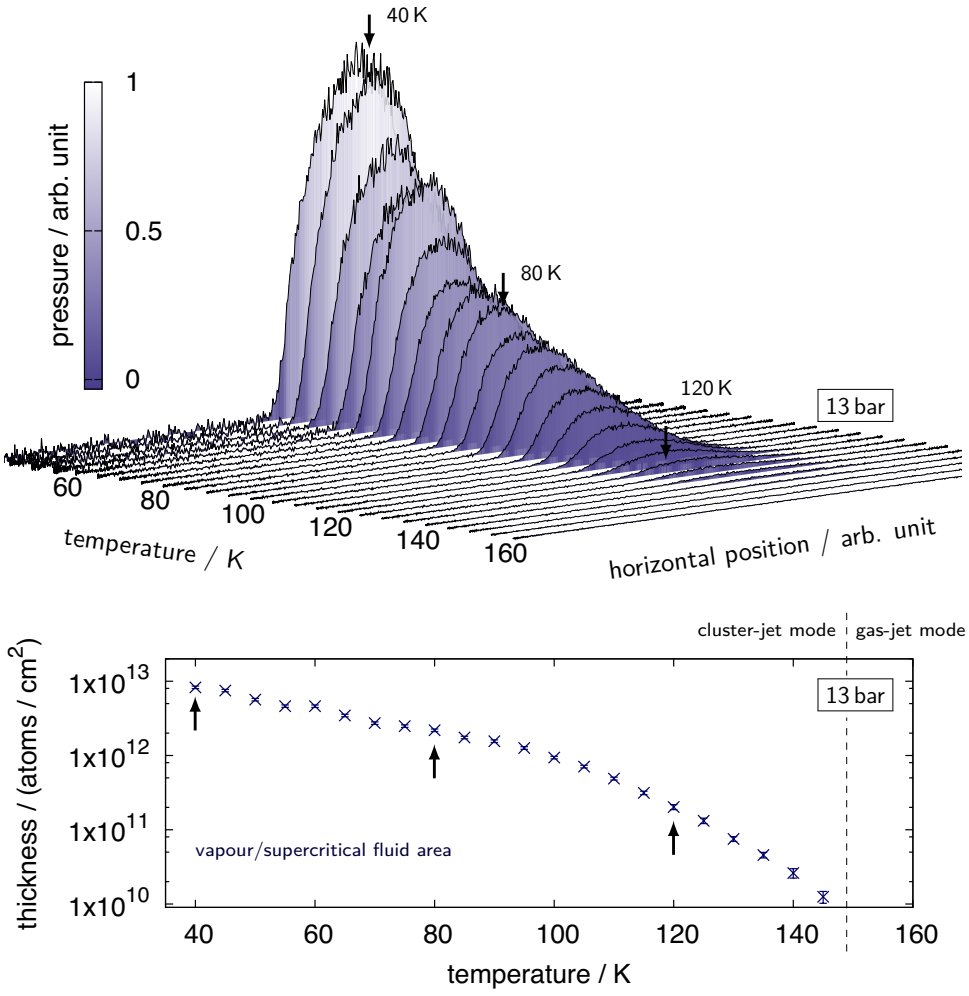

Figure 5.13.: Top: Recorded beam profiles at 13 bar within 40 K and 160 K (5 K steps, installed collimator with a diameter of 0.7 mm). The transition from gas-jet to cluster-jet operation occurs around 150 K. Bottom: Corresponding cluster thicknesses (logarithmic scale) varying over several orders of magnitude.

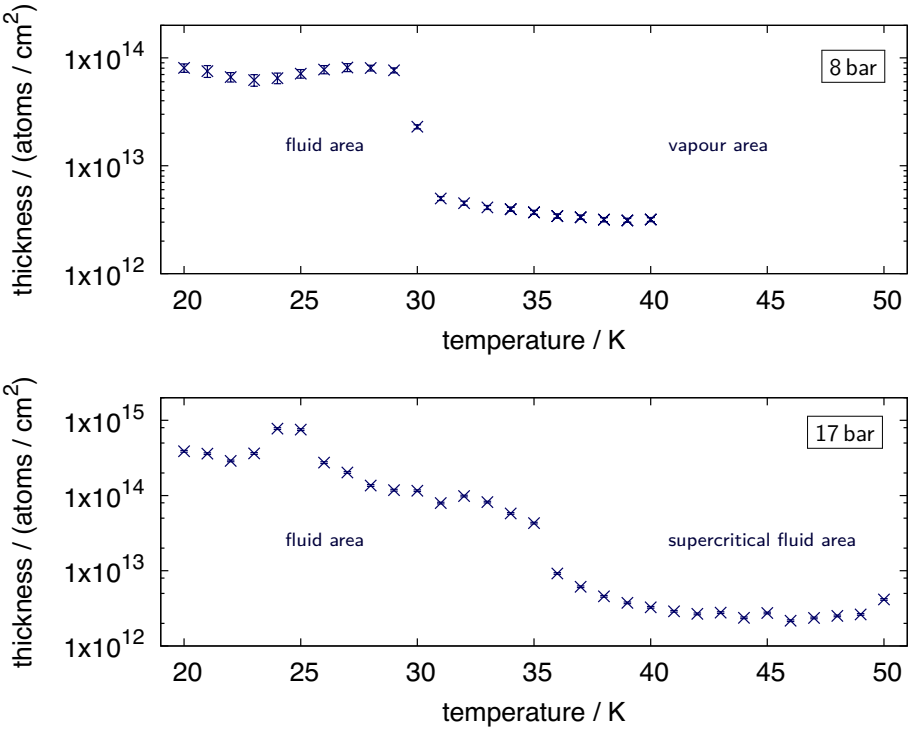

Figure 5.14.: Resulting target thicknesses (logarithmic scale) at 8 bar (top) and 17 bar (bottom). The areal density is easy to vary over several orders of magnitude, only depending on the pressure and temperature settings within the production process. A maximal target thickness in the order of 8×10^{14} atoms/cm^2 was achieved [Köh10, T$^+$11]. The 8 bar measurement series was performed with a collimator with a diameter of 0.5 mm, whereas the measurement series at 17 bar used an 0.7 mm collimator.

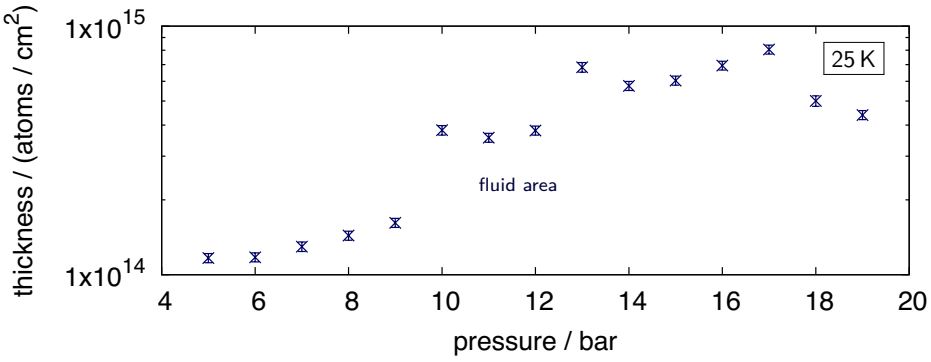

Figure 5.15.: Resulting target thicknesses (logarithmic scale) at 25 K. This measurement series was performed with an 0.7 mm collimator.

5.2. Observation of highly intense core beams

As already presented in Chapter 4, the skimmer chamber features a setup to visualise the cluster-jet beam directly behind the Laval nozzle, which contains a diode laser with beam expander as well as a CCD camera with a macro lense (see Fig. 4.8). The visualisation only arises at high densities (above 10^{13} atoms/cm^2 measured in a distance of 2.1 m from the nozzle), i.e. when hydrogen is in the phase of a liquid at the production process and also partly at the adjacent supercritical fluid area. Upon passing the Laval nozzle, liquid hydrogen breaks up and condensates in the skimmer chamber (vacuum pressure $< 10^{-1}$ mbar). The resulting target beam, example given in Figure 5.16, shows horizontal structures with stable highly intense core beams (cf. Section 5.2.3) and vertical structures caused by the expanded diode laser, which was used for illumination. The diode laser offers the advantage of a confined and intense illumination of the beam with minimal reflections within the stainless steel vacuum chamber and other reflecting objects therein.

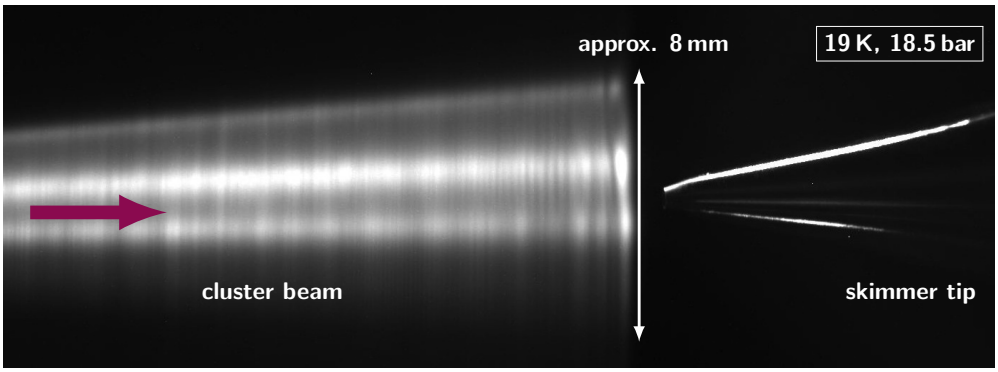

Figure 5.16.: Monochrome image of the cluster-jet beam with highly intense core beams recorded in the skimmer chamber at 19 K and 18.5 bar (beam direction from left to right marked with a violet arrow). The vertical structures are caused by the expanded diode laser, which was used for illumination.

The visualisation shows a very inhomogeneous intensity pattern of the cluster-jet beam with high density core beams. In Figure 5.16, the image indicates the extraction of a less bright part and probably a low dense part of the beam, pointing to the origin of the density variations presented in Figure 5.14 and 5.15. This assumption can be further supported by the variation of the cluster-jet beam with regard to the hydrogen pressure or temperature, which was observed in different measurement series. For example, the development of the density beam pattern was investigated:

1. at the transition fluid $\Leftrightarrow$ vapour
   (cf. Section A.2, $\boxed{7.5\,\text{bar}}$ between 19 K and 30 K, in steps of 1 K)

2 at the transition fluid ⇔ supercritical fluid
(cf. Fig. 5.18 and Section A.2, 18.5 bar between 19 K and 50 K, in steps of 1 K)
3 and in the fluid area
(cf. Section A.2, 25 K between 3 bar and 18 bar, in steps of 1 bar).

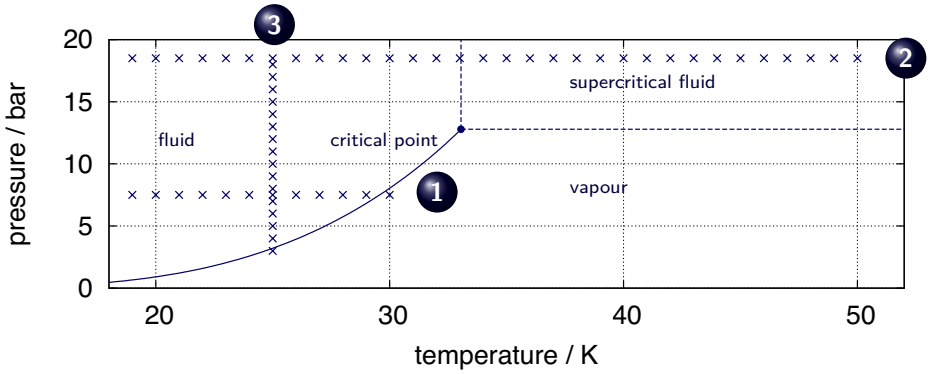

Figure 5.17.: Hydrogen vapour pressure curve, where the blue crosses present the various parameter settings of the selected measurement series, whereas the critical point (33.145 K, 12.964 bar [L$^+$09]) is marked by a dot.

These measurements (cf. Figure 5.17) were performed twice (consistency check) in the process of an increase and decrease of the temperature or pressure, respectively. Because of the small particle size and the low beam density (below 10^{13} atoms/cm^2 in a distance of 2.1 m from the nozzle), the cluster-jet beam is almost invisible within the vapour area. An exposure time around 10 s was adjusted and in the visible range exposure times around 2 s to 5 s were chosen.

Figure 5.18 presents only a selection of measurement series (1) at 18.5 bar, whereas the results of the entire data sample can be extracted from Section A.2 in the Appendix. The left-hand side contains the recorded cluster beam images in false colours based on the monochrome images (within the cooling process). Correspondingly, the right-hand side shows the projection of the ordinate, shown for decreasing (blue line) as well as increasing (red line) temperature. The cluster-jet beam becomes clearly visible at temperatures below 40 K. Between 19 K and 35 K, the inhomogeneity of the density pattern arises and core beams can be observed. This structure is reproducible, whereas the intensity differences are attributed to a target stability period of around ten minutes within each parameter variation. Extensive reproducibility and stability measurements will follow in Section 5.2.3.

The development and stability of the observed core beams are also confirmed within the measurement series (2) at 7.5 bar, which is presented in the Appendix A.2. Noticeable is

that the beam visualisation appears abruptly with high intensity between 30 K and 29 K due to the phase transition along the vapour pressure curve (with exposure times around 10 s and 5 s, respectively). Within the measurement series (3) at 25 K, the core beam structure remains between 3 bar and 18 bar, only the core beam width and the intensity changes (cf. Section A.2, exposure time around 2 s). The appearance of these core beams was also observed within the operation of different Laval nozzles (cf. Appendix A.5) as well as cluster-jet target setups [Gri14].

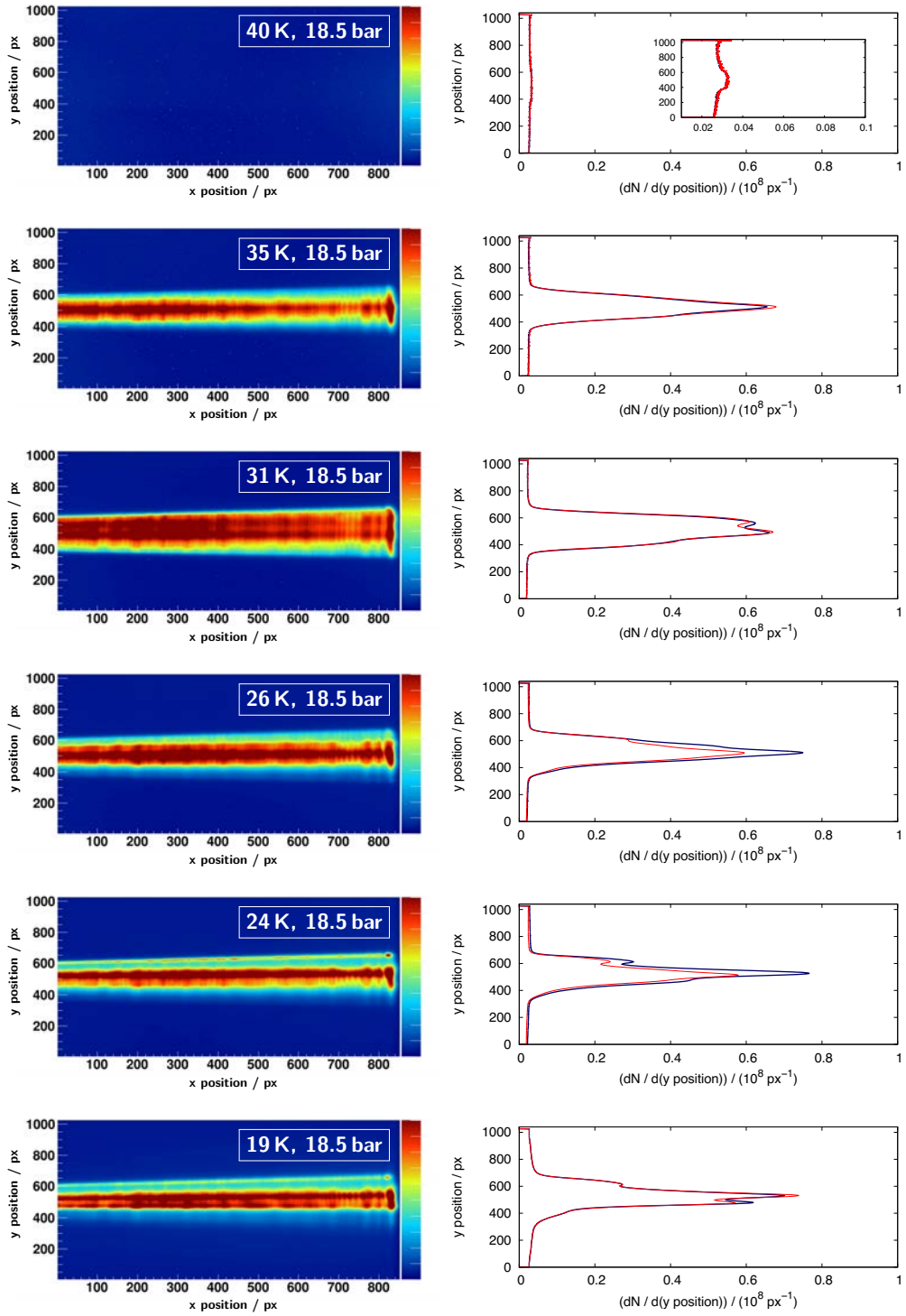

Figure 5.18.: Left: Selected beam images in false colours at 18.5 bar from 40 K down to 19 K with beam direction from left to right. The data is based on monochrome images with (1392×1024) px and the colour code represents the intensity. Right: Corresponding projections of the ordinate, within the cooling (blue line) and heating process (red line).

5.2.1. Beam opening angles and beam origin

The projections presented in Figure 5.18 show the intensity distribution in dependency of the pixel position of the ordinate $I(y_{\mathrm{pos}})$. However, an angle-resolved intensity distribution $I(\alpha)$ is preferable and will provide a refined resolution of the beam structure (cf. Figure 5.19). Moreover, the analysis enables the determination of the beam origin within the Laval nozzle and will give further insights into the cluster production process and the arising cluster characteristics. Due to different production processes, namely condensation and fragmentation, the beam origin could vary. This results could have an impact on the nozzle design, which is currently under investigation within [Gri15].
Velocity calculations in [Tä12] already point to two different positions inside the nozzle, the cut-off parameters $z_g = (1.67 \pm 0.20)\,\mathrm{mm}$ (condensation process) and $z_l = (0.445 \pm 0.014)\,\mathrm{mm}$ (fragmentation process) [T$^+$13], very close to the narrowest point of the nozzle, where the velocity remains unaffected by cluster-gas interactions. It shall be emphasised that these positions do not necessarily correspond to the beam origin. Furthermore, these cut-off parameters were calculated with regard to mean cluster velocities and a wide time-of-flight or velocity distribution occurs (cf. Section 5.1.3) within the cluster production process via fragmentation.

On the basis of the measurement series at 7.5 bar, 18.5 bar, and 25 K the angle α of each pixel can be extracted from

$$\alpha = \arctan\left(\frac{y_{\mathrm{pos}} - y_{\mathrm{off}}}{x_{\mathrm{pos}} + x_{\mathrm{off}}}\right), \tag{5.46}$$

where x_{pos} presents the x position and y_{pos} the y position within the beam image (cf. Figure 5.19).

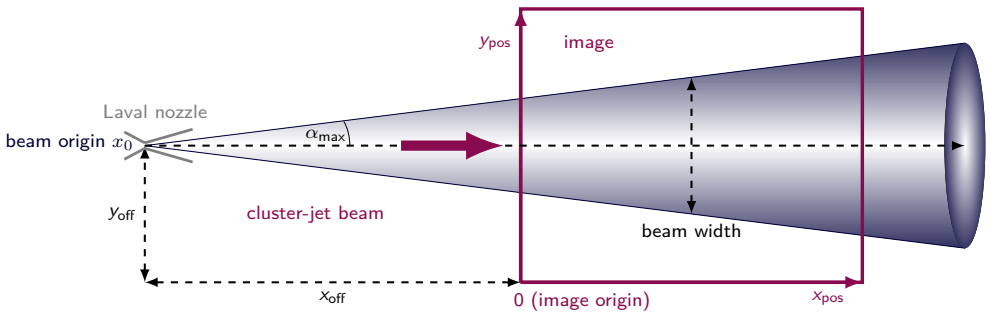

Figure 5.19.: Propagating cluster-jet beam from left to right with maximal opening angle α_{max}. The parameters x_{off} and y_{off} present the offset with regard to the origin of the recorded image (violet frame).

Furthermore, two offset parameters must be determined and considered in the analysis of each image: the offset of the cluster-jet beam origin in vertical (y position-offset y_{off}) and horizontal (x position-offset x_{off}) direction. Especially the x position-offset x_{off} offers the possibility to determine the beam origin within the Laval nozzle x_0.

Offset parameters

The offset parameters can be obtained from the individual analysis of the ordinate's projection of an image, which will be presented exemplary for the measurement at 18.5 bar and 19 K in the following.

The correction of the **vertical beam origin** (y position-offset y_{off}) was obtained from the mean pixel values of the projections of a measurement series, where the cluster-jet beam is expected to be homogeneous without core beams. Within these images, the cluster beam appears to be almost invisible and inseparable from the background but can be observed in its particular projections (cf. Figure 5.18, top). In the case of the measurement series (2) at 18.5 bar, measurements between 40 K and 50 K were considered (cf. Figure 5.20) and result in a y position-offset of $y_{\text{off}} = (518.4 \pm 0.2)$ px.

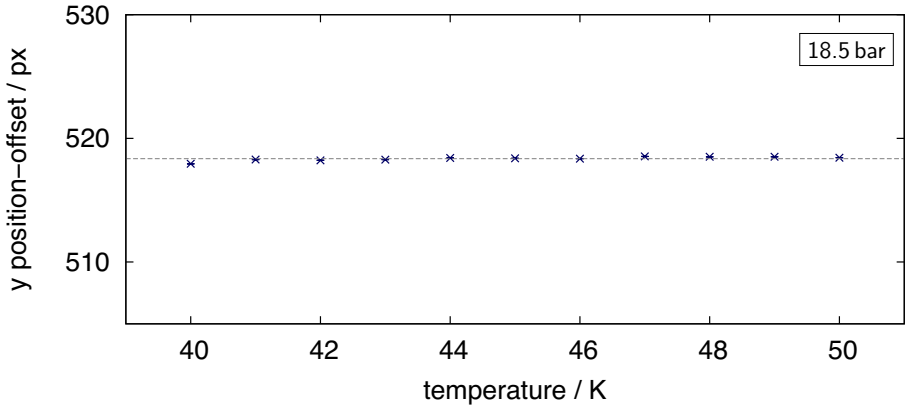

Figure 5.20.: Determination of the y position-offset y_{off} of the measurement series (2) at 18.5 bar, which results in (518.4±0.2) px. The mean pixel values are extracted from the particular projections of the ordinate within 40 K to 50 K.

For the correction of the **horizontal beam origin**, an image section of (1040 × 500) pixel was selected (see Fig. 5.21) and for each pixel column (500 columns), the projection of the ordinate and the appropriate beam width was determined. Figure 5.22 shows exemplary the projection of the ordinate for pixel column no. 2. The beam width was considered for eight heights of the projection's maximum, from 10 % to 80 % (cf. Figure 5.22 and 5.23). Because of the appearance of several core beams with various intensity, the determined

width at a specific height can alternate from the width of the whole intensity distribution to a single peak width (cf. Figure 5.23). Therefore, only heights of the projection with small variations were selected for the analysis, which are mainly caused by the illumination (standard deviation from fit normally around 10 px to 50 px, in exceptional cases up to maximal 150 px).

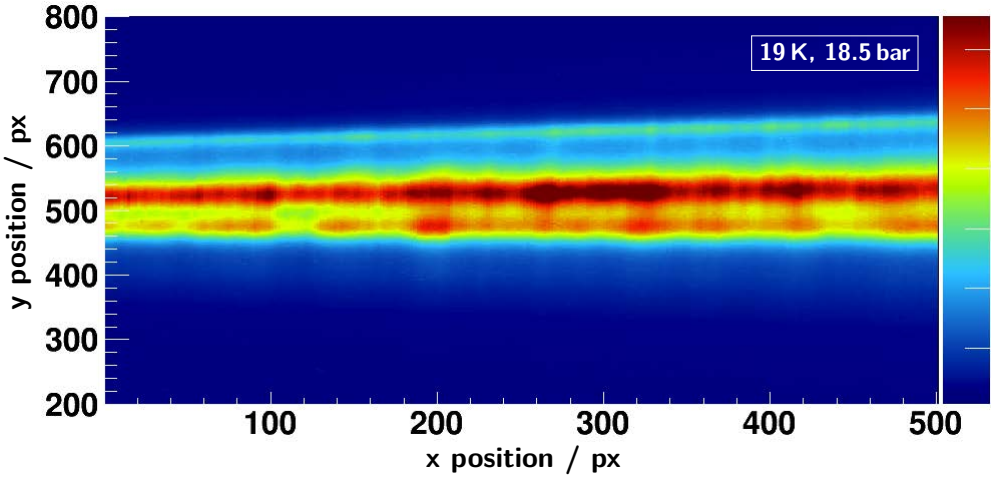

Figure 5.21.: Image section of the measurement at 19 K, 18.5 bar for the analysis of the x position-offset x_{off} (beam direction from left to right), where the colour code represents the intensity.

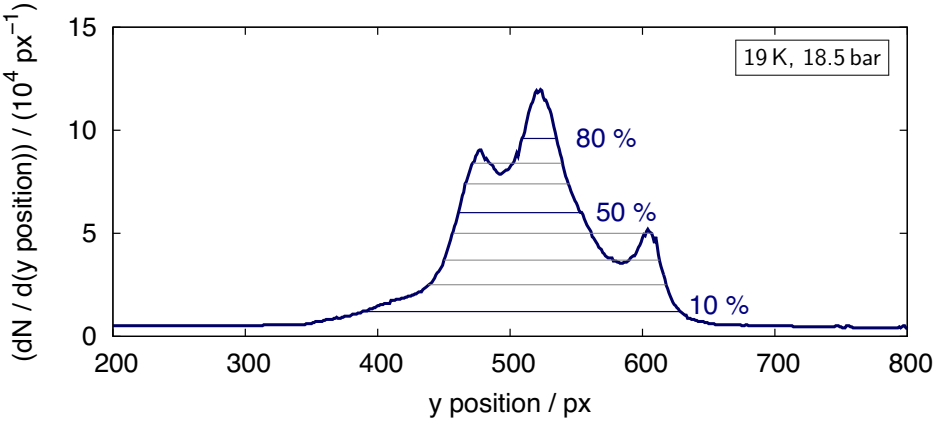

Figure 5.22.: Projection of the ordinate of a single pixel column (no. 2) at 19 K, 18.5 bar. The different peak heights and the corresponding widths of the intensity distribution are indicated by horizontal lines. Depending on the illumination, the peak intensity could vary for each pixel column and the width of a specific height can alternate between two values.

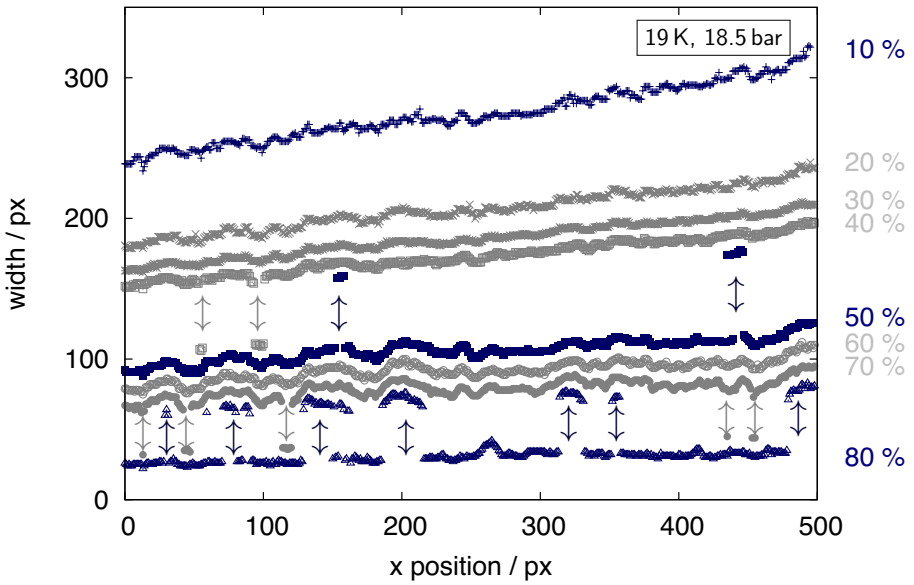

Figure 5.23.: Determined widths at 19 K and 18.5 bar (presented without their uncertainties). The widths at the heights 40 %, 50 %, 70 %, and 80 % clearly show the alternation between two widths (grey and blue arrows).

A linear fit of these widths in relation to a specific height $i = 10\,\%$ to $80\,\%$ via

$$f_i(x_{\mathrm{pos}}) = a_i x_{\mathrm{pos}} + b_i \tag{5.47}$$

with the correlated parameters a_i and b_i yields the x position-offset $x_{\mathrm{off}} = \mid -b_i/a_i \mid$, where $f_i(x_{\mathrm{pos}}) = 0$. The mean value of the horizontal beam origin (x position-offset x_{off}) could be gained individually for each image or parameter setting. For example, at 19 K and 18.5 bar, the x position-offset amounts (1855 ± 39) px. These values of the horizontal beam origin allow to determine the production point within the Laval nozzle and will be discussed in more detail in the next section.

Beam origin

The x position-offsets of the measurement series (1) to (3) (cf. Fig. 5.17) are presented in Figure 5.24, where especially the offsets of the isobars (top) show strong variations. Mean values can be extracted around $\overline{x}_{\mathrm{off}}^{(1,2)} = (2172 \pm 95)$ px for the isobars at 7.5 bar and 18.5 bar as well as $\overline{x}_{\mathrm{off}}^{(3)} = (2225 \pm 49)$ px for the isotherm at 25 K (see Fig. 5.24 bottom). The beam origin within the Laval nozzle x_0 can thus be estimated via

$$x_0 = x_{\mathrm{off}} + x_{\mathrm{skimmer}}, \tag{5.48}$$

with the x position-offset x_{off} and the distance of the image origin and the skimmer tip x_{skimmer}, which results in $x_{\mathrm{skimmer}}^{(1,2,3)}(884 \pm 1)\,\mathrm{px}$ for the measurement series (1) to (3) at 7.5 bar, 18.5 bar, and 25 K. The beam origin yields on average $\overline{x}_0^{(1,2)} = (3056 \pm 95)\,\mathrm{px}$ and $\overline{x}_0^{(3)} = (3109 \pm 49)\,\mathrm{px}$. With the depicted opening of the skimmer of 0.52 mm ($\approx 36\,\mathrm{px}$), one millimetre roughly corresponds to 70 px. Within these measurements, the present distance of the narrowest point of the nozzle to the skimmer amounted $(55.7 \pm 0.2)\,\mathrm{mm}$ (according to the CAD (Computer-Aided Design) model) and with an expected length contraction around 1.4 mm, this matches a beam origin located around 12.6 mm from the narrowest point of the nozzle and could vary up to more than 1 mm.

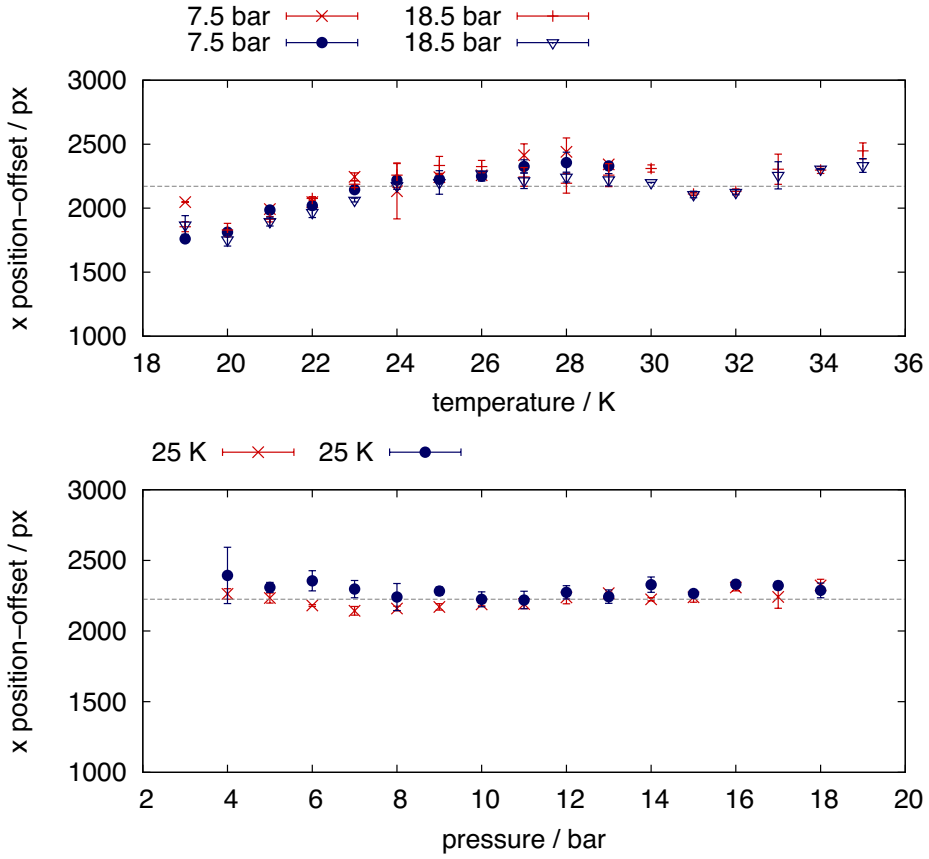

Figure 5.24.: Determined x position-offsets of the measurement series (1) to (3) at 7.5 bar and 18.5 bar (top) as well as 25 K (bottom). Mean values of $\overline{x}_{\mathrm{off}}^{(1,2)} = (2172 \pm 95)\,\mathrm{px}$ for the isobars and $\overline{x}_{\mathrm{off}}^{(3)} = (2225 \pm 49)\,\mathrm{px}$ for the isotherm can be extracted. The red and blue data points represent these measurement series with increasing and decreasing temperature or pressure, respectively.

This point can be further supported by an isotherm measurement series denoted with (4) within the fluid area (cf. Figure 5.25) at a temperature of 19 K to 25 K (in steps of 1 K), respectively, within a pressure range of 7 bar to 17 bar (in steps of 1 bar). In

the fluid area, stable cut-off parameters are expected and the determined beam origin values of the 25 K isotherm also show no further structures (cf. Figure 5.24 bottom). The resulting x position-offsets of measurement series (4) are presented in Figure 5.25. Above 11 bar, discrepancies between the 19 K to 22 K measurement series and the 24 K and 25 K isotherms arise. In addition, the x position-offset of the 23 K isotherm seems to alternate between these two regimes. A mean value of $\overline{x}_{\mathrm{off}}^{(4)} = (1543 \pm 58)\,\mathrm{px}$ can be extracted, whereas the distance from the image origin to the skimmer equals $x_{\mathrm{skimmer}}^{(4)} = (1177 \pm 1)\,\mathrm{px}$. The beam origin yields $\overline{x}_{0}^{(4)} = (2720 \pm 58)\,\mathrm{px}$ and corresponds to a length of $(47 \pm 2)\,\mathrm{mm}$ ($1\,\mathrm{mm} = (58 \pm 2)\,\mathrm{px}$ cf. Appendix A.3). This complies to a distance of around 6 mm from the narrowest point of the nozzle with a variation of around ±2 mm (present distance of the narrowest point of the nozzle to skimmer at 290 K: $(51.5 \pm 0.5)\,\mathrm{mm}$, observed length contraction around 1.6 mm).

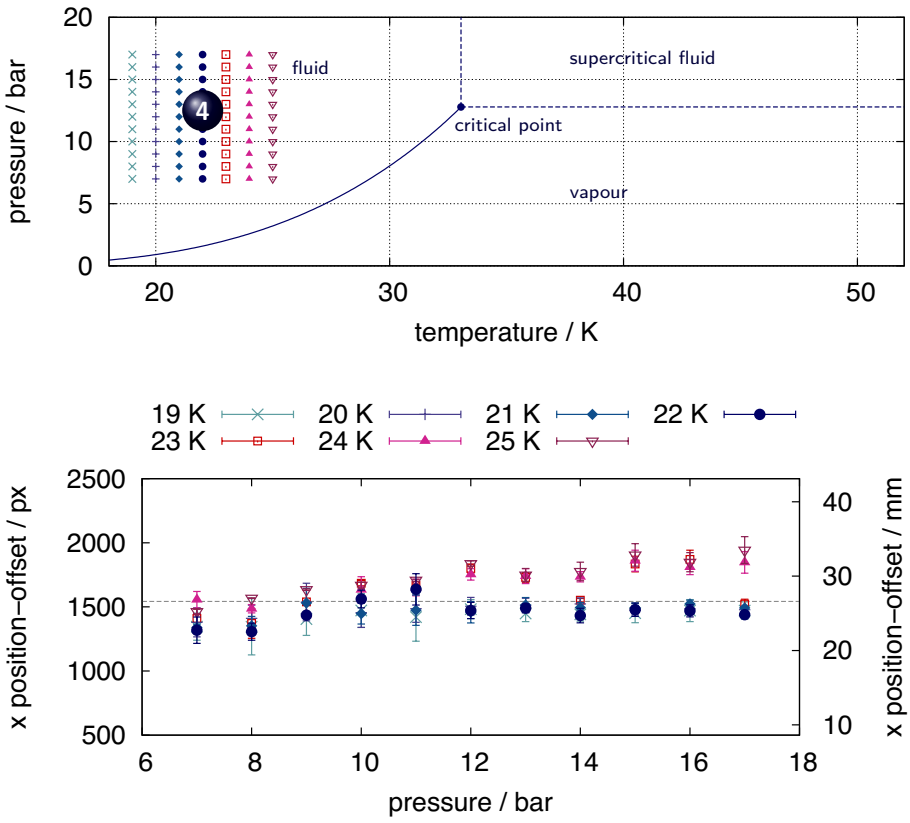

Figure 5.25.: x position-offsets of the measurement series at a temperature of 19 K to 25 K (in steps of 1 K) within a pressure range of 7 bar to 17 bar (in steps of 1 bar). A mean value of $\overline{x}_{\mathrm{off}}^{(4)} = (1543 \pm 58)\,\mathrm{px}$ can be extracted.

All four measurement series provide indications for a varying beam origin position of up to ±2 mm. Measurement series (4) points to an average distance of around 6 mm from the narrowest point of the nozzle (cf. Figure 5.26). Thus, with an outlet zone length around or below 6 mm the cluster production with Laval nozzles could be interrupted or even restricted. More insights into the cluster production process and the beam origin position will give systematic measurements with different Laval nozzle designs and materials, which will be investigated within [Gri15]. These measurements include optimisation studies, e.g. with a glass Laval nozzle with a short outlet zone of 2 mm.

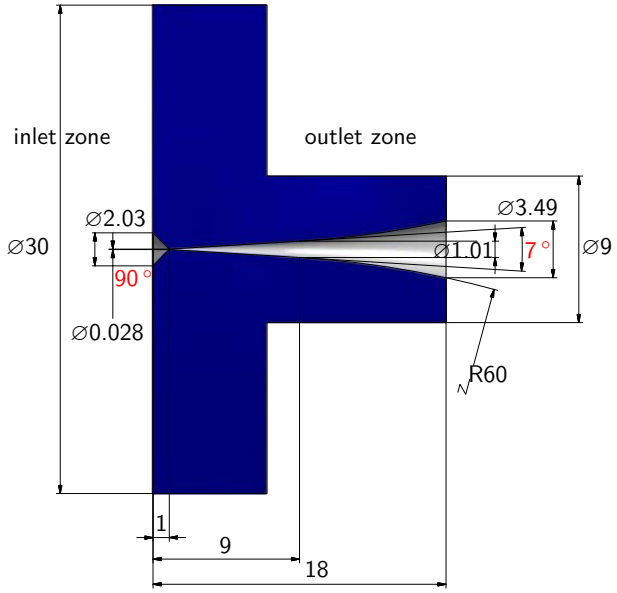

Figure 5.26.: Cross section of the installed Laval nozzle (generated by D. Bonaventura, edited) and its dimensions in millimetre, excluding the opening angles of 90 degree and 7 degree of the divergent inlet and convergent outlet zone. The narrowest diameter is around 28 µm.

Angles

With the offset parameters of the beam origin and the corresponding beam images, the intensity distribution in dependency of the beam opening angle $I(\alpha)$ can be gained via Equation (5.46) and yields a refined resolution of the beam structure. The resulting angles of the cluster-jet beam at 18.5 bar, which correspond to the red and blue coloured projections of Fig 5.18, are exemplary presented in Figure 5.27. The angular distributions of the complete measurement series (2) at 18.5 bar as well as angles for the measurement

series (1) and (3) at 7.5 bar and 25 K can be found in the Appendix A.4, excluding the images, where the cluster beam cannot be clearly separated from the background.
Opening angles up to 7 degree occur within the fluid area in accordance with the opening angle of the installed Laval nozzle (see Figure 5.26). Within the supercritical fluid area, smaller (visible) angular distributions down to 5 degree appear. The various intensity distributions as well as position and number of the core beams are once more clearly emphasised.

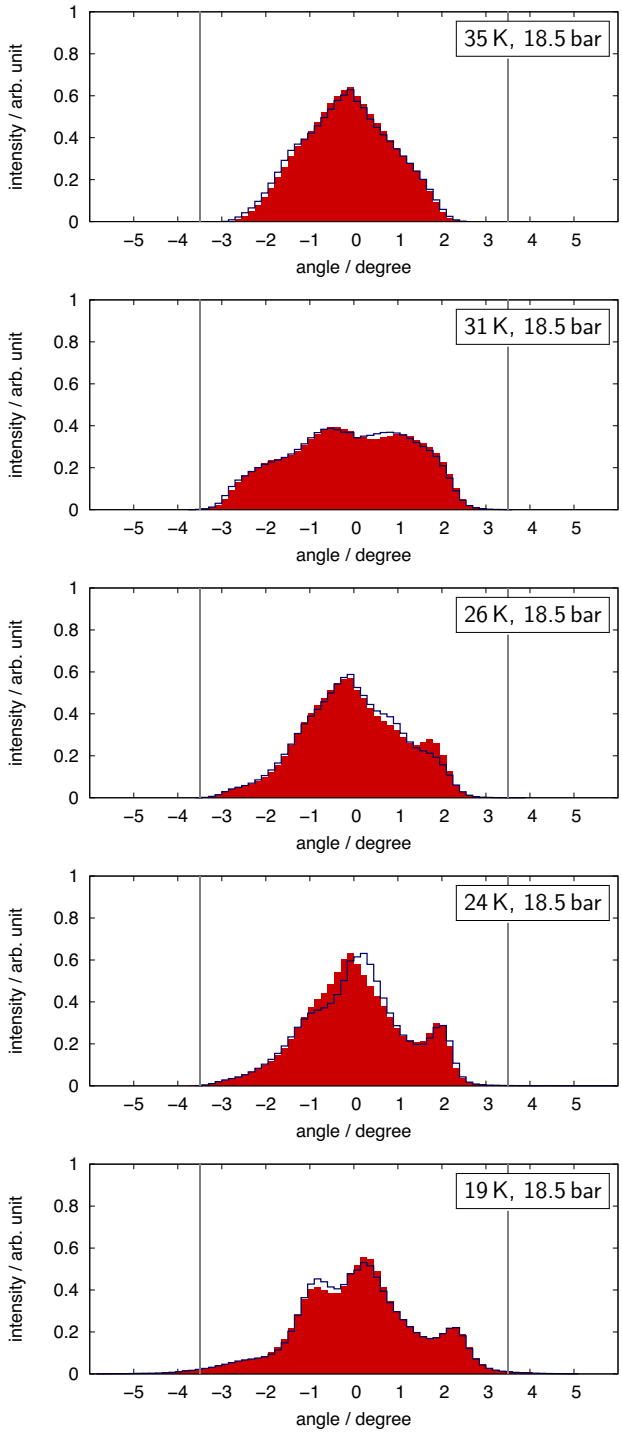

Figure 5.27.: Angle-resolved depiction of the intensity $I(\alpha)$ (background subtracted) of the cluster-jet beam at 18.5 bar at temperatures of 35 K, 31 K, 26 K, 24 K and 19 K (normalised to their integral). In addition to marginal reflections, the background was mainly defined by the noise of the camera and can be directly identified within the corresponding projection of the ordinate of each image. The presented histograms correspond to the appropriate red (heating process) and blue (cooling process) coloured projections in Fig. 5.18. The vertical grey lines indicate the opening angle of the nozzle.

5.2.2. Core beam extraction

The extraction and further investigation of the thickness of these core beams cannot be realised by simply adjusting skimmer and collimator (maximal ±2 mm), which are installed on cross tables. Feasibility studies with a beam deflector, which was directly installed at the nozzle exit, were insufficient as well. The deflector not only had an influence on the beam propagation (cf. Appendix A.5) but also on the beam structure and yielded in a rather smeared core beam. Therefore, a special nozzle tilting system was designed and installed (cf. Section 4.2.1). It allows to smoothly affect the nozzle alignment (approximately ±3.5 degree with the narrowest point of the nozzle as point of rotation) with regard to the skimmer position. Furthermore, cluster beam profiles within the skimmer chamber can be gained in connection with the monitoring system at the future interaction point and will be exemplary presented (cf. Figure 5.28) within the following hydrogen conditions at the production process.

1. vapour area at 50 K, 7 bar
   (cf. Fig. 5.29 and 5.30, top)
2. supercritical fluid area at 35 K, 17 bar
   (cf. Fig. 5.29 and 5.30, center)
3. fluid area at
   - 3.1 20 K, 8 bar (cf. Fig. 5.29 and 5.30, bottom)
   - 3.2 19 K, 18.5 bar (cf. Fig. 5.31 and 5.32)

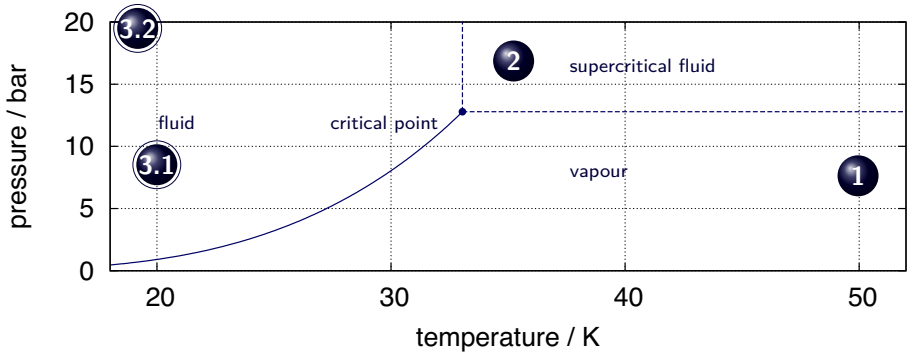

Figure 5.28.: Hydrogen vapour pressure curve, whereas the critical point (33.145 K, 12.964 bar [L+09]) is marked by a dot. The individual measuring points, which are emphasised in this section, are numbered.

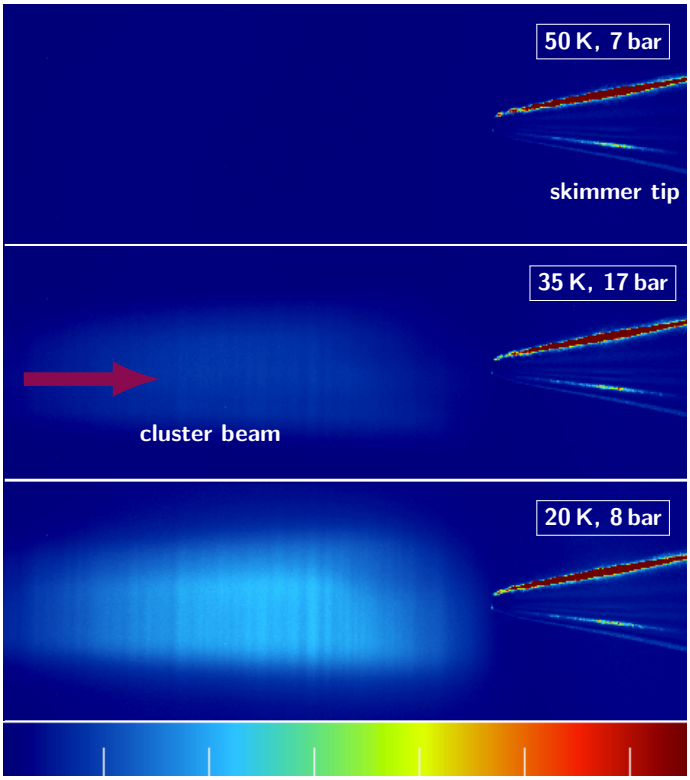

Figure 5.29.: Beam images within the skimmer chamber of measurement (1), (2), and (3.1) in false colours with beam direction from left to right (violet arrow). The data is based on monochrome images with (1392 × 1024) px, whereas the colour code represents the intensity (exposure time 5 s). Measurement series (3.2) will be presented more detailed in Figure 5.31 and 5.32.

The adjustment of the tilting system occurs manually via an adjusting screw. The modification of the serial nozzle orientation corresponds to a complete revolution of the screw (fine-adjusting possible), whereas the appropriate tilting angle is also specified at the following beam profiles.

Within measurement (1) at 50 K and 7 bar (vapour area), the cluster-jet beam is almost invisible (see Fig. 5.29, top), but the influence of the nozzle tilting system is mirrored by the development of the target thickness at the interaction chamber (in a distance of 2.1 m from the nozzle). Figure 5.30 (top) shows the thickness in dependency of the nozzle orientation or tilting angle, respectively. As expected from a homogeneous density distribution, the extraction at a tilting angle around zero (nozzle orientation = 0) shows the best results. At the peripheral areas of the beam the target thickness decreases, so that an opening angle around 4 degree can be identified.

Measurements (2) and (3.1) show a visible target beam with slight indications for an inhomogeneous intensity pattern (cf. Section 5.2 and see Fig. 5.29, center and bottom). The investigation with the nozzle tilting system clearly reveals at 35 K and 17 bar (supercritical fluid area around the critical point) as well as at 20 K and 8 bar (fluid area) that the beam profile shows strong variations (see Figure 5.30 center and bottom, ordinate with logarithmic scale). The peripheral areas of the beam cannot be captured due to mechanical restrictions of the tilting system. According to the previous Section 5.2.1 the maximal opening angle is around 7 degree.

Measurement series (3.2) at 19 K, 18.5 bar exemplary shows the influence of the nozzle tilting system on the nozzle alignment in detail. The left-hand side of Figure 5.31 presents the cluster beam images within the skimmer chamber, the right-hand side shows the corresponding beam profiles measured with the monitoring system within the interaction chamber. The beam images were recorded only from one direction, whereas the final $\overline{\text{P}}$ANDA cluster-jet target [Her15] contains two opposing camera ports both equipped with macro lenses (Zeiss Makro-Planar T* 2.0/100 mm ZF) and pco.pixelfly usb cameras. Skimmer and collimator (0.5 mm and 0.7 mm diameter by default) were fine adjusted and the nozzle orientation was changed from -2 to 6 (one step corresponds to a complete revolution of the screw). Steps within the beam profiles, e.g. see nozzle orientation 4, are related to the switching point of the installed pressure gauge (ITR 200). The resulting thickness can be obtained from Figure 5.32 and clearly shows an increase from the original thickness, according to the position of the highly intense core beams, around nozzle orientation 2, which corresponds to an shifting angle of 0.73 degree. For the first time, target thicknesses above 10^{15} atoms/cm^2 could be achieved at the required distance of 2.1 m from the Laval nozzle. So far, a maximal target thickness of more than 2×10^{15} atoms/cm^2 was achieved at 22 K and 17 bar (cf. Figure 5.33), which presents one main achievement of this thesis. Reproducibilty and stability measurements at these settings will follow in the next section. A density map will be performed at the final cluster-jet target for $\overline{\text{P}}$ANDA [Her15] and should reveal even higher thicknesses. The enhanced tilting system at the $\overline{\text{P}}$ANDA cluster-jet target captures angles up to ± 3.5 degree and is controlled via stepper motors. Furthermore, this system is equipped with two independent position indicators namely, rotary and linear encoder, whereas the traversed distance is limited by end switches.

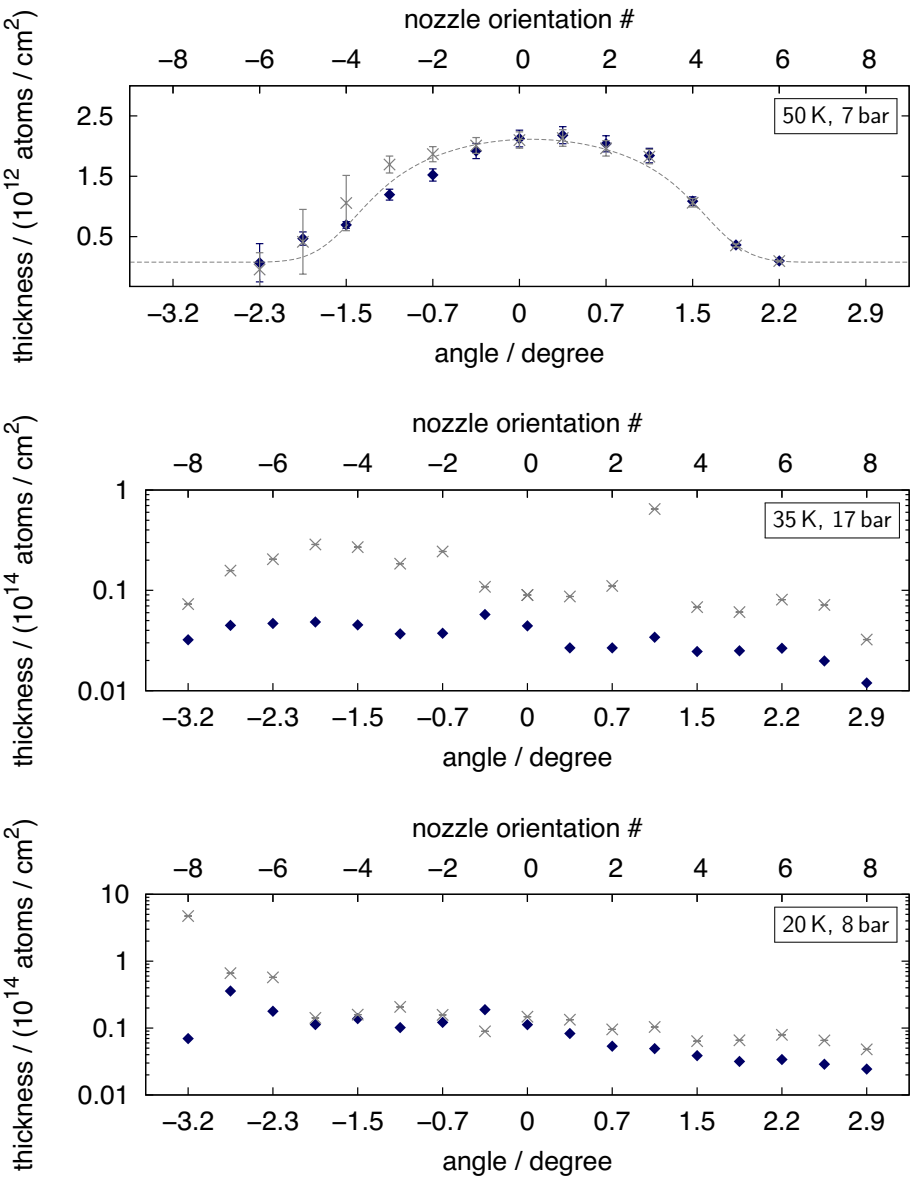

Figure 5.30.: Target thickness at the interaction chamber of measurement (1), (2), and (3.1), depending on the nozzle orientation (installed collimator with a diameter of 0.5 mm). The filled diamonds and crosses present the areal densities resulting from the horizontal and vertical beam profiles, whereas series (2), and (3.1) are presented with logarithmic scale. Discrepancies are attributed to the skimmer and collimator position, which are adjustable but remain unvaried within these measurements. Especially the vertical beam profiles arise partly unsymmetrical and are difficult to analyse. The applied fit function at the beam profile at 50 K, 7 bar (top) corresponds to Equation (5.26), which was used for beam profiles with circular beam shape (cf. Section 5.1.2).

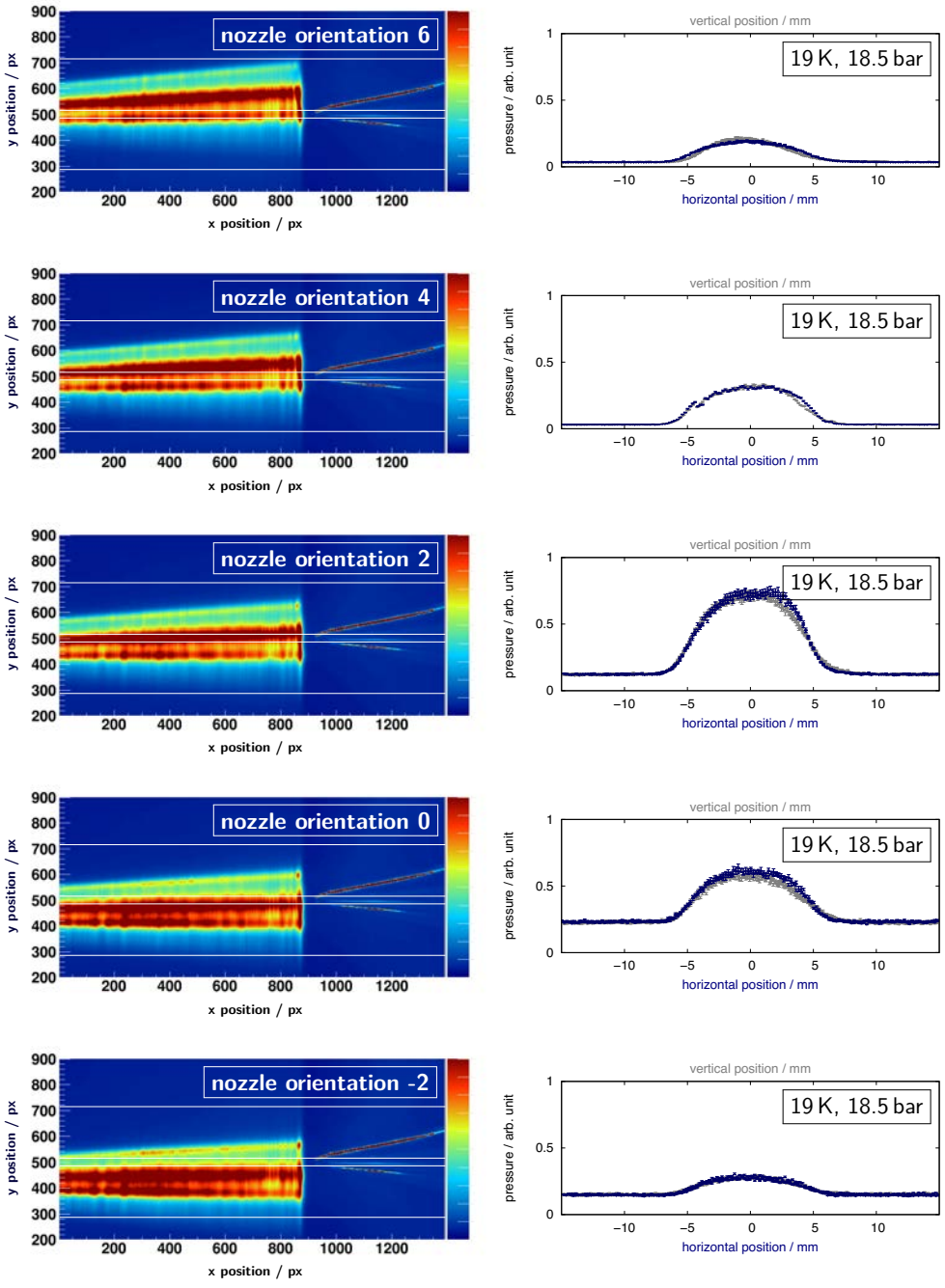

Figure 5.31.: Left: Cluster beam images within the skimmer chamber in false colours at 19 K, 18.5 bar with beam direction from left to right, where the data is based on monochrome images with (1392×1024) px and the colour code represents the intensity. Right: Corresponding horizontal (blue) and vertical (grey) beam profiles measured with the monitoring system within the interaction chamber.

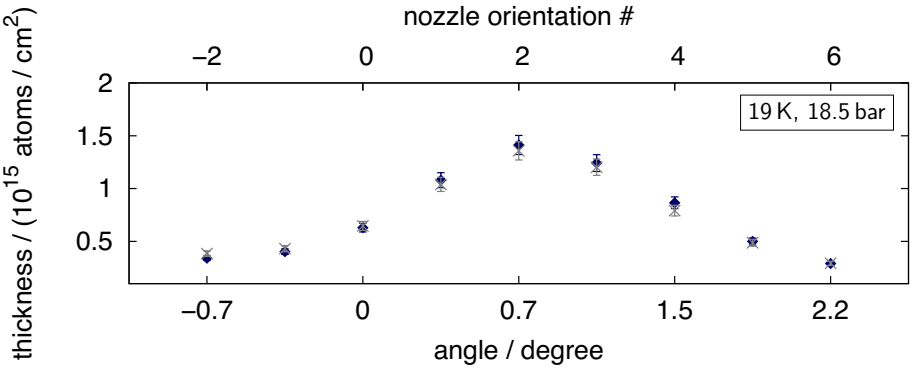

Figure 5.32.: Target thickness at the interaction chamber of measurement (3.2) depending on the nozzle orientation (installed standard collimator with a diameter of 0.7 mm). Areal densities above 10^{15} atoms/cm^2 could be achieved at a distance of 2.1 m from the Laval nozzle.

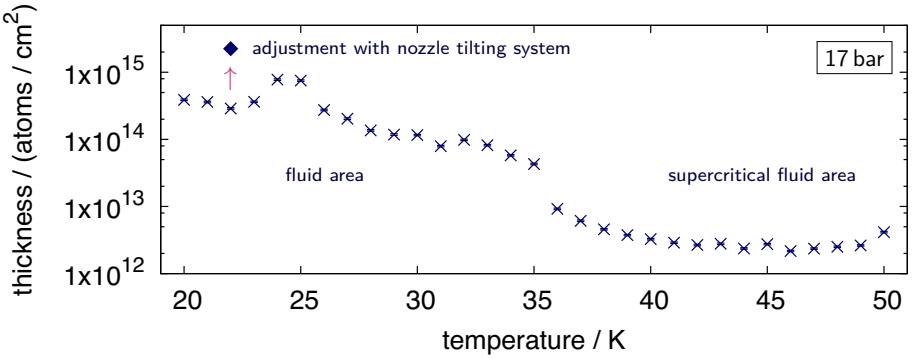

Figure 5.33.: Resulting target thicknesses (logarithmic scale) at 17 bar. With the nozzle tilting system a maximal target thickness of more than 2×10^{15} atoms/cm^2 was achieved at 22 K.

5.2.3. Reproducibility and stability measurements

Due to the installation and adjustment of the nozzle tilting system, initial progress to target thicknesses of more than 2×10^{15} atoms/cm^2 at a distance of 2.1 m from the production point was observed. The access to the high luminosity mode at $\overline{\text{P}}$ANDA with peak luminosities of $2 \times 10^{32}\,\text{cm}^{-2}\text{s}^{-1}$ (cf. Section 4.1.1) is thus tangible. To investigate the reproducibility of the beam structure and the corresponding thickness, the parameter settings (cf. Fig. 5.34 and 5.35) were varied in a sequence alternating between

1. the vapour area 50 K, 5 bar (standby operation)
2. the supercritical fluid area 35 K, 17 bar as well as
3. the fluid area 22 K, 17 bar and vice versa.

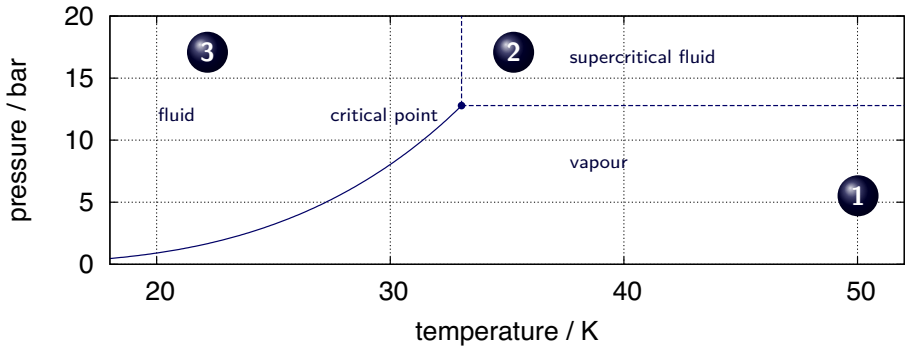

Figure 5.34.: Hydrogen vapour pressure curve, where the critical point (33.145 K, 12.964 bar [L$^+$09]) is marked by a dot. The individual measuring points, which are emphasised in this section, are numbered.

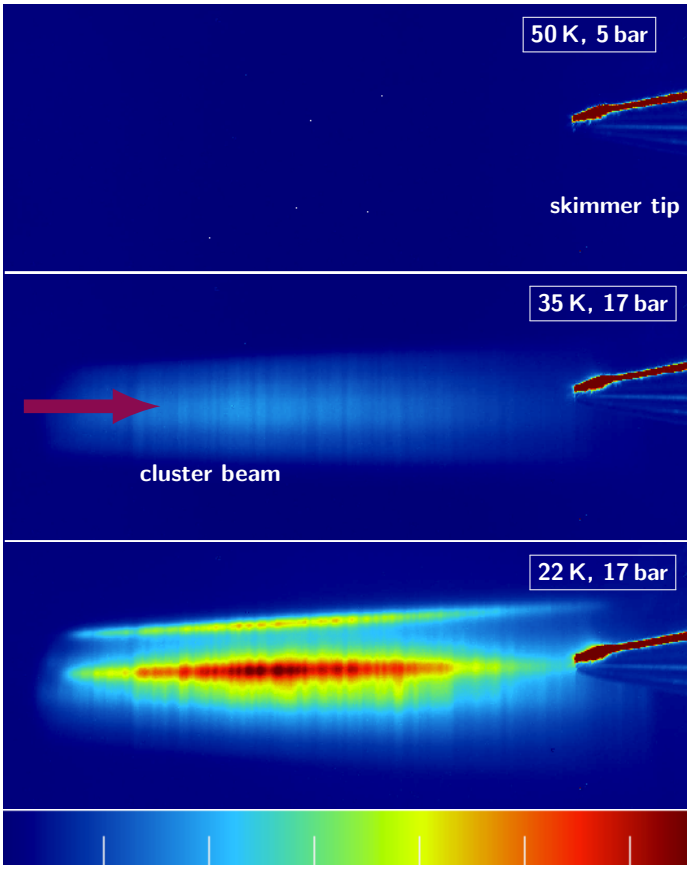

Figure 5.35.: Beam images within the skimmer chamber of measurement (1), (2), and (3) in false colours with beam direction from left to right (violet arrow). The data is based on monochrome images with a resolution of (1392 × 1024) px, where the colour code represents the intensity.

The results are presented in Figure 5.36 and show the straightforward switching from low ($> 2 \times 10^{12}$ atoms/cm^2, $> 6 \times 10^{13}$ atoms/cm^2) to high density ($> 2 \times 10^{15}$ atoms/cm^2). Moreover, the areal densities are reproducible and no further adjustments are necessary after an appropriate positioning of the nozzle tilting system including skimmer and collimator position. The appearance of core beams is most likely induced by the nozzle geometry or due to fine surface irregularities. Thus, the variation of the nozzle mounting position should have an impact on the core beam positions, which is demonstrated in Figure 5.37.

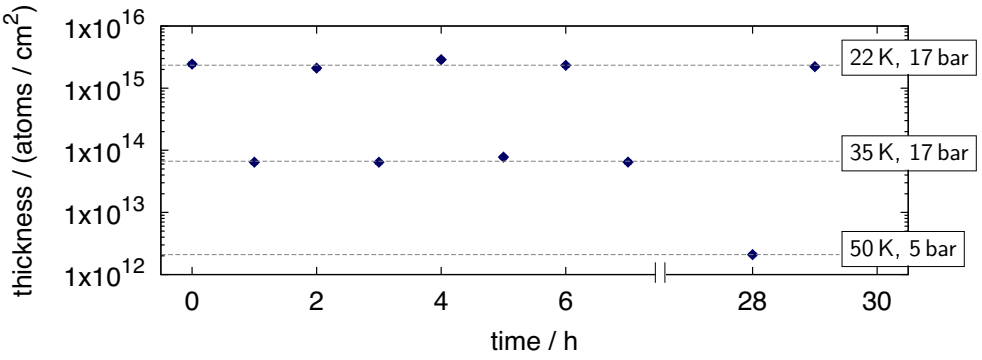

Figure 5.36.: Variation and reproducibility of the target thickness within (22 K, 17 bar), (35 K, 17 bar), and (50 K, 5 bar) with logarithmic scale.

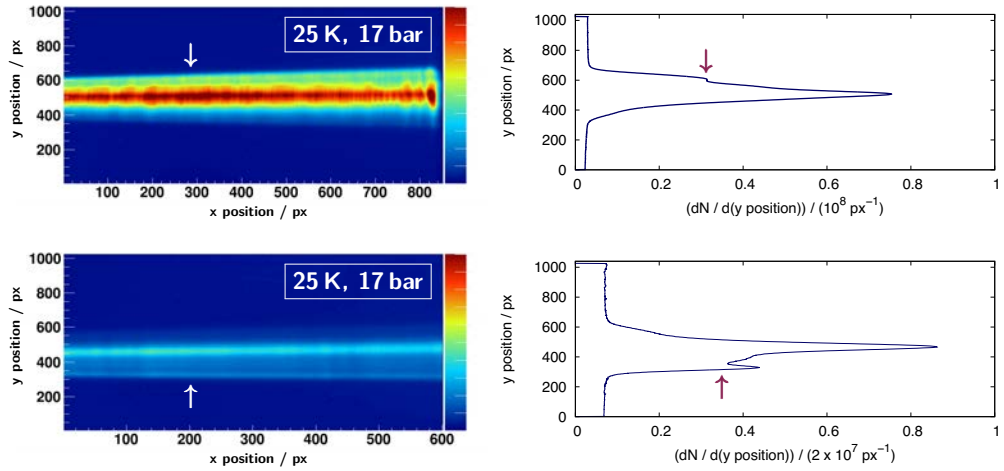

Figure 5.37.: Left: Cluster beam images in false colours of two different measurement series at 25 K, 17 bar. The beam direction is from left to right and the data is based on monochrome images with (1392×1024) px and the colour code represents the intensity. The intensity differences are attributed to different exposure times. Right: Corresponding projections of the ordinate. Both images and projections clearly show an highly intense core beam in the center and a second along the verge (see white and violet arrows). The different position is assigned to the varied nozzle mounting position.

If the mounting position of the Laval nozzle remains untouched, the reproducibility would be preserved. The influence of the nozzle mounting position will be further investigated at the final cluster-jet target for $\overline{\text{P}}$ANDA [Her15].
Furthermore, the stability of the thickness at 22 K, 17 bar was verified with two distinct, though interconnected, approaches: through the vacuum pressure distribution and the resulting target thickness within the interaction chamber. To obtain the vacuum pressure distribution (cf. Figure 5.38), the cluster-jet beam was retained with the monitoring system's rod at the beam center. The vacuum pressure was recorded every 3.5 s for an hour. As shown in Equation (5.17) and (5.45), the vacuum pressure is proportional to the density, which consequently results in a stable density with an accuracy better than 3.5 % (with a reproducibility of the vacuum gauge of 2.5 %).
Moreover, the long-term stability was investigated and beam profiles were recorded every 15 minutes within 5 h. As presented in Figure 5.39, the thickness has been observed to be on average $(2.14 \pm 0.03) \times 10^{15}$ atoms/cm^2 with a stability better than 10 %.

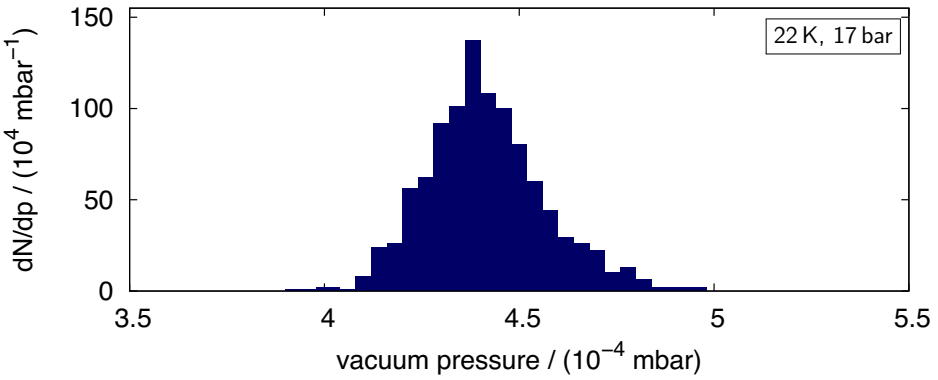

Figure 5.38.: Vacuum pressure distribution within the interaction chamber (accuracy better than 3.5 %). The cluster-jet beam was retained in the center using the rod of the monitoring system. The vacuum pressure was recorded every 3.5 s for one hour.

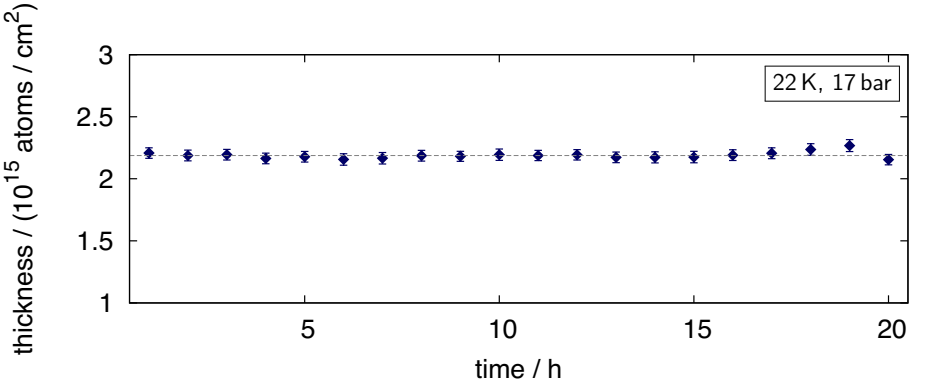

Figure 5.39.: Long-term stability test of the target thickness at 22 K, 17 bar (data obtained together with A.-K. Hergemöller [Her13]). The systematic uncertainties (of the velocity, pressure increase, and pumping speed) below 10 % were excluded.

5.3. Implementation of specially shaped collimators

In addition to the optimisation of the target thickness, the minimisation of the target expansion is of essential significance. As a result, background reactions would be reduced for a precise vertex reconstruction and a prolonged lifetime of the accelerator beam. The minimal target dimensions are initially limited to the expansion of the accelerator beam, in the case of the antiproton beam at $\overline{\mathrm{P}}$ANDA around 100 µm [PAN12a]. It should be noted that the interaction zone must remain of the same size with a constantly high thickness to achieve the required luminosities in the order of $10^{32}\,\mathrm{cm}^{-2}\mathrm{s}^{-1}$. As presented in Chapter 4, the definition of the cluster-jet beam size occurs through an orifice, the collimator. At the cluster-jet target prototype, a collimator with a diameter of 0.7 mm is installed by default and leads to a cluster-jet beam with a diameter around 10 mm and a maximal target thickness of more than $2 \times 10^{15}\,\mathrm{atoms/cm}^2$ at the interaction chamber, the future $\overline{\mathrm{P}}$ANDA interaction point. Through the installation of specially sized slit collimators, the dimensions of the cluster beam should be cut to a minimal effective size with highest thickness and unaffected vertex zone, as presented in Figure 5.40. The installation of different collimator blanks and the influence on the target thickness depending on the slit size (vertical size around 60 µm to 220 µm), which was especially investigated in the master thesis of A.-K. Hergemöller [Her13], will be presented in the following sections.

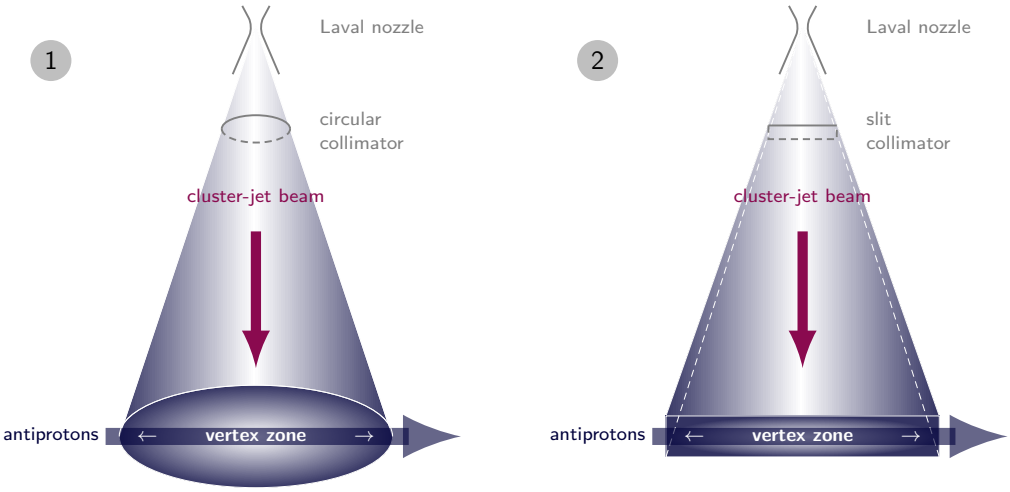

Figure 5.40.: Circular shaped (1) vs. rectangular shaped cluster-jet beam (2) with beam direction from top to bottom (violet arrow). The vertex zone remains unaffected.

5.3.1. Collimator blanks

In the past, the manufacture of slit collimators with exact sizes was very challenging. In the scope of this thesis, four different collimator blanks, were installed and tested. Figure 5.41 schematically shows collimator blanks shaped

1. cylindrical (stainless steel)
2. conical (stainless steel)
3. conical with truncated tip (stainless steel) and
4. conical with rounded tip (copper).

A cylindrical collimator shape offers the advantage to be able to apply precise etched slits, but investigations with a cylindrical cone (1) with initially round opening (see Fig. 5.42 (1)) show a reduced target thickness, caused by frontal reflections of the clusters leading to multiplied cluster-cluster interactions. At stagnation conditions of 22 K, 17 bar, the target thickness was decreased by a factor of 1.6 from initially 2.2×10^{15} atoms/cm^2 to 1.4×10^{15} atoms/cm^2. Therefore, this collimator blank proves inappropriate for additional applications. Conical collimators (2) which were used by default, complicate the introduction of the slit via a special laser cutting method (cf. Fig. 5.42 (2)), so that previously truncated cone collimators (3) delivered the best results (cf. Fig. 5.42 (3)). The analysis within [Her13] concentrates on collimators (type (3)) with the sizes (length $\leftrightarrow$ × width $\updownarrow$) of:

- 3.1 $(789 \times 116)\,\mu\text{m}^2$
- 3.2 $(798 \times 142)\,\mu\text{m}^2$
- 3.3 $(770 \times 189)\,\mu\text{m}^2$
- 3.4 $(765 \times 194)\,\mu\text{m}^2$
- 3.5 $(580 \times 221)\,\mu\text{m}^2$.

Through the efforts of the Laval nozzle production, which was presented in Section 4.2.1, the slit collimator production could be optimised. Throughout this process, a positive model of the slit was turned and milled out of a solid PolyMethyl MethAcrylate-rod and was coated with copper in a galvanic process to form the collimator body (cf. Figure 5.43 (1)). The outer shape of the collimator is then precisely turned and the extraction of the PMMA-positive results in an accurately prepared slit collimator (4) with the dimensions

- 4.1 $(800 \times 220)\,\mu\text{m}^2$
  (cf. Fig.5.42 (4) and Fig. 5.43 (2) and (3)).

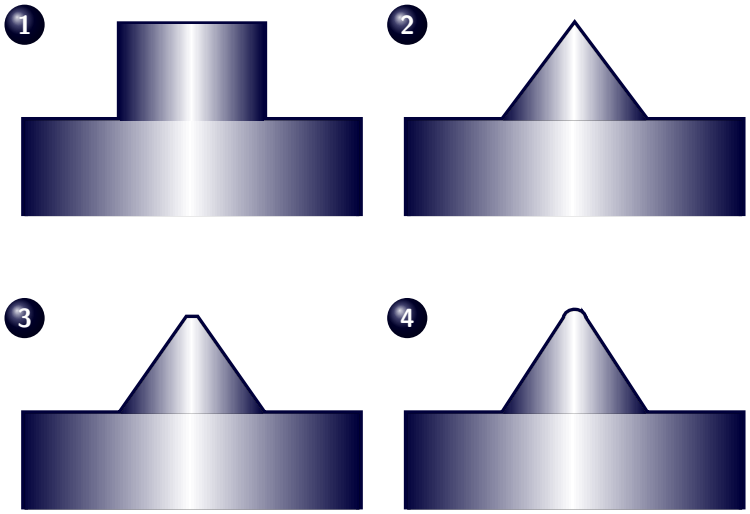

Figure 5.41.: Collimator blanks (side view) shaped cylindrical (1), conical (2), conical with truncated tip (3), and conical with rounded tip (4).

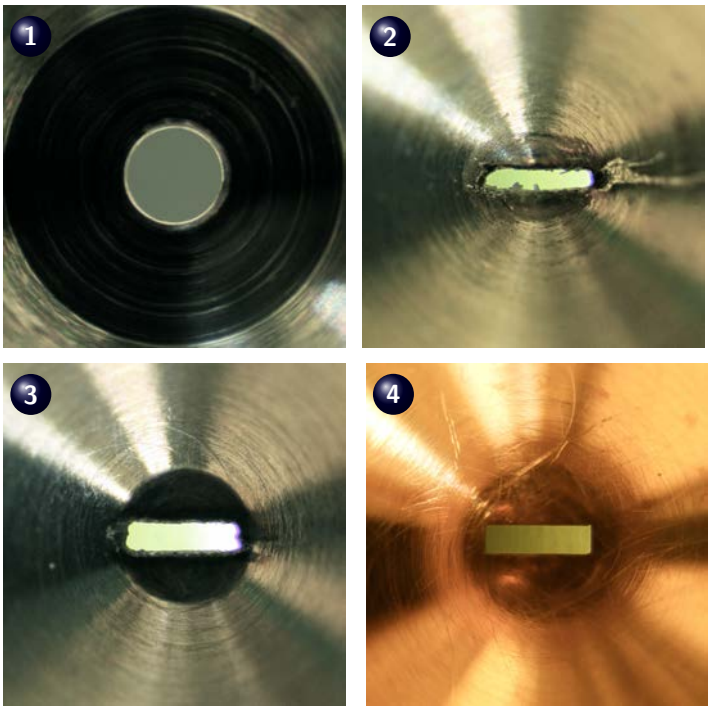

Figure 5.42.: Light-optical microscope images (LM-micrographs) of selected collimators (view from above): cylindrical with diameter 700 µm (1), conical with slit size $(890 \times 170)\,\mu m^2$ (2), conical with truncated tip with slit size $(780 \times 190)\,\mu m^2$ (3), and conical with rounded tip with slit size $(800 \times 220)\,\mu m^2$ (4).

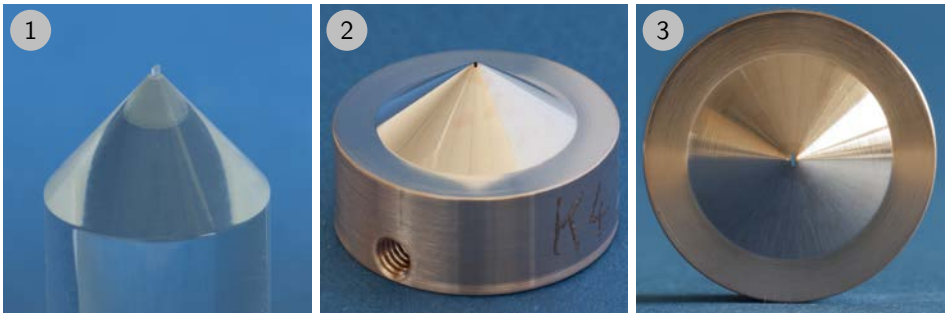

Figure 5.43.: Optimised slit collimator production. (1) positive model of the slit, which was turned and milled out of a solid PolyMethyl MethAcrylate-rod (2) and (3) finished slit collimator with size $(800 \times 220)\,\mu m^2$ (taken by D. Bonaventura).

This was recommended in [Her13] and implemented within this thesis. The results of the analysed beam profiles of the mentioned slit collimators will be presented in the following section.

5.3.2. Areal density (rectangular beam shape)

On the basis of the analysed beam profiles (cf. Equation (5.33)) together with Equation (5.44), the areal density of a rectangular shaped beam results in

$$\rho_{\text{areal,H,rect}} \overset{\text{[Her13]}}{=} \frac{p_{0/a}}{v} \frac{2\,S\,N_A}{R\,T}\, R_x\, \text{erf}\left(R_y/\tilde{s}\right) \tag{5.49}$$

with the maximal pressure increase $p_{0/a}$ (background subtracted) of the accumulated area, the cluster velocity v, the pumping speed S, Avogadro's constant N_A, the universal gas constant R, standard temperature T, the beam length R_x and width R_y as well as the smearing parameter $\tilde{s}$, and the errorfunction erf. The analysis of the truncated cone collimators (3.1) to (3.5) within [Her13] leads to the following results.

The smearing parameter $\tilde{s}$, which considers edge effects of the collimator, is approximately constant for various collimator widths (vertical size) [Her13]. In accordance with the results of the beam profiles with circular beam shape (collimator diameter 0.5 mm and 0.7 mm), the smearing parameter depends mainly on the target thickness, but also on the profile quality and therefore on the adjustment. A smearing factor of (1.39 ± 0.02) mm [Her13] on average can be extracted for thicknesses around 10^{15} atoms/cm^2 at the interaction chamber (2.1 m from the nozzle).

Furthermore, the reduction of the collimator width leads to a minimal FWHM (Full Width at Half Maximum) of around 2 mm at the interaction chamber. Collimator widths below 200 µm induce a decrease of the target thickness (cf. Figure 5.44) instead of beam size

reduction [Her13]. Thus, the target thickness cannot only be varied by the temperature and pressure settings, but also through the orifice size. For the reproducibility of highest densities, the collimator width must be larger than 200 µm.

Moreover, the analysis shows that the background at the interaction point is primarily induced by the target source and secondarily through backscattered clusters at the beam dump [Her13]. The pumping station for the $\overline{\text{P}}$ANDA cluster-jet target is hence equipped with high-performance vacuum pumps (cf. Section 4.2.1), which are tested at the prototype, described within this thesis.
A maximal target thickness of 2×10^{15} atoms/cm^2 was achieved with a slit collimator (3.4) with the size $(765 \times 194)\,\mu\text{m}^2$ [Her13] (cf. Figure 5.44). An extrapolation of the results of a slit collimator (3.5) with a size of $(580 \times 221)\,\mu\text{m}^2$ lead to a thickness of 2.2×10^{15} atoms/cm^2 with an effective beam width of 3.3 mm at the future interaction point [Her13]. Consequently, a slit collimator in the order of $(800 \times 220)\,\mu\text{m}^2$ will provide the maximal target thickness at minimal target expansion. That could be verified via a slit collimator with rounded cone (4.1), which achieves at 22 K, 17 bar a maximal target thickness of $(2.3 \pm 0.3) \times 10^{15}$ atoms/cm^2 at the required distance of 2.1 m from the target source.

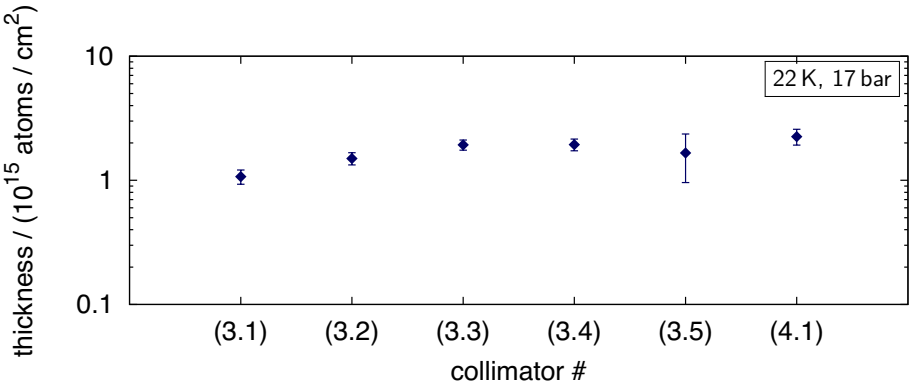

Figure 5.44.: Target thickness in logarithmic scale at stagnation conditions of 22 K and 17 bar with installed truncated cone slit collimators (3.1) to (3.5) (data extracted from [Her13]) as well as for the slit collimator with rounded cone (4.1).

5.3.3. Cluster beam visualisation via microchannel plates

The beam shaping through the installation of a collimator can be visualised by a MicroChannel Plate (MCP) detection system (cf. Figure 5.45), which was implemented and first tested within [Zan13]. Installed at the end of the target's beam dump, this system allows a two-dimensional real time observation and monitoring of an ionised cluster-jet beam (published in [K$^+$14b]), whereas the ionisation can occur via the application of an electron gun. The cluster beam shape, size, position, as well as the intensity can be investigated and offers the opportunity for adjustment checks and will facilitate the detection of possible beam constraints within the target setup. Moreover, the vertex zone with an accelerator beam can be observed, whereas the resulting intensity is correlated to the luminosity distribution. In this case, the ionisation occurs within the interaction with the accelerator beam. After an overview of the general MCP characteristics, the experimental setup and the resulting cluster beam images will be presented.

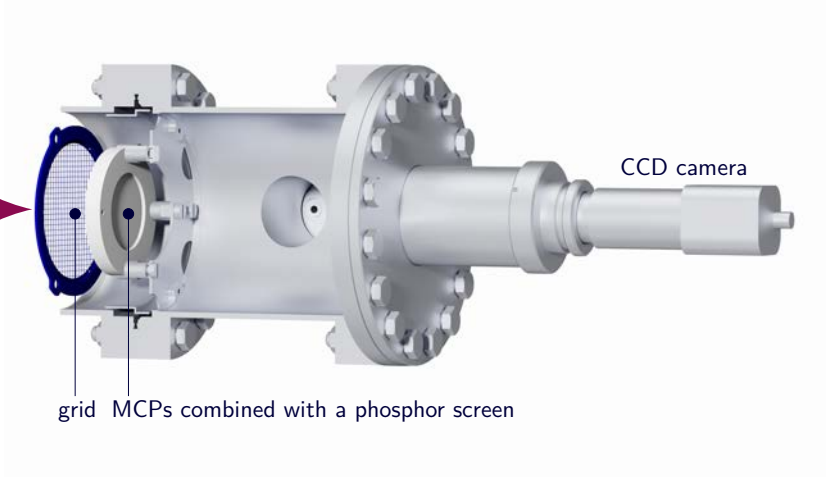

Figure 5.45.: Installed MCP detection system (basic design) containing a grounded grid with two MCPs in chevron assembly, a phosphor screen, and a CCD camera. The cluster beam direction is represented by a violet arrow.

MCP characteristics

A MCP contains millions of thin, conductive glass capillaries, which are merged together and then cutted into rectangular or circular sheets [Ham06]. Each capillary operates as a secondary-electron multiplier as indicated in Figure 5.46. Impinging charged particles generate secondary electrons, which are multiplied through the bias angle of the channel axis to the vertical MCP axis (around 5 degree to 15 degree [Ham06]). The electrons are accelerated within the channels affected by voltage across the first MCP. An amplification

of the signal can be implemented through the extension of a second MCP (chevron assembly, cf. Figure 5.46) or even a third MCP (z-stack assembly) with opposing bias angles (cf. Table 5.1). The gain g depends mainly on the length-to-diameter ratio $\tilde{\alpha} = {}^{L}/_{d}$ and a gain factor G, which describes the emission characteristics of a channel [Ham06]

$$g = \exp\left(G\ \tilde{\alpha}\right). \tag{5.50}$$

Moreover, the connection in series decreases the spatial resolution, because more channels were triggered in each MCP layer as shown in Figure 5.46. The noise (ion feedback), which is caused by signals of residual gas molecules ionised by the multiplied electrons, can be reduced. All essential parameters of the used MCP detection system are listed in Table 5.1, whereas Figure 5.47 shows an LM-micrograph of the MCP channels. The detector efficiency depends on the ratio of the open and effective area defined as Open Area Ratio (OAR), which should be as large as possible (typically around 60 %). Furthermore, the radiation type (e.g. electrons, ions, neutrons, X-rays, UV rays), their incident angle and energy as well as the MCP coating [Ham06] must be taken into account. Ions (H^+, He^+, Ar^+) with an energy between 0.5 keV to 2 keV show a detection efficiency around 5 % to 58 %. The 2 keV to 50 keV ions feature an efficiency between 60 % and 85 % [Ham06].

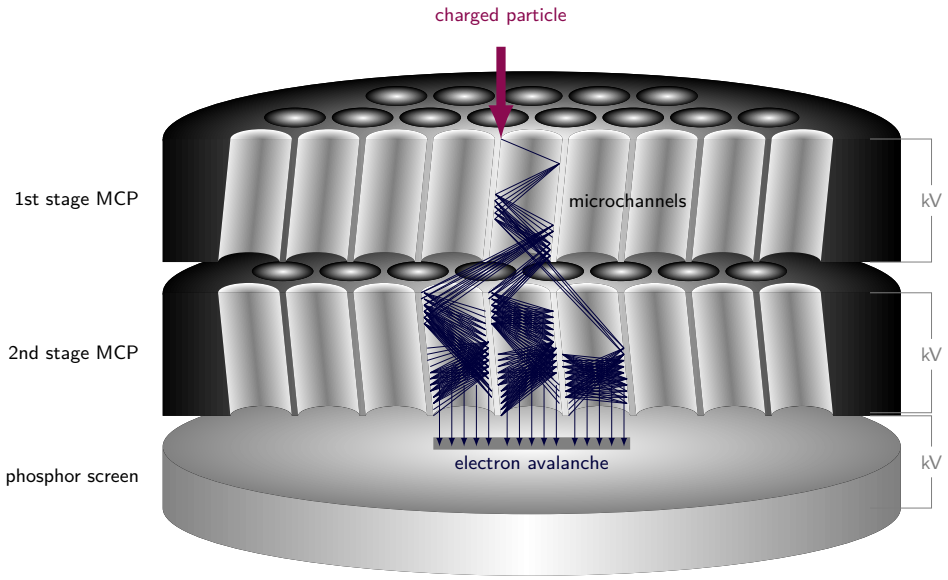

Figure 5.46.: Operating principle of a two stage, circular MCP (chevron assembly) in conjunction with a phosphor screen. Each capillary operates as secondary-electron multiplier, when a charged particle (violet arrow) impinges on the MCP. The accelerated electrons induce a two dimensional image on a phosphor screen.

MCP characteristics	
material	NiCr
shape	circular
diameter	(50.0 ± 0.1) mm
active diameter	40 mm (min)
open area ratio	60 %
thickness	(0.50 ± 0.05) mm
pore diameter	(12.0 ± 0.5) µm
bias angle	(11 ± 1) degree
length-to-diameter ratio α	40:1
single MCP gain	1×10^4 (min) at 1000 V
chevron gain	5×10^6 (min) at 2000 V
z-stack gain	1×10^8 (min) at 3000 V

Table 5.1.: Parameters of the MCP detection system model MCP-50-D-R-P43 (chevron assembly with phosphor screen P43 (Gd_2O_2S:Tb)) [tec].

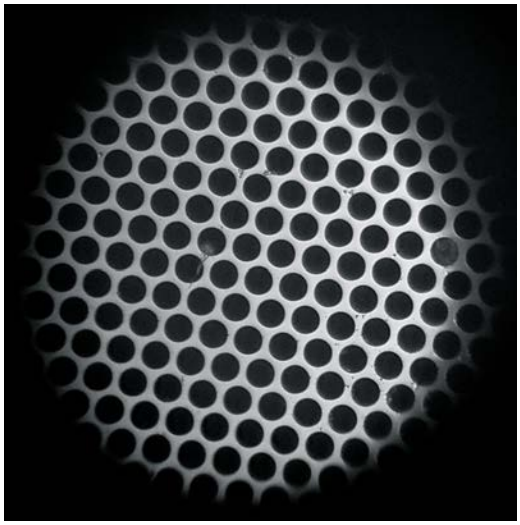

Figure 5.47.: LM-micrograph of the installed microchannel plates with pore diameter of (12.0 ± 0.5) µm.

Experimental setup (basic version)

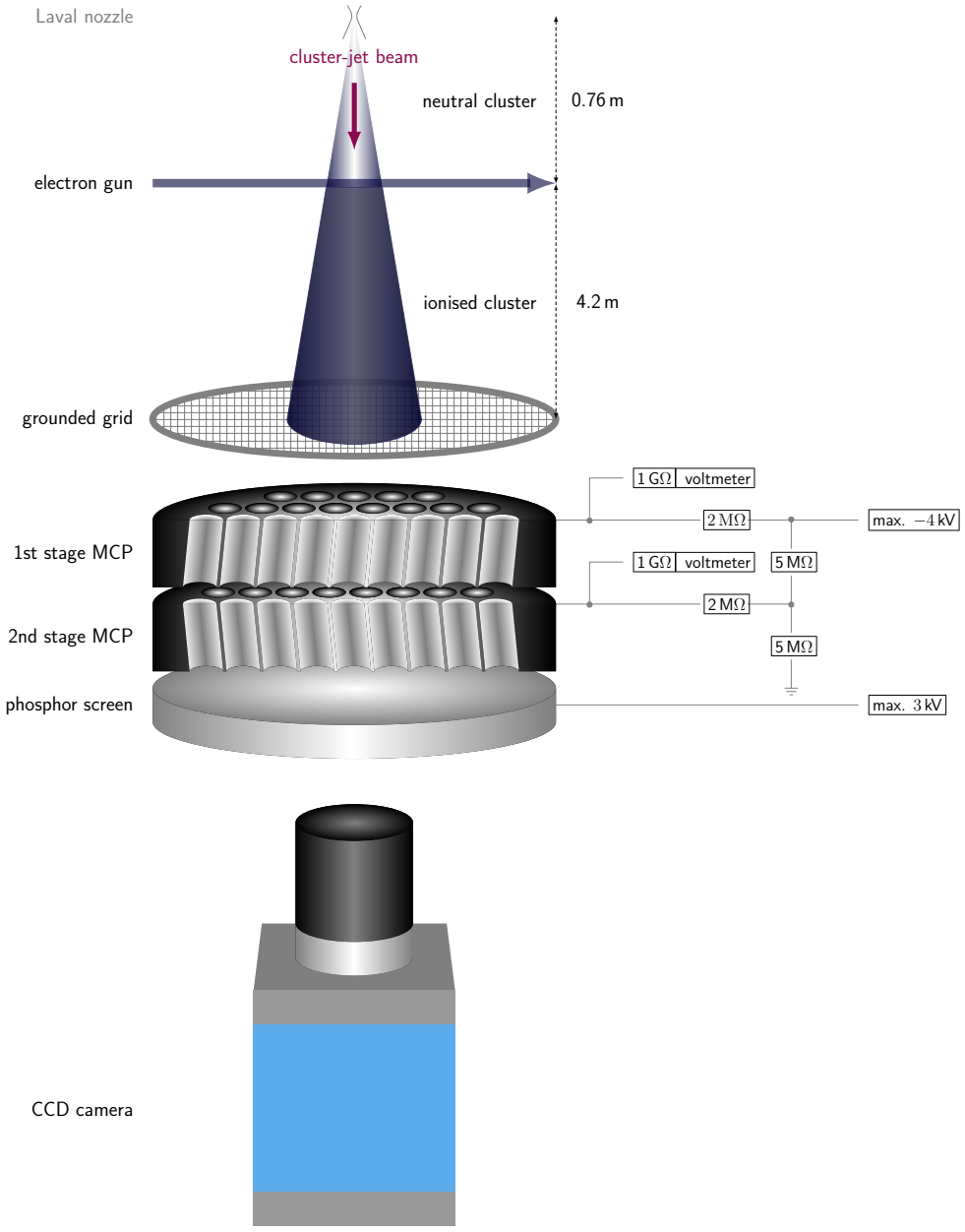

Figure 5.48.: Schematic overview of the experimental setup and wiring scheme of the installed MCP detection system (basic version). Cluster beam direction from top to bottom (violet arrow).

The ionisation of the hydrogen cluster-jet beam at the target prototype occurs around 0.76 m behind the nozzle (cf. Figure 5.48) via a continuously operated electron gun (pulsed mode possible). The 7 mm electron beam [Tä12] interferes with the cluster beam and mostly positively charged clusters are generated. The electron energy and current are variable but typically lie around 150 eV at a few microampere. After a further flight path of approximately 4 m, the positively charged clusters reach the MCP detection system. An electrically grounded grid with 2.5 mm lattice spacing (2.7 mm center-to-center), two stage MCP's (tectra GmbH MCP-50-D-R-P43), and a phosphor screen (Type P43) combined with a CCD camera (PCO.Pixelfly usb) belong to the main components of the detection system. The impinging clusters generate primary electrons, which are multiplied and detected by the phosphor screen. The emitted photons and the resulting image on the screen can be observed in real time and recorded by a CCD camera. Simultaneously, the fractured clusters are evacuated via the installed vacuum pumps at the beam dump.

MCP images

The resulting MCP images enable a two-dimensional visualisation of an ionised cluster-jet beam (cf. Figure 5.49), particularly with regard to the beam's

- shape
- size
- position
- intensity
- adjustment and
- possible mechanical constraints (e.g. beam pipes or orifices).

The visibility of an accurate image of the hydrogen cluster beam is only available at parameter settings within the fluid area, which corresponds to the operation settings at $\overline{\text{P}}$ANDA. Because of their size ($\gg 10^6$ atoms/cluster, see also Chapter 6), their flight path remains unaffected from deflecting fields, e.g. induced by the beam dump's turbomolecular pumps.

Figure 5.49 exemplary shows on the left hand side one MCP image of a circular shaped cluster-jet beam at 22 K, 4 bar (installed circular collimator with a diameter of 0.5 mm), whereas the right hand side presents an average of 128 images. The clearly visible grid structure offers the possibility to determine the size and position of the cluster-jet beam (1) at the beam dump. As expected, at a distance of nearly 5 m from the production point, the cluster beam results in a diameter of approximately 22 mm at the entrance grid of the MCP detection system ($1\,\text{px} = (44.32 \pm 0.01)\,\mu\text{m}$ with a spatial resolution of around 100 µm [K$^+$14b]). The fringe area of label (2) presents the last cool sheet of the installed cryopump, whereas label (3) shows the dimensions of the phosphor screen.

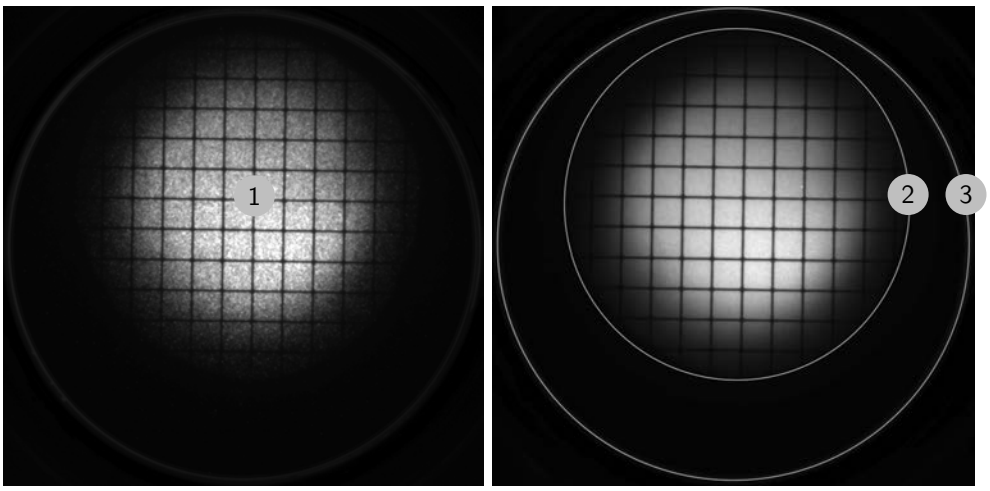

Figure 5.49.: Left: Monochrome MCP-image at 22 K around 4 bar with 2 s exposure time (data extracted from [Zan13]). Right: Average of 128 MCP-images at 22 K around 4 bar (data extracted from [Zan13]). Label (1) presents the cluster-jet beam and additionally shows the shadow of the entrance grid with a distance of 2.7 mm center-to-center. (2) and (3) indicate the dimensions of the installed cryopump cool sheet and the phosphor screen with a diameter of 25 mm and 40 mm.

Figure 5.50 demonstrates the corresponding intensity or relative density distribution of the monochrome MCP image of Fig. 5.49, right. The slight asymmetry is attributed to partial damages on the phosphor screen, which is exchangeable. Impairments of the phosphor screen can be prevented through a correct composition of the MCPs, the compliance of the allowed operation parameters, and a sufficient pumping speed at this beam dump section.

As presented in the previous Section 5.3, the dimensions of the cluster beam should be cut to a minimal effective size with highest thickness to reduce background reactions with the accelerator beam within storage ring experiments. The definition and shaping of the cluster-jet beam occur via a collimator (e.g. in Figure 5.51) and principally should be transferred from circular to rectangular beam shape. The resulting cluster-jet beam is illustrated in Figure 5.52 and additionally shows the effect of a heart shaped collimator. All images reflect completely the originating orifice shape.

Both orifices, skimmer and collimator, are moveable to thread the cluster-jet beam through the beam pipes and beam dump stages without constraints. In particular the position of the collimator is crucial for the beam position and the influence can be immediately visualised with this detection system. Figure 5.53 clearly shows the displacement of the cluster-jet beam interfering with the cool sheets of the installed cryopumps.

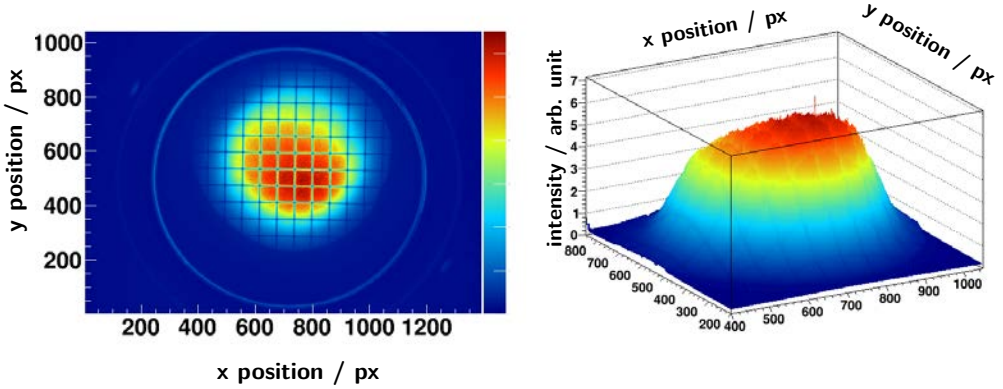

Figure 5.50.: Two dimensional intensity or relative intensity distribution of the circular cluster-jet beam based on the data in Figure 5.49, right. The colour code represents the relative intensity in arbitrary unit.

Figure 5.51.: Installed collimators with circular (diameter 0.5 mm), rectangular ($(780 \times 190)\,\mu m^2$), and heart shaped opening (maximal length $760\,\mu m^2$).

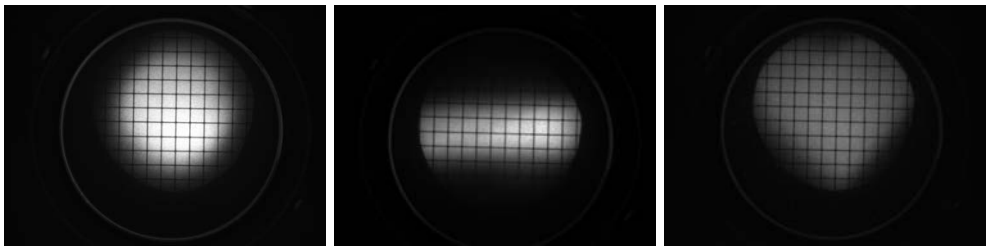

Figure 5.52.: Corresponding averaged MCP images of the presented collimators in Figure 5.51. The beam shape of the installed collimators are reproducible.

So far, beam adjustment checks were performed with the monitoring system at the interaction chamber, which gradually scans the cluster beam with rods in horizontal (cf. Figure 5.54) and vertical direction (destructive method). To obtain an almost 4π angle acceptance at the $\overline{\mathrm{P}}$ANDA experiment, no further setups can be implemented at the interaction point, where the beam pipe diameter amounts to only 20 mm. Therefore, the monitoring system cannot be installed and operated at $\overline{\mathrm{P}}$ANDA. The MCP detection

system though, classified as non destructive method, can be installed at the end of the targets beam dump and enables real time beam adjustment checks not only at the target prototype, but also at the $\overline{\text{P}}$ANDA experiment.

Possible mechanical disturbances can be immediately identified as presented in Figure 5.54. All figures show the intentional positioning of the monitoring system's rod to emphasise once more the possibility to clearly identify mechanical beam constraints. The propagation of the cluster beam without interferences leads to minimal background at the interaction point.

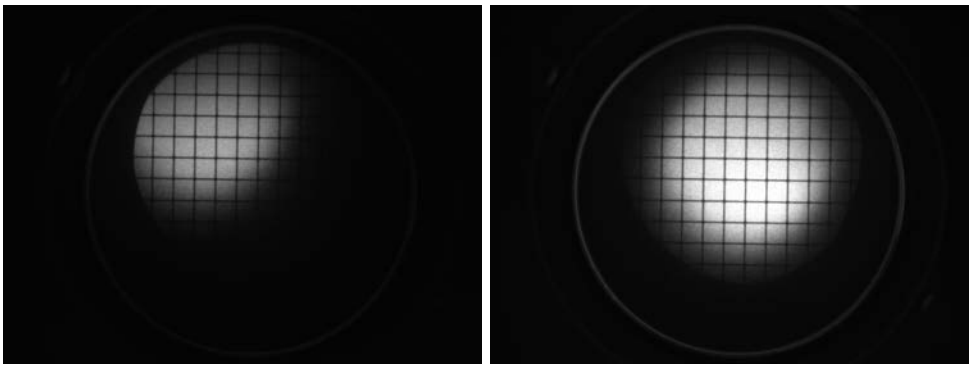

Figure 5.53.: Displaced and adjusted cluster-jet beam induced by the selected collimator position.

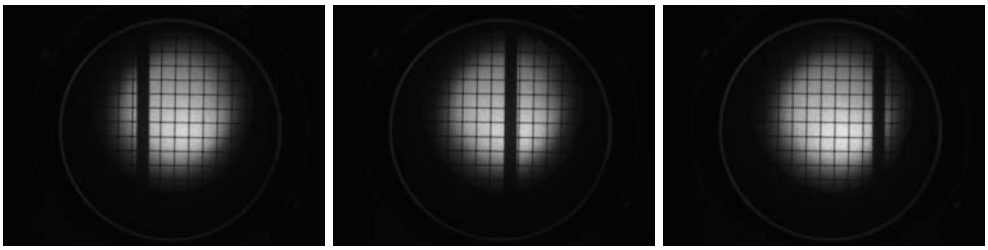

Figure 5.54.: Cluster-jet beam with intended interference with the monitoring system's rod at the interaction chamber for three different positions. The rod diameter at the interaction chamber amounts 1 mm.

Vertex zone visualisation

In addition to the mentioned applications of the MCP detection system, the vertex zone at storage ring experiments, e.g. at $\overline{\text{P}}$ANDA, can be visualised and monitored. At the point of intersection of cluster target and accelerator beam, the cluster beam will be partly ionised (Coulomb effects) only at their overlap region. Since the accelerator beam extension (diameter around 1 mm to 2 mm) is smaller compared to the cluster target beam

(diameter ≈ 10 mm), the residual neutral part of the target beam remains undetected and will not contribute to the intensity distribution of the resulting images (cf. Figure 5.55). Thus, the MCP images mirror the vertex zone, whereas the intensity is correlated to the luminosity distribution.

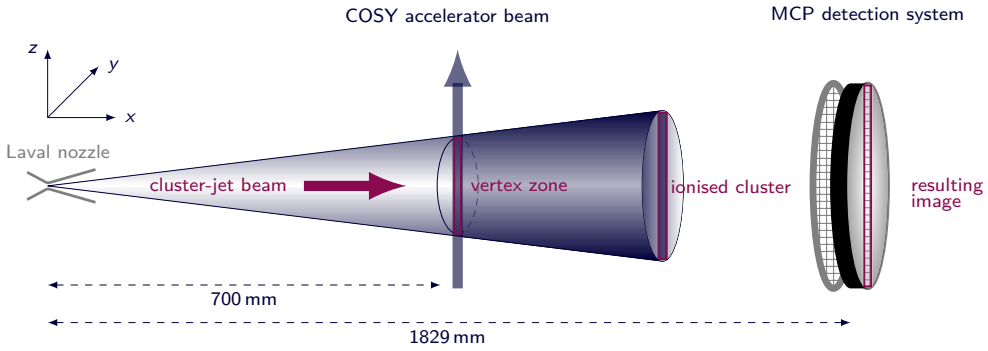

Figure 5.55.: Illustration of the vertex visualisation at the ANKE cluster-jet target at COSY. The cluster beam propagates from left to right (violet arrow), whereas the COSY accelerator beam from bottom to top (blue arrow).

Feasibility studies were performed at the ANKE cluster-jet target at COSY (Forschungszentrum Jülich, Germany), where the MCP detection system was installed at the end of the beam dump in exchange to a turbomolecular pump. ANKE was operated with hydrogen and used densities $\leq 10^{14}$ atoms/cm^2 in a distance of approximately 70 cm from the Laval nozzle. Protons with a beam momentum of 300 MeV/c were injected, stored, and further accelerated to 2100 MeV/c at COSY with a cycle time of 30 s.

Figure 5.56 exemplary presents the resulting MCP images (exposure time 5 s). Abscissa and ordinate correspond to horizontal and vertical expansion of the cluster beam, whereas the ordinate also reflects the accelerator beam direction. The variable intensity is directly attributed to the proton beam intensity and the view is limited by the cool sheets of the installed cryopumps.
Figure 5.56 top presents the interaction zone after COSY beam injection and reflects the broad distribution of the protons at low beam momentum. Within the acceleration up to 2100 MeV/c, adiabatic cooling induces a decrease of the proton beam expansion, which can be directly observed with the MCP detection system (cf. Figure 5.56, center). Furthermore, the COSY beam can be shifted transversal via a steerer magnet, which can also be captured within the MCP images (cf. Fig. 5.56, bottom). The width of the COSY beam at the vertex zone was estimated to be around $\sigma_{\mathrm{COSY,vertex}} = 1.2$ mm (RMS) with a resolution of approximately 150 µm (RMS) [K$^+$14b].

The investigated fields of application of the MCP detection system can be extended to the research of the cluster mass and will be presented in the following Chapter 6. With regard to the $\overline{\mathrm{P}}$ANDA experiment, the cluster mass in addition to the cluster velocity and the target thickness are crucial for an accurate and precise data analysis and simulation.

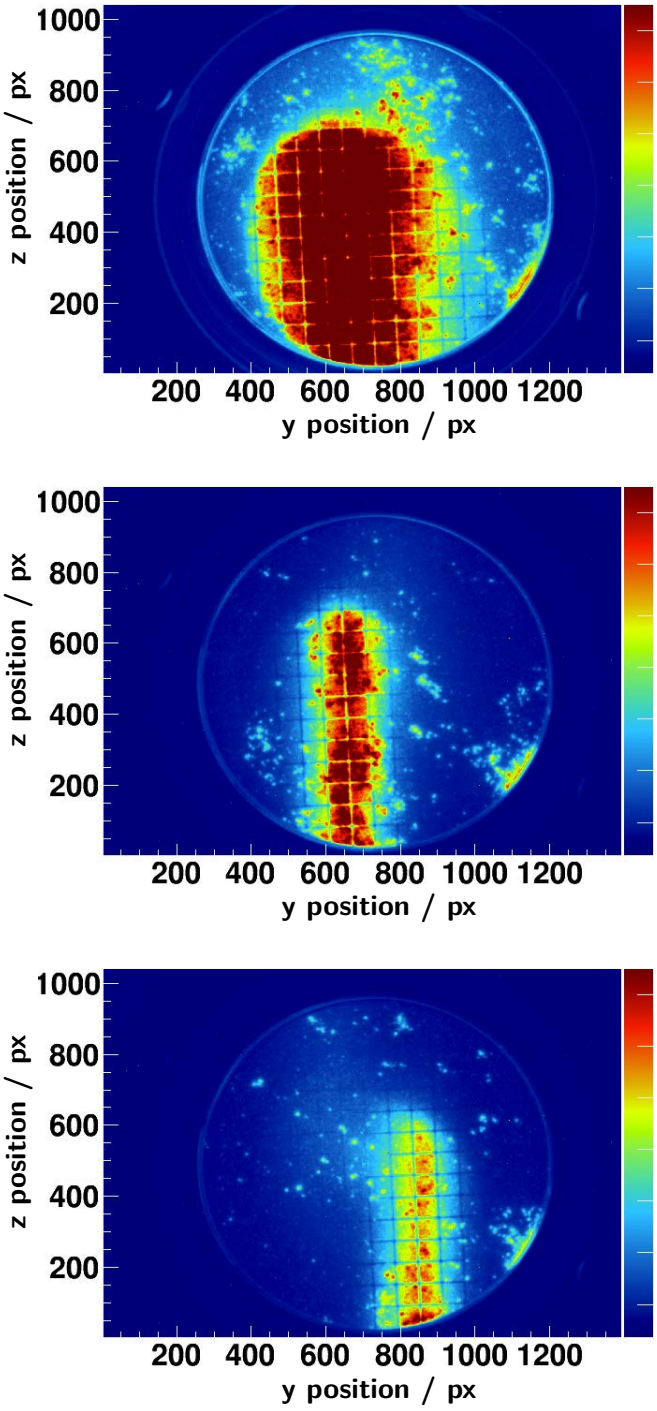

Figure 5.56.: Monitoring of the vertex zone at the ANKE cluster-jet target at COSY. Presented is the vertex zone at beam injection ($\approx 300\,\mathrm{MeV}/c$, top), at final beam momentum ($\approx 2100\,\mathrm{MeV}/c$, center), and with enabled steering magnet ($\approx 2100\,\mathrm{MeV}/c$, bottom). The colour code shows the relative intensity in arbitrary unit.

6. Mass distribution of hydrogen cluster-jets

Since the cluster characteristics could vary with increasing number of constituents, e.g. structure, stability, velocity or density etc., the theoretical description of these many-body systems holds a lot of unresolved challenges. Thus, it is essential to systematically investigate the properties of cluster-jets. This involves especially the velocity, the thickness, and the cluster mass or size. A detailed analysis of these correlated parameters allows for insights into the complex cluster production process within a Laval nozzle, enables the optimisation of the target design for highest performance, and provides the basis for a precise data analysis and simulation with regard to storage ring experiments. The previous Chapter 5 already concentrates on the velocity distribution [Köh10] and the calculation of mean cluster velocities [Tä12, T$^+$13] as well as on the optimisation of the target thickness, which gives access to both operation modes at the $\overline{\text{P}}$ANDA experiment, the high resolution and high luminosity mode (cf. Section 3.2). The determination of the mass distribution of hydrogen cluster-jets in context to the stagnation conditions (pressure and temperature), velocity as well as areal density remains and will be discussed in the following sections.

After a short overview of common diagnostic techniques, the application of the microchannel plate detection system with retardation field at the cluster-jet target prototype with installed Laval nozzle (28 µm diameter by default) will be presented. The retardation spectrometer serves as energy or rather mass filter for the hydrogen cluster beam ionised via electron impact. Thus, the cluster mass can be investigated and the mass distribution as well as the mean cluster size in dependency of the hydrogen temperature and pressure settings can be extracted from the resulting transmission spectra.

6.1. Mass diagnostic techniques

The investigation of the average cluster size or distribution can be performed via various (non-)destructive diagnostic techniques [Pau00b], e.g. through the diffraction of electrons or atoms, the scattering of light or gas, or by spectrometric methods using deflecting or retardation fields. A selection of these diagnostic techniques will be introduced within the following sections.

6.1.1. Non destructive techniques

Diffraction with electrons or atoms

Since particles are subjected to the particle-wave duality concept, electrons or atoms can be used for the investigation of the intrinsic structure of gas molecules, clusters, or crystals.
The application of **electron diffraction** results in Debye-Scherrer diffraction patterns, which can be recorded on photographic films, imaging plates, or with a CCD camera. The analysis of the diffraction pattern, e.g. of clusters, and the comparison with computed patterns based on simplified models provides details which are impliedly related to the structure (position of interference ring), temperature (damping of crystalline lines), and average size (width of interference maxima). The measured intensity $I(q)$ is proportional to the differential cross section $\mathrm{d}\sigma/\mathrm{d}\omega$ [Pau00b] with

$$I(q) \propto q^3 \frac{\mathrm{d}\sigma}{\mathrm{d}\omega}, \tag{6.1}$$

whereas value q results from

$$q = 2\ k \sin(\theta/2) \tag{6.2}$$

with the wave number $k = 2\pi/\lambda$, the de Broglie wavelength λ, and the scattering angle θ. The differential cross section of electron diffraction by atoms is given by [Pau00b]

$$\frac{\mathrm{d}\sigma}{\mathrm{d}\omega} = \frac{4m^2e^4}{\hbar^4 q^4} \left(Z - F(q)\right)^2, \tag{6.3}$$

where m is the rest mass and e the charge of the electron, $\hbar$ reduced Planck constant, Z the nuclear charge, and the form factor $F(q)$, which considers the nucleus shielding within an atom. Moreover, the factor of ρV must be applied for the diffraction by clusters [Pau00b], which implies the target volume density ρ and the scattering volume V.

Electron diffraction with rare gas cluster beams were performed within [RF73, F$^+$81] with collimated 50 eV electron beams with a few µA and 150 µm diameter at the detection plane. Ne, Ar, Kr, and Xe (within a mixture of Xe 5 %−Ne 95 %) clusters were investigated within various nozzle diameters ($50\,\mu\mathrm{m} < d < 400\,\mu\mathrm{m}$) and stagnation conditions (inlet pressure $1\,\mathrm{bar} < p < 30\,\mathrm{bar}$, temperature $100\,\mathrm{K} < T < 400\,\mathrm{K}$). The resulting diffraction patterns were recorded on photographic plates with a rotating sector (e.g. disc or fan-type), which caused an increase of the film exposure with increasing scattering angle to compensate intensity drops. The measured diffraction patterns $I(q)$ reveal that the structure of the investigated rare gas clusters only depends on the average size $\overline{N}$ and appears in a structural sequence (amorphous $\overline{N} < 50$ atoms, icosahedral 50 atoms $< \overline{N} < 800$ atoms,

and crystalline $\overline{N} > 800\,\text{atoms}$) [F+81] and references therein.

Within **atom diffraction**, the measured differential cross sections show a characteristic scattering pattern, which enables the identification of atom-atom and atom-molecule interactions. The observed oscillations with large angular spacing point to atom-atom collisions (rainbow scattering induced by the attractive part of the interaction potential, whose potential width is larger than the particle's de Broglie wavelength), whereas oscillations with small angular distance are attributed to atom-molecule scattering (diffraction scattering induced by the repulsive part of the interaction potential) [Pau00b]. Therefore, the angular distance of the oscillation $\Delta\theta$ is related to the particle size and can be approximated by

$$\Delta\theta = \frac{\pi}{k\ r_{sp}} = \frac{\lambda}{2r_{\text{sp}}} \tag{6.4}$$

with the scattering angle θ, the wave number k, the de Broglie wavelength λ, and the sphere radius r_{sp} [Pau00b]. A more precise description of the number of oscillations provides a potential model for (neutral charged) atom-molecule or rather atom-cluster scattering, which considers quantum mechanical calculations and regards clusters as homogeneous distributed sphere. Each cluster atom ($N = 1$) interacts via a Lennard-Jones potential $V(r)$ [Pau00b]:

$$V(r) = N\frac{4\epsilon\hat{\sigma}^6}{\left(r^2 - r_G^2\right)^3}\left(\frac{\hat{\sigma}^6\left(r^6 + (21/5)r^4r_G^2 + 3r^2r_G^4 + (1/3)r_G^6\right)}{(r^2 - r_G^2)^6} - 1\right) \tag{6.5}$$

with ϵ being the well depth, the distance $\hat{\sigma}$, where the atom-atom potential is zero, $r_G = r_N - r_1$, with the cluster radius r_N and the effective radius r_1 of a cluster atom [Pau00b, BK96]. Both values are accessible via

$$r_N = \left(\frac{3m_aN}{4\pi\rho}\right)^{1/3} = N^{1/3}r_1, \tag{6.6}$$

m_a being the atom mass and ρ the density of the solid. The measured scattering patterns can be analysed through the calculation of the differential cross section

$$\frac{\mathrm{d}\sigma}{\mathrm{d}\sigma} = |f(\theta)|^2 \tag{6.7}$$

with the scattering amplitude $f(\theta)$ (more details in [BK96]).

Helium atoms are particularly well suited for the structural analysis, interacting inertly and non-destructively with a large wavelength compared to their low mass. Diffractive helium atom scattering was performed with argon clusters, e.g. within [BK96] and analysed as described above. To prepare the helium atom beam, a nozzle diameter of

30 µm was installed with a nozzle temperature and pressure of 70 K and 30 bar. The argon cluster beam was generated with plain (diameters of 50 µm and 100 µm) and conical nozzles (diameters of 100 µm and 130 µm, opening angles 20 degree and 25 degree, lengths 12 mm and 2 mm). The applied detector unit contains an electron impact ioniser with quadrupol mass filter and secondary electron multiplier. Furthermore, beam velocities were measured to obtain the collision energy, which was around 25 meV. Stagnation conditions of 300 K and 0.6 bar up to 2.9 bar lead to an average size of $\overline{N} = 6$ atoms to $\overline{N} = 90$ atoms. Moreover, the measured differential cross sections show oscillations with large spacing pointing to (He)atom-(Ar)atom scattering at scattering angles from 2 degree to 40 degree. Angles between 40 degree and 60 degree present diffraction oscillations with small angular spacing attributed to (He)atom-(Ar_N)cluster interactions. The results within this size range are in good agreement with the conclusions of other introduced techniques. On the other hand, measurements with larger average sizes $\overline{N} > 90$ atoms show discrepancies (approximately a factor of three smaller) compared to the results of electron diffraction [BK96].

Scattering of light or gas

The **scattering of electromagnetic waves** by a homogeneous sphere with size N can be completely described by the Mie theory, which provides the exact solution of Maxwell's equations within assumed boundary conditions [vdH81]. If the particle with sphere radius r_{sp} is small compared to the wavelength λ of the photon

$$n\frac{2\pi r_{sp}}{\lambda} \ll 1 \tag{6.8}$$

with index of refraction n, the differential scattering cross section is angular independent and yields Rayleigh scattering [Pau00b]:

$$\frac{\mathrm{d}\sigma}{\mathrm{d}\Omega} = \frac{8}{3}\left(\frac{2\pi r_{\mathrm{sp}}}{\lambda}\right)^4 \pi r_{\mathrm{sp}}^2 \left(\frac{n^2-1}{n^2+2}\right), \tag{6.9}$$

which is proportional to the measured scattering signal (cf. Figure 6.1 (1)). If the particle size and wavelength are comparable, the differential cross section is angular dependent (further details in [vdH81]) and therefore, the measured intensity $I(\theta)$ provides a specific and predominately forward scattering structure for a single particle (cf. Figure 6.1 (2)), which is superimposed for clusters.
The scattering intensity $I(\theta)$ of photons at hydrogen clusters were investigated within [KM72] above the critical point at 34 K, up to 35 bar with a conical nozzle (30 mm length, 1 mm throat diameter, 10 degree cone angle). Moreover, a He-Ne laser (with 632.8 nm wavelength), a fibre optical light guide, and a photomultiplier belong to the

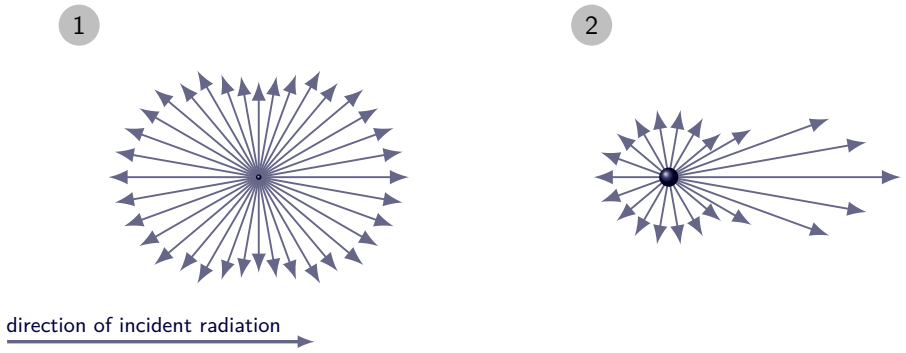

Figure 6.1.: (1) Scattering at small particles ($r_{sp} \ll \lambda$): The incident light affects an excitement of the electrons and induces a radiating dipole moment with the same frequency, known as Rayleigh scattering. (2) Scattering at large particles ($r_{sp} \approx \lambda$): Superposition of partial waves with preferred propagation in forward direction, often referred to as Mie scattering.

main components of the selected diagnostic technique. Mean cluster sizes up to 10^9 atoms were observed from the obtained cluster size distribution.
The average cluster size can also be determined through **the scattering of a cluster beam, for example within a gas**-filled target chamber. The total cross section σ_t is given by [Pau00b]

$$\sigma_t = \frac{1}{\rho L F_{a_0}} \ln(I_0/I) \tag{6.10}$$

with the initial intensity of the cluster beam (unscattered) I_0, the attenuated intensity of the cluster beam (scattered) I, the target volume density ρ, the target chamber length L, and the function F_{a_0} considering the average of the Maxwellian velocity distribution of the gas [Pau00b]. If the size distribution and the depending detection probability are known, a weighting function can also be adopted [Pau00b] and references therein.
Under the assumption that clusters can be described as spheres, the geometrical cross section σ_g takes the form [Pau00b]

$$\sigma_g = \pi r_N^2 \overset{\text{Eq.(6.6)}}{=} \pi r_1^2 N^{2/3}, \tag{6.11}$$

leading with $\sigma_t = \sigma_g$ to

$$N = \left(\frac{\ln(I_0/I)}{\rho L F_{a_0} \pi r_1^2} \right)^{3/2}, \tag{6.12}$$

where N corresponds to the average cluster size $\overline{N}$ [Pau00b].

Furthermore, various analysis methods can be applied to determine the cluster size and size distribution via gas scattering (within a target chamber or in crossed beam experiments), concentrating on the velocity loss, the broadening of beam profiles, the cross section for

capture, or collisional beam deflection. Even the size selection via gas scattering at certain conditions is possible and more details can be extracted from [Pau00b] and references therein.

6.1.2. Destructive techniques

Mass spectrometry with deflecting or retardation field

First insights into the mass distribution of clusters were provided within the investigation of ionised clusters and their mass spectrometric analysis, e.g. with deflecting or retardation fields. The mass selection through an electrical deflecting field $E(r)$ with orbit radius r_0 (e.g. in Figure 6.2) directly yields [BV64]

$$m = \frac{r_0 Z}{v^2} E(r) \tag{6.13}$$

with m and v beeing the particle's or cluster's mass and velocity with charge Z, whereas an electrical retardation field (cf. Figure 6.4) with voltage U gives

$$m = \frac{2ZU}{v^2}. \tag{6.14}$$

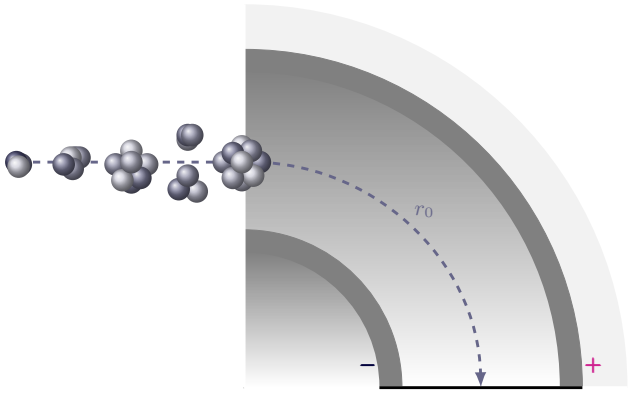

Figure 6.2.: Schematic illustration of a sector field mass analyser with electrical deflecting field $E(r)$, affecting the flight path of positive charged particles or clusters.

It should be emphasised, that the ionisation of the clusters via electrons or photo ionisation causes the fragmentation of the clusters, resulting in a distorted mass distribution compared to the distribution of the initial neutral clusters, which has to be considered. Initial measurements with an electrical retardation field ($< 200\,\mathrm{V}$) and CO_2 clusters were performed with an ionisation detector in [BH65]. Convergent nozzles with diameters of 0.05 mm and 0.81 mm were investigated at room temperature and with pressures up to 34 bar. Average cluster sizes $\overline{N}/Z$ from 50 to 2000 were captured. Furthermore, $\overline{N}/Z$ increases with increasing stagnation pressure, which in turn varies inversely with the

nozzle diameter. For example $\overline{N}/Z = 2000$ was achieved with 0.81 mm nozzle diameter at 7 bar stagnation pressure or via 0.05 mm nozzle diameter at 34 bar.

Every diagnostic technique demonstrates its advantages, whether in gaining insights into average size or details on the size distribution with appropriate assumptions, in the availability of calculations for the data analysis, or through the feasible and straightforward implementation into the existing experimental setup. However, only the comparison of data gained from various methods allows for accurate and realistic conclusions on the mass or size distribution of a cluster-jet beam. Thus, to obtain insights into the mass distribution of the hydrogen cluster-jets with regard to the $\overline{\text{P}}$ANDA experiment, two different approaches will be initially performed. The first technique comprises the implementation of a mass spectrometer with retardation field (destructive method) at the target prototype for $\overline{\text{P}}$ANDA, which is emphasised in this thesis. This method directly provides the mass distribution of an ionised cluster beam and a lower limit for the average cluster size within the vapour area. Secondly, the size analysis via Mie scattering (non-destructive method) will be performed at the final cluster-jet target for $\overline{\text{P}}$ANDA, especially in the fluid area within [Her15]. Both methods will lead to further insights into the complex cluster production processes and the coherent mass distribution.

6.2. Cluster mass spectrometry with retardation potential

In order to investigate the mass distribution of hydrogen cluster-jets of the target prototype for $\overline{\text{P}}$ANDA with a Laval nozzle, a mass spectrometer with retardation field was selected, which belongs to the destructive mass diagnostic techniques. Based on the gradual retardation and detection of an ionised cluster-jet beam, the analysis of the resulting transmission spectra yields the mass distribution and average cluster size depending on the stagnation conditions at the cluster production. Details on the analysis and the resulting mass distribution will follow after an overview of the experimental setup.

6.2.1. Experimental setup (extended spectrometer version)

The basic principle of operation focuses on the ionisation, gradual retardation, and detection of the cluster-jet beam. Figure 6.3 presents the schematic overview of the MicroChannel Plate (MCP) detection system, which was extended through a retardation section and was further on installed at the end of the target's beam dump (cf. Figure 6.5). The applied cryopumps at the beam dump (cf. Figure A.5) were substituted by several turbomolecular pumps as foreseen for the beam dump at the $\overline{\text{P}}$ANDA experiment. With this arrangement no further regeneration phases must be conducted at equal vacuum pressures. The updated vacuum design as well as the table of installed vacuum pumps are attached in Appendix A.1.

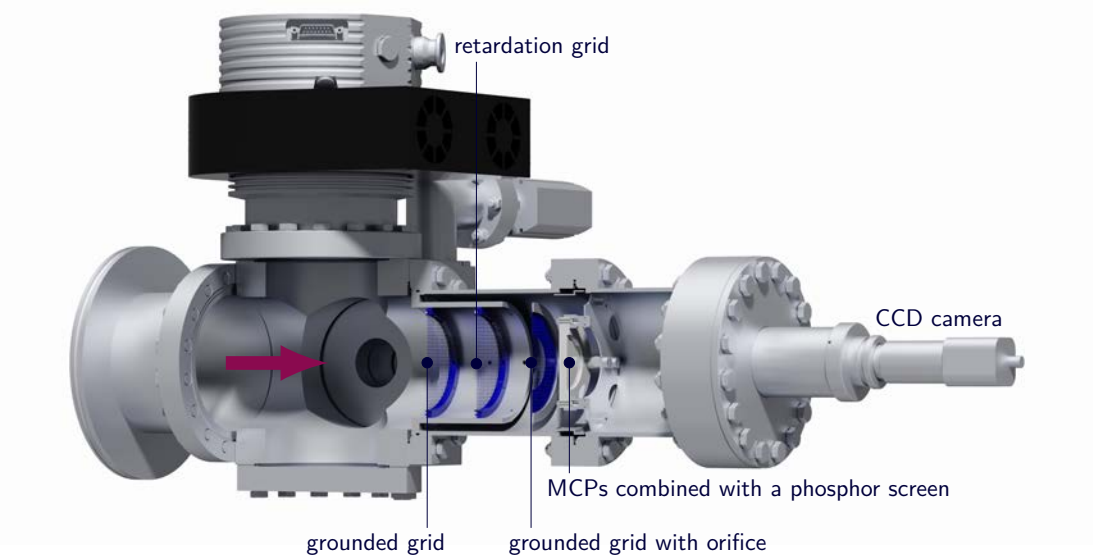

Figure 6.3.: MicroChannel Plate (MCP) detection system with included retardation section (generated by D. Bonaventura with Autodesk Showcase, edited). The violet arrow presents the cluster beam direction.

The ionisation of the hydrogen clusters occurs via electron impact generated by an electron gun (cf. Figure 6.5). For the installation, it must be considered that an excessive flight path (e.g. 4 m) would induce a significant reduction of light clusters due to slight deflecting fields of the installed turbomolecular pumps. On the other hand, an overly close installation of the electron gun to the MCPs (e.g. 0.2 m) would cause an increase of the background (residual gas ionisation). Hence, the electron gun position was verified and finally installed around 1 m from the MCP detector (cf. Figure 6.4). The electron gun contains an axial filament with maximal 10 W and 12 V (Philips 40970650), which is enclosed by a counter electrode with maximal −200 V. For a pulsed mode, an extraction aperture with positive potential can be conducted.

A grid with positive retardation potential enclosed by two identical grounded grids with 2.7 mm lattice spacing (center-to-center) are located in between the ion's flight path, to ensure almost even lines of the electric flux. The potential can be gradually increased up to 4 kV (via a Heinzinger voltage source, controlled by miniLAB 1008), whereas voltages above 4 kV induce discharges at the retardation grid. This effect would superimpose the observed intensity of the ionised cluster-jet beam, which is the most essential parameter for the determination of the cluster mass distribution. The last grid is equipped with an orifice of 35 mm diameter.

The MCPs and the phosphor screen are operated as described in Section 5.3.3. First and second MCP are connected via voltage divider (2:1) and conducted at −3 kV and −1.5 kV, whereas the phosphor screen runs at 2.2 kV by default, as specified by the manufacturer and verified within [Zan13].

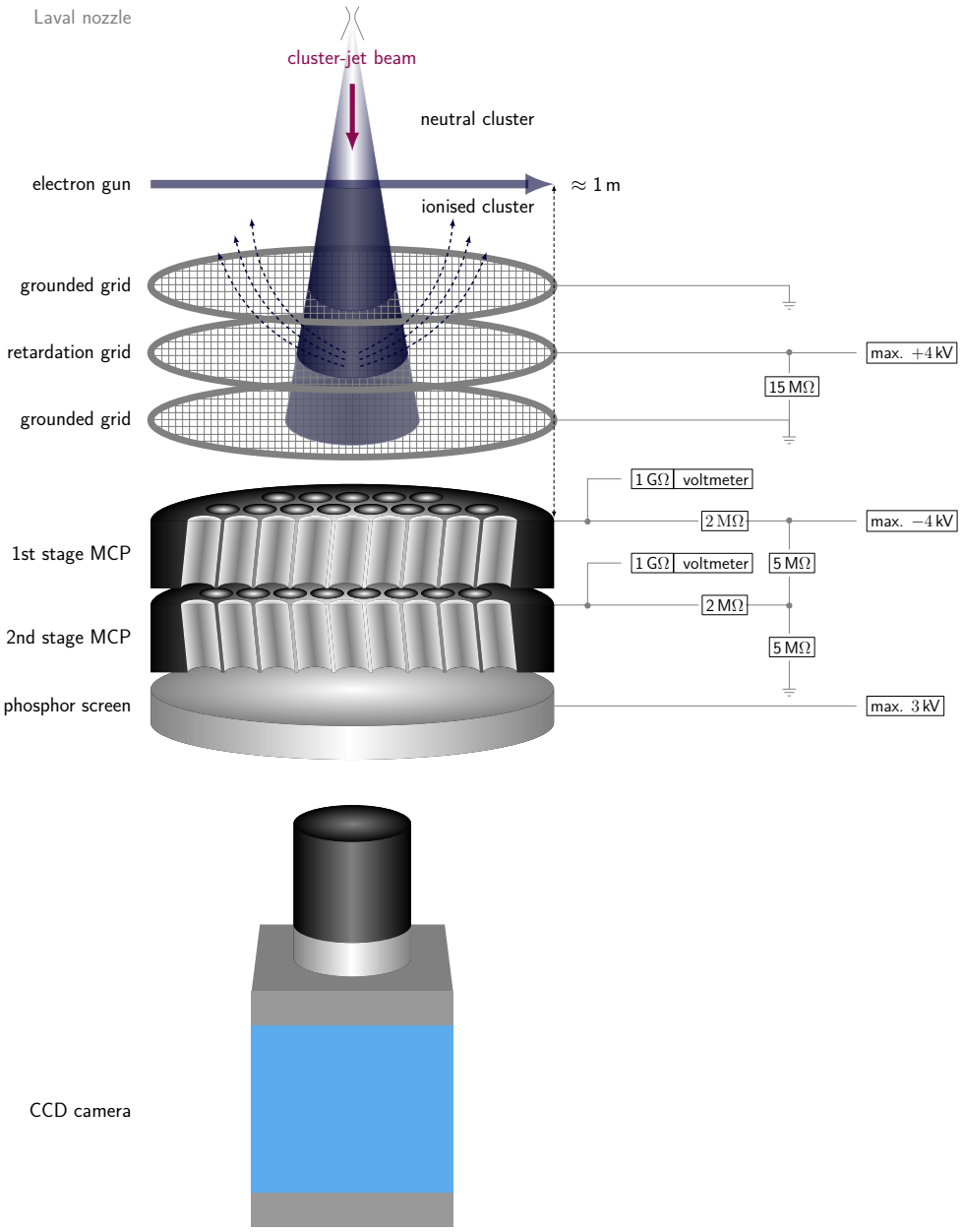

Figure 6.4.: Schematic overview of the mass spectrometer and wiring scheme of the installed MCP detection system including retardation section (extended spectrometer version). Cluster beam direction from top to bottom.

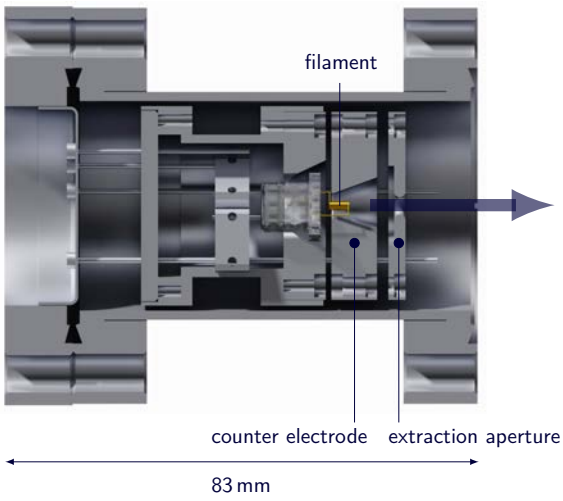

Figure 6.5.: Electron gun with axial filament and counter electrode (generated by D. Bonaventura with Autodesk Showcase, edited). The extraction aperture can be operated for a pulsed mode. The blue arrow presents the electron beam direction.

6.2.2. Ion trajectory simulation

Simulations of the retardation spectrometer with schematical grid dimensions were performed with SIMION 3D 7.0 to gain more insights into the flight paths of the ionised clusters and possible background effects. A sectional view of the spectrometer setup is presented in Figure 6.6 with the following components: (a) grounded grid, (b) retardation grid, (c) grounded grid with orifice, and (d) MCP detection system. Within the simulations the MCPs and the phosphor screen are lying at $-3\,\mathrm{kV}$, $-1.5\,\mathrm{kV}$, and $2.2\,\mathrm{kV}$ potential. An ion velocity of $1200\,\mathrm{m/s}$ on average was assumed, which corresponds to the maximal cluster velocity within the selected field of investigation at stagnation conditions in the vapour area (more details in Section 6.2.5). The ion mass was varied up to maximal 10^5 atoms, which can be handled effortlessly with the available retardation field (maximal $U_{\mathrm{red}} = 4\,\mathrm{kV}$). Moreover, the ion (or cluster) charge, mass, and energy assumed within these simulations are denoted with Z_{ion}, m_{ion}, and E_{ion}. The presented simulations concentrate on:

- negatively charged heavy ions (10^5 atoms)
  (without retardation field, cf. Figure 6.7)
- comparison between positively charged light (< 1000 atoms) and heavy (10^5 atoms) ions (without retardation field, cf. Figure 6.8 (1) and (2)) and the influence of an orifice within the last grid (without retardation field, cf. Figure 6.8 (3) and (4))
- positively charged light (< 500 atoms) ions with $\pm 1\,\mathrm{V}$ retardation potential
  (cf. Figure 6.9 and 6.10).

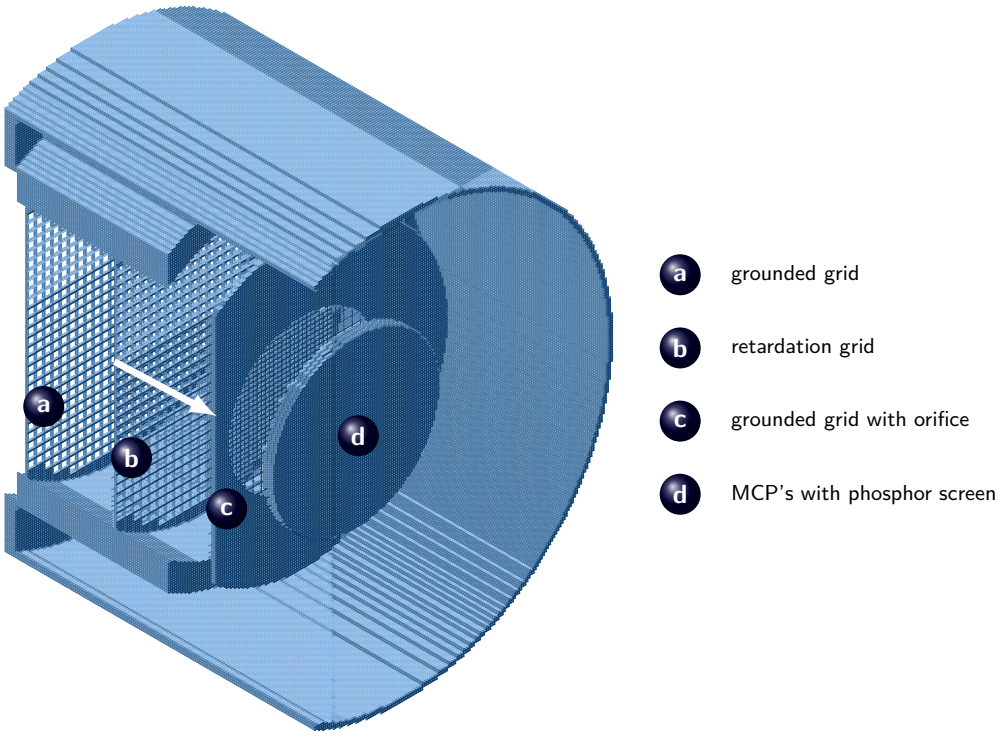

Figure 6.6.: Simulation of the retardation spectrometer with schematically grid dimensions via SIMION 3D 7.0. MCPs and phosphor screen are conducted to −3 kV, −1.5 kV, and 2.2 kV. The ion flight direction is denoted with a white arrow.

The applied voltage at the first MCP of −3 kV assures thus the detection of almost only positively charged ions, since negatively charged ions with an energy below 3 kV are reflected (cf. Figure 6.7). On the other hand, light positive ions (with e.g. <1000 atoms and 5 eV) are strongly attracted from the −3 kV potential of the MCP and focussing effects can occur as demonstrated in Figure 6.8 (1), simulated without orifice. Moreover, heavy positively charged ions (with e.g. 10^5 atoms and 750 eV) are rejected from the following 2.2 kV potential of the phosphor screen at the peripheral areas (cf. Figure 6.8 (2)). To minimise both effects, an orifice was implemented, which leads to a significant reduction of focussed ions above 5 eV (more than 40 %) and a complete suppression of rejected heavy ions (cf. Figure 6.8 (3) and (4)).

With increasing mass, the amount of focussed ions decreases and completely disappears below an energy of 200 eV. Therefore, this setup shows its highest accuracy at retardation potentials ≥ 200 V within the expected transmission spectra. Increasing the retardation potential up to 4 kV in steps of 200 V ensures a precise data acquisition, except for the intensity at 0 V potential with an estimated uncertainty of maximal 10 %. To gain the accurate proportion of light clusters, an improved setup must contain orifices at each

grid, additional pumping sections, and a very precise and stable voltage source. Already small deviations of $\pm 1\,\mathrm{V}$ could cause an increase of the originated total intensity. At $-1\,\mathrm{V}$, light clusters are increasingly focussed and additionally contribute to the total intensity (cf. Figure 6.9). At $+1\,\mathrm{V}$, clusters at the peripheral areas could cause additional signals (cf. Figure 6.10). These variations are unobjectionable for the measured data at retardation potentials $\geq 200\,\mathrm{V}$, because light clusters are already reflected and cannot add additional signals to the measured intensity.

This setup concentrates on the first access to the mass distribution of ionised hydrogen clusters, produced via a Laval nozzle within the vapour area, and enables insights into the average cluster mass. The analysis and interpretation of the measured transmission spectra will be discussed in the next section. Further investigations will follow within [Her15] via Mie scattering, which belongs to the non-destructive methods, in the vapour and especially in the fluid area. With the results of both independent methods, a realistic and precise mass distribution and average cluster size can be found.

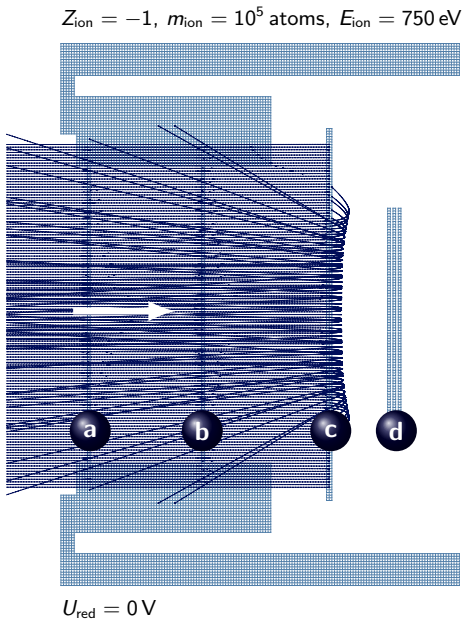

Figure 6.7.: Simulation of the retardation spectrometer and the ion flight path of negatively charged ions containing 10^5 atoms with 750 eV (without retardation field $U_{\mathrm{red}} = 0$) via SIMION 3D 7.0. The notation corresponds to the following components: (a) grounded grid, (b) retardation grid, (c) grounded grid with orifice, and (d) MCP detection system as introduced in Figure 6.6. Negatively charged ions with an energy below 3 kV are reflected through the MCP potential of $-3\,\mathrm{kV}$.

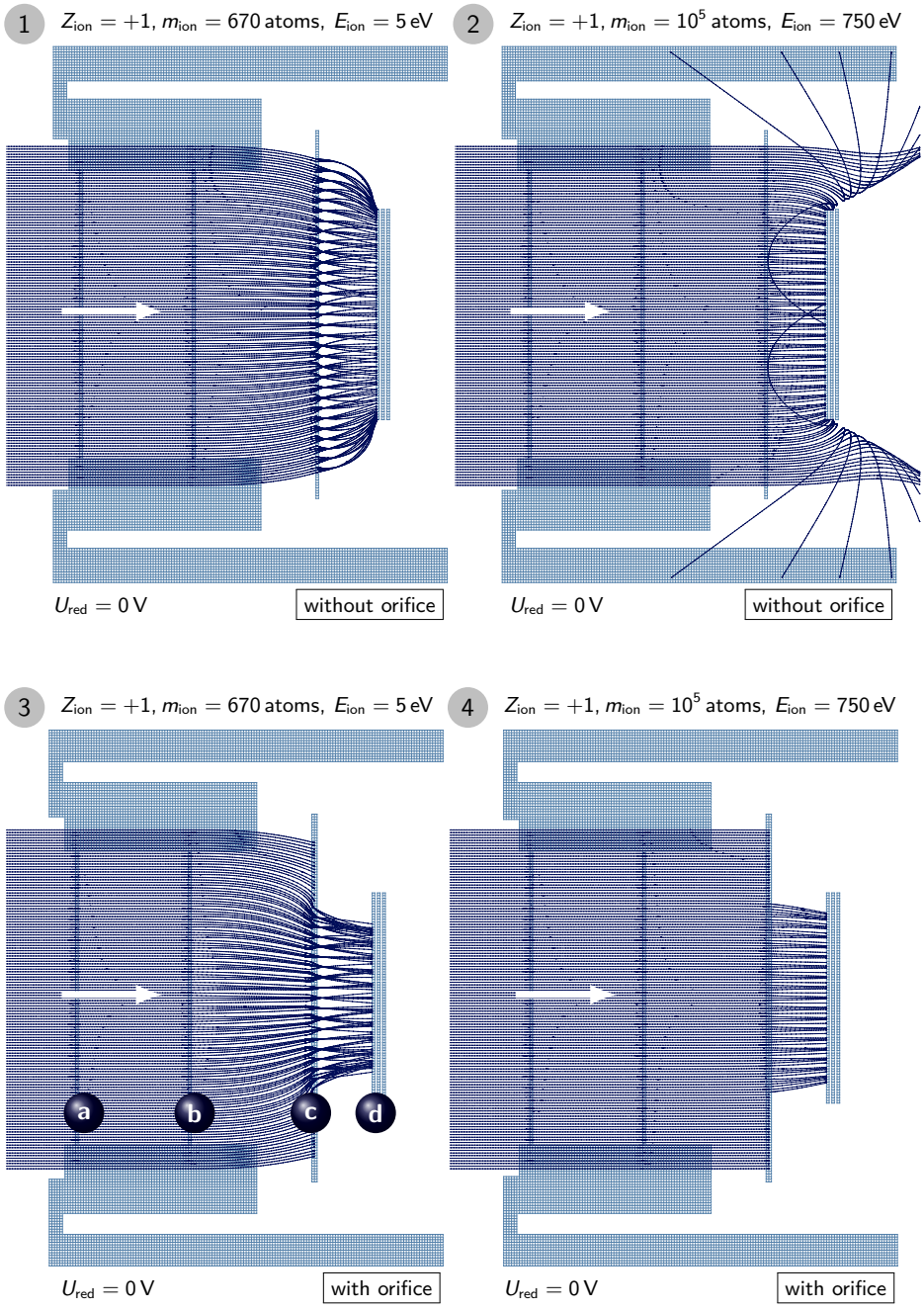

Figure 6.8.: Simulation of the retardation spectrometer and the ion flight path without retardation field via SIMION 3D 7.0. The notation corresponds to the following components: (a) grounded grid, (b) retardation grid, (c) grounded grid with orifice, and (d) MCP detection system. MCPs and phosphor screen are operated at −3 kV, −1.5 kV, and 2.2 kV. Image (1) and (2) show the flight path of positively charged ions (without orifice) containing either 670 atoms or 10^5 atoms with a velocity of 1200 m/s, which corresponds to an energy of around 5 eV and 750 eV, respectively. Light positive ions were strongly attracted from the −3 kV potential of the MCP and heavy positively charged ions were rejected from the following 2.2 kV potential of the phosphor screen at the peripheral areas. Image (3) and (4) presents the flight path of the ions with installed orifice minimising both effects.

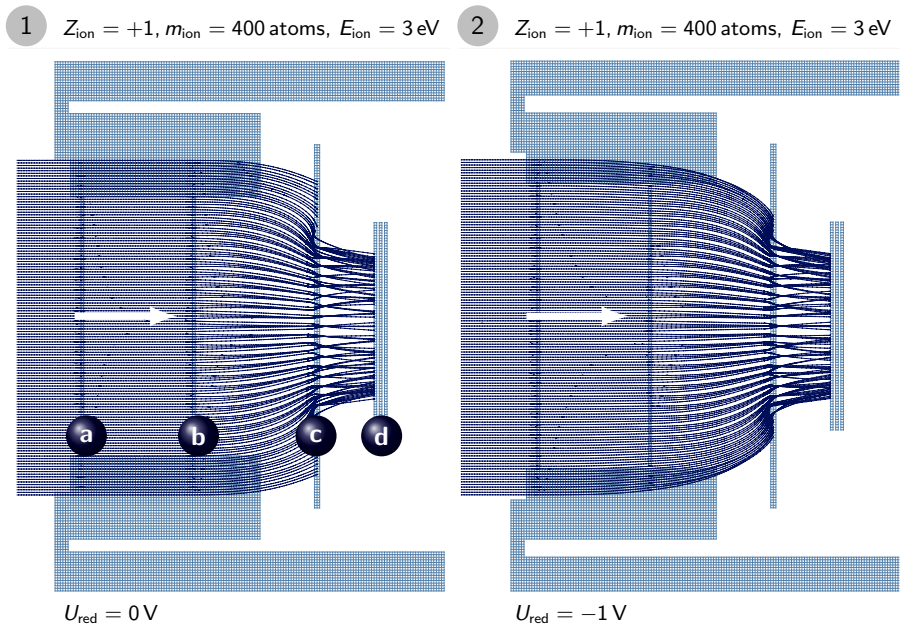

Figure 6.9.: Simulation of the retardation spectrometer and the ion flight path of positively charged light ions (3 eV, velocity of 1200 m/s) and varying retardation potential (0 V, −1 V) via SIMION 3D 7.0. The notation corresponds to the following components: (a) grounded grid, (b) retardation grid, (c) grounded grid with orifice, and (d) MCP detection system. The focussing of ions is presented in (1) with around 400 atoms with 3 eV (without retardation field, around 25 % additional signals) and in (2) with around 400 atoms with 3 eV (with −1 V retardation potential, around 35 % additional signals).

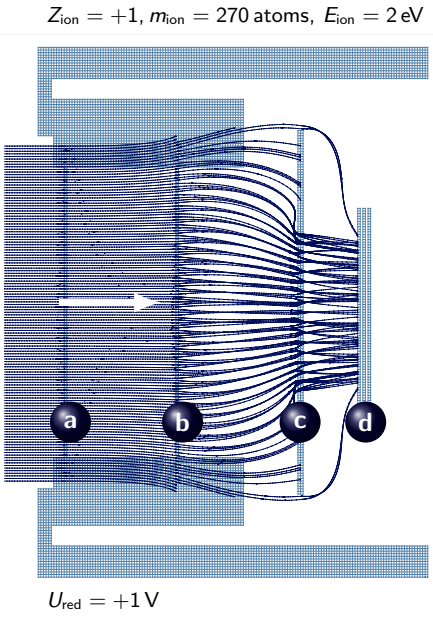

Figure 6.10.: Simulation of the retardation spectrometer and the ion flight path of positively charged light ions (2 eV, velocity of 1200 m/s) and 1 V retardation potential via SIMION 3D 7.0. The notation corresponds to the following components: (a) grounded grid, (b) retardation grid, (c) grounded grid with orifice, and (d) MCP detection system. Additional signals are induced by ions at the peripheral area with around 270 atoms with 2 eV (with +1 V retardation potential).

6.2.3. Transmission spectra and mass distribution

The determination of the cluster mass distribution and average cluster size occur via the analysis of the recorded cluster beam images in dependency of the retardation potential. Therefore, the total beam image intensity presents the most crucial parameter and results from the amount of each pixel intensity (cf. Figure 6.11). In the scope of the mass measurements within the vapour area, which is characterised by the condensation production process, the beam images already indicate mass differences in contrast to cluster formed within the fluid area via fragmentation. Cluster beam images within the fluid area show high intensity with defined contours (cf. Figure 5.50, left), whereas images within the vapour area appear faded and smeared out. Within the vapour area, the flight path of ionised clusters with around 10^5 atoms is influenced by slight deflecting fields of the installed turbomolecular pumps compared to clusters of the fluid area with most likely more than 10^9 atoms [KM72]. The influence of the different cluster production processes (condensation vs. fragmentation) was already apparent within the velocity and density measurements (cf. Chapter 5).

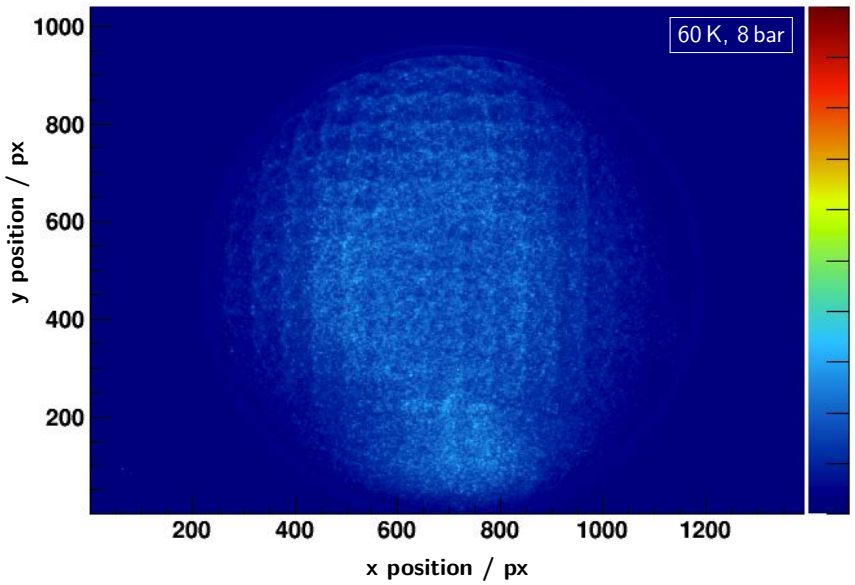

Figure 6.11.: Analysed MCP-image at 60 K, 8 bar with 5 s exposure time. The data is based on the recorded monochrome image with (1392 × 1024) px. The colour code represents the intensity in arbitrary unit.

The increase of the retardation potential results in a decrease of total beam image intensity and the analysis yields a characteristic transmission spectrum, which is exemplary presented in Figure 6.12 for 60 K and 8 bar (vapour area). Each spectrum at specific stagnation conditions was performed twelve times to identify systematic uncertainties

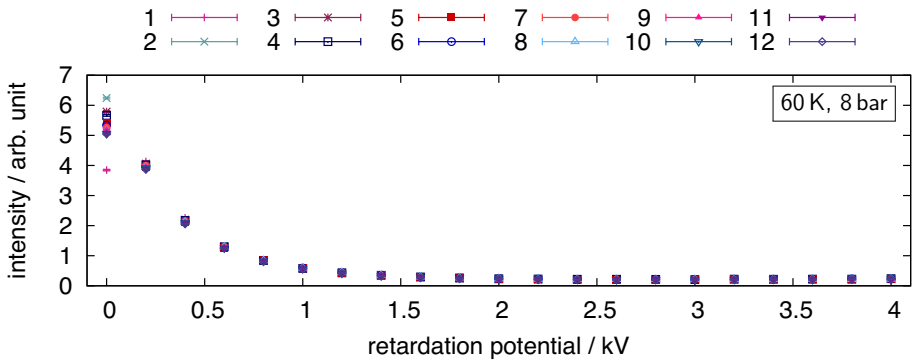

Figure 6.12.: Transmission spectrum at 60 K and 8 bar, repeated twelve times. The measured intensities are reproducible apart from the intensity at 0 V, which mirrors the temporal enhancement of the accuracy of the applied voltage source (induced by the intrinsic components and their temperature dependency).

of the complete setup. The retardation potential was gradually increased up to 4 kV at every run (in steps of 200 V) and after each step subsequently decreased down to 0 V (i.e. 0 V, 200 V, 0 V, 400 V, 0 V, 600 V, etc.). Possible charging effects can be avoided with this procedure (waiting period: 20 s, exposure time: 5 s, measuring time for each stagnation condition: ≈ 4.5 h).

As expected, all measured spectra show a high reproducibility of the resulting intensity, except for intensities at supposedly 0 V potential. The fluctuations are induced by the voltage source and in all likelihood light clusters (e.g. < 500 atoms). As shown with ion tracking simulations in the previous Section 6.2.2, already small deviations of ± 1 V could cause an increase of the total intensity. At -1 V, light clusters are increasingly focussed and at $+1$ V, clusters at the peripheral areas could cause additional signals (cf. Figure 6.10). Test measurements with a grounded retardation grid demonstrate no further intensity fluctuations and only mirror the stability of the cluster beam and the electron gun (see Appendix A.7), which is better than 5 %. Moreover, the development of charged clouds, charge reversal effects, or reflections and a multiplied detection can be excluded and would appear within the entire spectra. However, the accuracy of the voltage source enhances temporally (induced by the temperature dependency of the intrinsic components) and the first measurement runs were thus not considered for the analysis.

The background is linearly subtracted and mainly composed of a constant camera noise and the signal noise of the MCP detection system. Neutral clusters (without operating electron gun) as well as the ionisation of the residual gas (without cluster beam) show no significant contribution. Each spectrum is then normalised to the 0 V potential (cf. Figure 6.13).

A conventional approach to describe mass or size distributions represents the log-normal distribution $f(x, \mu, \sigma)$:

$$f(x, \mu, \sigma) = \frac{1}{x\sigma\sqrt{2\pi}} \exp\left(\frac{(\ln(x) - \mu)^2}{2\sigma^2}\right), \tag{6.15}$$

where the parameters $\mu \in \mathbb{R}$ and $\sigma > 0$ are known as location and scaling parameter [SJ64]. Contrary to the normal distribution, which describes additive processes of random variables, the log-normal distribution characterises a multiplicative product of positive, random variables, whose logarithm is then again normally distributed. Thus, the log-normal distribution is an appropriate model for many growth processes, especially for the particle size distribution, and consequently considered in the following analysis.

The transmission spectrum can be adapted via

$$t(x, \mu, \sigma) = 1 - F(x, \mu, \sigma), \tag{6.16}$$

whereas $F(x, \mu, \sigma)$ is the Cumulative Distribution Function (CDF) of the log-normal distribution (cf. Figure 6.13) with [SJ64]

$$F(x, \mu, \sigma) = \frac{1}{2}\left(1 + \operatorname{erf}\left(\frac{\ln(x) - \mu}{\sigma\sqrt{2}}\right)\right). \tag{6.17}$$

The correlated parameters μ and σ yield the assumed Probability Density Function (PDF also known as frequency function) of the log-normal distribution (cf. Equation 6.15), which corresponds to the cluster mass distribution (cf. Figure 6.14, top).

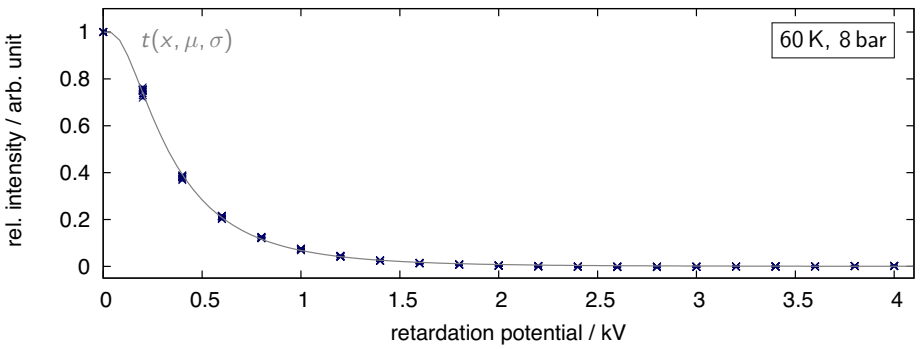

Figure 6.13.: Normalised transmission spectrum at 60 K and 8 bar with adapted Cumulative Distribution Function (CDF) of the log-normal distribution (cf. Equation (6.17)).

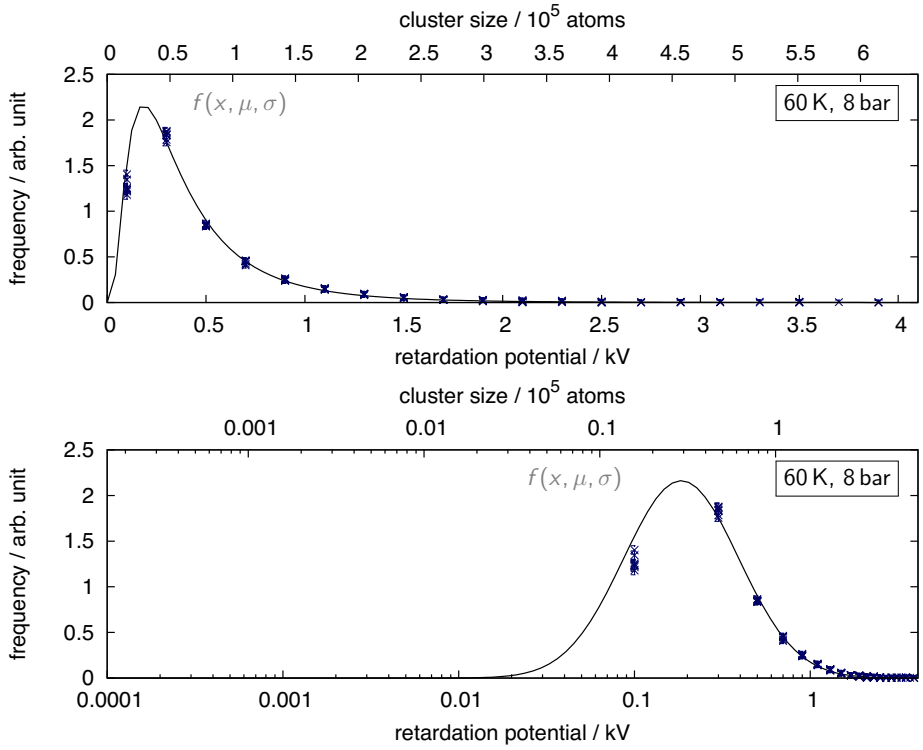

Figure 6.14.: Cluster mass distribution which can be described with the Probability Density Function (PDF or frequency function, cf. Eq. 6.15) of a log-normal distribution (top). The logarithm of this distribution is then again normally distributed (bottom).

The arithmetic mean $\tilde{\mu}$ and standard deviation $\tilde{\sigma}$ can be gained from

$$\tilde{\mu} = \exp\left(\mu + \frac{\sigma^2}{2}\right) \tag{6.18}$$

$$\tilde{\sigma} = \sqrt{(\exp(\sigma^2) - 1)(\exp(2\mu + \sigma^2))}. \tag{6.19}$$

With Equation 6.14 and under the assumption of single charged ($Z = 1$), positive clusters, the average atomic cluster size results in the order of 10^4 atoms at 60 K, 8 bar.

6.2.4. Commissioning measurements

Initial test measurements focussed the operating parameters of the setup which must ensure a sufficient intensity within the entire range of the mass measurement programme (cf. Section 6.2.5). On the one hand, the intensity must be high enough for an adequate separation from the background and on the other hand, an overexposure of the recorded images must be prevented. Measurements within the vapour, supercritical fluid, and fluid area demonstrate significant effects especially in the vapour area, which was therefore selected as a field of investigation.

Commissioning reveals a voltage of $-3\,\mathrm{kV}$ and thus $-1.5\,\mathrm{kV}$ of the MCPs as well as an filament current of $0.57\,\mathrm{A}$ with an electron energy of $150\,\mathrm{eV}$ of the electron gun with an exposure time of $5\,\mathrm{s}$. Moreover, the cluster beam extraction was adjusted to the highest density (nozzle orientation = 0). These parameters were further verified, in particular with regard to the cluster mass distribution within the following measurements. The presented average cluster sizes at each parameter setting result from the analysed transmission spectra (repetition: 12 times, measuring time: $\approx 4.5\,\mathrm{h}$), as exemplary described in Section 6.2.3 under the assumption of single charged, positive clusters. Systematic uncertainties around $10\,\%$ are expected, mainly induced by the stability of the cluster-jet beam and the electron gun (around $3\,\%$ within stagnation conditions in the vapour area) and the variation of the total intensity at $0\,\mathrm{V}$ retardation potential, where the setup shows its highest sensitivity (maximal $10\,\%$).

MCP properties

To investigate the efficiency stability of the MCP detector in dependency of the gain, the operating voltage was modified as follows:

- MCP voltage: variation between $-3000\,\mathrm{V}$ and $-2600\,\mathrm{V}$ at $\boxed{60\,\mathrm{K},\ 8\,\mathrm{bar}}$
  - electron gun: $0.57\,\mathrm{A}$ filament current and energy $150\,\mathrm{eV}$
  - phosphor screen: $2.2\,\mathrm{kV}$.

The first and second MCP are connected via a voltage divider (2:1) and the variation of the potential simultaneously affects both. Figure 6.15 shows the resulting mean cluster size at $60\,\mathrm{K}$, $8\,\mathrm{bar}$ in dependency of the first MCP voltage or gain, respectively. On average, a mean cluster size of $(0.65 \pm 0.02) \times 10^5$ atoms can be determined and no further efficiency variations were evident. At voltages above $-2600\,\mathrm{V}$, the background dominated. Operating voltages below $-3000\,\mathrm{V}$ would reduce the MCP's lifetime according to the manufacturer. Unless otherwise indicated, the MCPs are operated at $-3\,\mathrm{kV}$ and $-1.5\,\mathrm{kV}$ by default.

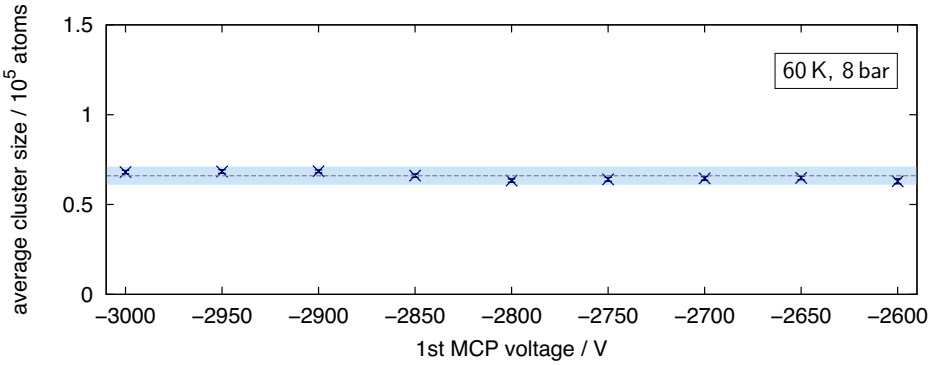

Figure 6.15.: Variation of the MCP potential at 60 K, 8 bar in dependency of the mean cluster size, which is on average $(0.65 \pm 0.02) \times 10^5$ atoms. The blue area denotes the systematic uncertainty interval of 10 % around the mean value.

Influence of electron gun parameter

Moreover, the change of the filament current and/or electron energy could have an impact on the mass distribution. Particularly, the electron energy could induce the fragmentation of clusters [Pau00b] and thus influence the resulting mass distribution. The following variations of the parameter settings were investigated:

- filament current: variation between 0.45 A and 0.61 A at 60 K, 8 bar
  - electron gun: electron energy 150 eV
  - MCPs: −3 kV and −1.5 kV
  - phosphor screen: 2.2 kV
- electron energy: variation between 80 eV and 170 eV at 60 K, 8 bar
  - electron gun: 0.57 A filament current
  - MCPs: −3 kV and −1.5 kV
  - phosphor screen: 2.2 kV.

The variation of both parameters is presented in Figure 6.16 and shows no systematic influence on the average cluster size. To gain a sufficient intensity, the filament current and energy were set to 0.57 A and 150 eV by default. The stability of clusters within the selected vapour area and the amount of fractured clusters will be revealed through the investigation via the non-destructive Mie scattering technique in [Her15].

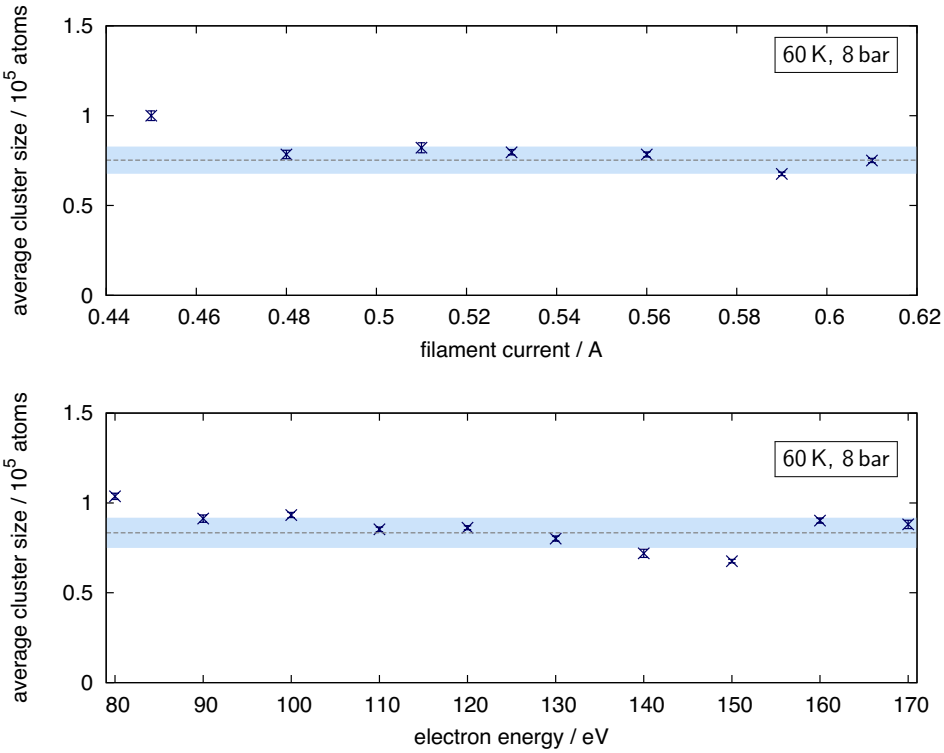

Figure 6.16.: Modification of the filament current (top) and energy (bottom), showing no further systematic influence on the mean cluster size, which is on average $(0.75 \pm 0.09) \times 10^5$ atoms and $(0.83 \pm 0.1) \times 10^5$ atoms. The blue area denotes the systematic uncertainty interval of 10 % around the mean value.

Cluster beam extraction

The influence of the nozzle orientation was investigated at 70 K, 9 bar. Within these stagnation conditions, the cluster-jet beam is expected to be homogeneous. The adjustment of the nozzle tilting system occurs via:

- nozzle orientation: variation between −1.1 degree and +1.5 degree at 70 K, 9 bar
  - electron gun: 0.57 A filament current and energy 150 eV
  - MCPs: −3 kV and −1.5 kV
  - phosphor screen: 2.2 kV.

Figure 6.17 (top) shows a decrease of the average cluster size with increasing angle. On the one hand, an inhomogeneous mass distribution within the beam could be responsible for this effect. However, the conducted density measurements (cf. Figure 5.30) point more likely to a homogeneous cluster beam with a density decrease at the peripheral areas

of the beam. On the other hand, the decrease could be induced by the fragmentation of clusters within their flight path due to interferences with orifices and beam pipes (around 5 m). Systematic studies on the mass distribution, including the influence on the nozzle orientation, will be performed at the final cluster-jet target for $\overline{\text{P}}$ANDA via Mie Scattering [Her15]. The adjustment of the nozzle orientation is required at the highest density and a horizontal orientation (0 degree) was thus selected by default (cf. Figure 6.17, bottom). The final parameter settings and target conditions for the following cluster mass measurement programme, which will be discussed in the next section, are summarised in Table 6.1.

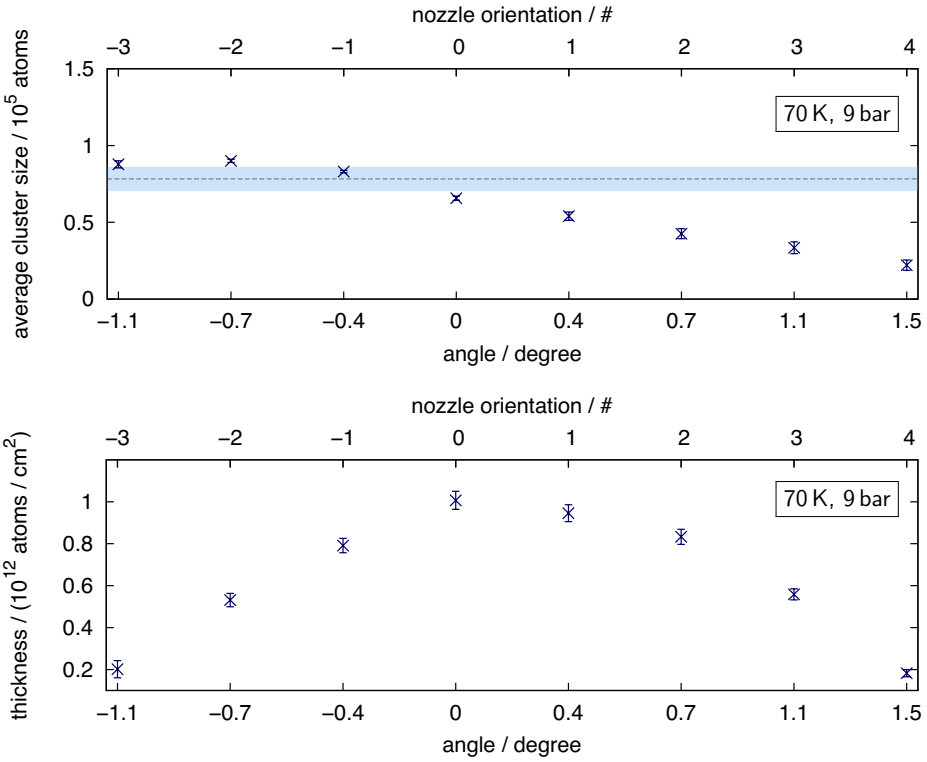

Figure 6.17.: Variation of the nozzle orientation depending on the average cluster size at 70 K, 9 bar (top) and the corresponding target thickness at the interaction chamber (bottom) resulting from its monitoring system (cf. Figure 4.12). The blue area denotes the systematic uncertainty interval of 10 % around the mean value.

Spectrometer settings	
1st MCP	−3 kV
2nd MCP	−1.5 kV
phosphor screen	2.2 kV
filament current	0.57 A
electron energy	150 eV
exposure time	5 s
Target conditions	
nozzle orientation	0
collimator diameter	0.5 mm & 0.7 mm

Table 6.1.: Parameter settings of the retardation spectrometer and target conditions within the cluster mass measurement programme (cf. Section 6.2.5).

6.2.5. Mass measurement programme

The presented retardation spectrometer serves as energy or mass filter and allows the detection of positively charged clusters, which can be reflected up to an energy of 4 keV. A step size of 200 V ensures a precise data acquisition, except for the total intensity at 0V potential with an uncertainty below 10 % (cf. Figure 6.12). The inaccuracy is primary induced through additional signals of light focussed clusters (most likely below 500 atoms) as discussed in Section 6.2.2. The stability of the cluster beam (within stagnation conditions in the vapour area) and the electron beam yields additional systematic uncertainties below 5 %, whereas commissioning measurements reveal no further systematic effects of the detector and electron gun parameters (cf. Section 6.2.4). Under the assumption of a homogeneous cluster-jet beam, the beam extraction was adjusted to the highest density. In summary, the presented retardation spectrometer allows a cluster mass determination within systematic uncertainties of approximately 10 %.

The measurement programme concentrates on stagnation conditions within the vapour area at the isobars (cf. Figure 6.18):

1. at 7 bar between 46 K and 80 K, in steps of 1 K
2. at 8 bar between 46 K and 80 K, in steps of 1 K
3. at 9 bar between 46 K and 80 K, in steps of 1 K
4. at 10 bar between 46 K and 80 K, partly in steps of 1 K and 2 K.

Each parameter setting was measured twelve times within a measurement time of around $\approx 4.5\,\mathrm{h}$ under the listed parameter settings and conditions in Table 6.1. The cluster mass distribution results from the analysis of the measured transmission spectra, which agrees well with the conventional approach of a log-normal distributed cluster mass. Assuming single positive charged clusters with $Z = 1$, the log-normal distribution was adapted for the present analysis (cf. Section 6.2.3). Moreover, the required velocity at each stagnation condition to assign each retardation potential to a cluster mass m (cf. via Equation (6.14)) or atomic size N (with $1\,\mathrm{u} = 1.66 \times 10^{-27}\,\mathrm{kg}$ [oSN]) was extracted from the model calculation of a quasi-one-dimensional flow [Tä12, T$^+$13] (cf. Section 5.1.3). Within this mass measurement programme, mean velocities between 950 m/s and 1200 m/s occur. Figure 6.19 presents the calculated velocities of the selected isobars (7 bar to 10 bar) in dependency of the temperature (46 K to 80 K). As expected, the velocity increases with increasing temperature and within an isotherm the velocity is almost constant (cf. [Köh10, Tä12, T$^+$13]).

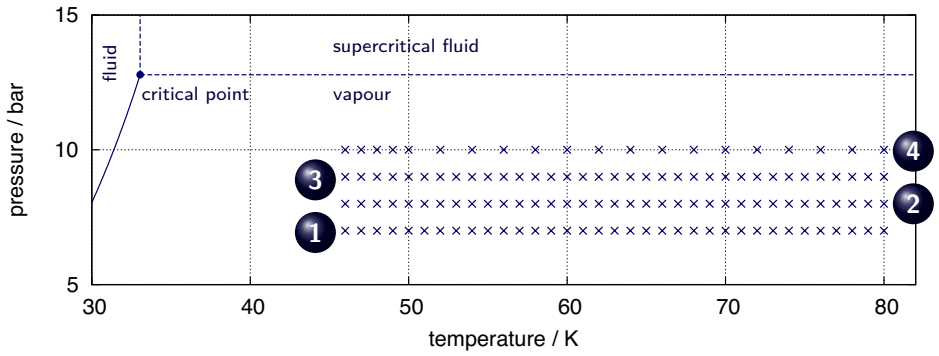

Figure 6.18.: Hydrogen vapour pressure curve in dependency of the temperature, where the critical point (33.145 K, 12.964 bar [L$^+$09]) is marked by a dot. The individual stagnation conditions within the mass measurement programme are labelled with blue crosses, whereas the isobars are numbered.

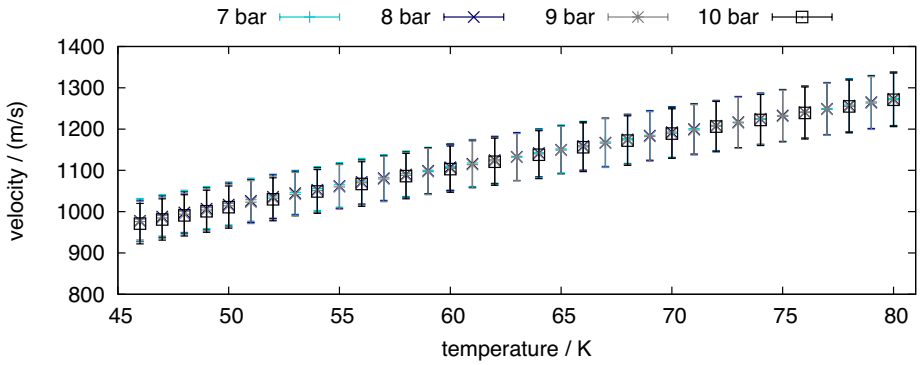

Figure 6.19.: Calculated mean cluster velocities with regard to the investigated stagnation conditions, based on the model calculation of a quasi-one-dimensional flow [Tä12, T$^+$13].

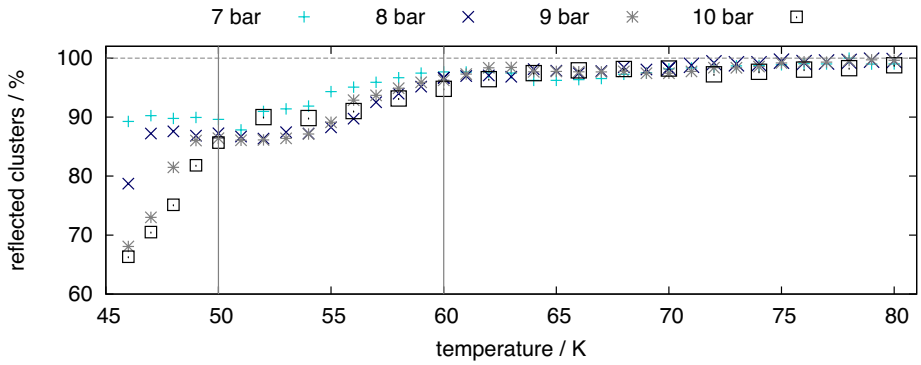

Figure 6.20.: Total amount of reflected clusters with a maximal retardation potential of 4 kV within the mass measurement programme depending on the stagnation conditions. Different collimators with 0.5 mm and 0.7 mm diameter were installed, which are indicated by a different character size. This applies to the measurement series at 8 bar and 10 bar.

For further analysis, the average cluster size is emphasised and was extracted via Equation (6.18). Figure 6.20 shows the total amount of reflected clusters at each parameter setting which can be covered with the presented retardation spectrometer. Around 65 % up to 100 % of the ionised cluster beam can be reflected with the applied retardation field of maximal 4 kV within a temperature range of 46 K to 80 K and pressures between 7 bar and 10 bar. Three temperature areas can thereby be defined and further investigated:

- 60 K to 80 K shows a reflection of clusters around 95 % to 100 % without a difference in pressure
- 50 K to 60 K shows a reflection of clusters around 90 % to 95 % with small variations in pressure
- 46 K to 50 K shows a reflection of clusters around 65 % to 90 % with strong differences in pressure.

The resulting average cluster sizes with regard to the temperature of the selected isobars are presented in Figure 6.21. Atomic cluster sizes in the order of 10^4 atoms to 10^5 atoms appear. Since collimators with 0.5 mm and 0.7 mm diameter were applied to verify further systematic effects on the cluster mass, the data of the collimator with 0.7 mm diameter are indicated by a larger character size. This applies to the measurement series at 8 bar (cf. $\times \rightarrow \boldsymbol{\times}$) and 10 bar (cf. $\boxdot \rightarrow \boxdot$).

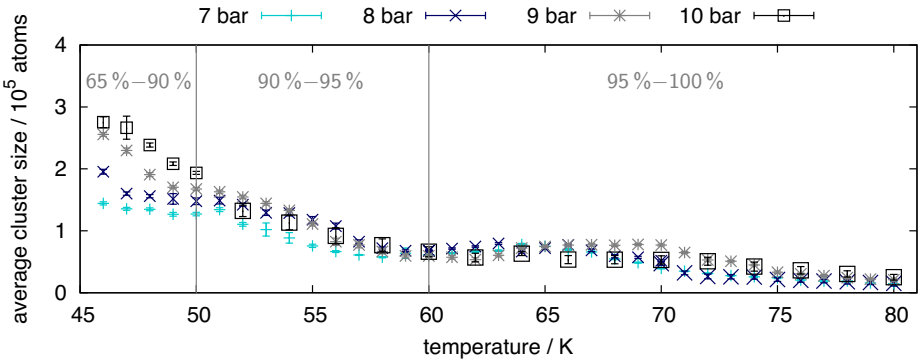

Figure 6.21.: Average cluster size (cf. Equation 6.18) depending on the stagnation conditions (systematic uncertainties around 10 % excluded). The vertical lines indicate the total amount of reflected clusters within 65 % up to 100 %. Within the presented stagnation conditions, the average cluster sizes occur in the order of 10^4 atoms to 10^5 atoms. Their increase is primarily induced by the decrease of the temperature and the influence of the pressure became apparent below 50 K within this measurement.

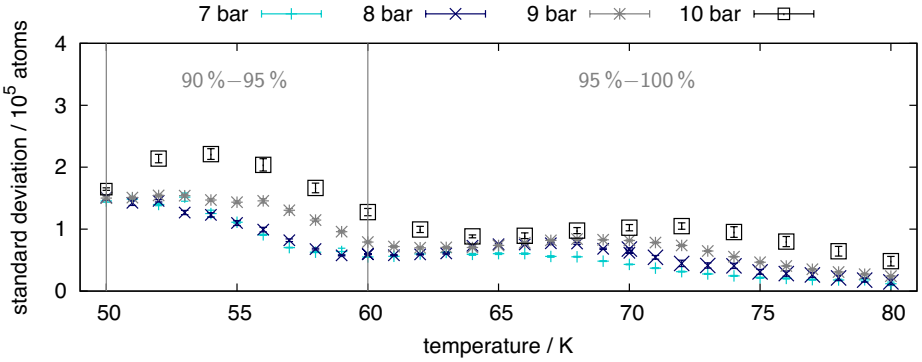

Figure 6.22.: Standard deviation (cf. Equation 6.19) of the isobars at 7 bar to 10 bar depending on the temperature, whereas the corresponding mass distributions are illustrated within the Appendix A.8. The vertical lines indicate the total amount of reflected clusters around 90 % up to 100 %.

The cluster size increases with decreasing temperature and shows no considerable increase with rising pressure between 50 K and 80 K with regard to the systematic uncertainties. Below 50 K, the cluster size growths significantly with decreasing temperature and increasing pressure, which could not be completely covered by the present retardation spectrometer. Moreover, the application of different collimator sizes shows no further systematic effects on the average cluster size. The emerging plateau around 60 K and 70 K cannot be further discussed due to the given systematic uncertainties. In addition,

the strong increase of the cluster size below 50 K cannot be induced by the beginning of the cluster production via fragmentation. The isobars below 50 K are clearly within the vapour area. Figure 6.22 shows the corresponding standard deviation of the isobars at 7 bar to 10 bar within 50 K and 80 K. The widths of the mass distributions at 7 bar and 8 bar are within the same range and increase with decreasing temperature. The measurement series at 9 bar and 10 bar show an increase of the standard deviation up to 56 K and 54 K, respectively. Widths up to a factor of two compared the isobars at 7 bar and 8 bar occur. Their decrease below 56 K and 54 K is most likely induced by the restricted capability of the retardation field (cf. Figure 6.20). The development of the mass distribution depending on the stagnation conditions is presented within Appendix A.8, which also covers tables including the velocity, average cluster size, standard deviation within 50 K and 80 K. Further mass measurements of hydrogen clusters with the identical Laval nozzle will follow within [Her15] at the final PANDA cluster-jet target and will lead to a finer resolution and higher masses, especially within the fluid area.

Hagena Parameter

The Hagena parameter Γ^* provides an empirical access to the prediction of cluster sizes [Pau00a]. It considers the gas type, the stagnation conditions, and the nozzle geometry [Hag87, HO72]. The Hagena parameter Γ^* for an axisymmetric expansion in a conical nozzle can be described via [Hag92]

$$\Gamma^* = \frac{\hat{k}\ p_0 \left(\frac{0.74\ d_n}{\tan \alpha_{1/2}}\right)^{0.85}}{{T_0}^{2.29}}, \tag{6.20}$$

with a gas dependent constant $\hat{k}$, the stagnation pressure p_0 (in mbar) and temperature T_0 (in K) of the gas, nozzle diameter d_n (in µm), and the expansion half angle $\alpha_{1/2}$ (in degree). For rare gases and metal vapours, the resulting values define the following conditions [Hag87]:

- $\Gamma^* < 200$: flow without cluster formation
- $200 < \Gamma^* < 1000$: transition to cluster formation
- $\Gamma^* > 1000$: immense condensation of clusters ($N > 100$ atoms [Hag87]).

The relation to the average cluster size N is known as Hagena's scaling law [Hag92]:

$$N = A_N \left(\frac{\Gamma^*}{1000}\right)^{\gamma_N}, \tag{6.21}$$

with the empirical Hagena parameter Γ^*, and the empirical values A_N and γ_N, which are available for small ($A_N = 38.4$, $\gamma_N = 1.64$ for $350 \leq \Gamma^* \leq 1800$) and large ($A_N = 33$, $\gamma_N = 2.35$ for $\Gamma^* > 1800$) values of Γ^* [Hag92].

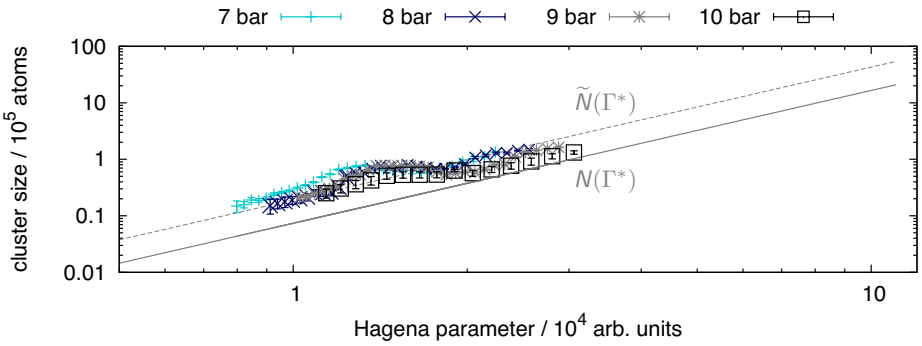

Figure 6.23.: Measured hydrogen cluster size (systematic uncertainties around 10 % excluded) of the selected isobars above 50 K as function of the Hagena parameter in double-log scale (with $\hat{k}_{H_2} = 184$ [SDT98] and references therein, $d_n = 28\,\mu m$, and $\alpha_{1/2} = 3.5$ degree). The grey solid line shows the expected cluster size $N(\Gamma^*)$ according to Hagena's scaling law (cf. Equation (6.21)) up to stagnation conditions within the vapour pressure curve. In addition, the grey dashed line presents a fit $\widetilde{N}(\Gamma^*)$ through the data via Equation (6.21) and varied parameter $A_N = 86 \pm 3$. The measured data and the predicted sizes agree by a factor of 2.6.

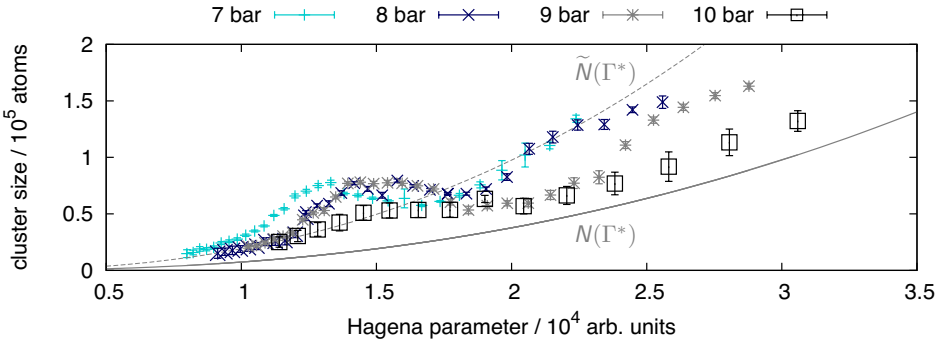

Figure 6.24.: Detailed presentation of the measured hydrogen cluster size (systematic uncertainties around 10 % excluded) of the selected isobars above 50 K as function of the Hagena parameter in linear scale. The grey solid line shows the expected cluster size $N(\Gamma^*)$ according to Hagena's scaling law (cf. Equation (6.21)) and the grey dashed line presents a fit $\widetilde{N}(\Gamma^*)$ through the data via Equation (6.21) and varied parameter $A_N = 86 \pm 3$.

A conclusive comparison with Hagena's parameter reveals a massive condensation process within 50 K and 80 K, confirmed by the observed average cluster masses (cf. Figure 6.24). The measured average cluster sizes differ with Hagena's scaling law by a factor of 2.6. However, the empirical values of the relation were mostly investigated for rare gases and metal vapours and not especially for hydrogen. Moreover, discrepancies were also confirmed within other publications with focus on large clusters, which suggest experimental corrections of the Hagena parameter [DSM08, DKS08]. The measured

magnitude of the cluster size in the order of 10^4 atoms to 10^5 atoms is in good agreement with the estimates of Hagena's scaling law (cf. Equation 6.21). The occurring oscillations and variations of the measurements series below 60 K (amount of reflected cluster around 90 % to 95 %) must be further investigated within future cluster mass measurements (cf. [Her15]).

Density relation

For realistic calculations and simulations within storage ring experiments with an internal cluster-jet target, the relation between the target thickness and cluster mass in dependency of the stagnation conditions is mandatory. Therefore, the corresponding target thickness for each stagnation condition of the selected isobars within the mass measurement programme was measured at the future interaction point with the presented monitoring system (cf. Figure 4.12). Figure 6.25 shows the target thickness normalised to the beam radius, since collimators with 0.5 mm and 0.7 mm diameter were installed (cf. Section 5.1.4). The measurements with 0.7 mm diameter are indicated by a larger character size, which applies to the measurement series at 8 bar (cf. $\times \rightarrow \times$) and 10 bar (cf. $\boxdot \rightarrow \boxdot$).

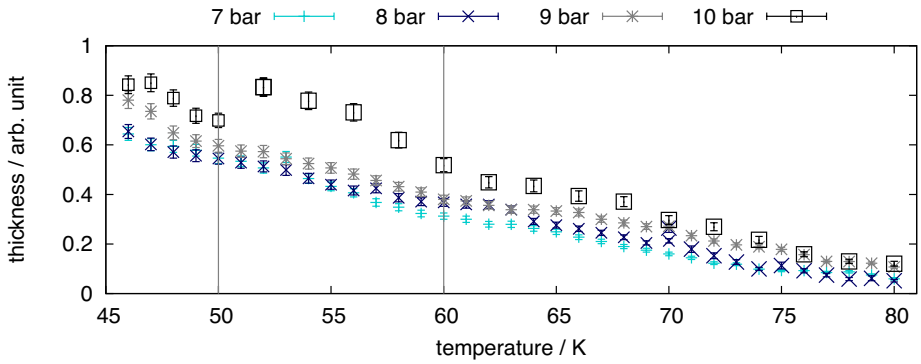

Figure 6.25.: Target thickness normalised to the beam radius, depending on the stagnation conditions. The significant steps around 50 K and 52 K at 10 bar as well as at 70 K and 8 bar arise from the application of two different collimator diameters (0.5 mm and 0.7 mm). The data of the collimator with 0.7 mm diameter are indicated by a larger character size and the vertical lines characterise the relevant areas of the mass measurement programme. Within the presented stagnation conditions, the target thickness appears in the range of 10^{11} atoms/cm^2 to 10^{12} atoms/cm^2.

In this case, the curve of the target thickness shows significant steps around 50 K and 52 K at 10 bar as well as at 70 K and 8 bar, contrary to the measured cluster size. This is attributed to systematic effects induced by the size, the current adjustment, and the quality of the installed collimators. Furthermore, this effect appears more significant with increasing thickness. Despite the normalisation of the target thickness to the beam radius,

a straight comparison of the complete measurement is not feasible. Nevertheless, the data show that an enhancement of the target thickness depends in particular on the decreasing temperature as well as on the pressure increase. Below 50 K, the measurement series are more separated, which could be induced by the considerable raise of the cluster size with rising pressure (cf. Figure 6.21). Within this field of investigation, the target thickness appears to be in the range of 10^{11} atoms/cm^2 to 10^{12} atoms/cm^2. To gain more insights on the relation between the target thickness and cluster size, further investigations should concentrate on one collimator size and shape. An unaffected adjustment of e.g. the nozzle alignment or skimmer and collimator position will reduce systematic effects. Moreover, measurements can only be compared within the stagnation conditions of a defined area (vapour, supercritical fluid, or fluid) of the material's vapour pressure curve.

7. Conclusion

The present thesis focusses on the detailed analysis of hydrogen cluster-jets and their characteristics with the objective to develop a cluster-jet target for the $\overline{\mathrm{P}}$ANDA experiment, which covers the following requirements [PAN12a]:

- the target source must be installed around 2.1 m from the interaction point to obtain an almost 4π angle acceptance at the $\overline{\mathrm{P}}$ANDA detector
- a maximal target thickness of $4.5 \times 10^{15}\,\mathrm{atoms/cm^2}$ at the interaction zone will ensure highest luminosities (around $2 \times 10^{32}\,\mathrm{cm^{-2}s^{-1}}$) and an optimal exploitation of the injected antiproton beam
- the target thickness must be constant in time to avoid luminosity fluctuations within the data acquisition and adaptable for the individual experimental programme
- a variable target beam size and shape is preferable to define the effective target beam size as small as possible for a precise vertex reconstruction and minimal background reactions
- to further reduce background reactions, the target material must exhibit highest purity.

Investigations on the cluster characteristics were performed at the operating cluster-jet target prototype (published in [T$^+$11]), which was already constructed in complete $\overline{\mathrm{P}}$ANDA geometry (cf. Chapter 4.2.1). The following measurements and results concentrate on the cluster velocity, density as well as cluster mass and will provide the basis for precise data analyses and realistic simulations. The different operating ranges or stagnation conditions were outlined within Figure 7.1, which shows the hydrogen pressure vapour curve. Based on the results of a diploma thesis [Köh10], the measurements were focussed on the optimisation of the target thickness (cf. Chapter 5) and allowed first access to the hydrogen cluster mass distribution as well as the average cluster size (cf. Chapter 6).

Previous measurements [Köh10] and calculations [Tä12] of the cluster velocity (published in [T$^+$13]) with regard to the stagnation conditions reveal two different cluster production processes: the cluster production via condensation (in the vapour and adjacent supercritical fluid area) and fragmentation (within the fluid area). These regimes were evident within the appearing time-of-flight or velocity distributions of the clusters and their mean velocities (around 200 m/s to 1000 m/s). The transition of both processes was also

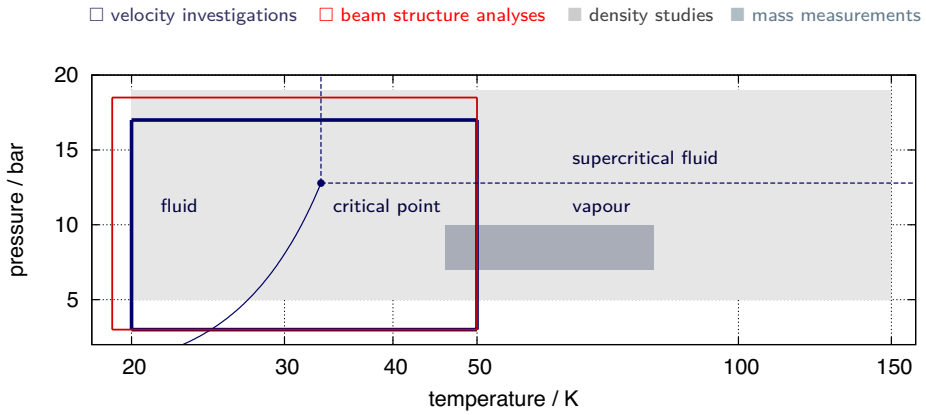

Figure 7.1.: Hydrogen vapour pressure curve, whereas the critical point (33.145 K, 12.964 bar [L$^+$09]) is marked by a dot. The open and filled boxes indicate the operating range of the presented measurement programme.

reflected through a clear step within measurement series of the target thickness around the vapour pressure curve. Moreover, these measurements yield large variations at stagnation conditions, primarily in the fluid and the adjacent supercritical fluid area. Within this thesis, these observations could be clearly attributed to the arising of highly intense core beams, produced within the fragmentation process.

Cluster beam structure

A detailed analysis of the beam structure was performed at the transition of vapour to fluid (and vice versa), supercritical fluid to fluid (and vice versa) and within the fluid area (cf. Section 5.2). The measurements reveal the visibility and reproducibility of the cluster-jet beam structure within the fluid and partly supercritical fluid area, which was expected to be homogeneous. Moreover, the results show the variation of the intensity, beam opening angle (around 5 degree up to maximal 7 degree), number of core beams (with possibly cylindrical surface, further investigations within [Her15,Het15]) and their position, depending most likely on the intrinsic nozzle geometry and the stagnation conditions. As a consequence, the skimmer extracts within one measurement series alternating bright or less bright parts, which induce the observed density fluctuations. Further investigations on the production and application of different Laval nozzle geometries (aperture length, opening angle) and materials (e.g. copper, glass, etc.) and their influence on the cluster beam structure will be performed within [Gri15].

Beam origin

Moreover, the analysis of the beam opening angles within the fluid area allow to estimate the possible beam origin within the Laval nozzle, which results in (6 ± 2) mm from the

narrowest point of the nozzle (cf. Section 5.2.1). Velocity calculations within [Tä12] yield two cut-off parameters at $z_g = (1.67 \pm 0.20)\,\mathrm{mm}$ and $z_l = (0.445 \pm 0.014)\,\mathrm{mm}$ for the condensation and fragmentation process, where the velocity remains unaffected by cluster-gas interactions. However, these cut-off parameters do not necessarily correspond to the beam origin. Particularly because these positions were calculated with regard to mean cluster velocities and within the cluster production process via fragmentation, a wide time-of-flight or velocity distribution occurs (cf. Section 5.1.3). Therefore, the analysis of different Laval nozzle geometries within [Gri15] will provide more insights into the complex cluster production process. An accurate and realistic position of the beam origin can be determined with the comparison and discussion of the various assumptions and results.

Target thickness

For a precise extraction of the observed core beams, a novel nozzle tilting system was developed (cf. Section 5.2.2), which allows to vary the nozzle enhancement manually with regard to the skimmer position (approximately ±3.5 degree with the narrowest point of the nozzle as point of rotation). The application of this tilting system permits the first access to the high luminosity mode for $\overline{\mathrm{P}}$ANDA with target thicknesses of more than $2\times10^{15}\,\mathrm{atoms/cm^2}$ at the required distance of 2.1 m. Thus, the target prototype represents the most efficient hydrogen cluster-jet target worldwide. The thickness is constant in time, reproducible, and stable with an accuracy better than 10 %. Depending on the stagnation conditions, the target thickness can be adjusted within $10^{10}\,\mathrm{atoms/cm^2}$ and $10^{15}\,\mathrm{atoms/cm^2}$. A density map will reveal further improvements of the target thickness and will be performed within the final cluster-jet target for $\overline{\mathrm{P}}$ANDA within [Her15,Het15].

Beam definition

Furthermore, the reduction of the cluster-jet beam to a minimal effective size with unaffected vertex zone and maximal target density was studied through the implementation of specially shaped collimators [Her13]. Investigations with different collimator blanks and slit sizes [Her13] show influences on the resulting target thickness. Within [Her13] an optimal slit size for the $\overline{\mathrm{P}}$ANDA experiment of $(800 \times 220)\,\mu\mathrm{m^2}$ was determined (cf. Section 5.3). Through an improved production process of slit collimators (based on the Laval nozzle manufacture, cf. Section 4.2.1), accurate slit sizes are now available and were investigated within this thesis. As expected, the proposed slit size yields target thicknesses of more than $2 \times 10^{15}\,\mathrm{atoms/cm^2}$ with minimised beam dimensions. So far, the maximal achieved target thickness amounts to $(2.3 \pm 0.3) \times 10^{15}\,\mathrm{atoms/cm^2}$ with a beam size of $(13 \times 3)\,\mathrm{mm^2}$ at the distance of the future $\overline{\mathrm{P}}$ANDA interaction point.

Cluster beam and vertex zone visualisation

The beam shaping through the installation of different collimators can be visualised by a MicroChannel Plate (MCP) detection system (cf. Section 5.3.3). This system permits the two-dimensional real time observation and monitoring of an ionised cluster-jet beam, e.g. via electron impact. The cluster beam shape, size, position, as well as the intensity can be investigated and offer the opportunity for adjustment checks. In addition, the vertex zone with an accelerator beam can be visualised, which was verified within feasibility studies at the ANKE cluster-jet target at COSY (Forschungszentrum Jülich, Germany). The resulting intensity is thus correlated to the luminosity distribution, whereas in this case, the ionisation occurs within the interaction with the accelerator beam (published in [K$^+$14b]). This system is suitable for applications at storage ring experiments such as $\overline{\text{P}}$ANDA and can be adapted at the target beam dump.

Mass distribution and average cluster size

In order to investigate the mass distribution of hydrogen cluster-jets with a Laval nozzle, a mass spectrometer with retardation field was selected, which belongs to the destructive mass diagnostic techniques (cf. Chapter 6). Based on the gradual retardation and detection of an ionised cluster-jet beam, the resulting transmission spectra were analysed with regard to various stagnation conditions within the vapour area. The results yield log-normal distributed cluster masses and average cluster sizes in the order of 10^4 atoms to 10^5 atoms with systematic uncertainties around 10 %. The resulting average cluster sizes are in good agreement with the estimates of Hagena's scaling law (cf. Equation (6.21)) within a factor of 2.6. Further investigations on the cluster mass will be performed at the $\overline{\text{P}}$ANDA cluster-jet target via Mie scattering within [Her15], which belongs to the non-destructive methods. The measurement programme will concentrate on stagnation conditions in the fluid and the adjacent vapour area with the objective to gain realistic mass distributions and cluster sizes with consideration of all systematic uncertainties.

$\overline{\text{P}}$ANDA cluster-jet target

Based on the presented results of this thesis within the cluster-jet target prototype for $\overline{\text{P}}$ANDA, the final target (cf. Figure 7.2) was designed and constructed with the following special features:

- high-end vacuum pumping station with up to 9800 m^3/h to obtain the required vacuum pressures at highest densities
- improved nozzle tilting system ($\pm$3.5 degree) equipped with stepper motors, end switches, two independent position indicators, and electronic level (cf. [Het15])

- monitoring system at the skimmer chamber including two opposing CCD cameras with macro lense for comfortable adjustment of the nozzle alignment and skimmer position.

Furthermore, the final cluster-jet target [Her15, Het15] is embedded within a support frame with adjustable mounting points to the $\overline{\mathrm{P}}$ANDA magnet. An included automatic lifting system enables a service position of the insulation vacuum chamber, separated from the skimmer chamber, for maintenance activities. The connection to the $\overline{\mathrm{P}}$ANDA magnet is ensured by special snap connectors. Moreover, all relevant devices for the gas system are composited within substitutable gas modules controlled via PLC (Programmable Logic Controller) with separate hydrogen purifier, which provides a purity level of 9.0. The first commissioning of the complete target will be in summer 2015 [Her15, Het15]. The final cluster-jet target defines the state of the art of cluster-jet target technology and will fulfil all crucial requirements to realise the implementation and operation at $\overline{\mathrm{P}}$ANDA.

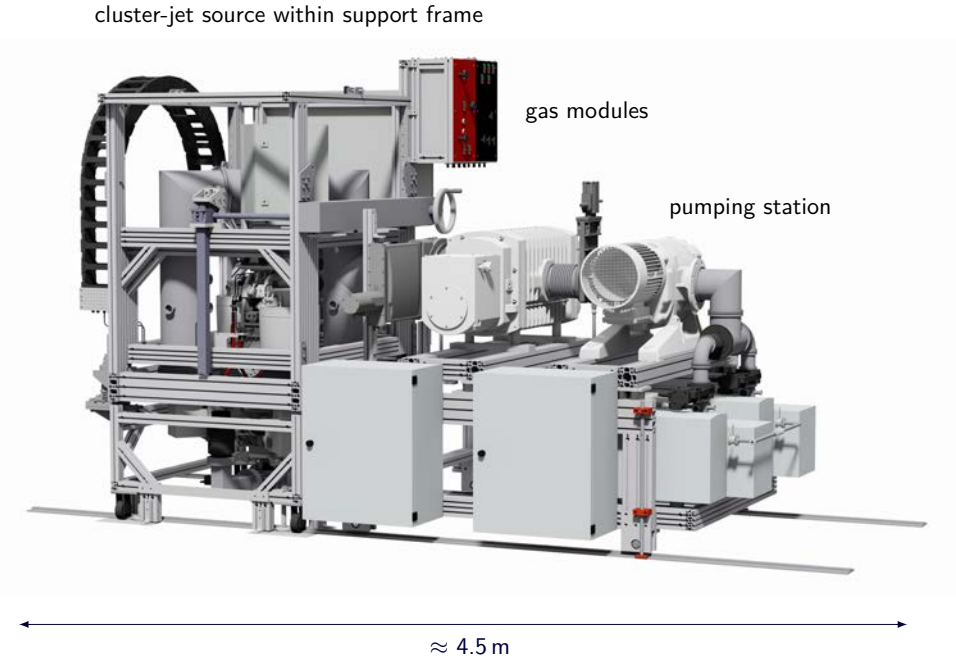

Figure 7.2.: Overview of the final cluster-jet target for the $\overline{\mathrm{P}}$ANDA experiment (generated by D. Bonaventura with Autodesk Showcase, edited).

A. Appendix

A.1. Pumping speed

The pumping speed S of a vacuum chamber can be determined through an induced gas flow q_{pV} and the leveled vacuum pressure p therein (cf. Equation 5.4). A gas flow controller with maximal $3\,\mathrm{m}\ell_\mathrm{n}/\mathrm{min}$ (n denotes under normal conditions) was applied at the interaction chamber and was varied from 10 % to 100 % [Köh10]. The pumping speed results in $S = (215 \pm 6)\,\ell/\mathrm{s}$ (including statistical and systematic uncertainties around $\pm 2\,\ell/\mathrm{s}$ and $\pm 6\,\ell/\mathrm{s}$), which is an essential parameter for the determination of the target density at the future interaction point of the $\overline{\mathrm{P}}$ANDA experiment (cf. Section 5.1.2).

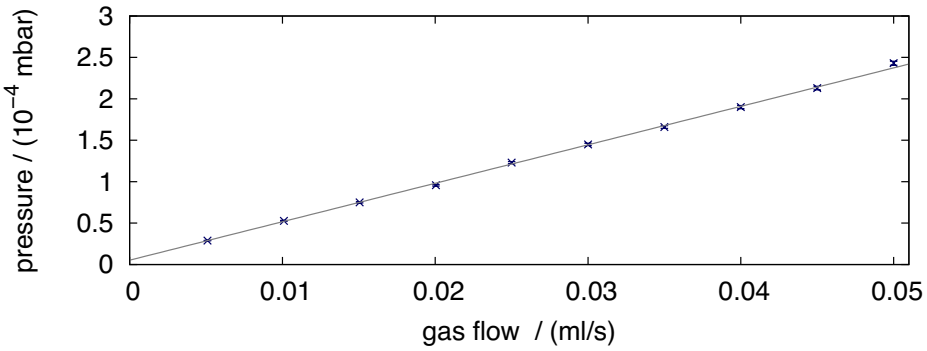

Figure A.1.: Determination of the pumping speed S (S^{-1} proportional to the slope) within the interaction chamber of the cluster-jet target prototype for $\overline{\mathrm{P}}$ANDA (data extracted from [Köh10]) via the measured vacuum pressure p (statistical uncertainty around 2 %) as function of the induced gas flow q_{pV}.

A.2. Visualisation of the cluster-jet beam

The visualisation of the cluster-jet beam at the skimmer chamber shows partly a very inhomogeneous intensity pattern and points to high and low dense parts within the beam. With regard to the hydrogen pressure and temperature at the cluster production, the development of the density beam pattern was investigated:

1. at the transition fluid ⇔ vapour
   (cf. Section A.2, 7.5 bar between 18 K and 30 K, in steps of 1 K)
2. at the transition fluid ⇔ supercritical fluid
   (cf. Fig. 5.18 and Section A.2, 18.5 bar between 19 K and 40 K, in steps of 1 K)
3. and in the fluid area
   (cf. Section A.2, 25 K between 3 bar and 18 bar, in steps of 1 bar).

In the following sections, the left-hand side figure shows the beam images in false colours with the beam direction from left to right. The data is based on monochrome images with 1392×1024 pixels and the colour code represents the intensity. These measurements were performed twice (consistency check) in the process of an increase and decrease of the temperature or pressure, respectively. Therefore, the right-hand side figure presents the corresponding projections of the ordinate, within the cooling (blue line) and heating process (red line). At 7.5 bar and 20 K only data within the cooling process was available.

Beam images and projections at 7.5 bar

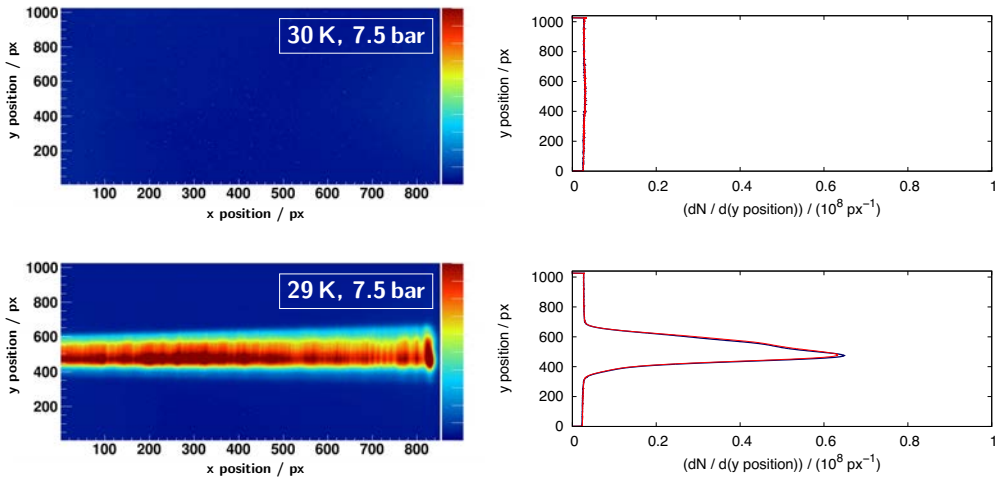

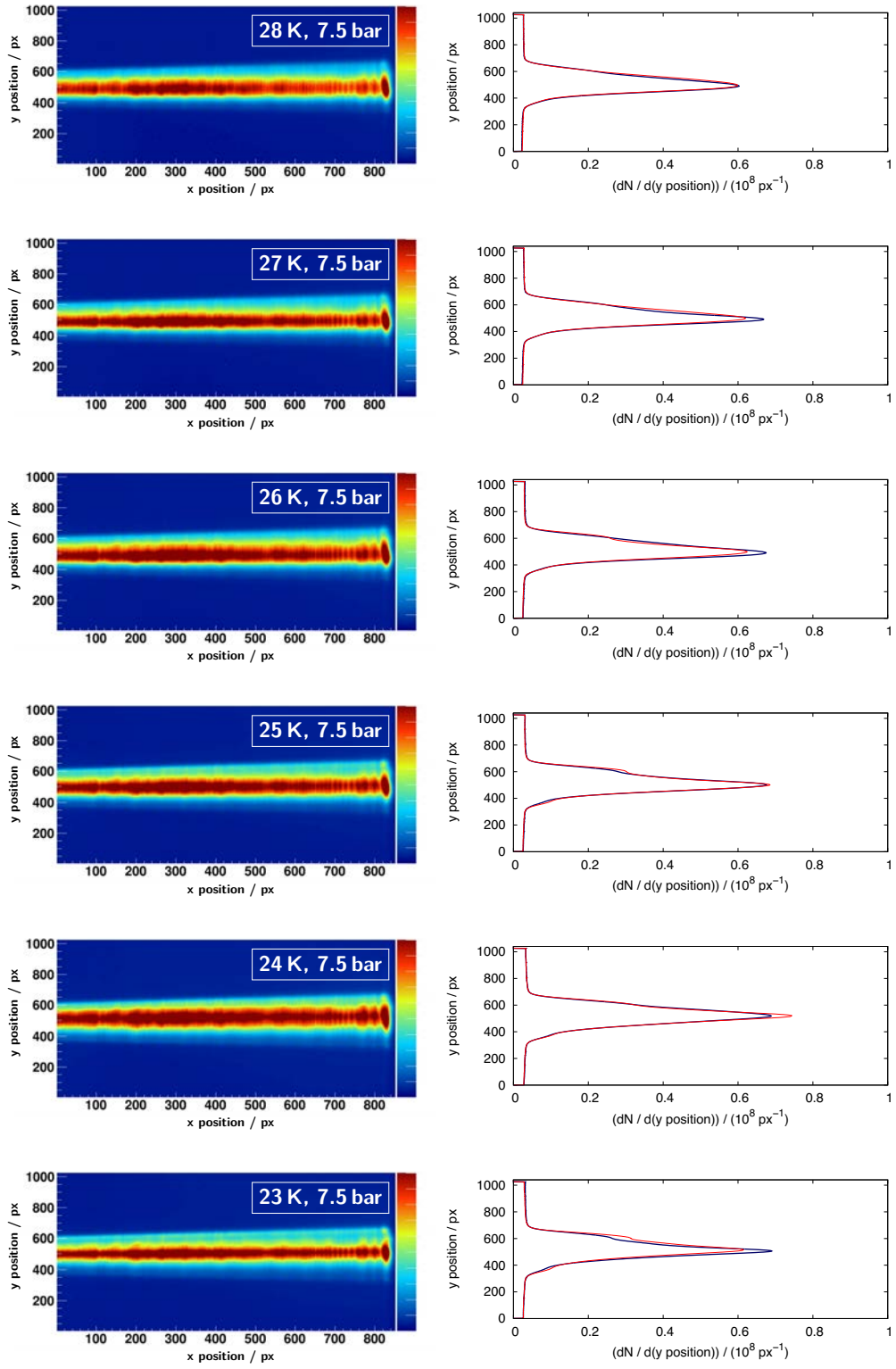
28 K, 7.5 bar
27 K, 7.5 bar
26 K, 7.5 bar
25 K, 7.5 bar
24 K, 7.5 bar
23 K, 7.5 bar
y position / px
x position / px
(dN / d(y position)) / (10^8 px^-1)

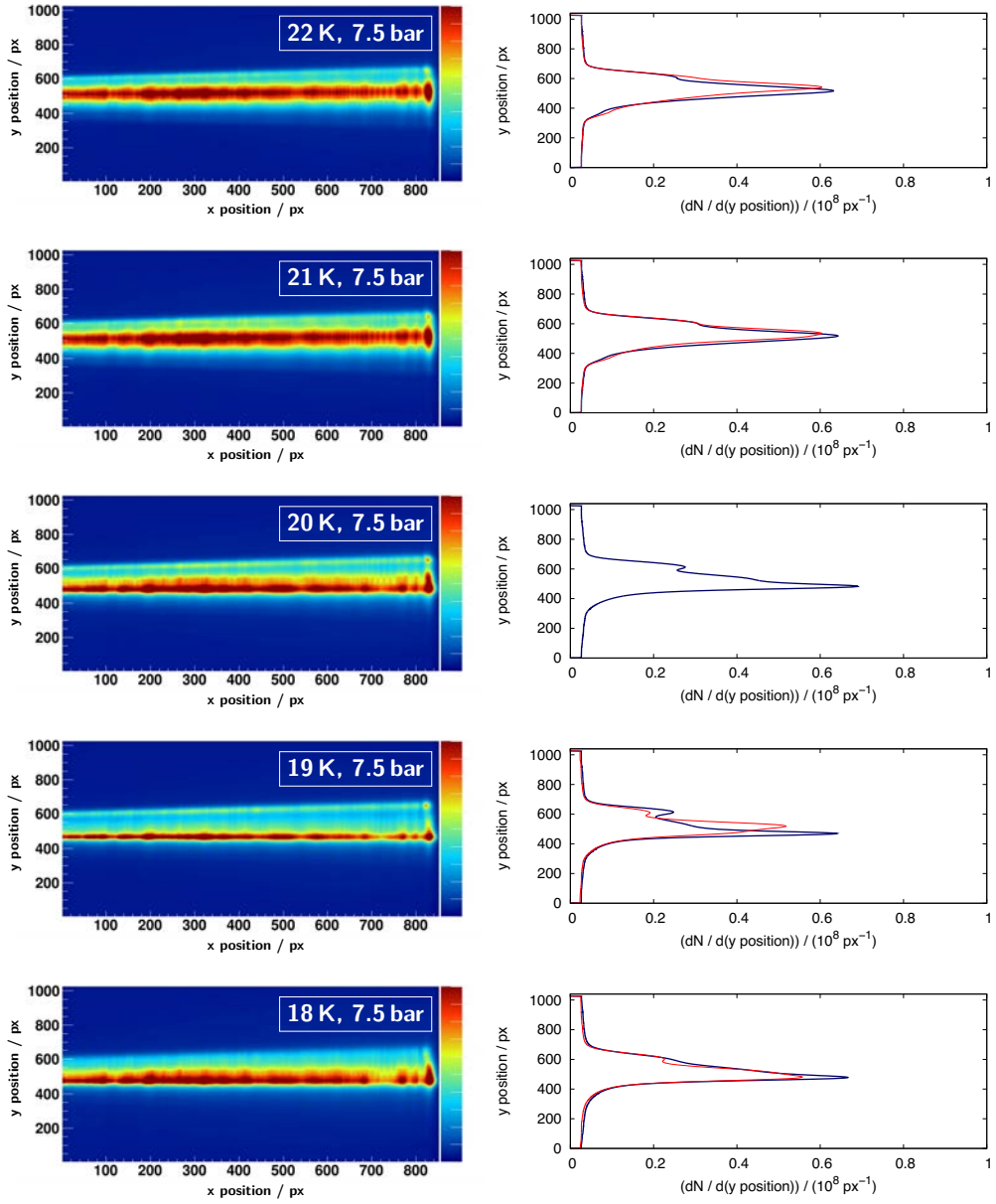
22 K, 7.5 bar
21 K, 7.5 bar
20 K, 7.5 bar
19 K, 7.5 bar
18 K, 7.5 bar
y position / px
x position / px
(dN / d(y position)) / (10^8 px^-1)

Beam images and projections at 18.5 bar

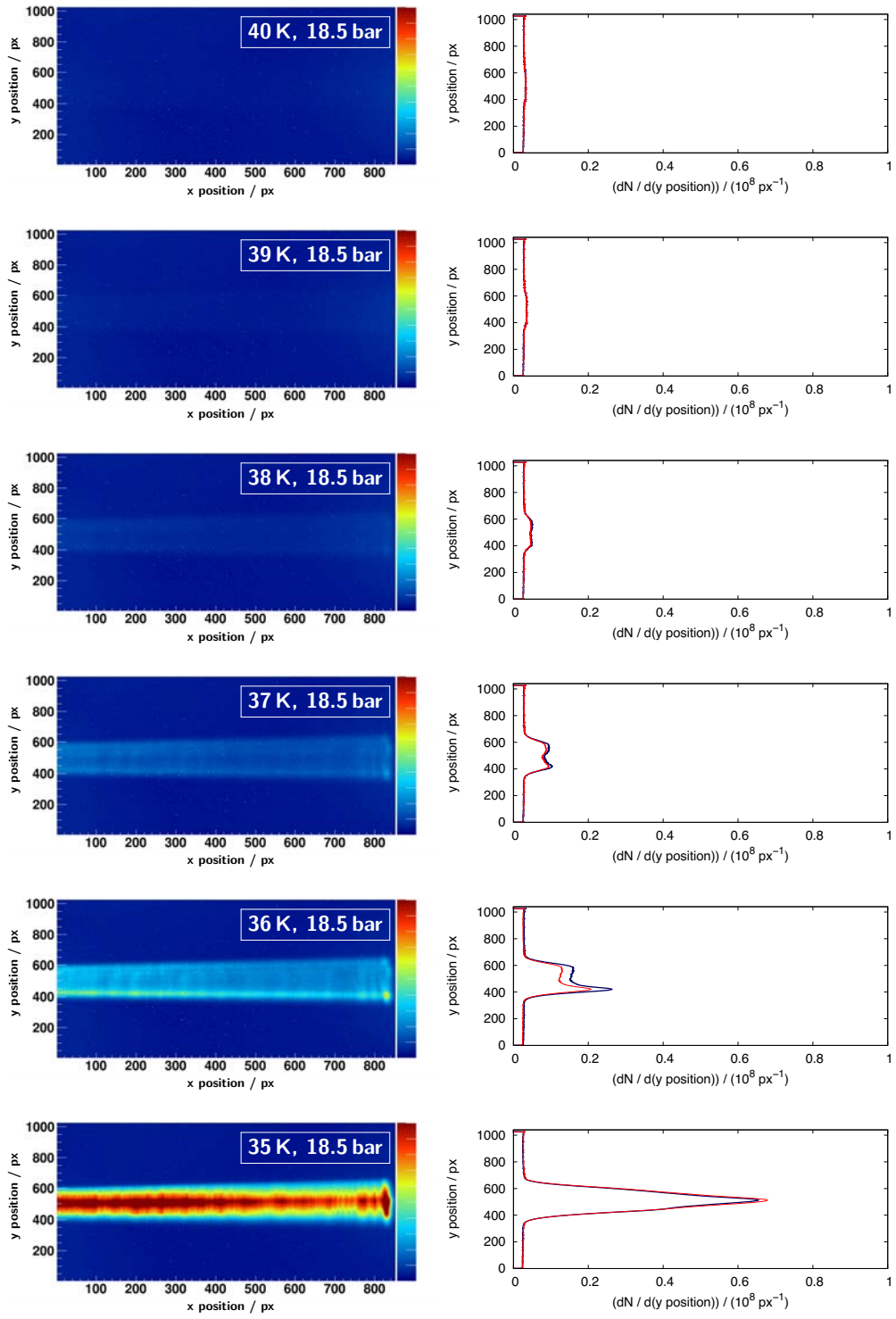

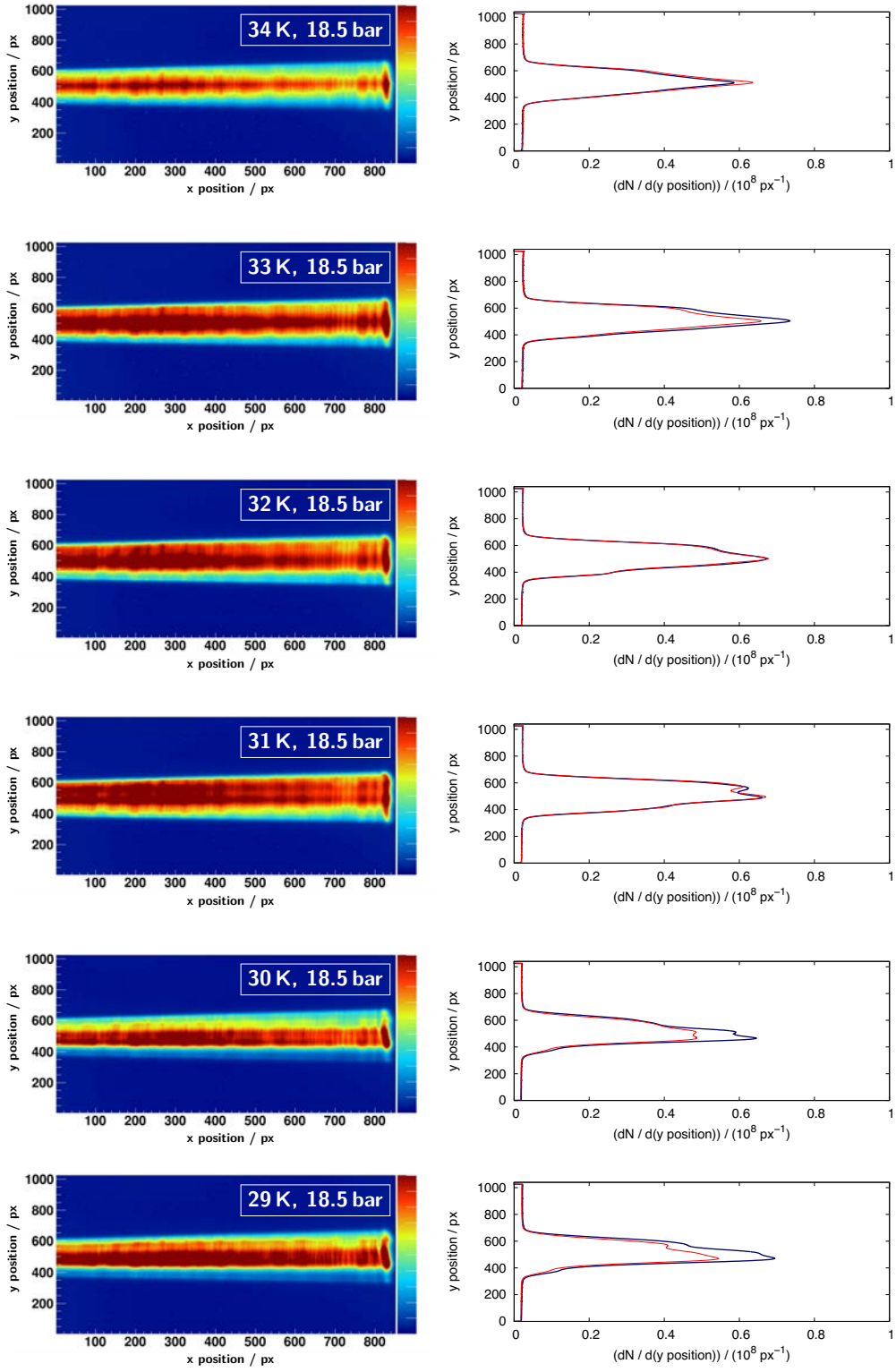
34 K, 18.5 bar
33 K, 18.5 bar
32 K, 18.5 bar
31 K, 18.5 bar
30 K, 18.5 bar
29 K, 18.5 bar
y position / px
x position / px
(dN / d(y position)) / (10^8 px^-1)

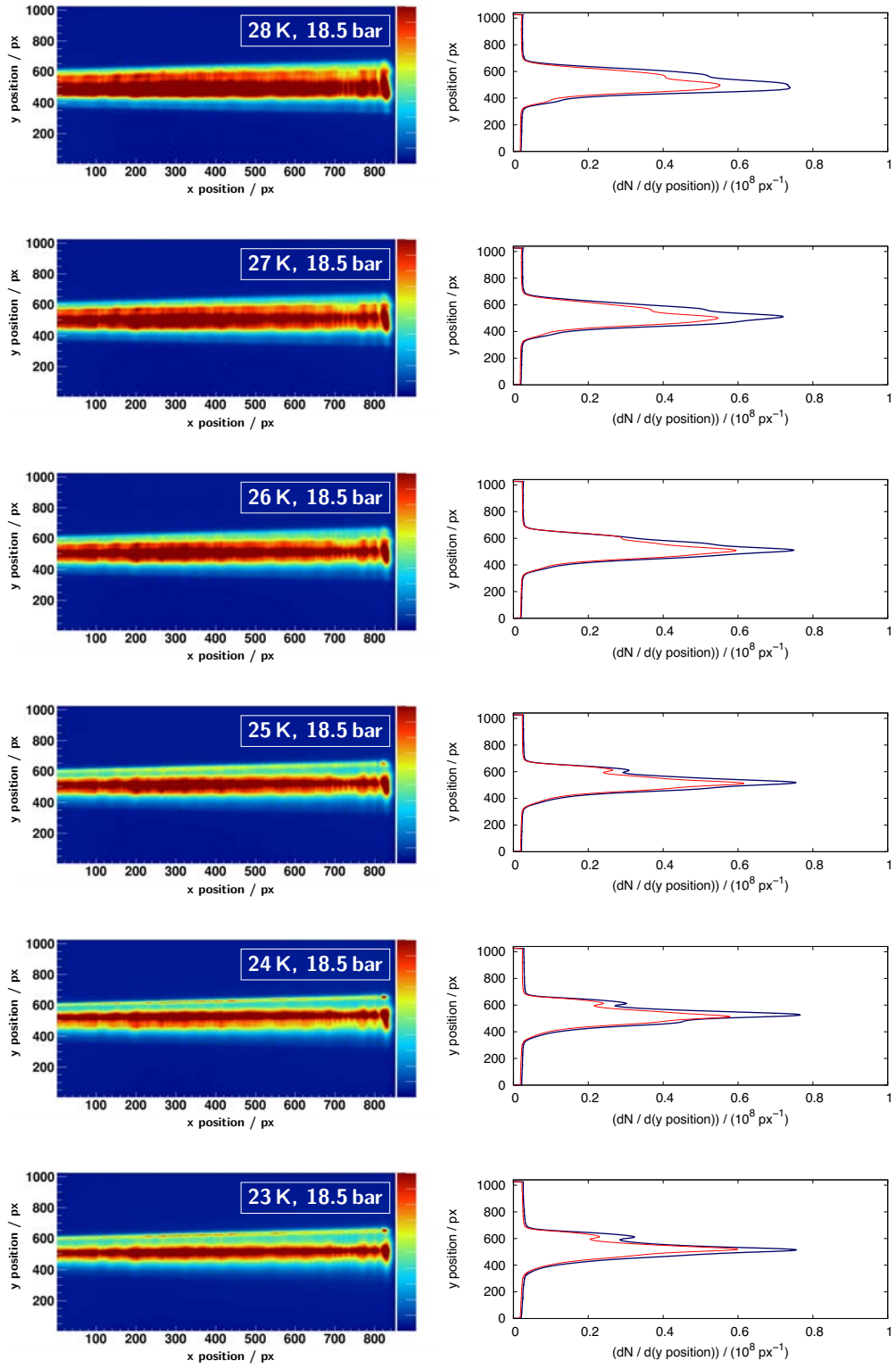
28 K, 18.5 bar
27 K, 18.5 bar
26 K, 18.5 bar
25 K, 18.5 bar
24 K, 18.5 bar
23 K, 18.5 bar
y position / px
x position / px
(dN / d(y position)) / (10^8 px^-1)

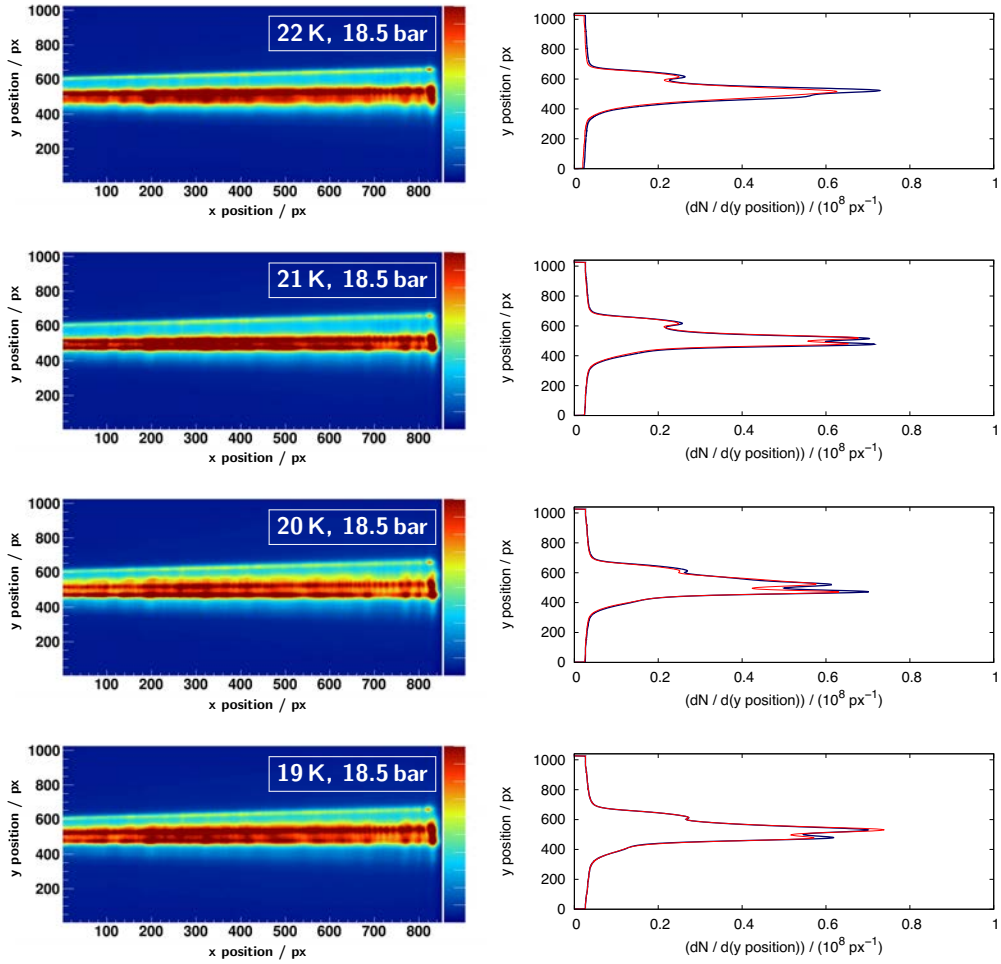
22 K, 18.5 bar
21 K, 18.5 bar
20 K, 18.5 bar
19 K, 18.5 bar
y position / px
x position / px
(dN / d(y position)) / (10^8 px^-1)

Beam images and projections at 25 K

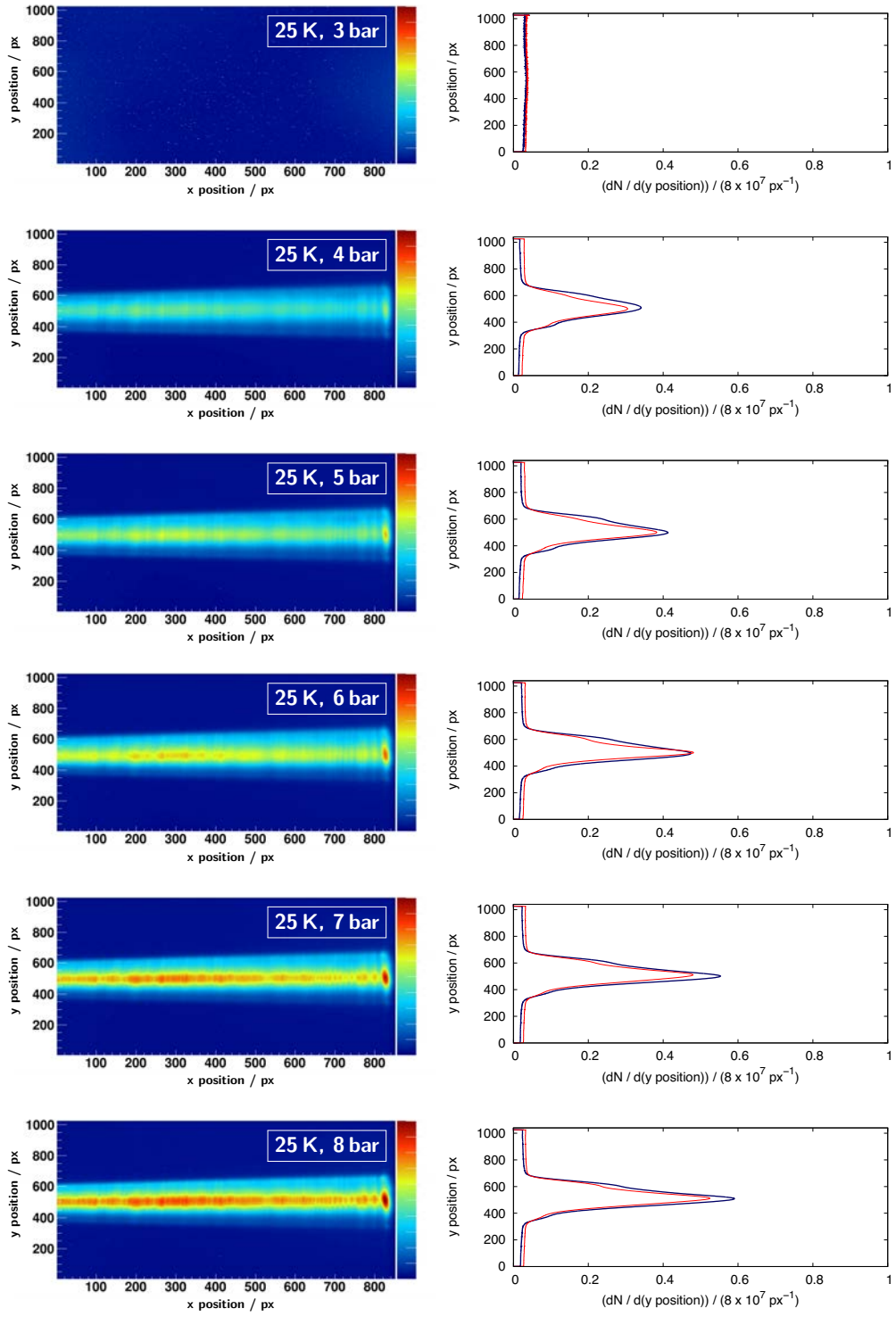

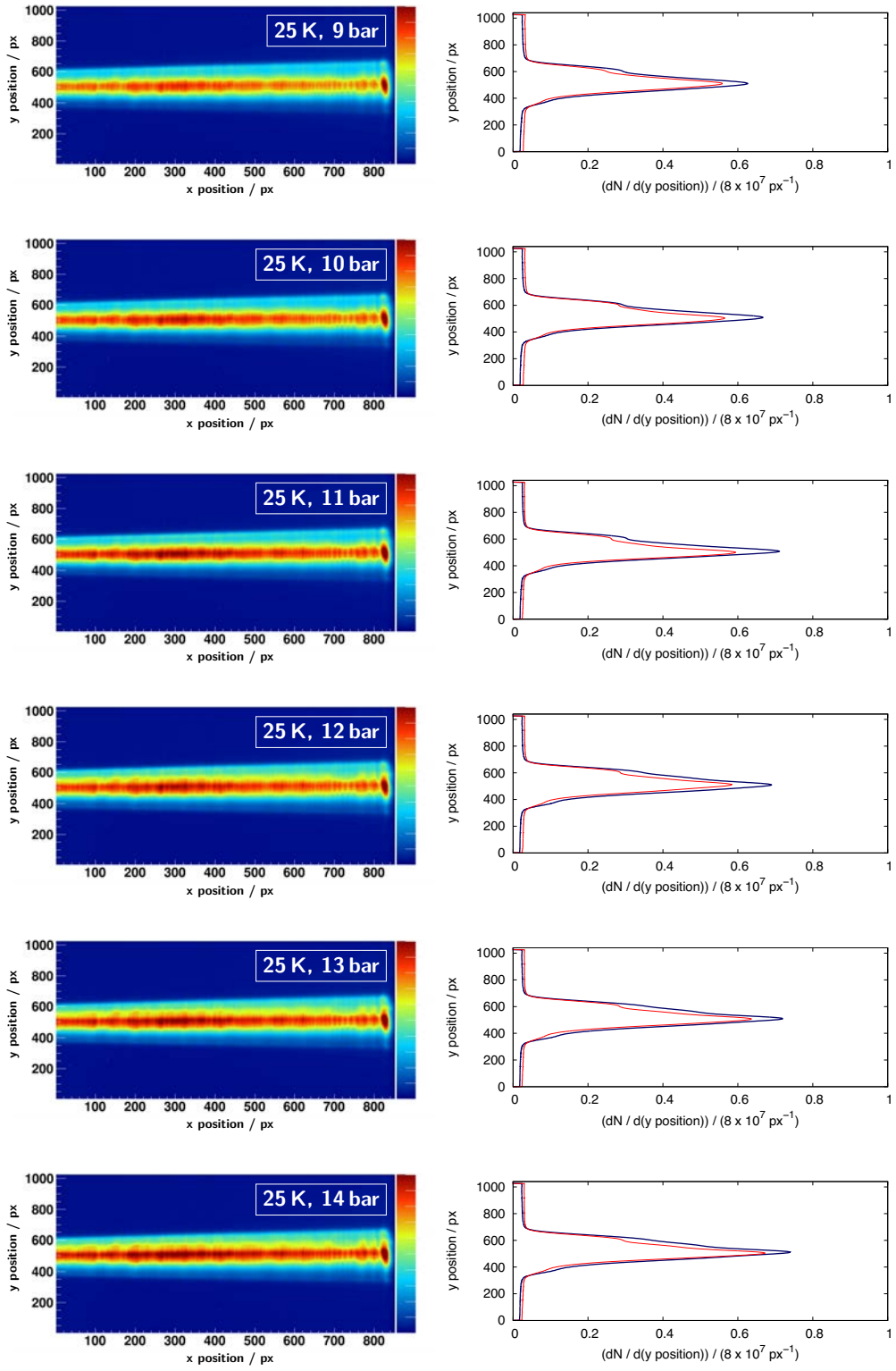
25 K, 9 bar
25 K, 10 bar
25 K, 11 bar
25 K, 12 bar
25 K, 13 bar
25 K, 14 bar
y position / px
x position / px
(dN / d(y position)) / (8 x 10^7 px^-1)

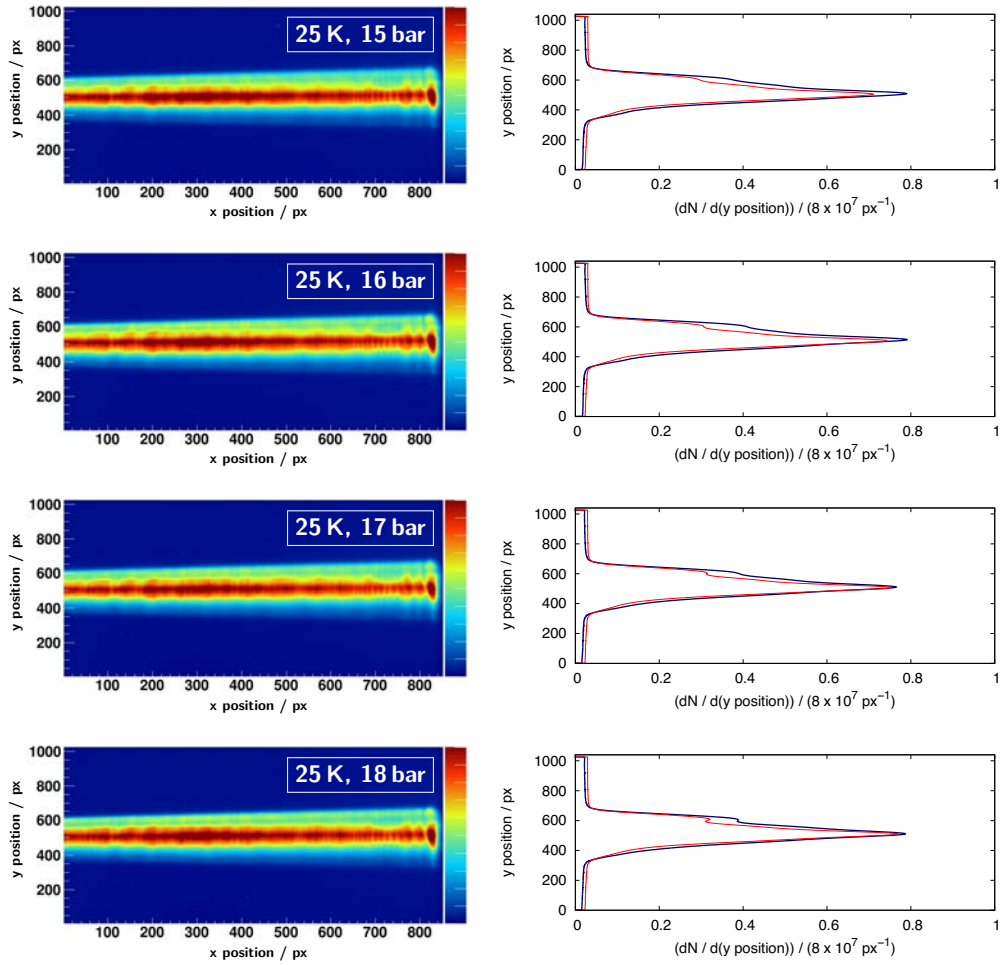
25 K, 15 bar
25 K, 16 bar
25 K, 17 bar
25 K, 18 bar
y position / px
x position / px
(dN / d(y position)) / (8 x 10^7 px^-1)

A.3. Conversion factor px to mm

In order to verify the variation of the cluster beam origin, which is emphasised in Section 5.2.1, measurement series within 19 K to 24 K and 7 bar to 17 bar were performed and analysed. Since the resulting values of the beam origin were given in units of pixel, the conversion factor from pixel to millimetre has to be determined. Thus, a sample was recorded with identical camera settings and displaced by a defined length. Figure A.2 show the results and reveal a conversion factor of $1\,\mathrm{mm} = (58 \pm 2)\,\mathrm{px}$.

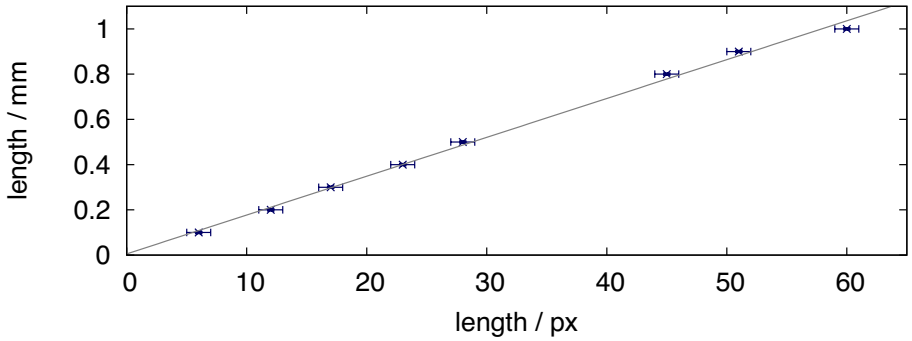

Figure A.2.: Determination of the conversion factor of pixel to millimetre. The data was extracted from different images of a depicted razor blade with defined displacement and results in $1\,\mathrm{mm} = (58 \pm 2)\,\mathrm{px}$.

A.4. Beam opening angles

In the following sections, the extracted beam opening angles of measurement series at 7.5 bar, 18.5 bar, and 25 K were presented. The histograms correspond to the appropriate red (heating process) and blue (cooling process) coloured projections in Section A.2. At 7.5 bar and 20 K only data within the cooling process was available. The vertical grey lines indicate the opening angle of the installed Laval nozzle.

Beam opening angles at 7.5 bar

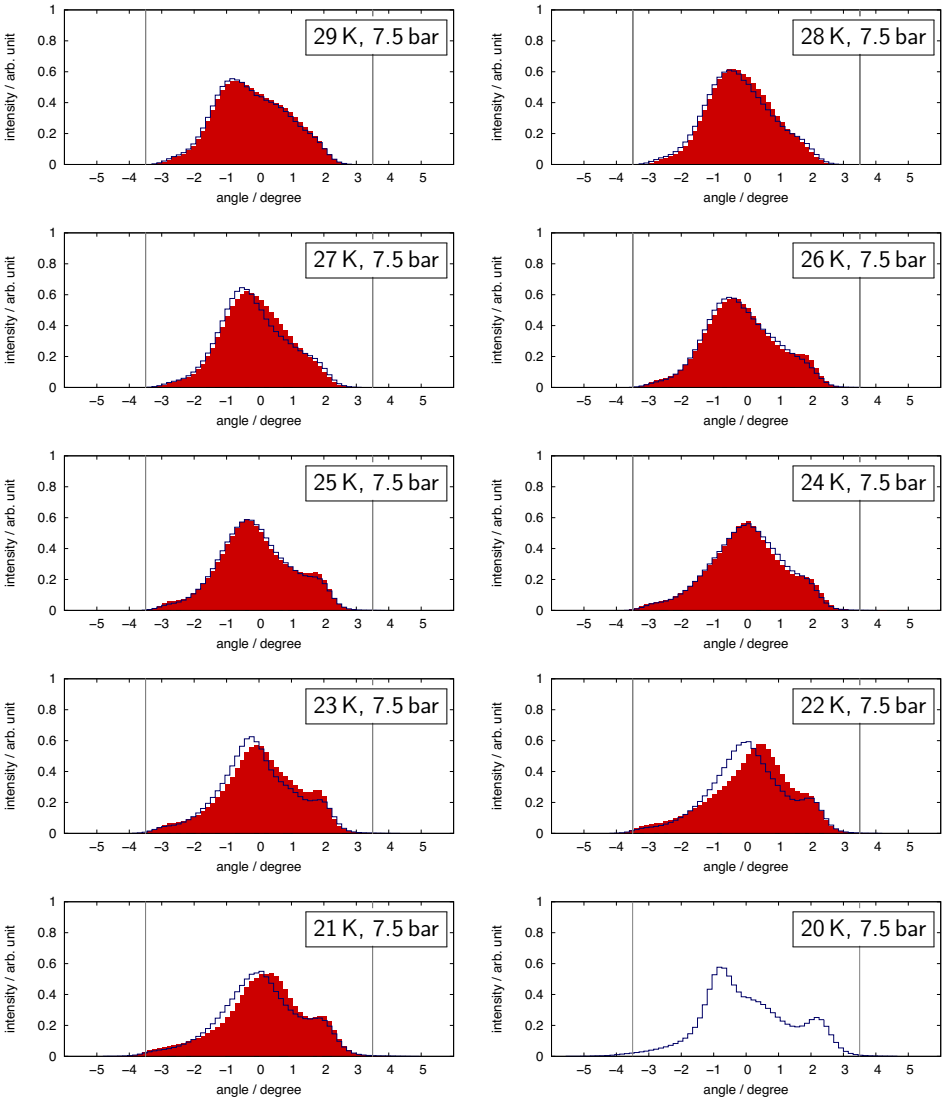

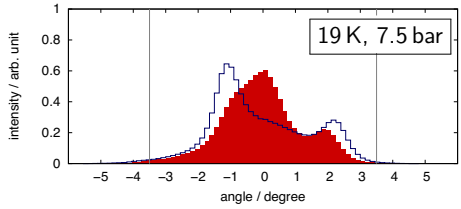

Beam opening angles at 18.5 bar

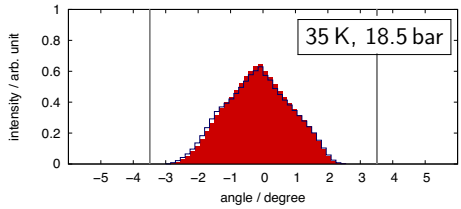

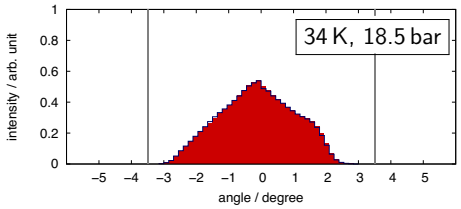

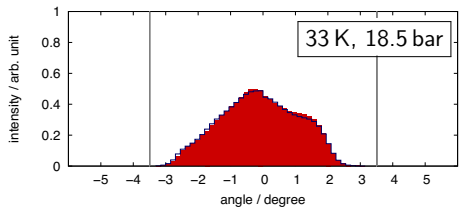

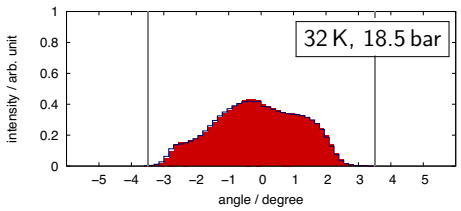

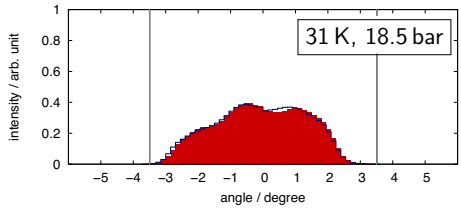

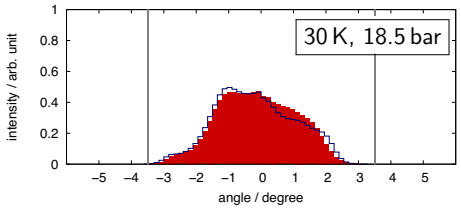

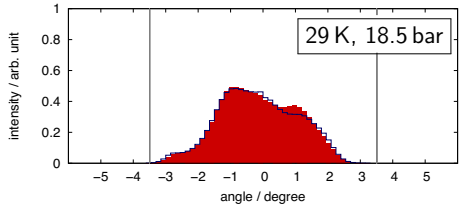

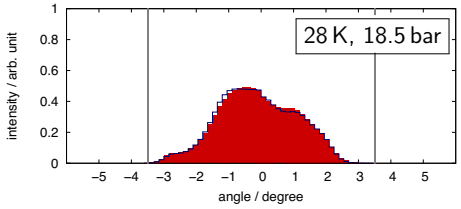

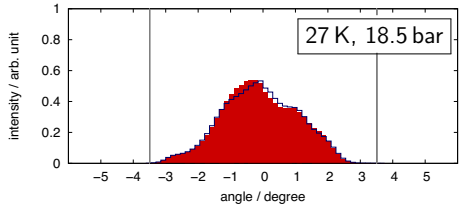

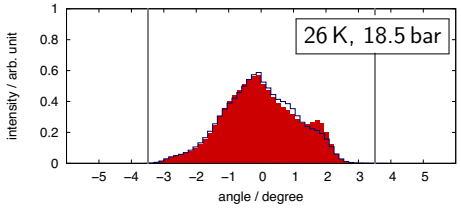

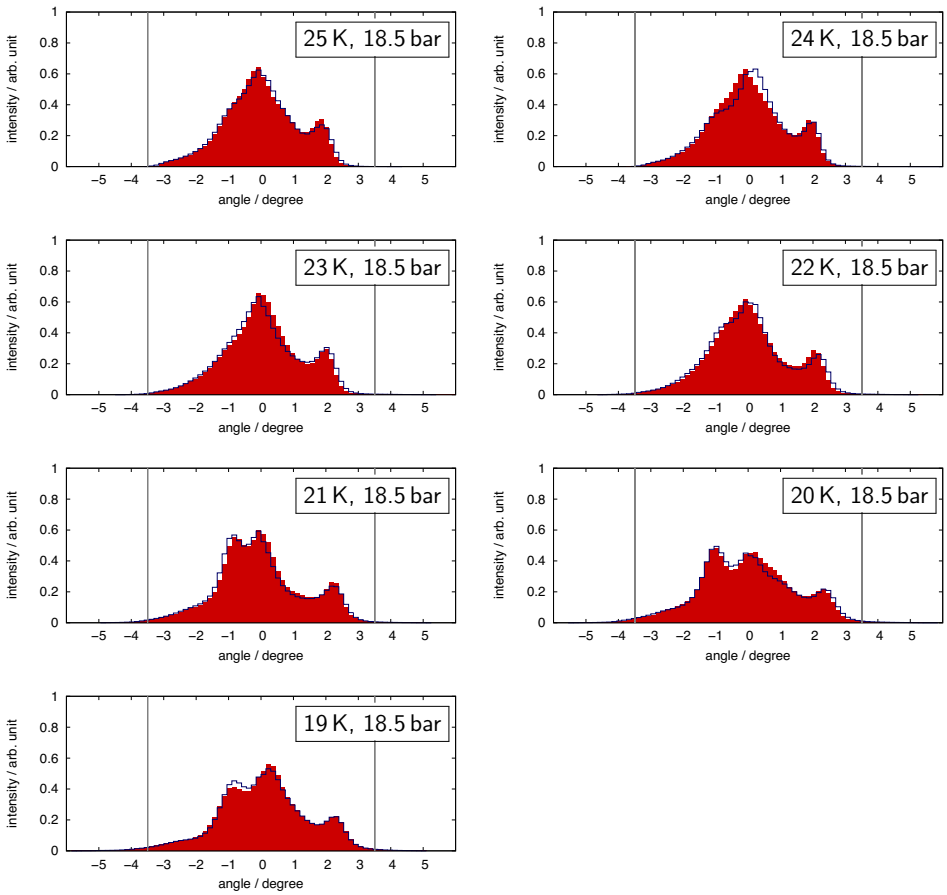

Beam opening angles at 25 K

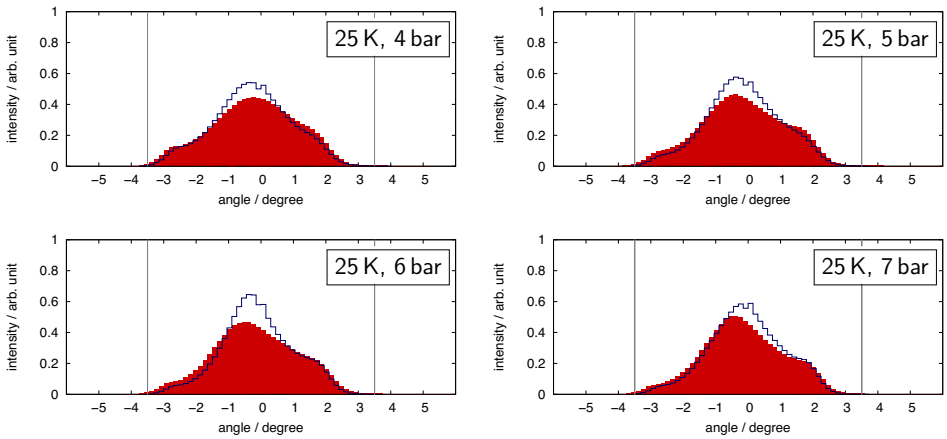

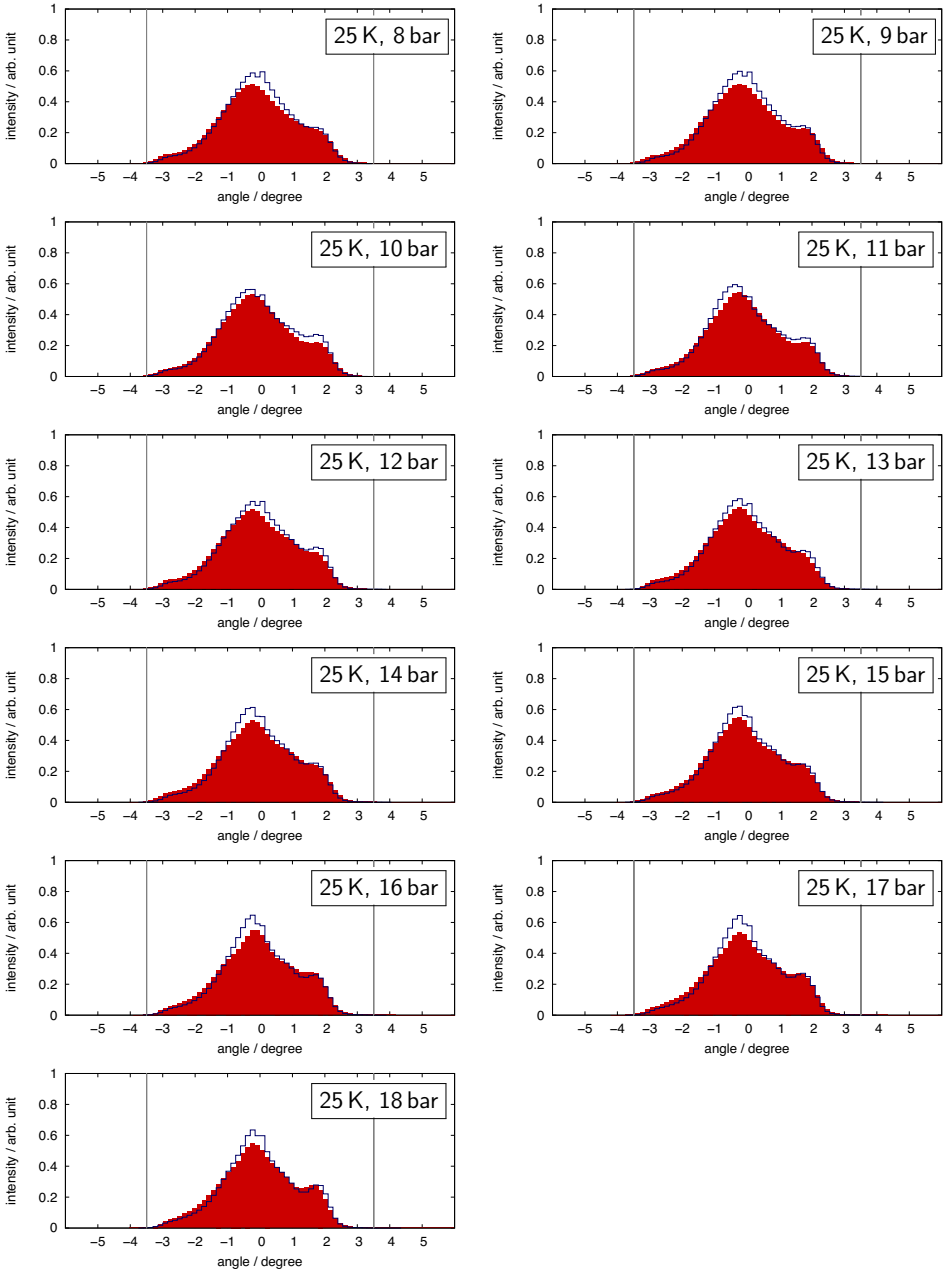
25 K, 8 bar
25 K, 9 bar
25 K, 10 bar
25 K, 11 bar
25 K, 12 bar
25 K, 13 bar
25 K, 14 bar
25 K, 15 bar
25 K, 16 bar
25 K, 17 bar
25 K, 18 bar
intensity / arb. unit
angle / degree

A.5. Beam deflector feasibility study

An optimal extraction of the observed high intense core beams cannot be realised just through the adjustment of the skimmer and collimator, if the core beams are not parallel to the axis defined by the skimmer and collimator center. Moreover, within accelerator experiments the skimmer-collimator axis has to be aligned relative to the interaction point. Therefore, a beam deflector was installed around the Laval nozzle to affect the propagation of the emergent cluster-jet beam. The results of three selected deflector positions can be obtained from the associated beam profiles and reveal that the deflector not only has an influence on the beam propagation, but also on the beam structure and yields a rather smeared core beam.

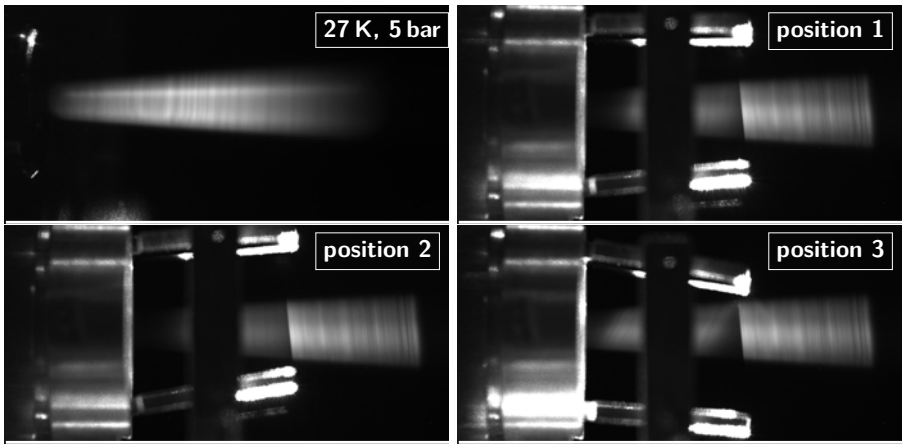

Figure A.3.: Cluster beam within the skimmer chamber at 27 K and 5 bar with beam direction from left to right. The applied Laval nozzle with an inner diameter around 47 µm was manufactured at the University of Münster (see also Figure 4.6). The installation of the beam deflector at 'position 1' had a direct influence on the beam structure and yielded a rather smeared core beam. Moreover, the variation of the deflector position affected the beam propagation and can be observed through the beam profiles in the interaction chamber.

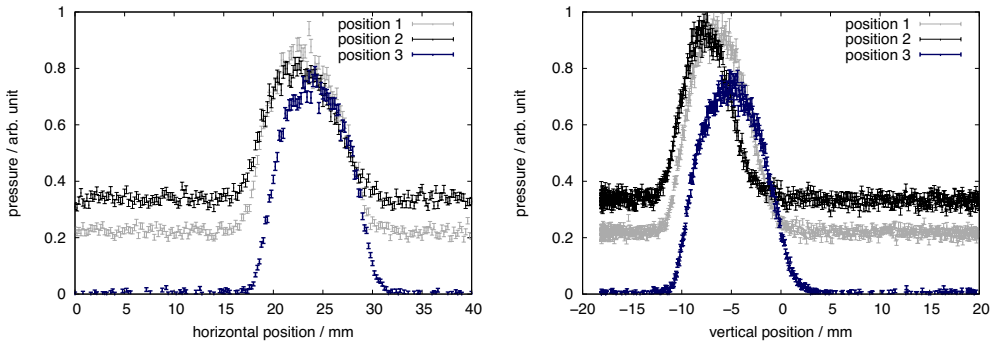

Figure A.4.: Recorded beam profiles at 27 K and 5 bar (background subtracted with respect to position 3) with installed beam deflector and different deflector positions. The beam deflector affects the beam position, background, and thickness within the interaction chamber, which corresponds to the future interaction point.

A.6. Vacuum design (update)

Cryopumps repeatedly need to regenerate, therefore, they are not foreseen in the vacuum design of the final $\overline{\mathrm{P}}$ANDA cluster source and the beam dump. The substitution of cryopumps by turbomolecular pumps was effectively implemented at the beam dump of the cluster-jet target prototype. The pumping speed of the present vacuum pumps are listed in Table A.1, whereas the resulting vacuum design is presented in Figure A.5. Within the follwing updated version fore pumps are denoted with $\mathsf{FP}^*_{\mathsf{no.}}$, roots pumps with $\mathsf{RP}^*_{\mathsf{no.}}$, turbomolecular pumps with $\mathsf{TP}^*_{\mathsf{no.}}$ and cryopumps with $\mathsf{CP}^*_{\mathsf{no.}}$.

no.	**fore pump $\mathsf{FP}^*_{\mathsf{no.}}$ in m^3/h**	**roots pump $\mathsf{RP}^*_{\mathsf{no.}}$ in m^3/h**	**turbo pump $\mathsf{TP}^*_{\mathsf{no.}}$ in ℓ/s**
1	300	2000	450
2	25	7000	2000
3	300	–	2000
4	16	–	360
5	–	–	450
6	–	–	1000
7	–	–	1300
8	–	–	1000
9	–	–	450
10	–	–	300

Table A.1.: Updated list of the currently installed vacuum pumps of the cluster-jet target prototype and their nominal pumping speed for air.

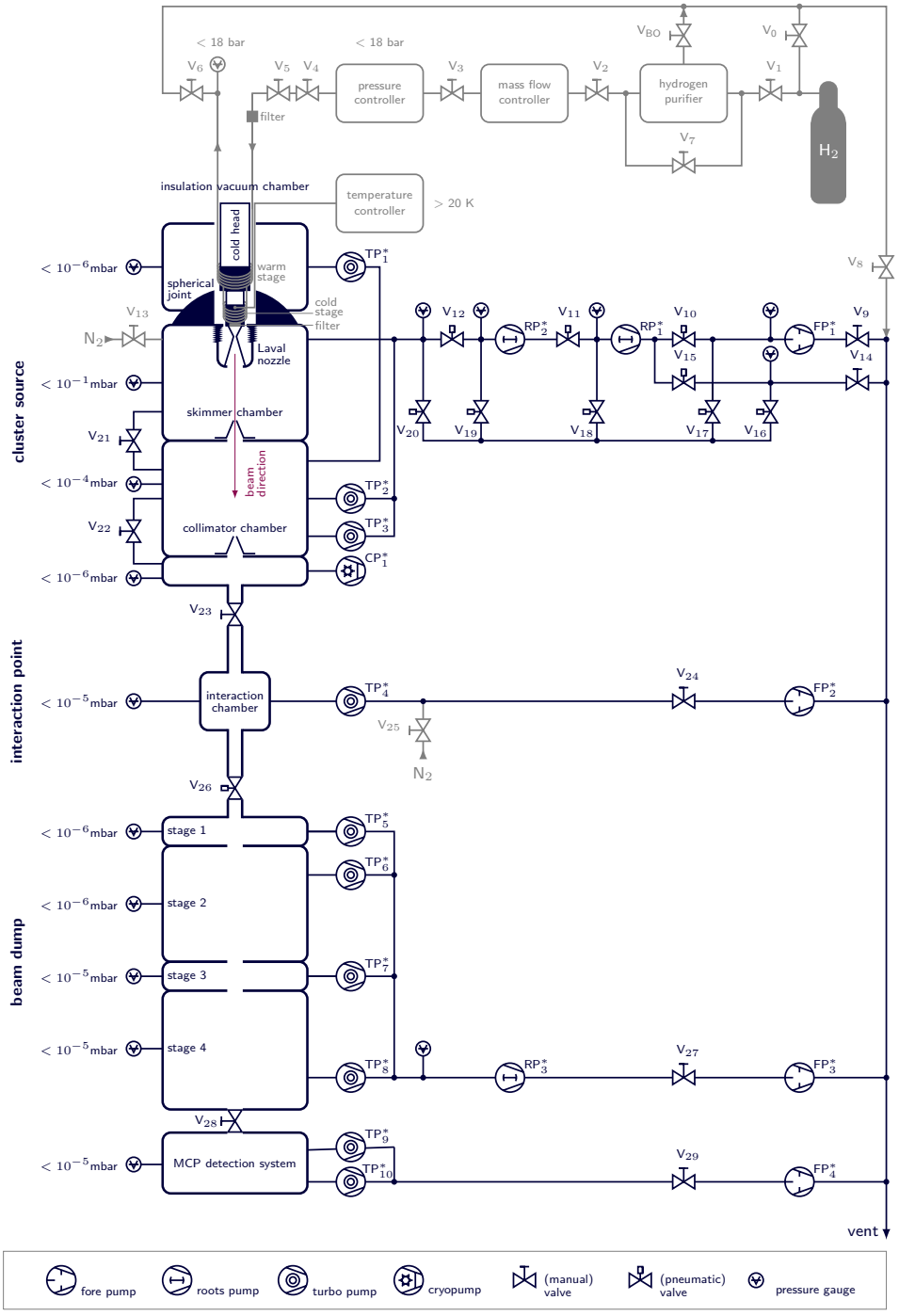

Figure A.5.: Updated schematic vacuum design of the cluster-jet target prototype for $\overline{\mathrm{P}}$ANDA. Fore pumps are denoted with $\mathsf{FP}^*_{\mathsf{no.}}$, roots pumps with $\mathsf{RP}^*_{\mathsf{no.}}$, turbomolecular pumps with $\mathsf{TP}^*_{\mathsf{no.}}$, cryopumps with $\mathsf{CP}^*_{\mathsf{no.}}$, and valves with $\mathsf{V}_{\mathsf{no.}}$ (except for the bleed out valve V_{BO}). Hydrogen gas H_2 is used as target material and nitrogen gas N_2 is applied to ventilate the target.

A.7. Beam stability

To investigate systematic effects at the retardation spectrometer (cf. Section 6.2) induced by the applied voltage source, test measurements with a grounded retardation grid were performed. The intensity of an ionised cluster-jet beam was recorded around 16 h and shows the stability of the cluster beam in conjunction with the electron beam.

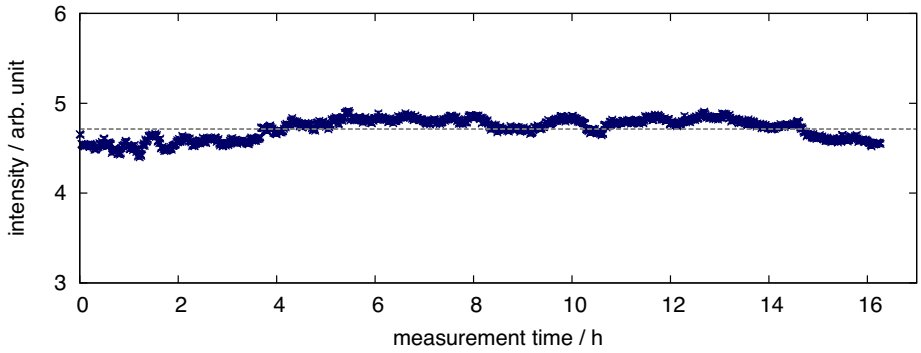

Figure A.6.: Temporal development of the cluster beam intensity with grounded retardation grid, which is around (4.7 ± 0.1) arb.unit.

A.8. Cluster mass distribution

The following Figures A.7 to A.10 show the development of the extracted cluster mass distribution (normalised to their height) of the isobars at 7 bar to 10 bar within 50 K and 80 K. The left-hand side shows the distribution in linear and the right-hand side in logarithmic mass scale. Furthermore, Tables A.2 to A.5 shows the average cluster size and standard deviation of the selected isobars, which are presented in Section 6.2.5. Two different collimator sizes were applied, 0.5 mm and 0.7 mm, whereas measurements with collimator diameter 0.7 mm are marked with *.

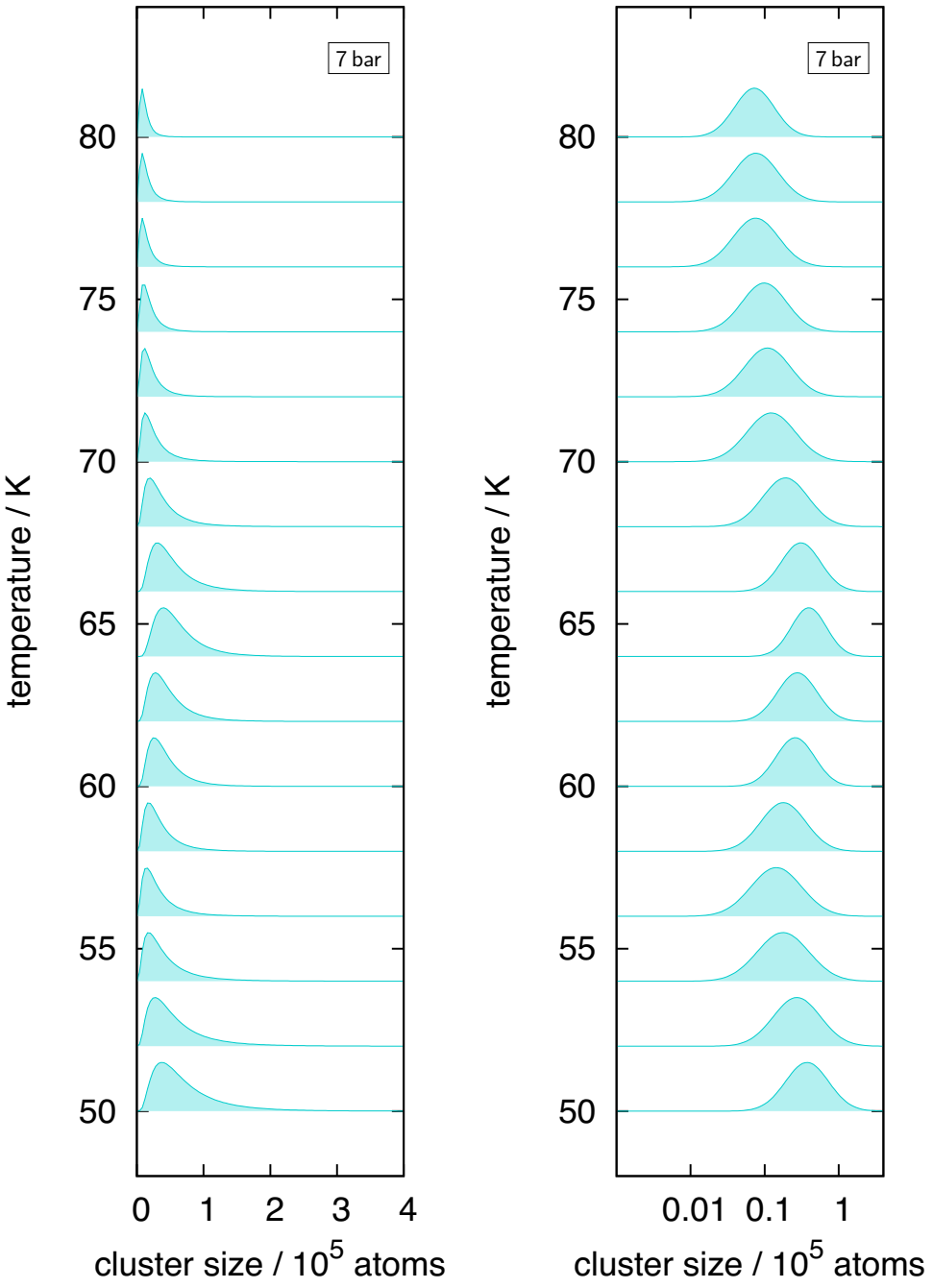

Figure A.7.: Development of the cluster mass distribution at 7 bar within 50 K and 80 K (in steps of 2 K) in linear (left) and logarithmic scale (right).

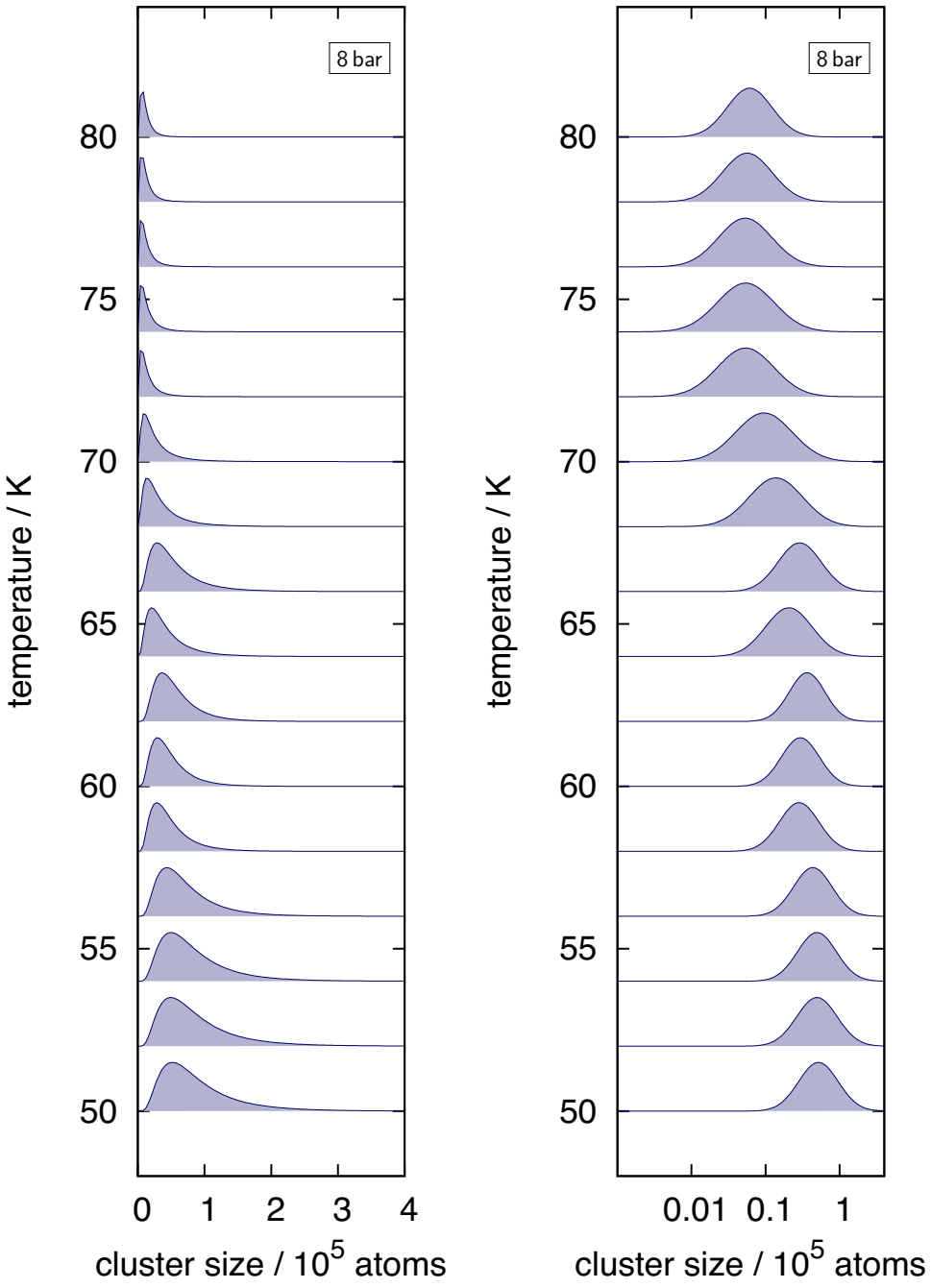

Figure A.8.: Development of the cluster mass distribution at 8 bar within 50 K and 80 K (in steps of 2 K) in linear (left) and logarithmic scale (right).

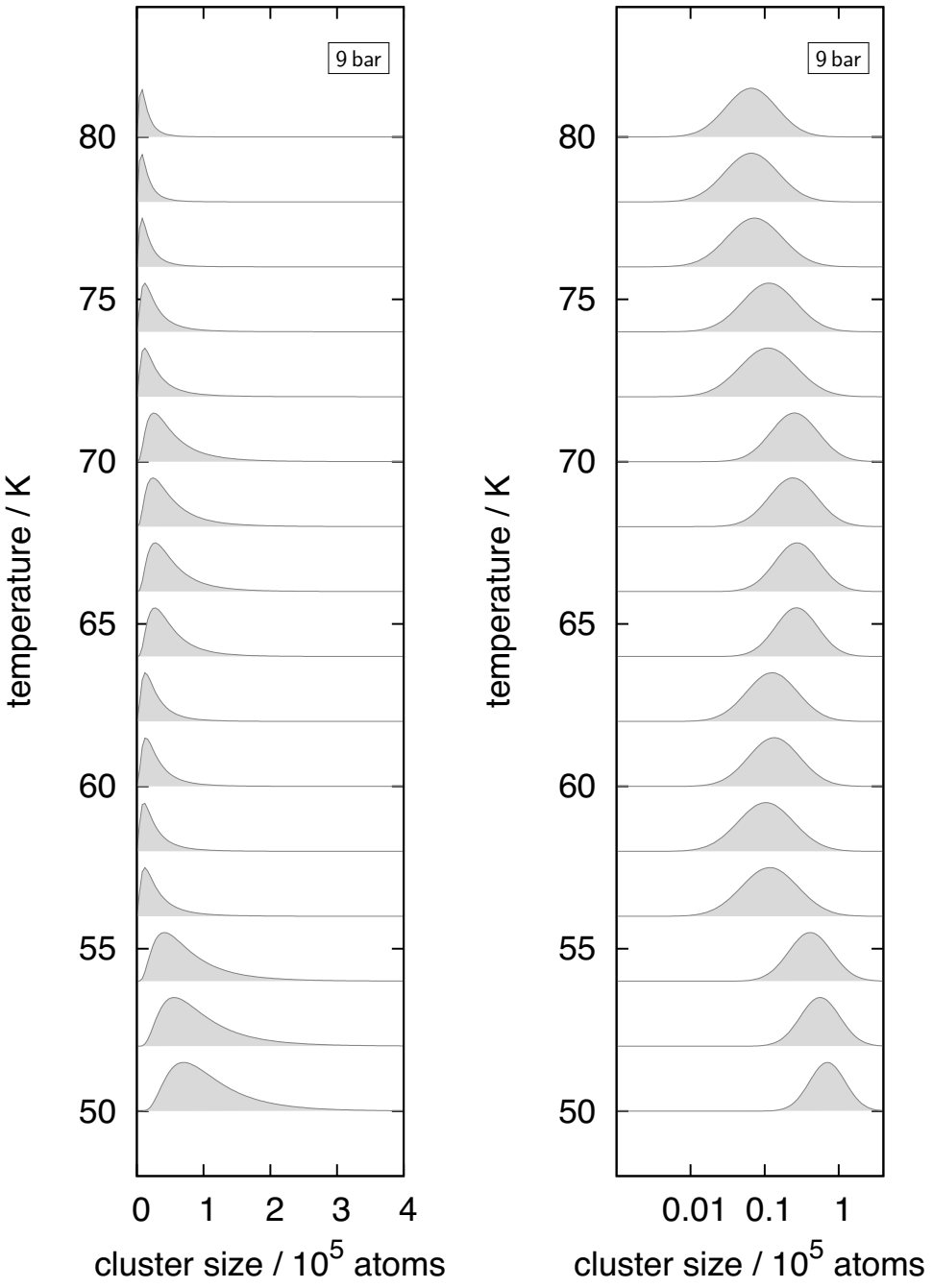

Figure A.9.: Development of the cluster mass distribution at 9 bar within 50 K and 80 K (in steps of 2 K) in linear (left) and logarithmic scale (right).

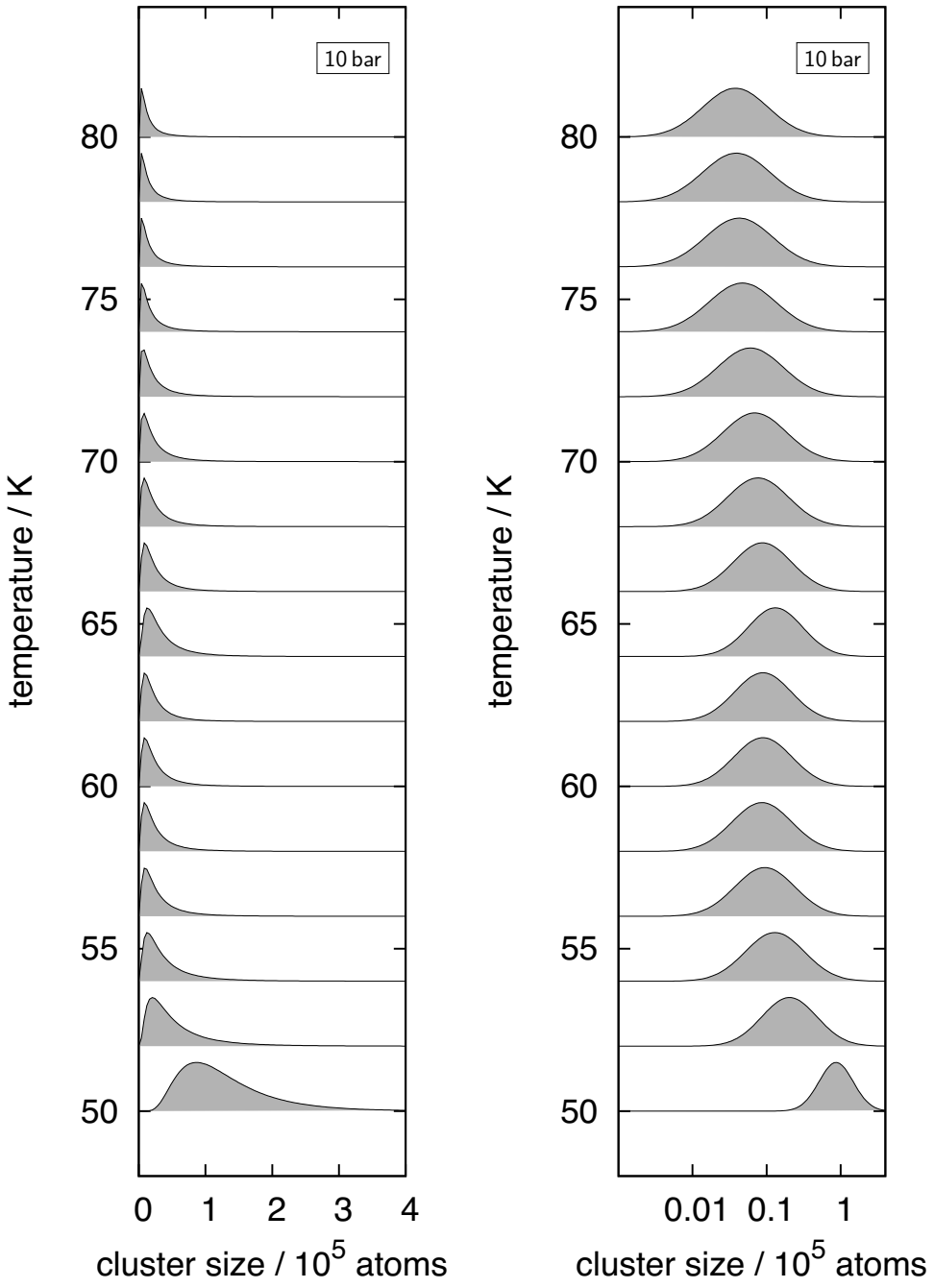

Figure A.10.: Development of the cluster mass distribution at 10 bar within 50 K and 80 K (in steps of 2 K) in linear (left) and logarithmic scale (right).

setpoint temperature in K (±0.01 K)	setpoint pressure in bar (±0.1 bar)	velocity in m/s	average cluster size in 10^5 atoms	standard deviation in 10^5 atoms
50	7	1020 ± 52	1.27 ± 0.03	1.46 ± 0.02
51	7	1029 ± 52	1.34 ± 0.03	1.48 ± 0.02
52	7	1038 ± 53	1.11 ± 0.03	1.40 ± 0.02
53	7	1047 ± 53	1.02 ± 0.11	1.52 ± 0.07
54	7	1056 ± 53	0.89 ± 0.09	1.25 ± 0.05
55	7	1065 ± 54	0.76 ± 0.03	1.11 ± 0.02
56	7	1074 ± 55	0.66 ± 0.02	0.91 ± 0.01
57	7	1083 ± 55	0.61 ± 0.01	0.70 ± 0.01
58	7	1092 ± 55	0.57 ± 0.01	0.63 ± 0.01
59	7	1100 ± 56	0.64 ± 0.08	0.64 ± 0.05
60	7	1109 ± 56	0.62 ± 0.01	0.55 ± 0.01
61	7	1118 ± 57	0.64 ± 0.01	0.56 ± 0.01
62	7	1126 ± 57	0.66 ± 0.01	0.60 ± 0.01
63	7	1134 ± 58	0.68 ± 0.01	0.62 ± 0.01
64	7	1143 ± 58	0.78 ± 0.02	0.59 ± 0.02
65	7	1152 ± 58	0.75 ± 0.02	0.61 ± 0.01
66	7	1160 ± 59	0.70 ± 0.02	0.61 ± 0.01
67	7	1169 ± 59	0.66 ± 0.02	0.56 ± 0.01
68	7	1177 ± 60	0.55 ± 0.01	0.56 ± 0.01
69	7	1185 ± 60	0.49 ± 0.01	0.48 ± 0.01
70	7	1193 ± 61	0.39 ± 0.01	0.43 ± 0.01
71	7	1201 ± 61	0.35 ± 0.01	0.37 ± 0.01
72	7	1209 ± 61	0.31 ± 0.01	0.32 ± 0.01
73	7	1217 ± 62	0.28 ± 0.01	0.28 ± 0.01
74	7	1225 ± 62	0.26 ± 0.01	0.25 ± 0.01
75	7	1233 ± 63	0.24 ± 0.01	0.22 ± 0.01
76	7	1242 ± 63	0.20 ± 0.01	0.20 ± 0.01
77	7	1250 ± 63	0.19 ± 0.01	0.19 ± 0.01
78	7	1258 ± 64	0.19 ± 0.02	0.18 ± 0.01
79	7	1266 ± 64	0.16 ± 0.02	0.18 ± 0.03
80	7	1274 ± 65	0.15 ± 0.03	0.12 ± 0.03

Table A.2.: Parameter list of the mass measurement series at 7 bar within 50 K and 80 K (in steps of 1 K) conducted with a collimator diameter of 0.5 mm.

setpoint temperature in K (±0.01 K)	setpoint pressure in bar (±0.1 bar)	velocity in m/s	average cluster size in 10^5 atoms	standard deviation in 10^5 atoms
50	8	1017 ± 52	1.48 ± 0.05	1.51 ± 0.04
51	8	1026 ± 52	1.49 ± 0.05	1.43 ± 0.04
52	8	1036 ± 53	1.42 ± 0.03	1.46 ± 0.02
53	8	1045 ± 53	1.29 ± 0.04	1.27 ± 0.03
54	8	1053 ± 54	1.29 ± 0.05	1.23 ± 0.04
55	8	1062 ± 54	1.18 ± 0.05	1.10 ± 0.04
56	8	1072 ± 54	1.08 ± 0.05	0.99 ± 0.04
57	8	1081 ± 55	0.83 ± 0.03	0.82 ± 0.02
58	8	1090 ± 55	0.72 ± 0.02	0.68 ± 0.01
59	8	1099 ± 56	0.68 ± 0.01	0.58 ± 0.01
60	8	1107 ± 56	0.68 ± 0.01	0.60 ± 0.01
60	8	1107 ± 56	0.68 ± 0.01	0.60 ± 0.01
61	8	1116 ± 57	0.71 ± 0.01	0.58 ± 0.01
62	8	1125 ± 57	0.75 ± 0.01	0.59 ± 0.01
63	8	1133 ± 58	0.79 ± 0.01	0.61 ± 0.01
64	8	1142 ± 58	0.67 ± 0.03	0.73 ± 0.02
65	8	1150 ± 58	0.72 ± 0.02	0.76 ± 0.01
66	8	1159 ± 59	0.77 ± 0.01	0.75 ± 0.01
67	8	1167 ± 59	0.68 ± 0.02	0.77 ± 0.01
68	8	1175 ± 60	0.59 ± 0.03	0.77 ± 0.01
69	8	1184 ± 60	0.57 ± 0.02	0.68 ± 0.01
70	8	1192 ± 61	0.52 ± 0.01	0.62 ± 0.01
70*	8	1192 ± 61	0.47 ± 0.03	0.68 ± 0.02
71*	8	1200 ± 61	0.32 ± 0.03	0.55 ± 0.03
72*	8	1208 ± 61	0.26 ± 0.04	0.45 ± 0.05
73*	8	1217 ± 62	0.26 ± 0.04	0.41 ± 0.04
74*	8	1225 ± 62	0.25 ± 0.04	0.41 ± 0.04
75*	8	1233 ± 63	0.22 ± 0.03	0.31 ± 0.04
76*	8	1241 ± 63	0.20 ± 0.03	0.28 ± 0.04
77*	8	1249 ± 63	0.19 ± 0.03	0.26 ± 0.04
78*	8	1257 ± 64	0.18 ± 0.04	0.21 ± 0.04
79*	8	1265 ± 64	0.17 ± 0.03	0.18 ± 0.03
80*	8	1273 ± 65	0.15 ± 0.04	0.15 ± 0.05

Table A.3.: Parameter list of the mass measurement series at 8 bar within 50 K and 80 K (in steps of 1 K) conducted with a collimator diameter of 0.5 mm and 0.7 mm (marked with *).

setpoint temperature in K (±0.01 K)	setpoint pressure in bar (±0.1 bar)	velocity in m/s	average cluster size in 10^5 atoms	standard deviation in 10^5 atoms
50	9	1014 ± 51	1.68 ± 0.02	1.50 ± 0.02
51	9	1023 ± 52	1.63 ± 0.03	1.51 ± 0.02
52	9	1033 ± 53	1.55 ± 0.03	1.54 ± 0.02
53	9	1042 ± 53	1.44 ± 0.03	1.54 ± 0.02
54	9	1051 ± 53	1.33 ± 0.03	1.47 ± 0.02
55	9	1060 ± 54	1.11 ± 0.03	1.44 ± 0.02
56	9	1070 ± 54	0.82 ± 0.06	1.46 ± 0.03
57	9	1079 ± 55	0.77 ± 0.05	1.30 ± 0.03
58	9	1088 ± 55	0.67 ± 0.04	1.15 ± 0.02
59	9	1097 ± 56	0.60 ± 0.03	0.96 ± 0.02
60	9	1105 ± 56	0.59 ± 0.02	0.79 ± 0.01
61	9	1114 ± 57	0.57 ± 0.03	0.72 ± 0.02
62	9	1123 ± 57	0.53 ± 0.03	0.70 ± 0.02
63	9	1132 ± 57	0.60 ± 0.03	0.71 ± 0.01
64	9	1140 ± 58	0.72 ± 0.02	0.70 ± 0.01
65	9	1149 ± 58	0.75 ± 0.02	0.74 ± 0.01
66	9	1157 ± 59	0.77 ± 0.02	0.78 ± 0.01
67	9	1166 ± 59	0.78 ± 0.02	0.82 ± 0.01
68	9	1174 ± 60	0.77 ± 0.02	0.84 ± 0.01
69	9	1182 ± 60	0.78 ± 0.02	0.83 ± 0.01
70	9	1190 ± 60	0.77 ± 0.02	0.82 ± 0.01
71	9	1198 ± 61	0.65 ± 0.02	0.78 ± 0.01
72	9	1207 ± 61	0.53 ± 0.02	0.74 ± 0.01
73	9	1215 ± 62	0.51 ± 0.01	0.65 ± 0.01
74	9	1224 ± 62	0.45 ± 0.01	0.56 ± 0.01
75	9	1231 ± 63	0.33 ± 0.02	0.47 ± 0.01
76	9	1240 ± 63	0.30 ± 0.01	0.41 ± 0.01
77	9	1248 ± 63	0.28 ± 0.02	0.35 ± 0.01
78	9	1255 ± 64	0.24 ± 0.01	0.31 ± 0.01
79	9	1263 ± 64	0.22 ± 0.02	0.27 ± 0.01
80	9	1271 ± 65	0.21 ± 0.01	0.24 ± 0.01

Table A.4.: Parameter list of the mass measurement series at 9 bar within 50 K and 80 K (in steps of 1 K) conducted with a collimator diameter of 0.5 mm.

setpoint temperature in K (±0.01 K)	setpoint pressure in bar (±0.1 bar)	velocity in m/s	average cluster size in 10^5 atoms	standard deviation in 10^5 atoms
50	10	1011 ± 51	1.94 ± 0.02	1.66 ± 0.02
52*	10	1030 ± 52	1.32 ± 0.09	2.14 ± 0.07
54*	10	1049 ± 53	1.13 ± 0.12	2.21 ± 0.09
56*	10	1067 ± 54	0.92 ± 0.13	2.04 ± 0.10
58*	10	1086 ± 55	0.77 ± 0.10	1.67 ± 0.08
60*	10	1103 ± 56	0.66 ± 0.08	1.28 ± 0.06
62*	10	1121 ± 57	0.57 ± 0.07	0.99 ± 0.05
64*	10	1138 ± 58	0.63 ± 0.03	0.88 ± 0.02
66*	10	1156 ± 59	0.54 ± 0.07	0.89 ± 0.05
68*	10	1172 ± 60	0.53 ± 0.07	0.98 ± 0.05
70*	10	1189 ± 60	0.53 ± 0.07	1.02 ± 0.05
72*	10	1206 ± 61	0.51 ± 0.06	1.05 ± 0.05
74*	10	1222 ± 62	0.42 ± 0.07	0.95 ± 0.09
76*	10	1239 ± 63	0.36 ± 0.06	0.80 ± 0.08
78*	10	1255 ± 64	0.30 ± 0.05	0.64 ± 0.08
80*	10	1271 ± 65	0.25 ± 0.05	0.48 ± 0.08

Table A.5.: Parameter list of the mass measurement series at 10 bar within 50 K and 80 K (in steps of 2 K) conducted with a collimator diameter of 0.5 mm and 0.7 mm (marked with *).

Bibliography

[A+95] Abe, F. et al.: *Observation of Top Quark Production in $\overline{p}p$ Collisions with the Collider Detector at Fermilab.* Phys. Rev. Lett., 74:2626–2631, Apr 1995.

[A+98a] Abele, A. et al.: *Exotic $\eta\pi$ State in antiproton-deuterium Annihilation at Rest into $\pi^-\pi^0\eta p_{spectator}$.* Phys. Rev. B, 423:175, 1998.

[A+98b] Adams, G. S. et al.: *Observation of a New $J^{PC} = 1^{-+}$ Exotic State in the Reaction $\pi^- p \to \pi^+\pi^-\pi^- p$ at 18 GeV/c.* Phys. Rev. Lett., 81:5760–5763, Dec 1998.

[A+98c] Allspach, D. et al.: *The variable density gas jet internal target for Experiment 835 at Fermilab.* Nucl. Instr. Meth. Phys. Res. Section A: Accelerators, Spectrometers, Detectors and Associated Equipment, 410(2):195–205, 1998.

[A+99] Abele, A. et al.: *Evidence for a $\pi\eta$-wave with odd angular momentum in antiproton-proton-annhilations at rest into $\pi^0\pi^0\eta$.* Phys. Rev. B, 446:349, 1999.

[A+02] Aubert, B. et al.: *The BABAR detector.* Nucl. Instr. Meth. Phys. Res. Section A: Accelerators, Spectrometers, Detectors and Associated Equipment, 479(1):1–116, 2002. Detectors for Asymmetric B-factories.

[A+04] Adam, H.-H. et al.: *Proposal for the Wide Angle Shower Apparatus (WASA) at COSY-Jülich.* Technical Report, Forschungszentrum Jülich, 2004.

[A+05a] Aubert, B. et al.: *Observation of a Broad Structure in the $\pi^+\pi_- J/\Psi$ Mass Spectrum around 4.26 GeV/c^2.* Phys. Rev. Lett., 95:142001, Sep 2005.

[A+05b] Aubert, B. et al.: *Study of the $B^- \to J/\psi K^-\pi^+\pi^-$ decay and measurement of the $B^- \to X(3872)K^-$ branching fraction.* Phys. Rev. D, 71:071103, Apr 2005.

[A+08] Asner, D. M. et al.: *Physics at BES-III.* Sep 2008. arXiv:0809.1869v1.

[A+09] Amsler, C. et al.: *New charmonium-like states.* Phys. Lett. B, 667(1), 2009. (Particle Data Group).

[A+13] Ablikim, M. et al.: *Observation of a Charged Charmoniumlike Structure in $e^+e^- \to \pi^+\pi- J/\Psi$ at $\sqrt{s} = 4.26$ GeV.* Phys. Rev. Lett., 110:252001, Jun 2013.

[Ams98] Amsler, C.: *Proton-antiproton annihilation and meson spectroscopy with the Crystal Barrel.* Rev. Mod. Phys., 70:1293–1339, Oct 1998.

[And90] Anderson, J. D.: *Modern Compressible Flow: With Historical Perspective.* McGraw-Hill, 1990.

[AT04] Amsler, C. and N.A. Törnquist: *Mesons beyond the naive quark model.* Phys. Rep., 389:61–117, 2004.

[B+90] Buchenau, H. et al.: *Mass spectra and time-of-flight distributions of helium cluster beams.* J. Chem. Phys., 92(11):6875–6889, 1990.

[B+99] Barberis, D. et al.: *A coupled channel analysis of the centrally produced K^+K^- and $\pi^+\pi^-$ final states in pp interactions at 450 GeV/c.* Phys. Lett. B, 462:462–470, Sep 1999.

[B+01] Barsov, S. et al.: *ANKE, a new facility for medium energy hadron physics at COSY-Jülich.* Nucl. Instr. Meth. Phys. Res. Section A: Accelerators, Spectrometers, Detectors and Associated Equipment, 462(3):364–381, 2001.

[B+11] Brambilla, N. et al.: *Heavy quarkonium: progress, puzzles, and opportunities.* Eur. Phys. J. C, 71(2):1–178, 2011.

[B+12a] Bondar, A. et al.: *Observation of Two Charged Bottomoniumlike Resonances in $\Upsilon(5S)$ Decays.* Phys. Rev. Lett., 108:122001, Mar 2012.

[B+12b] Brodzicka, Jolanta et al.: *Physics Achievements from the Belle Experiment.* Dec 2012. arXiv:1212.5342v1.

[Bel10] Belle II collaboration: *Belle II Technical Design Report.* Technical Report, Institute of Particle and Nuclear Studies, 2010. arXiv:1011.0352v1.

[Ber06] Bergmann, Schäfer: *Lehrbuch der Experimentalphysik, Gase, Nanosysteme, Flüssigkeiten*, volume 5. Walter de Gruyter, 2006.

[Ber09] Bergmann, F.: *Studien zum seltenen Zerfall des η-Mesons $\eta \to \pi^0 + e^+ + e^-$ am Experimentaufbau WASA-at-COSY.* Diploma thesis, Westfälische Wilhelms-Universität Münster, 2009.

[Ber14] Bernards, M., 2014. FAIR – Facility for Antiproton and Ion Research, private communication.

[BH65] Bauchert, J. and O.-F. Hagena: *Massenbestimmung ionisierter Agglomerate in kondensierten Molekularstrahlen nach einer elektrischen Gegenfeldmethode.* Z. Naturforschg., 20 a:1135–1142, 1965.

[BK96] Buck, U. and R. Krohne: *Cluster size determination from diffractive He atom scattering.* J. Chem. Phys., 105(13):5408–5415, 1996.

[BKS79] Bittner, G., W. Kretschmer and W. Schuster: *The Erlangen windowless high density gas target for nuclear scattering experiments.* Nucl. Instr. Meth., 161(1):1–8, 1979.

[B$^+$on] Beringer, J. et al.: *Review of Particle Physics.* Phys. Rev. D 86, 010001, 2012 and 2013 partial update for the 2014 edition. (Particle Data Group).

[BV64] Brunèe and Voshage: *Massenspektrometrie.* Verlag Karl Thiemig KG München, 1964.

[C$^+$89] Conover, C. W. S. et al.: *A time-of-flight mass spectrometer for large molecular clusters produced in supersonic expansions.* Rev. Sci. Instrum., 60(6):1065–1070, 1989.

[C$^+$99] Chung, S. U. et al.: *Evidence for exotic $J^{PC} = 1^{-+}$ meson production in the reaction$\pi^- p \to \eta\pi^- p$ at* 18 GeV/c. Phys. Rev. D, 60:092001, Oct 1999.

[C$^+$02] Chung, S.U. et al.: *Exotic and q anti-q resonances in the pi+ pi- pi- system produced in pi- p collisions at 18-GeV/c.* Phys. Rev. D, 65:072001, 2002.

[C$^+$03] Choi, S.-K. et al.: *Observation of a Narrow Charmoniumlike State in Exclusive $B^\pm \to K^\pm\pi^+\pi^- J/\psi$ Decays.* Phys. Rev. Lett., 91:262001, Dec 2003.

[C$^+$06] Chen, Y. et al.: *Glueball spectrum and matrix elements on anisotropic lattices.* Phys. Rev. D, 73:014516, Jan 2006.

[C$^+$08] Choi, S.-K. et al.: *Observation of a Resonancelike Structure in the $\pi^\pm\psi'$ Mass Distribution in Exclusive $B \to K\pi^\pm\psi'$ Decays.* Phys. Rev. Lett., 100:142001, Apr 2008.

[D$^+$97a] Diakonov, D. et al.: *Exotic anti-decuplet of baryons: prediction from chiral solitons.* Z. Phys. A Hadrons and Nuclei, 359(3):305–314, 1997.

[D$^+$97b] Dombrowski, H. et al.: *The Münster cluster target for internal storage ring experiments.* Nucl. Instr. Meth. Phys. Res. Section A: Accelerators, Spectrometers, Detectors and Associated Equipment, 386(2–3):228–234, 1997.

[D$^+$11] Dietrich, J. et al.: *Status of 2 MeV electron cooler for COSY-Jülich/HESR.* In *Sources and Medium Energy Accelerators.* Proceedings of 2011 Particle Accelerator Conference, New York, NY, USA, 2011.

[Dem13] Demmich, K.: *Energiekalibrierung des Vorwärtsdetektors an WASA-at-COSY unter besonderer Berücksichtigung der Reaktion* $p + d \rightarrow {}^3He + \eta'$. Master's thesis, Westfälische Wilhelms-Universität Münster, 2013.

[DKS08] Danylchenko, O.G., S.I. Kovalenko and V.N. Samovarov: *Experimental verification of the Hagena relation for large clusters formed in a conical nozzle.* Tech. Phys. Lett., 34(12):1037–1040, 2008.

[Dom89] Dombrowski, H.: *Entwicklung eines Cluster-Targets als internes Target an Speicherringen und Bedingungen der Clusterentstehung.* Diploma thesis, Westfälische Wilhelms-Universität Münster, 1989.

[DSM08] DeArmond, F. M., J. Suelzer and M. F. Masters: *Rayleigh scattering from argon clusters in a planar expansion.* J. Appl. Phys., 103(9), 2008.

[Eks95] Ekström, C.: *Internal targets — a review.* Nucl. Instr. Meth. Phys. Res. Section A: Accelerators, Spectrometers, Detectors and Associated Equipment, 362(1):1–15, 1995. Proceedings of the 17th World Conference of the International Nuclear Target Development Society.

[F+81] Farges, J. et al.: *Structure and temperature of rare gas clusters in a supersonic expansion.* Surf. Sci., 106(1–3):95–100, 1981.

[F+05] Fischer, U. et al.: *Tabellenbuch Metall.* VERLAG EUROPA LEHRMITTEL, 2005.

[Fri14] Fritzsch, C.: *Untersuchung verschiedener Normierungsreaktionen für dp-Kollisionen am ANKE-Experiment.* Master's thesis, Westfälische Wilhelms-Universität Münster, 2014.

[G+89] Gruber, A. et al.: *Internal gas-jet target for the ESR at GSI.* Nucl. Instr. Meth. Phys. Res. Section A: Accelerators, Spectrometers, Detectors and Associated Equipment, 282(1):87–93, 1989.

[Gau86] Gaul, G. Habilitation, Westfälische Wilhelms-Universität Münster, 1986.

[GE13] Gilardoni, S. and D. Manglunki (Editors): *Fifty years of CERN Proton Synchrotron.* CERN-2013-005, II, 2013.

[Gen08] General, S.: *Massenspektroskopische Untersuchung von Wasserstoffclustern am Münsteraner Cluster-Jet-Target.* Diploma thesis, Westfälische Wilhelms-Universität Münster, 2008.

[GF06a] GSI Helmholtzzentrum für Schwerionenforschung and Facility for Antiproton and Ion Research FAIR: *FAIR Baseline Technical Report, Executive Summary.* Technical Report, Sep 2006.

[GF06b] GSI Helmholtzzentrum für Schwerionenforschung and Facility for Antiproton and Ion Research FAIR: *An International Accelerator Facility for Beams of Ions and Antiprotons, Conceptual Design Report.* Technical Report, Sep 2006.

[GF09] GSI Helmholtzzentrum für Schwerionenforschung and Facility for Antiproton and Ion Research FAIR: *Green Paper - The modularised Start Version.* Technical Report, Okt. 2009.

[Glu05] GlueX collaboration: *The GlueX Experiment Design Report Version 5.* Technical Report, Sep 2005.

[Gos09] Goslawski, P.: *Hochpräzise Impulsbestimmung des COSY-Beschleunigerstrahls im Rahmen der Messung zur Bestimmung der η-Masse am Experimentaufbau ANKE.* Diploma thesis, Westfälische Wilhelms-Universität Münster, 2009.

[Gos13] Goslawski, P.: *High precision measurement of the η meson mass at COSY-ANKE.* Phd thesis, Westfälische Wilhelms-Universität Münster, 2013.

[Gri14] Grieser, S.: *The cluster-jet target MCT1S and the analysis of cluster beams.* Master's thesis, Westfälische Wilhelms-Universität Münster, 2014.

[Gri15] Grieser, S. Phd thesis, Westfälische Wilhelms-Universität Münster, 2015. in preparation.

[Hag81] Hagena, Otto F.: *Nucleation and growth of clusters in expanding nozzle flows.* Surf. Sci., 106(1–3):101–116, 1981.

[Hag87] Hagena, O.F.: *Condensation in free jets: Comparison of rare gases and metals.* Z. Phys. D Atoms, Molecules and Clusters, 4(3):291–299, 1987.

[Hag92] Hagena, Otto F.: *Cluster ion sources (invited).* Rev. Sci. Instrum., 63(4):2374–2379, 1992.

[Ham06] Hamamatsu: *MCP Assembly*, September 2006. Technical Information.

[Her13] Hergemöller, A.-K.: *Preparation of Cluster Beams and the Construction of the final Cluster Source for the $\overline{P}$ANDA Experiment.* Master's thesis, Westfälische Wilhelms-Universität Münster, 2013.

[Her15] Hergemöller, A.-K. Phd thesis, Westfälische Wilhelms-Universität Münster, 2015. in preparation.

[Het15] Hetz, B. Master's thesis, Westfälische Wilhelms-Universität Münster, 2015. in preparation.

[Hin08] Hinterberger, F.: *Physik der Teilchenbeschleuniger und Ionenoptik.* Springer, 2008.

[HO72] Hagena, O. F. and W. Obert: *Cluster Formation in Expanding Supersonic Jets: Effect of Pressure, Temperature, Nozzle Size, and Test Gas.* J. Chem. Phys., 56(5):1793–1802, 1972.

[Hus12] Husmann, C.: *Untersuchungen zur Optimierung der Dropleterzeugung innerhalb des Pellettargets des Experimentaufbaus WASA-at-COSY.* Diploma thesis, Westfälische Wilhelms-Universität Münster, 2012.

[Hö88] Hölker, G.: *Entwicklung eines Cluster-Targets als internes Target an Speicherringen.* Diploma thesis, Westfälische Wilhelms-Universität Münster, 1988.

[Hü13] Hüsemann, P.: *Operation and Upgrade of a Nozzle Test Rig combined with Investigations on Pentane Droplets.* Bachelor's thesis, Westfälische Wilhelms-Universität Münster, 2013.

[Hü14] Hüsken, N.: *Untersuchung der Reaktion p+d→ ^3He+η' am Experimentaufbau WASA-at-COSY.* Master's thesis, Westfälische Wilhelms-Universität Münster, 2014.

[I+01] Ivanov, E. I. et al.: *Observation of Exotic Meson Production in the Reaction $\pi^- p \to \eta' \pi^- p$ at 18 GeV/c.* Phys. Rev. Lett., 86:3977–3980, Apr 2001.

[Joh98] Johnson Matthey: *Technical Manual HE 20 Hydrogen purifier*, 1998. Gas Processing Technology.

[K+95] Knuth, E. L. et al.: *Supercooling of H_2 clusters produced in free-jet expansions from supercritical states.* J. Chem. Phys., 102(15):6258–6271, 1995.

[K+99] Khoukaz, A. et al.: *Systematic studies on hydrogen cluster beam production.* Eur. Phys. J. D - Atomic, Molecular, Optical and Plasma Physics, 5(2):275–281, 1999.

[K+05] Klempt, E. et al.: *The antinucleon–nucleon interaction at low energy: Annihilation dynamics.* Phys. Rep., 413(4–5):197–317, 2005.

[K+12] Knie, K. et al.: *Concept for the Antiproton Production Target at Fair.* In *Proceedings of IPAC2012*, 2012. New Orleans, USA.

[K+14a] Kamerdzhiev, V. et al.: *2 MeV electron cooler for COSY and HESR- first results.* Proceedings of IPAC2014, Dresden, Germany, 2014.

[K+14b] Khoukaz, A. et al.: *Two-dimensional visualization of cluster beams by microchannel plates.* Nucl. Instr. Meth. Phys. Res. Section A: Accelerators, Spectrometers, Detectors and Associated Equipment, 735(0):12–18, 2014.

[Kho92] Khoukaz, A.: *Arbeiten zum Aufbau eines Wasserstoff-Clustertargets.* Diploma thesis, Westfälische Wilhelms-Universität Münster, 1992.

[Kho96] Khoukaz, A.: *Messungen zur schwellennahen Produktion geladener Pionenpaare in der Proton-Proton-Streuung.* Phd thesis, Westfälische Wilhelms-Universität Münster, 1996.

[Kho00] Khokhlov, Yu.: *Study of $X(1600)$ 1^{-+} hybrid.* Nuclear Physics A, 663–664(0):596c–599c, 2000.

[Kle00] Klempt, E.: *Meson Spectroscopy: Glueballs, Hybrids and $Q\overline{Q}$ Mesons.* PSI Zuoz Summer School, Phenomenology of Gauge Interactions, 2000.

[KM72] Klingelhöfer, R. and H. O. Moser: *Production of large hydrogen clusters in condensed molecular beams.* J. Appl. Phys., 43(11):4575–4579, 1972.

[Köh10] Köhler, E. D.: *Das Münsteraner Cluster-Jet Target MCT2, ein Prototyp für das $\overline{P}ANDA$-Experiment, & die Analyse der Eigenschaften des Clusterstrahls.* Diploma thesis, Westfälische Wilhelms-Universität Münster, 2010.

[KZ07] Klempt, E. and A. Zaitsev: *Glueballs, hybrids, multiquarks - Experimental facts versus QCD inspired consepts.* Phys. Rep., 454:1–202, 2007.

[L+09] Leachman, J. W. et al.: *Fundamental Equations of State for Parahydrogen, Normal Hydrogen, and Orthohydrogen.* J. Phys. Chem. Ref. Data, 38(3):721–748, 2009.

[L+13] Liu, Z. Q. et al.: *Study of $e^+e^- \to \pi^+\pi - J/\Psi$ and Observation of a Charged Charmoniumlike State at Belle.* Phys. Rev. Lett., 110:252002, Jun 2013.

[Loh05] Lohrmann, E.: *Hochenergiephysik.* Teubner, 5th edition, 2005.

[McK88] McKeever, S. W.S.: *Thermoluminescence of solids.* Cambridge University Press, 1988.

[Mie07] Mielke, M.: *Untersuchung des ABC-Effekts in der Reaktion $p + d \to {}^3He + \pi^+ + \pi^-$ am Magnetspektrometer ANKE.* Diploma thesis, Westfälische Wilhelms-Universität Münster, 2007.

[MK02] Mayer-Kuckuk, T.: *Kernphysik - Eine Einführung.* Teubner, 7th edition, 2002.

[MP99] Morningstar, Colin J. and Mike Peardon: *Glueball spectrum from an anisotropic lattice study.* Phys. Rev. D, 60:034509, Jul 1999.

[N+10a] Nakamura, K. et al.: *Particle Physics Booklet.* J. Phys. G 37, 075021, 2010. (Particle Data Group).

[N+10b] Nakamura, K. et al.: *Review of Particle Physics.* J. Phys. G 37, 075021, 2010. (Particle Data Group).

[Noba] Nobelprize.org: *The Nobel Prize in Physics 1976.* http://www.nobelprize.org/nobel_prizes/physics/laureates/1976/.

[Nobb] Nobelprize.org: *The Nobel Prize in Physics 2008.* http://www.nobelprize.org/nobel_prizes/physics/laureates/2008/.

[Nobc] Nobelprize.org: *The Nobel Prize in Physics 2013.* http://www.nobelprize.org/nobel_ qprizes/physics/laureates/2013/.

[Nol05] Nolting, W.: *Grundkurs Theoretische Physik.* Springer, 2005.

[oSN] Standards, National Institute of and Technology (NIST): *The NIST Reference on Constants, Units, and Uncertainty.* http://physics.nist.gov/cgi-bin/cuu/Value?u.

[Ott07] Otte, J.: *Messung der Clustergeschwindigkeit und der Teilchendichte am Münsteraner Cluster-Jet-Target.* Diploma thesis, Westfälische Wilhelms-Universität Münster, 2007.

[P+08] Povh, B. et al.: *Teilchen und Kerne.* Springer, 8th edition, 2008.

[PAN05] PANDA Collaboration: *Technical Progress Report for the PANDA.* Technical Report, FAIR, 2005.

[PAN08a] PANDA Collaboration: *Technical Design Report for: PANDA Electromagnetic Calorimeter (EMC).* Technical Report, FAIR, 2008.

[PAN08b] PANDA Collaboration: *Technical Design Report for the PANDA Muon Detectors.* Technical Report, FAIR, 2008.

[PAN09] PANDA Collaboration: *Physics Performance Report for: $\overline{P}$ANDA, Strong Interaction Studis with Antiprotons*, March 2009.

[PAN12a] PANDA Collaboration: *Technical Design Report for the PANDA Internal Targets.* Technical Report, FAIR, 2012.

[PAN12b] PANDA Collaboration: *Technical Design Report for the PANDA Micro Vertex Detector.* Technical Report, FAIR, 2012.

[PAN12c] PANDA Collaboration: *Technical Design Report for the PANDA Straw Tube Tracker*. Technical Report, FAIR, 2012.

[Pap08] Papenbrock, M.: *Luminositätbestimmung und Untersuchung des $^3He\pi^0$ - Reaktionskanals bei d-p-Streuexperimenten am Experimentaufbau ANKE*. Diploma thesis, Westfälische Wilhelms-Universität Münster, 2008.

[Pau00a] Pauly, Hans: *Atom, Molecule, and Cluster Beams I*. Springer, 2000.

[Pau00b] Pauly, Hans: *Atom, Molecule, and Cluster Beams II*. Springer, 2000.

[Pfa86] Pfannkuche, H.-W.: *Arbeiten zur Entwicklung eines Cluster-Targets*. Diploma thesis, Westfälische Wilhelms-Universität Münster, 1986.

[Que97] Quentmeier, C. A.: *Aufbau eines Clustertargets und systematische Untersuchungen zur Clusterproduktion*. Diploma thesis, Westfälische Wilhelms-Universität Münster, 1997.

[R+97] Reich, H. et al.: *The ESR internal target*. Nuclear Physics A, 626(1–2):417–425, 1997. Proceedings of the Third International Conference on Nuclear Physics at Storage Rings.

[Rau04] Rausmann, T.: *Arbeiten zum Aufbau eines Clustertargets für 4π-Experimente an Speicherringen und Untersuchungen zur Clusterproduktion*. Diploma thesis, Westfälische Wilhelms-Universität Münster, 2004.

[RF73] Raoult, B. and J. Farges: *Electron Difraction Unit with Supersonic Molecular Beam and Cluster Beam*. Rev. Sci. Instrum., 44(4):430–434, 1973.

[S+08] Stassen, R. et al.: *The HESR RF-System and Tests in COSY*. In *Proceedings of EPAC08*, 2008. Genoa, Italy.

[Sch12] Schröer, D.: *Strahlzeitvorbereitungen zur Untersuchung der schwellennahen Produktion von η-Mesonen in der quasifreien Reaktion $p+d\rightarrow d+\eta+p_{spec}$ bei ANKE*. Master's thesis, Westfälische Wilhelms-Universität Münster, 2012.

[SDT98] Smith, R. A., T. Ditmire and J. W. G. Tisch: *Characterization of a cryogenically cooled high-pressure gas jet for laser/cluster interaction experiments*. Rev. Sci. Instrum., 69(11):3798–3804, 1998.

[SJ64] Smith, John Elvans and Myra Lee Jordan: *Mathematical and graphical interpretation of the log-normal law for particle size distribution analysis*. J. Colloid Sci., 19(6):549–559, 1964.

[T+79] Tietsch, W. et al.: *High density windowless gas jet target*. Nucl. Instr. Meth, 158(0):41–50, 1979.

[T+97] Thompson, D. R. et al.: *Evidence for Exotic Meson Production in the Reaction $\pi^- p \to \eta\pi^- p$ at* 18 GeV/c. Phys. Rev. Lett., 79:1630–1633, Sep 1997.

[T+07] Toelle, R. et al.: *HESR at FAIR: Status of Technical Planning.* In *Proceedings of PAC07*, 2007. Albuquerque, New Mexico, USA.

[T+11] Täschner, A. et al.: *High density cluster jet target for storage ring experiments.* Nucl. Instr. Meth. Phys. Res. Section A: Accelerators, Spectrometers, Detectors and Associated Equipment, 660(1):22–30, 2011.

[T+13] Täschner, A. et al.: *Determination of hydrogen cluster velocities and comparison with numerical calculations.* J. Chem. Phys., 139(23), 2013.

[tec] tectra GmbH Physikalische Instrumente: *MCP Detector 50 mm 40:1 MCP-50-D-R-P43.* data sheet.

[Tä12] Täschner, A.: *Entwicklung und Untersuchung von Cluster-Jet-Targets höchster Dichte.* Phd thesis, Westfälische Wilhelms-Universität Münster, 2012.

[vdH81] Hulst, H.C. van de: *Light scattering by small particles.* Dover, 1981.

[W+07] Winnemöller, A. et al.: *The WASA-at-COSY pellet target.* Technical Report, Forschungszentrum Jülich, 2007. Annual Report JUEL-4262.

[Wal12] Wallace, D. F.: *Das hier ist Wasser / This Is Water.* Kiepenheuer & Witsch, 5th edition, 2012.

[Wil96] Wille, K.: *Physik der Teilchenbeschleuniger und Synchrotronstrahlungsquellen*, volume 2. Teubner, 1996.

[Win11] Winnemöller, A.: *Analyse des verbotenen η-Meson Zerfalls $\eta \to \pi^0 + e^+ + e^-$ am Experimentaufbau WASA-at-COSY.* Phd thesis, Westfälische Wilhelms-Universität Münster, 2011.

[Wä88] Wähning, M.: *Entwicklung eines Monitorsystems zur Untersuchung von Dichteprofilen eines Gas-Jets.* Diploma thesis, Westfälische Wilhelms-Universität Münster, 1988.

[Y+06a] Yao, W.-M. et al.: *Note on Non $q\bar{q}$ Mesons.* J. Phys. G, 33(1), 2006. (Particle Data Group).

[Y+06b] Yao, W.-M. et al.: *PENTAQUARK UPDATE.* J. Phys. G, 33(1), 2006. (Particle Data Group).

[Y+07] Yuan, C. Z. et al.: *Measurement of the $e^+e^- \to \pi^+\pi^- J/\psi$ Cross Section Via Initial-State Radiation at Belle.* Phys. Rev. Lett., 99:182004, Nov 2007.

[Yua12] YUAN, C.Z.: *The Belle II Experiment at the SuperKEKB.* Aug 2012. arXiv:1208.3813v1.

[Zan13] ZANNOTTI, A.: *Implementation and test of fundamental production, adjustment, and detection components of the $\overline{P}ANDA$ cluster-jet target.* Bachelor's thesis, Westfälische Wilhelms-Universität Münster, 2013.

List of Figures

List of Tables

Acknowledgements

First and foremost, I would like to thank my supervisor, Prof. Dr. A. Khoukaz, not only for the great academic opportunity and inspiration, but also for his support, patience, and understanding. The last years in Münster contributed immensely to my professional and personal development.

I am obliged to Prof. Dr. D. Frekers for agreeing to be the co-examiner and to PD Dr. J. Heitger for being the third examiner for my dissertation.

I would never have studied physics without the encouragement of my former physics teacher B. Stratmann, thank you so much for that.

I would like to thank the people, past and present, of my working group, Florian, Stefan, Daniel B., Kay, Christopher, Silke, Ann-Katrin, Benjamin, Fabian, Nils, David, Marcel, Daniel S., Karsten, Lisa, Juliane, Michael E., Paul, Daniel G., Timo, Malte, Michael P., Julian, Alexander T., Alexander W., Alessandro and for the excellent and friendly collaboration. Thanks for your open ears, helpful advices, precious discussions, bad jokes and quotes, and especially for your help after the great storm in July 2014 and each fight against giant spiders. I also want to thank all my student interns, in particular Kendra and Theresa.

U. Mayer, W. Grundschöttel, W. Hassenmeier, N. Heine, H.-W. Ortjohann, thank you so much for your help and support in all questions. Furthermore, I would like to thank the mechanical workshop under the supervision of G. Bourichter and the electronics workshop under the supervision of R. Berendes for your excellent work. I would like to thank the $\overline{\text{P}}$ANDA and our target collaboration, especially Prof. Dr. H. Orth for his support and inspiration.

I am grateful for my target crew and especially for my target girls. Alexander, thank you so much for your professional advice and great support throughout this thesis. Daniel B., thank you for your technical advice, great ideas, perfectionism, and your patience (especially within the preparation of our target images). Benny, thank you for 'nickelige' fridays and your support and help in programming issues. Anky and Silke, my target

girls, thank you so much for your unlimited help, understanding, joy, and especially for your strong support throughout the last year. Anky, thanks a lot for running the student lab work, while I was focussing on my thesis.

Florian and Kay, thank you for being such excellent officemates. Special thanks to CF3 for your help and support within this thesis, hydrogen bottle changes, and the reconstruction of our drowned laboratory (although it would have been faster without you ;)). Nils, stay one of the good guys! I would like to thank Dr. Gosloveski for his honest and meticulous criticism and suggestions for this thesis. Thank you so much for your inspiration, understanding, and help, particularly in life matters. Jonas, thank you for your friendship and support within the last years and especially for the delicious lunch times.

I also want to thank all people, who always believed in me and crossed fingers for me, family Vollbrecht, family Schulz, family Schäfer, family Gamper-Shamsi, family Bette, Martin and Vroni, and the foxes.

I would also like to thank my beloved family, Mom, Dad, Almi, Phil, Karima, Angi, Aless, and Bubi for your love, support, and for always giving me a home. I'm thankful for having you all in my life.

Last but not least I would like to thank Nina and Steffi, for your indispensable friendship, for your help and support to fulfil my heart's wishes. You always give me strength and courage to face life's challenges. Thank you so much.

Eidesstattliche Erklärung

Ich versichere, dass ich die vorliegende Arbeit selbstständig verfasst und keine anderen als die angegebenen Quellen und Hilfsmittel benutzt habe. Die Stellen der Arbeit, die anderen Werken dem Wortlaut oder Sinn nach entnommen wurden, wurden unter Angabe der Quellen kenntlich gemacht.

Münster, 10.08.2015

.....
(Esperanza Diane Köhler)